Covariant Density Functional Calculations for Atomic Nuclei in the3-dimensional Coordinate Space

著者	Tanimura Yusuke
学位授与機関	Tohoku University
学位授与番号	11301甲第15993号
URL	http://hdl.handle.net/10097/58843

Doctor thesis

Covariant Density Functional Calculations for Atomic Nuclei in the 3-dimensional Coordinate Space

(3次元座標表示の相対論的密度汎関数計算に対する新しい方法)

Yusuke Tanimura

Department of physics, Tohoku University

August, 2014

Abstract

Density functional theory (DFT) has been successfully employed in nuclear physics in the past decades. It describes nuclear systems with a universal energy density functional, which in principle contains all many-body correlations. DFT is the only method at present which is able to describe atomic nuclei throughout the nuclear chart at a reasonable computational cost. One of the important features of DFT is that it describes the deformation of the intrinsic nuclear shape in a self-consistent way.

In nuclear DFT calculations, both the non-relativistic and the relativistic density functionals have been employed. Among them, the relativistic variant of DFT (Covariant Density Functional Theory: CDFT) has been attracting much of attention because of its success in several aspects in nuclear physics, which mainly originate from the most important underlying symmetry of quantum chromodynamics (QCD), that is, the Lorentz invariance. The saturation mechanism of nuclear matter, the large spin-orbit splittings which yield the shell structure of nuclei, and the origin of the pseudo-spin symmetry are consistently understood as consequences of a delicate balance between the large attractive scalar and repulsive vector mean fields in nuclear medium. The time-odd components in the mean field, which emerges in discussions of, e.g., rotating nuclei, nuclear magnetic moment, and odd-even mass staggering, are entirely fixed by the Lorentz symmetry, while the counterparts in the non-relativistic models have been pointed out to have some ambiguity.

In the non-relativistic calculations, the so-called imaginary time method has been successfully employed for solving problems in the three-dimensional (3D) coordinate-space representation, which can efficiently describe arbitrary nuclear shape. In contrast to the non-relativistic calculations, however, CDFT calculations in 3D coordinate space have not been realized yet. There are two problems called “variational collapse” and “fermion doubling”, which must be overcome in order to realize 3D calculations with CDFT. The former is related to the existence of negative energy nucleon states and the latter the formulation of a Dirac equation on lattice. Because of these difficulties, usually, relativistic calculations for deformed nuclei have been performed by expanding single-particle wave functions with harmonic oscillator (HO) basis. A drawback of this basis expansion method is that efficiency of the method depends on the shape and structure of nuclei, and one needs to optimize the parameters of the basis functions. Moreover, the HO basis is not suitable to describe a long asymptotic tail in the halo structure of unstable nuclei.

In order to describe unknown or exotic structure of nuclei, a development of flexible and efficient method not assuming any spatial symmetry is required. In this respect, 3D coordinate-space representation is advantageous, with which one is able to perform calculations for nuclei of any structure with a similar computational cost.

In this thesis, we develop a novel method for CDFT calculations on 3D lattice without the variational collapse and fermion doubling problems [1,2]. With our method, we realize for the first time relativistic calculations on 3D lattice without assuming any spatial symmetry.

With our new numerical code developed in this thesis, we study non-axial octupole de-

formation in the $N = Z = 30-40$ region in which octupole deformation is expected. This is the first application of the new code to provide a new result which is not easy to obtain with existing methods. We examine two nuclei, ^{68}Se and ^{80}Zr, and find, with a relativistic model, that the spherical shape of ^{80}Zr nucleus is unstable against the tetrahedral deformation, which is consistent with the result obtained with the previous non-relativistic calculations. On the other hand, the triangular deformation in the oblate ground state of ^{68}Se, which was observed in the non-relativistic calculations, is not observed in the present calculation.

We emphasize that our new relativistic 3D code allows us to study arbitrary shape of nuclei such as exotic deformations, halo structure, complicated shape of a fissioning nucleus, or even a cluster structure without any restriction on the spatial symmetry and without an increase of the numerical cost. Our new method will enable us to

- Study any complicated structure (halo, fission, exotic shape, ...) of nuclei with a single numerical code,
- Compare the results of relativistic models to those of non-relativistic models at the same level of the symmetry restriction,
- Give reliable theoretical predictions with relativistic models for unknown nuclei without missing symmetry-breaking solutions.

We consider that this is an important step to significantly extend the flexibility of the CDFT calculations.

[1] K. Hagino and Y. Tanimura, Phys. Rev. C **82**, 057301 (2010).

[2] Y. Tanimura, K. Hagino, and P. Ring, Phys. Rev. C **88**, 017301 (2013).

Contents

Chapter 1

Introduction

1.1 Theoretical methods for the nuclear many-body problem – an overview

An atomic nucleus is a quantum many-body system whose constituents are protons and neutrons. Since nucleons have spin and isospin degrees of freedom and a nucleon-nucleon interaction strongly depends on them, a nucleus exhibits rich phenomena involving these degrees of freedom. Correlations among nucleons induce variety of properties of a nucleus as a many-body system such as superfluidity, various collective excitations, and clustering.

Physics in unstable nuclei is one of the hot recent topics in nuclear physics. Recent developments of experimental facilities have opened up new possibilities to systematically explore unstable nuclei up to the vicinity of the neutron drip line in the light mass region, and revealed exotic structure in neutron-rich nuclei such as neutron skin and halo, disappearance of empirical shell structure, and excitation modes associated with the exotic structure. They have also stimulated theoretical efforts to interpret or predict characteristic structure properties in unstable nuclei.

There are several different theoretical approaches to the nuclear many-body problem. In Fig. 1.1 are shown three major theoretical methods and the corresponding mass regions of their applications. For very light nuclei, *ab initio* calculations [1] such as Green's function Monte Carlo [2–4], no-core shell model [5], coupled cluster theory [6] and stochastic variational approach [7] are possible. In these calculations, a many-body Schrödinger equation is exactly solved with a bare nucleon-nucleon interaction which reproduces the nucleon-nucleon scattering phase shift in free space.

Shell model (configuration interaction) approach with a truncated model space has been employed for light to medium heavy nuclei [8]. In the shell model calculation, an interaction is adjusted to experimental data in each mass region. Since the size of the model space rapidly grows up as a nucleus becomes heavier, an application of the method is still limited in the medium-mass region.

The density functional calculations are the only method at present which can be applied to the whole nuclear chart except for very light nuclei [9]. A universal energy density functional for nuclear many-body system, which is derived from a phenomenological effective interaction [10,11] based on the mean-field theory, is used in this class of calculations. It has been employed for studies of nuclear structure from light to the heaviest elements, and from valley of β-stability to the drip lines using the same energy density functionals throughout the nuclear chart.

1.2 Density functional theory (DFT) in nuclear physics

Among the three major theoretical methods shown in Fig. 1.1, we focus our topic on the DFT in this thesis. Density functional theory (DFT) has been successfully employed in nuclear physics in the past decades. The theory is based on a theorem [12,13] which shows the existence of universal energy density functional for many-body system, which in principle contains all many-body correlations. DFT was originally developed for many electron systems [12,14] and has been successful in condensed matter physics and quantum chemistry [13]. There are two remarkable advantages in DFT. First, it is guaranteed that there exists a universal energy density functional which is applicable to any nucleon many-body system [12,13]. Although the exact form of energy density functional for nuclear system is not known, phenomenological energy functionals have been built by fitting the parameters to experimental data, and they have been successful to reproduce the bulk properties of nuclear matter and finite nuclei. Second, since it reduces a problem of an interacting system to a problem of a non-interacting system, numerical cost increases moderately with the number of particles in the system [13,14]. Thanks to these advantages, DFT is the only method at present which is able to describe atomic nuclei in the whole nuclear chart at a reasonable computational cost. Energy functionals based on phenomenological effective interactions of Skyrme [10] or Gogny [11] types are used in non-relativistic calculations.

The relativistic variant of DFT (Covariant Density Functional Theory, CDFT) [13,15] has been employed as widely as the non-relativistic DFT in studies of nuclear structure. A covariant energy density functional is obtained from a Lorentz invariant model Lagrangian which describes an effective interaction among nucleons via meson exchanges. Relativistic treatment of nuclei has the several characteristic features mainly due to the Lorentz invariance, the most important underlying symmetry of quantum chromodynamics (QCD). CDFT has been attracting much attention because of its success in several aspects in nuclear physics. The saturation mechanism of nuclear matter [16,17], the large spin-orbit splittings which yields the shell structure of nuclei [17,18], and the origin of the pseudo-spin symmetry [19,20] are consistently understood as consequences of a delicate balance between the large attractive scalar and repulsive vector fields in nuclear medium. The time-odd components in the mean field, which emerges in discussions of, e.g., rotating nuclei, nuclear magnetic moment, and odd-even mass staggering, are entirely fixed by the Lorentz symmetry, [21,22], while the counterparts in the non-relativistic models have been pointed out to have some ambiguity [23].

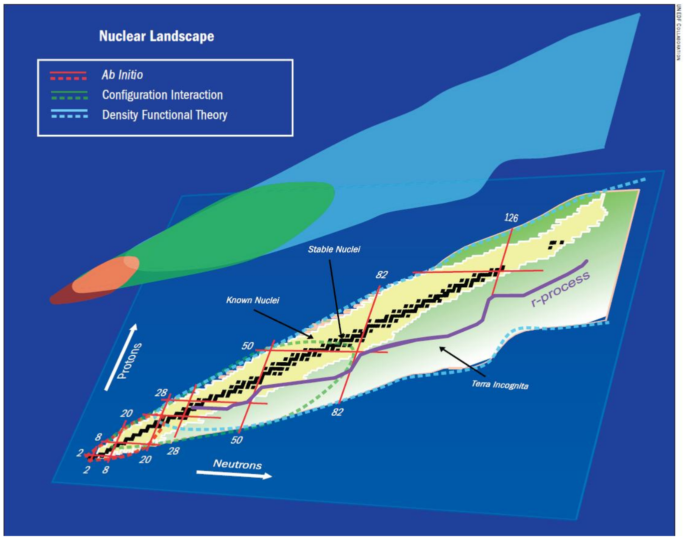

Figure 1.1: Theoretical methods for the nuclear many-body problem. The figure is taken from [9]. The black squares represent stable nuclei and the yellow squares indicate unstable nuclei which have been produced by experiments. The green squares (terra incognita) are nuclei yet to be explored. The red vertical and horizontal lines are located along the magic numbers for neutron and proton. The thick purple line shows the anticipated path of r-process which is responsible for synthesis of heavy elements in supernova phenomenon. The thick dotted lines indicate the domains of major theoretical approaches. For the lightest nuclei, ab initio methods with a bare nucleon-nucleon force are possible (red). Nuclei in medium heavy region are can be treated shell model (configuration interaction). Only the density functional calculations based on the mean-field theory can cover heavy nuclei as well as the light nuclei (blue).

1.3 Nuclear deformation and DFT

One of the important features of DFT is that it describes the spontaneous symmetry breaking in nuclear system in a self-consistent way. It is known that majority of nuclei are deformed from the spherical shape in their ground states. Static ground state deformation is expected in open-shell nuclei, whose proton and neutron numbers are far from the magic number $Z, N = 2, 8, 20, 28, 50, 82, 126, ...$

Deformed nuclei exhibit characteristic collective excitation spectra as compared to those in spherical nuclei. One example in low-lying collective excitation in deformed nuclei is the rotational band which is characterized by a sequence of low-lying states with excitation energies following the rule $E \propto J(J+1)$, where J is the spin of a nuclear state. Since a rotational motion around a symmetry axis is not allowed quantum mechanically, a spherical nucleus, which is symmetric around any axis passing through its center, does not have a ground-state rotational band. On the other hand, spherical nuclei exhibits a vibrational spectra in which the energies of second excited states are roughly twice that of the first excited state. Some typical vibrational states and rotational bands observed in even-even nuclei are shown in Fig. 1.2.

Another known experimental evidence of deformation which is observed in high-lying collective excitation is the splitting of the giant dipole resonance (GDR) observed in photonuclear reactions. The GDR is dipole oscillation of protons against neutrons induced by an external electromagnetic field. The peak energy is expected to split into two if the nucleus is, e.g., prolately deformed because an oscillation in the direction of the shorter axis has higher energy than an oscillation along the longer axis as shown in a schematic figure in Fig. 1.3. Fig. 1.4 shows the experimental data for the photoneutron cross sections of Nd isotopes. It shows an evolution of the GDR peak caused by adding neutrons from the closed-shell ($N = 82$) nucleus ^{142}Nd to the deformed ^{150}Nd nucleus whose resonance splits into two peaks.

Effect of deformation is also observed in the fusion reactions as an enhancement of fusion cross sections at subbarrier energies or a structure of the barrier distribution [25].

The nuclear deformation is driven by the shell structure of single-particle states. When valence nucleons partially occupies a degenerate single-particle orbital, and a symmetry breaking violates the degeneracy to lower some of the degenerate states in energy, the system spontaneously break the symmetry to gain more binding energy by placing the last particle on the lowered orbital. This is in analogy with the Jahn-Teller effect yielding a spontaneous symmetry breaking in molecules [26]. In heavy nuclei, the Coulomb repulsion among protons also prefers deformed shape to spherical shape, and it can make nuclei undergo a spontaneous fission. This is a classical effect whereas the former is a quantum mechanical effect.

The spontaneous symmetry breaking in the intrinsic shape of a nucleus discussed above can be described by DFT in a self-consistent way without, in principle, presuming any specific symmetry. In practical numerical calculations, one may assume certain symmetry, e.g., spherical, axial, or reflection symmetry, in order to reduce the computational cost. However, variety of deformation degrees of freedom are expected to play important roles in

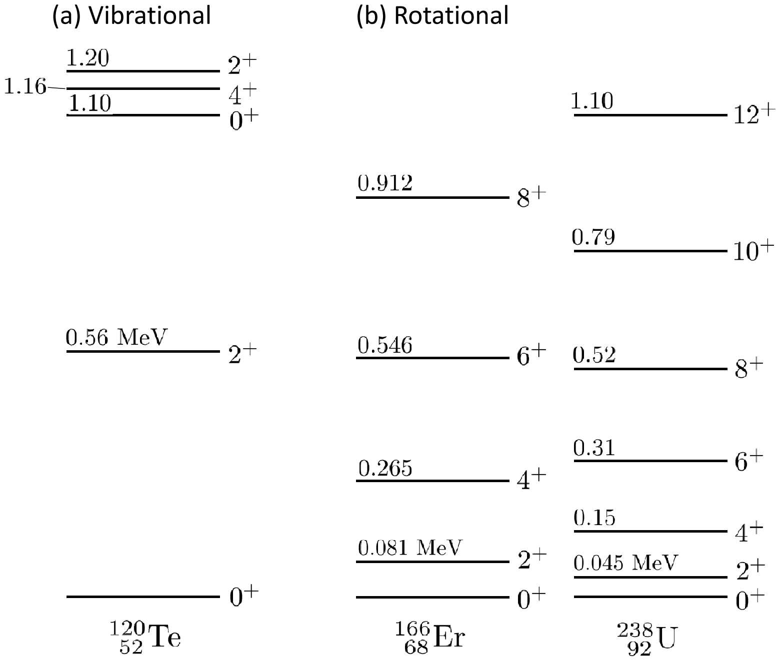

Figure 1.2: Some typical examples of (a) vibrational states and (b) rotational bands on top of the ground states of even-even nuclei. The values above each level are excitation energies in MeV

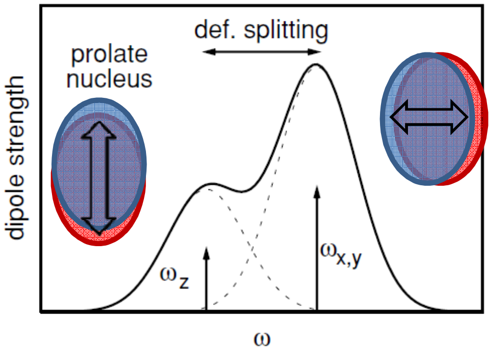

Figure 1.3: Schematic picture showing a splitting of a peak of a giant dipole resonance in prolately deformed nuclei. The higher peak ($\omega = \omega_{x,y}$) corresponds to an oscillation of protons against neutrons in the direction of the shorter axes, whereas the lower one ($\omega = \omega_z$) corresponds to a oscillation along the longer (symmetry) axis. The higher peak has larger fraction of the dipole strength because there are two different shorter axes.

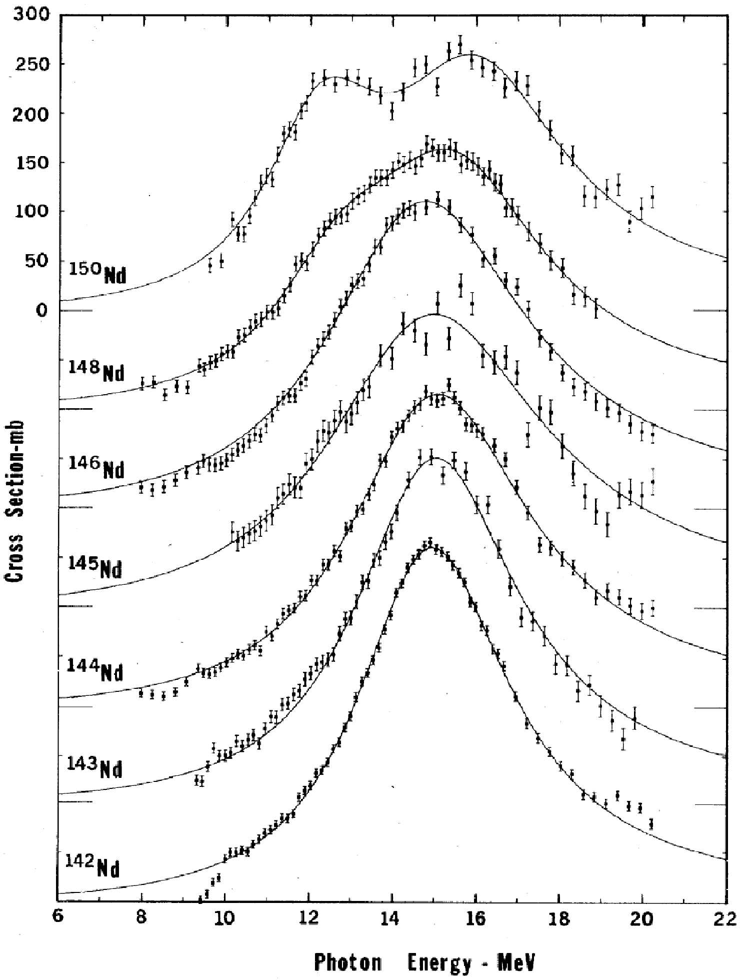

Figure 1.4: Total $(\gamma, 2n)$ cross sections of Nd isotopes which shows the evolution of the giant resonance from the closed shell $(N = 82)$ ^{142}Nd to deformed static deformation. The figure is taken from Fig. 27 in Ref. [24]

nuclear phenomena. For instance, deformation violating axial and reflection symmetries is pointed out to have significant effect on determination of height and position of the fission barriers and the fission path [27, 28], and exotic octupole, and even hexadecapole[1] deformations are expected in several regions on the nuclear chart [29–41]. Cluster states are expected to emerge in the excited states of *sd*-shell nuclei [42–47]. Thus flexible and efficient computational technique for DFT calculations allowing various deformations are needed in order to cover diverse nuclear phenomena.

There are two major numerical methods for DFT calculations, i.e., basis expansion and coordinate space calculations. In the former the wave functions are represented with a finite set of basis functions while in the latter wave functions are represented in the coordinate space, that is, the real space is discretized into lattice on which the value of the wave function is obtained. The coordinate space calculations are advantageous in its flexibility to describe any kind of deformations including exotic deformations or complicated cluster structure with a similar computational cost if the full real space is discretized into 3D lattice.

In the non-relativistic DFT, the so-called imaginary time method [48, 49] has been successfully employed for solving problems in the 3D coordinate space representation. It has been extensively applied to calculations not only for the ground states but also for excited states in atomic nuclei including global systematic calculations [50, 51], exotic excitation modes in neutron-rich nuclei [52], and exotic structure in high-spin states [53–55]. It is also recently applied to study of deformation of Λ hypernuclei [56]. It is also employed in a indirect way in deformed Hartree-Fock-Bogoliubov calculations through the two-basis method [35, 57].

In contrast to non-relativistic calculations, however, CDFT calculations in 3D coordinate space has not been realized yet because of two problems called "variational collapse" and "fermion doubling." The former is related to the existence of negative energy nucleon states and the latter the formulation of a Dirac equation on lattice.

Usually, relativistic calculations for deformed nuclei have been performed by expanding the single-particle wave functions with harmonic oscillator (HO) basis. A drawback of this basis expansion method is that efficiency of the method depends on the shape of nuclei, and one needs to optimize the parameters of the basis functions. Expansion by single-center basis is not very efficient for describing fission process or cluster structure in which nuclei takes complicated density distribution. Moreover, the HO basis is not suitable to describe a long asymptotic tail in the halo structure of unstable nuclei.

The most advanced implementations of deformed CDFT calculations have been realized in the following two schemes. The multi-dimensionally constrained (MDC) CDFT [27] with HO basis expansion, which allows all $Y_{\ell,m=\text{even}}$ deformations, is employed for studies of fission properties [28], tetrahedral deformation in heavy nuclei [40], and deformation

---

[1] Especially, tetrahedral(Y_{32}) and octahedral ($Y_{40} + Y_{44}$) deformations are expected to have strong shell effect due to the highly degenerate single-particle energies with such deformations [36–38]. The characteristic degeneracy is consequence of the fact that the point groups T_d and O_h, which are associated with the tetrahedral and octahedral symmetry, have high dimensional irreducible representations. See Sec. 7.2 and Appendix E.

properties of hypernuclei [58, 59]. Since it is based on HO basis expansion, it is not well suited for description of drip-line nuclei.

Another one is the deformed relativistic Hartree-Bogolibov theory in continuum, which takes into account the pairing correlation and continuum effects in very weakly-bound nuclei [60–62]. A discrete set of Woods-Saxon (WS) wave functions, which are obtained by using box boundary conditions to discretize the continuum states, are employed in stead of the HO basis so that the proper asymptotic behaviors of weakly-bound or continuum states are more efficiently described than the HO basis [63]. The method is applied to investigate deformed halo [60–62]. Since the computation of the matrix elements with the WS wave functions is much more time-consuming as compared to the HO basis, applications of the method is still limited to axially symmetric cases.

In order to describe unknown or exotic structure of nuclei, a development of flexible and efficient method not assuming any spatial symmetry is required. In this respect, 3D coordinate space calculation is advantageous, with which one is able to perform calculations for nuclei of any structure with a similar computational cost.

1.4 Difficulties in relativistic calculations

In this thesis we attempt to develop a new method for relativistic calculations on 3D lattice, which had been impossible because of some technical reasons. Here we focus on the difficulties in the relativistic calculations as compared to the non-relativistic models.

For more than 40 years, many people have preferred the non-relativistic mean field to relativistic mean field models. There are several reasons why the non-relativistic schemes have been widely chosen. The main reason might be that relativistic kinematics does not play an important role in nuclei since the Fermi momentum of nucleon is roughly 230 MeV, which is significantly smaller than the rest mass of the nucleon.

There are also two major technical reasons. The most crucial and unpleasant feature, which is widely recognized, in the relativistic mean field is the existence of the bottomless negative energy spectrum (Dirac sea) in the relativistic theory. In most of relativistic treatments, the densities are constructed with occupied Fermi sea states only, without the states in the Dirac sea (no-sea approximation), which means that the vacuum polarization effect is neglected [64]. With the no-sea approximation, the ground state mean-field solution always corresponds to a saddle point on the energy surface in the model space, while in the non-relativistic case the ground state corresponds to the absolute minimum [2]. It prevents the application of the standard iterative technique, that is, the imaginary time evolution [48, 49], for coordinate-space calculations which has been successfully employed in non-relativistic calculations. This is called a *variational collapse* (See Chapter 4), that

---

[2] In non-relativistic systems, a particle-hole excited state, which can be constructed by promoting nucleon(s) up to unoccupied states above the Fermi level, also corresponds to a saddle point on the energy surface. In a similar way, a relativistic ground state within the no-sea approximation is a saddle point which is minimum with respect to a variation within the subspace spanned by the positive energy states, but is maximum with respect to a variation within the subspace of negative energy states.

is, with a Dirac equation, an iterative solution inevitably dives into the Dirac sea during the imaginary time evolution, leading to a divergence of the solution.

Another big difficulty in relativistic calculations is the *fermion doubling* problem, which arises in the formulation of the Dirac equation on lattice in the real space, as long as the first derivative in the Dirac Hamiltonian is approximated by the finite difference (See Chapter 5). It has been well-known in the field of lattice quantum chromodynamics (QCD).

In addition, there are some disadvantages with computational cost. In relativistic treatment, the dimension of wave function is twice as that of a non-relativistic one due to the structure of a Dirac spinor, which requires more memory and numerical effort. In random phase approximation (RPA) calculations, it has been known [65] that one has to take into account not only usual particle-hole excitations formed by a hole in the occupied Fermi sea and a particle above the Fermi sea but also configurations with a hole in the Fermi sea and a particle in the empty Dirac sea. This also increases the numerical cost in relativistic RPA calculations compared to non-relativistic RPA.

1.5 Purpose of this work

Density functional calculations in the 3D coordinate space representation is an efficient and flexible method for investigating complicated structure of nuclei. It has been implemented in non-relativistic Skyrme Hartree-Fock calculations for a long time and extensively applied to studies of nuclear structure and excitations.

As seen in the preceding sections, however, relativistic density functional calculations on 3D lattice had not been realized in the past. Calculations for deformed systems have been performed only with basis expansion method, whose accuracy and efficiency depends on the structure of the solution. In addition to this, a drawback of HO basis expansion is that it is not suitable for describing weakly-bound nuclei, in which the wave function has a long asymptotic tail and the coupling to the continuum states becomes important. The Woods-Saxon basis is an alternative choice for such weakly-bound systems, but numerical cost for calculating the matrix elements becomes quite high, and its application is so far limited to axially symmetric cases.

In this thesis we propose a new iterative method for relativistic density functional calculations in the coordinate space representation, which can avoid the two major problems, variational collapse and fermion doubling. With our method we can realize a relativistic calculations on 3D coordinate space without assuming any spatial symmetry. Our new method will enable us to

- Study any complicated structure (halo, fission, exotic shape, cluster, ...) of nuclei with a single numerical code,

- Compare the results of relativistic models to those of non-relativistic models with the symmetry restriction at the same level,

- Give reliable theoretical predictions with relativistic models for unknown nuclei without missing symmetry-breaking solution.

As the first application of our new numerical code, we study non-axial octupole deformation in $N = Z = 30 - 40$ region for which octupole deformation is expected. In Refs. [33,34], Takami et al. showed that there are local minima in $^{68}_{34}\mathrm{Se}_{34}$ and $^{80}_{40}\mathrm{Zr}_{40}$ nuclei with non-axial octupole deformations by their Skyrme Hartree-Fock + BCS calculations, in which the pairing correlation is taken into account by the BCS approximation [66]. Afterwards, Yamagami et al. [35] have investigated the same nuclei with Skyrme Hartree-Fock-Bogoliubov calculations to give quite a similar results as in Refs. [33, 34]. However, in experiments no sign of octupole deformation, i.e., the negative parity bands [30], is observed for these two nuclei [67, 68]. Thus it is important to study the possibility of octupole deformations in those two nuclei with another interaction and clarify whether the conclusions in Refs. [33–35] holds independently to the nucleon-nucleon interaction.

The thesis is organized as follows. In Ch. 2, we introduce the important theorems in DFT and some numerical methods to perform DFT calculations. In Ch. 3, we introduce the relativistic variant of DFT and review the relativistic mean-field theory in nuclear physics. In Chs. 4 and 5, two major difficulties, variational collapse and fermion doubling in the coordinate space CDFT calculations are explained, and we give and discuss the strategies to overcome them. In Ch. 6, we perform numerical check of the validity and accuracy of our new 3D code with spherical nuclei. In Ch. 7, we apply our code to deformed nuclei and to a discussion of non-axial octupole deformation of ^{68}Se and ^{80}Zr nuclei. In Ch. 8, we summarize the thesis.

Chapter 2

Density Functional Theory

2.1 Basic theorems in the density functional theory

To find a solution of quantum many-body system is a challenging problem. In order to obtain the ground state of an N-body system, one may try to solve the many-body Schrödinger equation

$$\hat{H}\Psi(\boldsymbol{r}_1\sigma_1, \boldsymbol{r}_2\sigma_2, \ldots, \boldsymbol{r}_N\sigma_N) = E\Psi(\boldsymbol{r}_1\sigma_1, \boldsymbol{r}_2\sigma_2, \ldots, \boldsymbol{r}_N\sigma_N), \tag{2.1.1}$$

where $\hat{H}$ is the many-body Hamiltonian, E is the ground-state energy, and Ψ is the ground-state wave function. The variables $\boldsymbol{r}_i$ and σ_i denotes the coordinate and the z-component of spin of the i-th particle. In general, Eq. (2.1.1) is a complicated partial differential equation which involves $4N - 3$ independent variables. A numerical effort required to solve the Schrödinger equation becomes extremely high and not realistic with an increase of N up to, for instance, a few tens or a few hundreds that is typical in atomic and nuclear physics [69]. Hohenberg and Kohn have invented a theory in which the one-body density of the ground state, $\rho(\boldsymbol{r})$, plays an essential role instead of the wave function $\Psi(\boldsymbol{r}_1\sigma_1, \boldsymbol{r}_2\sigma_2, \ldots, \boldsymbol{r}_N\sigma_N)$ [12]. The starting point of any discussions of the density functional theory is the Hohenberg-Kohn (HK) theorem.

Let us consider a system of N interacting spin-1/2 particles with an external one-body field,

$$\hat{H} = \hat{T} + \hat{W} + \hat{V}_{\text{ext}}, \tag{2.1.2}$$

which consists of the kinetic energy

$$\hat{T} = \sum_{i=1}^{N} \frac{\boldsymbol{p}_i^2}{2m} = -\frac{\hbar^2}{2m} \sum_{\sigma=\uparrow,\downarrow} \int d^3r \ \hat{\psi}^\dagger(\boldsymbol{r}\sigma)\boldsymbol{\nabla}^2\hat{\psi}(\boldsymbol{r}\sigma), \tag{2.1.3}$$

an inter-particle interaction

$$\begin{aligned} \hat{W} &= \frac{1}{2}\sum_{i,j=1}^{N} w(\boldsymbol{r}_i, \boldsymbol{r}_j) & (2.1.4) \\ &= \frac{1}{2}\sum_{\sigma\sigma'}\int d^3r d^3r'\ \hat{\psi}^\dagger(\boldsymbol{r}\sigma)\hat{\psi}^\dagger(\boldsymbol{r}'\sigma')w(\boldsymbol{r},\boldsymbol{r}')\hat{\psi}(\boldsymbol{r}'\sigma')\hat{\psi}(\boldsymbol{r}\sigma), & (2.1.5) \end{aligned}$$

and an external field

$$\hat{V}_{\text{ext}} = \sum_{i=1}^{N} v_{\text{ext}}(\boldsymbol{r}_i) = \int d^3r\ v_{\text{ext}}(\boldsymbol{r})\hat{\rho}(\boldsymbol{r}), \tag{2.1.6}$$

$$\hat{\rho}(\boldsymbol{r}) = \sum_{\sigma}\hat{\psi}^\dagger(\boldsymbol{r}\sigma)\hat{\psi}(\boldsymbol{r}\sigma), \tag{2.1.7}$$

where we have also used the second-quantized expressions in terms of the field operator $\hat{\psi}(\boldsymbol{r}\sigma)$. The field operators $\hat{\psi}(\boldsymbol{r}\sigma)$ and $\hat{\psi}^\dagger(\boldsymbol{r}\sigma)$ describes the annihilation and creation of a particle at $\boldsymbol{r}$ with spin orientation σ, respectively. It satisfies the anticommutation relations

$$\begin{aligned} \left\{\hat{\psi}^\dagger(\boldsymbol{r}\sigma), \hat{\psi}^\dagger(\boldsymbol{r}'\sigma')\right\} &= \left\{\hat{\psi}(\boldsymbol{r}\sigma), \hat{\psi}(\boldsymbol{r}'\sigma')\right\} = 0, & (2.1.8) \\ \left\{\hat{\psi}(\boldsymbol{r}\sigma), \hat{\psi}^\dagger(\boldsymbol{r}'\sigma')\right\} &= \delta(\boldsymbol{r}-\boldsymbol{r}')\delta_{\sigma\sigma'}. & (2.1.9) \end{aligned}$$

Note that the one-body density $\rho(\boldsymbol{r})$ of the ground-state $|\Psi\rangle$ is given by

$$\rho(\boldsymbol{r}) = \langle\Psi|\hat{\rho}(\boldsymbol{r})|\Psi\rangle = \sum_{\sigma}\langle\Psi|\hat{\psi}^\dagger(\boldsymbol{r}\sigma)\hat{\psi}(\boldsymbol{r}\sigma)|\Psi\rangle. \tag{2.1.10}$$

The statement of the HK theorem is that the ground state $|\Psi\rangle$ is a unique and universal functional of the external field $v_{\text{ext}}(\boldsymbol{r})$, and that the ground-state density $\rho(\boldsymbol{r})$ is also a unique functional of the ground state $|\Psi\rangle$ [12,13,69], i.e., there is one-to-one correspondence among $v_{\text{ext}}(\boldsymbol{r})$ (or the Hamiltonian), $|\Psi\rangle$, and $\rho(\boldsymbol{r})$. Here, "universal" means that the same functional applies for any many-body system with a given inter-particle interaction $\hat{W}$. In Coulombic systems it means that a single unique functional is valid for any atoms, molecules, and solids, and in nuclear systems for any finite nuclei and nuclear matter. In other words, the ground-state density $\rho(\boldsymbol{r})$ uniquely determines $|\Psi\rangle$ and $v_{\text{ext}}(\boldsymbol{r})$ and thus it *in principle* contains the complete information of the full ground state and even those of the excited states, that is, the local one-body density $\rho(\boldsymbol{r})$ of the ground state is the most important variable in the theory.

The theorem also implies that, for a given $\hat{W}$, the ground-state expectation value of any observable is also given by a certain functional of the ground-state density,

$$\langle\Psi[\rho]|\hat{O}|\Psi[\rho]\rangle = O[\rho]. \tag{2.1.11}$$

In particular, the ground-state energy is a functional of the ground-state density

$$\langle \Psi[\rho] | \hat{H} | \Psi[\rho] \rangle = E[\rho], \tag{2.1.12}$$

which is often called an energy density functional (EDF). Notice that the HK theorem only guarantees the existence of a functional and does not tell its explicit form. In principle, an EDF, which must contain all the many-body correlations, does exists, and $\rho(\boldsymbol{r})$ minimizing the EDF is the exact ground-state density.

The so-called Kohn-Sham scheme [13, 14, 69] gives a way to perform DFT calculation based on a EDF. It renders the interacting N-particle problem into an auxiliary non-interacting N-particle problem. An auxiliary system in which each particle moves freely in an effective single-particle potential, $v_s(\boldsymbol{r})$, is considered. The density ρ_s and the kinetic energy T_s of the exact ground state for this auxiliary system is given by

$$\rho_s(\boldsymbol{r}) = \sum_{i=1}^{N} |\phi_i(\boldsymbol{r})|^2, \text{ and} \tag{2.1.13}$$

$$T_s[\rho] = \frac{\hbar^2}{2m} \sum_{i=1}^{N} |\boldsymbol{\nabla} \phi_i(\boldsymbol{r})|^2, \tag{2.1.14}$$

respectively, where $\phi_i(\boldsymbol{r})$ $(i = 1, ..., N)$ are the N lowest single-particle orbitals in $v_s(\boldsymbol{r})$. The single-particle orbitals are given by solving the Kohn-Sham equations

$$\left[-\frac{\hbar^2}{2m} \Delta + v_s(\boldsymbol{r}) \right] \phi_i(\boldsymbol{r}) = \epsilon_i \phi_i(\boldsymbol{r}) \tag{2.1.15}$$

Note that T_s is a unique functional of the ground-state density (or v_s) as a consequence of the HK theorem[1].

The assertion of the Kohn-Sham scheme [13, 69] is that for any interacting system, there exists a unique local single-particle potential, $v_s(\boldsymbol{r})$, such that the exact ground-state density of the interacting system equals the ground-state density of the auxiliary non-interacting system. The EDF is given by

$$E[\rho] = T_s[\rho] + E_{\mathrm{H}}[\rho] + E_{\mathrm{ext}}[\rho] + E_{\mathrm{xc}}[\rho], \tag{2.1.16}$$

where T_s as given in Eq. (2.1.14) is the kinetic energy of the *non-interacting* N-particle system, E_{H} is the Hartree energy, E_{ext} is the energy due to the coupling of the particles to the external field, and E_{xc} is *defined* by this equation as the exchange-correlation energy which contains everything else than E_{H} such as exchange effect and all the many-body correlations. The Hartree energy $E_{\mathrm{H}}[\rho]$ and the energy due to the external field $E_{\mathrm{ext}}[\rho]$ are respectively given as

$$E_{\mathrm{H}}[\rho] = \frac{1}{2} \int d^3r d^3r' \; w(\boldsymbol{r}, \boldsymbol{r}') \rho(\boldsymbol{r}) \rho(\boldsymbol{r}') \tag{2.1.17}$$

---

[1] The total energy E_s of the auxiliary system is given by $E_s = T_s + \int d^3r \; v_s(\boldsymbol{r})\rho(\boldsymbol{r})$, which is a unique functional of the ground-state density.

and

$$E_{\mathrm{ext}}[\rho] = \int d^3r \; v_{\mathrm{ext}}(\boldsymbol{r})\rho(\boldsymbol{r}), \tag{2.1.18}$$

and the corresponding local potentials are

$$v_{\mathrm{H}}[\rho](\boldsymbol{r}) = \frac{\delta E_{\mathrm{H}}}{\delta\rho(\boldsymbol{r})} \tag{2.1.19}$$

and

$$\frac{\delta E_{\mathrm{ext}}}{\delta\rho(\boldsymbol{r})} = v_{\mathrm{ext}}(\boldsymbol{r}). \tag{2.1.20}$$

Similarly the local exchange-correlation potential is given by

$$v_{\mathrm{xc}}[\rho](\boldsymbol{r}) = \frac{\delta E_{\mathrm{xc}}}{\delta\rho(\boldsymbol{r})}. \tag{2.1.21}$$

Thus

$$v_s[\rho](\boldsymbol{r}) = v_{\mathrm{ext}}(\boldsymbol{r}) + v_{\mathrm{H}}[\rho](\boldsymbol{r}) + v_{\mathrm{xc}}[\rho](\boldsymbol{r}). \tag{2.1.22}$$

Since v_s depends on the ground-state density, Eqs. (2.1.13), (2.1.15), and (2.1.22) have to be solved self-consistently.

In nuclear physics, the non-relativistic density functional calculations based on the mean field, or the Hartree-Fock theory with phenomenological effective interactions have been employed since 1970's, initiated by Vautherin and Brink [70]. In such calculations, an EDF is obtained in a phenomenological way. An effective two-body interaction with adjustable parameters are given by fitting the parameters to the empirical properties of nuclear matter and finite nuclei, and an total energy within the Hartree-Fock approximation, that is, the many-body ground state is approximated by a single Slater determinant, is calculated. The energy so obtained is interpreted as an approximate EDF for many-nucleon systems of the DFT sense, in which the exchange-correlation effect is taken into account through the parameter fitting. Thus, in the Hartree-Fock, or the mean-field theory with a phenomenological effective interaction, the Hartree and Fock (exchange) energies in the HF sense do not exactly correspond to the Hartree and exchange-correlation energies in the DFT sense, i.e., one cannot in principle separate the exchange-correlation energy from the HF energy.

2.2 Numerical solution of Kohn-Sham equations

Once an EDF is given, our task is to solve the single-particle Kohn-Sham (mean-field) equations

$$\hat{h}\phi_i = \epsilon_i\phi_i, \tag{2.2.1}$$

self-consistently, where $\hat{h}$ is the single-particle Hamiltonian $\hat{h} = -\hbar^2\nabla^2/2m + v_s(\boldsymbol{r})$. The self-consistent calculation for a A-particle system is performed by the following iterative procedure:

- Prepare a set of single-particle wave functions $\{|\phi_i\rangle\}$, and construct the density $\rho = \sum_{i=1}^{A} |\phi_i|^2$ and the single-particle Hamiltonian $\hat{h}$.

- Solve $\hat{h}\phi = \epsilon\phi$ (or somehow improve ϕ) to obtain a new set $\{|\phi_i\rangle\}$ consisting of the A lowest orbitals in the mean field.

- Construct a new density and single-particle Hamiltonian.

The second and the third steps are repeated until one gets a convergence.

In the following sections we illustrate the two major methods to solve the self-consistent mean-field equations, the basis expansion method and the imaginary time method for the 3D coordinate space representation.

2.2.1 Basis expansion method

One method to solve the KS equation is the basis expansion method. In this method the single-particle wave functions are represented by a truncated set of basis functions such as the harmonic oscillator (HO) basis and Woods-Saxon (WS) basis. The method has long been employed both in the non-relativistic [71] and relativistic calculations [72] since the early stages of the developments of mean-field calculations.

Let us denote the basis set by $\{|i\rangle\}$, $(i = 1, 2, ..., N)$, where the basis is assumed to be orthonormal $\langle i|j\rangle = \delta_{ij}$. The mean-field equation in the representation with the basis is given by

$$\sum_{j=1}^{N} \langle i|\hat{h}|j\rangle = \epsilon\langle i|\phi\rangle. \tag{2.2.2}$$

This is an eigenvalue problem and approximate eigenvalues and eigenstates of the Hamiltonian is obtained by a diagonalization. Thus the self-consistent iteration procedure described above proceeds with a diagonalization of the single-particle Hamiltonian within the truncated subspace spanned by $\{|i\rangle\}$.

A popular choice for the basis is the eigenfunctions of either spherical or deformed harmonic oscillator whose analytical form is known. All the HO basis functions have the gaussian tail at large distance from the origin. With the HO basis computation of the matrix elements is relatively simple because of its analytic form. However, the gaussian asymptotic tail of the HO basis is not suitable for weakly-bound nuclei, in which the long asymptotic tail of loosely-bound states and the coupling to the continuum states plays an important role in their structure.

Another choice of the basis is the set of Woods-Saxon (WS) wave functions, which are obtained by using box boundary conditions to discretize the continuum states. An advantage of the WS basis over the HO basis is its correct asymptotic behavior of the continuum states at large radius. A drawback is that computation of the matrix elements requires high computational cost since the basis could be obtained only numerically.

2.2.2 Imaginary time method for the 3D lattice

An alternative way to solve a single-particle Hamiltonian is to use the imaginary time step method [48]. Here we explain this method for non-relativistic Hartree-Fock calculations in the 3D coordinate space representation. It is an iterative method to obtain a self-consistent solution and the procedure goes as follows.

1. Prepare an initial set of single-particle wave functions $\{\psi_k^{(0)}\}$ $(k = 1, 2, ..., A)$. One could take, for example, a set of harmonic oscillator or Nilson wave functions. It can also be eigenstates in a (deformed) Woods-Saxon potential.
2. Construct the density $\rho^{(0)}$ and the single-particle Hamiltonian $h^{(0)}$ from the set of the single-particle wave functions.
3. Generate a new set of the single-particle wave functions, $\{\tilde{\psi}_k\}$, by applying the imaginary time evolutions on each wave functions:
$$|\tilde{\psi}_k\rangle = \exp(-\Delta\tau h^{(n+1/2)})|\psi_k^{(n)}\rangle, \; k = 1, \; \dots, \; A, \tag{2.2.3}$$
where $h^{(n+1/2)}$ is defined as $h^{(n+1/2)} = \frac{1}{2}(h^{(n)} + h^{(n+1)})$ for density-independent two-body interaction [48, 74]. In practical calculations, it is approximated by $h^{(n)}$ [49].
4. Orthonormalize the set $\{\tilde{\psi}_k\}$ to obtain $\{\psi_k^{(n+1)}\}$. Go back to the step 2.

The steps from 2 to 4 are iterated until a convergence is achieved. It is equivalent to a time-dependent Hartree-Fock (TDHF) equation

$$i\hbar\frac{\partial\psi_k}{\partial t} = h(t)\psi_k(t) \tag{2.2.4}$$

evolved in imaginary time, $t \to -i\tau$.

First we show that, for a given and fixed single-particle potential h, the imaginary time evolution of an arbitrary initial state leads to the ground state in h. It is of course assumed that the initial state is not orthogonal to the ground state. In other words, the iterative solution will converge to the lowest eigenstate which has non-vanishing overlap with the initial state. Let us denote the eigenvalues of h by ϵ_k and the associated eigenstates by $|\phi_k\rangle$. The initial state $\psi^{(0)}$ is evolved as follows,

$$\lim_{\tau\to\infty} \exp(-\tau h)|\psi^{(0)}\rangle = \lim_{\tau\to\infty} \sum_k \exp(-\tau\epsilon_k)\langle\phi_k|\psi^{(0)}\rangle|\phi_k\rangle, \tag{2.2.5}$$

where the initial state is expanded by $|\phi_k\rangle$ in the right hand side. From Eq. (2.2.5) it is clear that the state will converge to the lowest eigenstate $|\phi_1\rangle$ since the exponential factor is the largest for the state. As τ becomes larger, $|\phi_1\rangle$ grows up most rapidly among the eigenstates contained in the initial state. If one starts with a set of initial wave functions and apply the Gram-Schmidt orthogonalization that starts from the lowest energy state at each time step, the set converges to the lowest eigenstates. This is true because the

Gram-Schmidt method orthonormalizes the j-th state to the subspace spanned by the 1, 2, …, and $(j-1)$-th states. Notice that a shift of the Hamiltonian by a constant W: $h \rightarrow h - W$ gives no effect to speed-up in convergence. By the shift every component acquires exactly the same factor of $e^{-\tau W}$, which is removed by the orthonormalization.

Let us next consider a self-consistent problem. We can now show that, to the first order of the imaginary time step $\Delta\tau$, $h^{(n)}$ converges to the self-consistent solution by the procedure given above, following the proof given in Ref. [48]. The evolution of the wave functions by a small time step $\Delta\tau$ may be approximated by

$$|\tilde{\psi}_k^{(n+1)}\rangle = (1 - \Delta\tau h^{(n+1/2)})|\psi^{(n)}\rangle + O(\Delta\tau^2),\ \ k = 1,\ 2,\ \ldots, A. \tag{2.2.6}$$

With the Gram-Schmidt orthonormalization, one obtains the wave functions

$$|\psi_k^{(n+1)}\rangle = [1 + \Delta\tau(\epsilon_{kk}^{(n)} - h^{(n+1/2)})]|\psi_k^{(n)}\rangle - 2\Delta\tau \sum_{l<k} \epsilon_{lk}^{(n)} |\psi_l^{(n)}\rangle + O(\Delta\tau^2), \tag{2.2.7}$$

where the matrix elements of the Hamiltonian is denoted by $\langle\psi_k^{(n)}|h^{(n+1/2)}|\psi_l^{(n)}\rangle = \epsilon_{kl}^{(n)}$. The change in the density matrix from the n-th step to the $(n+1)$-th step is given by

$$\rho^{(n+1)} - \rho^{(n)} = \sum_{k=1}^{A} (|\psi_k^{(n+1)}\rangle\langle\psi_k^{(n+1)}| - |\psi_k^{(n)}\rangle\langle\psi_k^{(n)}|) \tag{2.2.8}$$

Substituting Eq. (2.2.7), we obtain

$$\rho^{(n+1)} - \rho^{(n)} = -\Delta\tau \left[\rho^{(n)} h^{(n+1/2)} (1 - \rho^{(n)}) + (1 - \rho^{(n)}) h^{(n+1/2)} \rho^{(n)}\right], \tag{2.2.9}$$

to the first order of $\Delta\tau$. Then the change in the HF energy is given by

$$\begin{aligned} E^{(n+1)} - E^{(n)} &= \mathrm{Tr}\left[h^{(n+1/2)}(\rho^{(n+1)} - \rho^{(n)})\right] && (2.2.10) \\ &= -2\Delta\tau \left[\rho^{(n)} h^{(n+1/2)} (1 - \rho^{(n)}) h^{(n+1/2)}\right]. && (2.2.11) \end{aligned}$$

Defining an operator $A^\dagger = \rho^{(n)} h^{(n+1/2)} (1 - \rho^{(n)})$, and using the cyclic property of the trace and the fact that ρ is a projection operator ($\rho^2 = \rho$), we have

$$\begin{aligned} \mathrm{Tr}(A^\dagger A) &= \mathrm{Tr}\left[\rho^{(n)} h^{(n+1/2)} (1 - \rho^{(n)})(1 - \rho^{(n)}) h^{(n+1/2)} \rho^{(n)}\right] && (2.2.12) \\ &= \mathrm{Tr}\left[\rho^{(n)} h^{(n+1/2)} (1 - \rho^{(n)}) h^{(n+1/2)}\right]. && (2.2.13) \end{aligned}$$

Thus we have found that

$$E^{(n+1)} - E^{(n)} = -2\Delta\tau \mathrm{Tr}(A^\dagger A) \leq 0, \tag{2.2.14}$$

that is, the total energy monotonically decreases as the system is evolved in imaginary time by a small step so that $O(\Delta\tau^2)$ can be ignored. The energy decreases down until $A^\dagger$ becomes equal to zero, i.e.,

$$[h^{(n+1/2)}, \rho^{(n)}]\rho^{(n)} = 0, \tag{2.2.15}$$

which is equivalent to the self-consistent condition

$$[h, \rho] = 0. \tag{2.2.16}$$

We have consequently shown that for values of $\Delta\tau$ sufficiently small to justify the linear expansion, the imaginary time step method results in a monotonic decrease in the HF energy, from iteration to iteration, until the density converges to the HF density.

2.3 Advantage of the coordinate space representation

In the preceding sections we have introduced the two major methods for the self-consistent solution of mean-field equations. Between them the 3D coordinate space (3D lattice) representation is preferable to the other because it has many advantages in various aspects due to its flexibility and simplicity compared to the basis expansion methods as described below.

First, the 3D lattice calculation can describe arbitrarily complicated shape of nuclei with similar computational cost and similar accuracy. A lattice representation is flexible in describing, e.g., exotic shapes along a fission path of nuclei or those occurring in heavy ion collisions. Although the accuracy of a solution depends on the parameters of the lattice, the mesh size and the box size, it is relatively easy to optimize them since the finer the mesh size is, the better the solution. The appropriate value for the box size can also be chosen easily depending and the size of the system. On the other hand, with the basis expansion method, accuracy of the solution depends on shape of the solution and the choice of parameters in the basis, such as the oscillator lengths, in a complicated way and the parameter optimization is much more difficult than in the coordinate space representation. For example, one may have to change the parameters of the basis depending on the deformation of the solution so that energy of the solution is minimized. With a careless choice of the parameters, it may happen in a deformation constraint calculation that accuracy is different from one point to another point on a potential energy surface (see Sec. 2.4). At a point on a fission path where the nucleus is about to fission into two fragments, two-center basis may be more appropriate choice, but the number of the parameter increases to make the optimization more complicated (see Fig. 2.1). The situation becomes even worse if the proton and neutron density distributions are considerably different, in which case the dimension of the parameter space is squared. On the 3D lattice, one does not face any of the difficulties illustrated above.

Second, the halo structure in weakly-bound nuclei can also properly be described with the mesh representation since wave function can have arbitrary asymptotic behavior at large distance. The halo structure is characterized by an anomalously long tail in the density distribution as the one shown in Fig. 2.2. Fig. 2.2 shows calculated neutron and proton densities in a logarithmic scale for neutron-rich nuclei. For the solid lines in the Figure (coordinate space calculations) one can see neutron halo structures, where the density distribution has an exponentially decaying long tail. However, the results with HO basis in Fig. 2.2 (dashed line) quickly fall down as compared to the coordinate results due to its asymptotic Gaussian form. The HO basis with the Gaussian tail is not efficient to describe neither a weakly-bound or a continuum single-particle states which plays important roles in formation of halo structure [60,61]. The WS basis is an alternative choice but the computational cost to calculate the matrix elements becomes quite high.

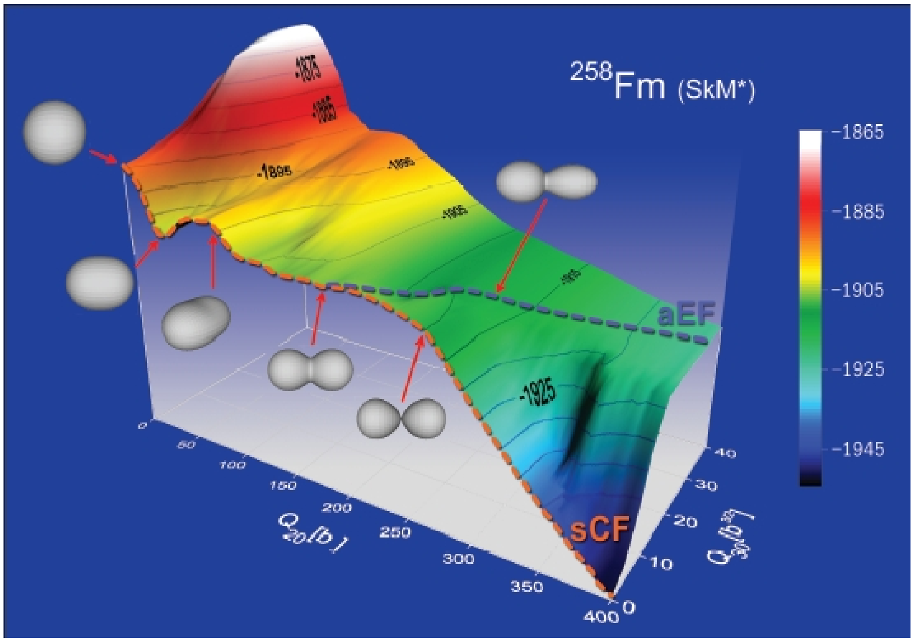

Figure 2.1: Calculated potential energy surface of ^{258}Fm nucleus as a function of quadrupole and octupole moments. Various complicated shapes emerges on fission paths. The figure is taken from Ref. [9].

2.4 Constrained mean-field calculations

The numerical techniques introduced in this chapter are employed to investigate not only spherical nuclei but also deformed nuclei. In the discussions of deformation property or fission property of a nucleus, one needs not only the energy minimum but also more global information such as the curvature and the height of the barrier between local minima in the total energy of the system as a function of its deformation. Such a function $E = E(q)$, where q is a certain deformation parameter(s), is called potential energy curve (PEC) or potential energy surface (PES, in the case more than one deformation are considered). In order to obtain a PES, we need to find a mean-field solution $|\Phi(q)\rangle$ which minimizes energy under a condition that

$$q = \langle\Phi|\hat{Q}|\Phi\rangle \tag{2.4.1}$$

takes the desired value $q = q^0$. $\hat{Q}$ is an appropriate operator to get the deformation of the system.

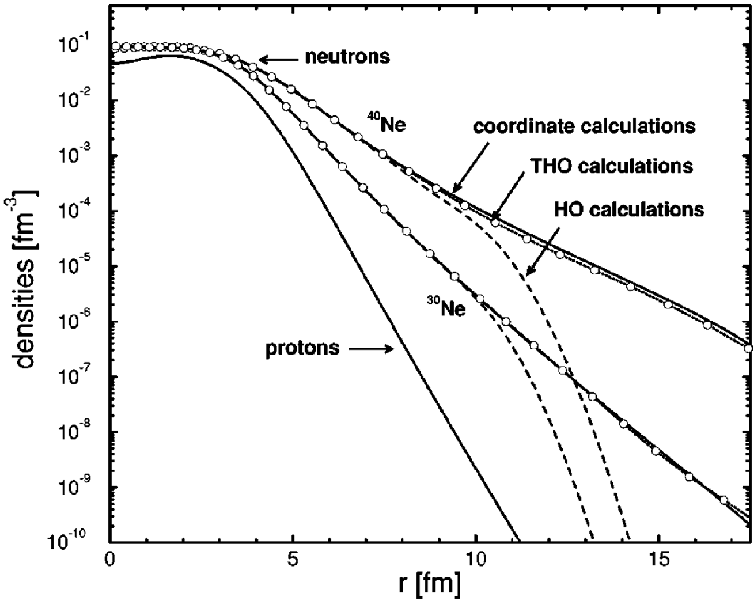

Figure 2.2: Self-consistent proton and neutron densities for the ground states of ^{30}Ne and ^{40}Ne nuclei obtained with relativistic Hartree-Bogoliubov calculations. Neutron densities calculated with HO basis are shown with the dashed lines. The solid line shows the densities obtained in the coordinate space calculations. The solid line with the open circles are obtained with the transformed HO (THO) basis introduced in Ref. [75]. Proton densities are practically the same between the two nuclei. The figure is taken from Fig. 2 of Ref. [75].

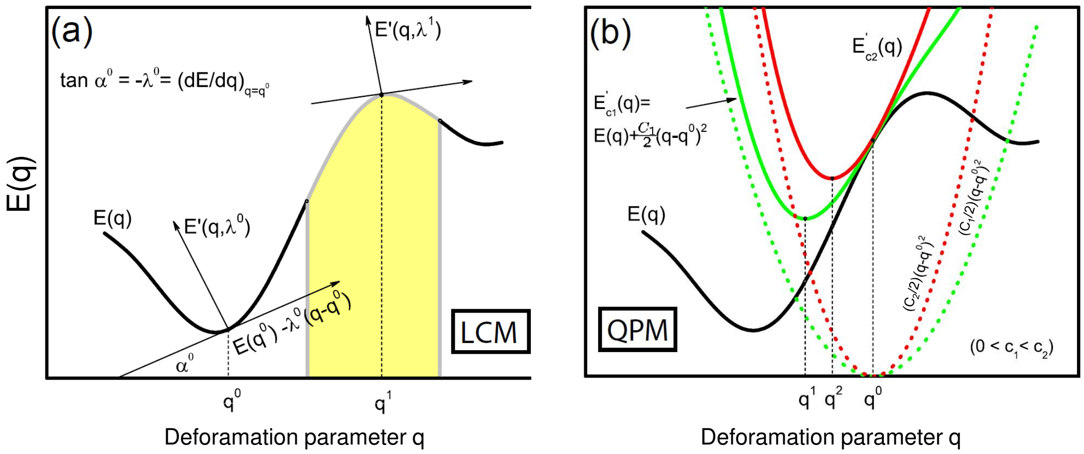

Figure 2.3: Schematic figures showing (a) geometric interpretation of the linear constraint method (LCM). This method is not applicable to the yellow shaded region, where the PEC $E(q)$ is concave. (b) Behavior of the penalty function for one-dimensional quadratic penalty method (QPM). The figure was taken from Fig. 1 of Ref. [76].

2.4.1 Linear constraint method (LCM)

A simple way to obtain a solution with a desired deformation is the linear constraint method (LCM) [66, 76], in which a variation of the following functional yields $|\Phi(q^0)\rangle$:

$$E'(q,\lambda) = E(q) + \sum_{i=1}^{m} \lambda_i (q_i - q_i^0), \tag{2.4.2}$$

where E is the expectation value of the original Hamiltonian, q_i and q_i^0 are the deformation parameters and their desired values, respectively, and m is the number of constraints. See Fig. 2.3 (a) for a schematic picture to show the LCM. It shows a simple one-dimensional case with only a single deformation parameter q to be constrained. With the additional term in Eq. (2.4.2), one draws a line tangent to the PES at $q = q^0$, and uses this line as a new "x-axis" of the coordinate system which is obtained by rotating the frame by an angle α_0 ($\tan\alpha_0 = \lambda$), then the "y-axis" corresponds to E' in Eq. (2.4.2). Thus minimization leads to the desired solution $|\Phi(q^0)\rangle$ which has the desired deformation. However, this method clearly fails when the PES is concave around $q = q^0$ (shaded region in Fig. 2.3 (a)), where E' is maximum rather than minimum at $q = q^0$. The LCM is only applicable in the region where PES is convex.

2.4.2 Quadratic penalty method (QPM)

An alternative method is the quadratic penalty method (QPM). What one should minimize in this case is

$$E'_C(q) = E(q) + \sum_{i=1}^{m} \frac{1}{2} C_i (q_i - q_i^0)^2, \tag{2.4.3}$$

where $C_i > 0$ is the penalty parameter which gives a positive additional contribution to the energy when q is different from its desired value q^0. This method is applicable even if the curvature of PES at $q = q^0$ is negative as long as $C > |d^2E/dq^2|$ which is necessary for a local convexity of E' at $q = q^0$. In Fig. 2.3 (b) we show a schematic picture again showing a one-dimensional case. The PEC $E(q)$ is drawn with a black solid line, while the quadratic penalty function is plotted with dashed lines around the desired point q^0 for two different values C_1 and C_2 of the penalty parameter C. The resulting function E' is indicated by colored solid lines. It is immediately seen in Fig. 2.3 (b) that the minimum of E' is shifted from q^0 to different values q_1 and q_2 corresponding to the penalty parameter C_1 and C_2, respectively. In the limit $C \to \infty$ the minimum of E' corresponds exactly to q^0. Thus one may take a large value in order to reduce the shift but there is no way in advance to know an appropriate values for C_i to constrain the deformations to a sufficient accuracy.

2.4.3 Augmented Lagrangian method (ALM)

Since the two methods introduced in the last two sections have drawbacks in constraining the deformations, we employ in our constrained mean-field calculations the augmented Lagrangian method (ALM) [76], which can be viewed as a combination of the LCM and QPM. In the ALM one minimizes

$$E'(q) = E(q) + \sum_{i=1}^{m} \left[\lambda_i (q_i - q_i^0) + \frac{1}{2} C_i (q_i - q_i^0)^2 \right] \tag{2.4.4}$$

In this case the resulting mean-field Hamiltonian is given by

$$h' = h + \sum_{i=1}^{m} [\lambda_i + C_i (q_i - q_i^0)] \hat{Q}_i \tag{2.4.5}$$

The value of λ is updated during the self-consistent iteration. It is changed from the k-th step to the the next as [76]

$$\lambda_i^{k+1} = \lambda_i^k + C_i (q_i - q_i^0), \tag{2.4.6}$$

where q_i is the value of a deformations parameter at the k-th step. The λ effectively changes the strength of the constraint potential so that the deformations converge precisely to the desired values. The iterations can start from a zero value, $\lambda^0 = 0$. It is numerically shown in Ref. [76] that the ALM yields very precisely the requested values of deformation parameters, while the QPM yields often very different values from the requested ones.

2.4.4 Center of mass and principal axis of inertia

The ALM is used to constrain various parameters in 3D calculations. First of all, we must impose constraint on the position of the center of mass and the orientation of the principal axis. Since no spatial symmetry is assumed in our calculations, the position of center of mass and the orientation of the principal axis of inertia may take arbitrary value for one ground state. In order to correctly estimate the deformation and to make sure that we can obtain a stable convergence, we fix the center of mass at the origin:

$$\int d^3r \; x\rho(\boldsymbol{r}) \equiv \langle x \rangle = 0, \;\; \langle y \rangle = 0, \;\; \text{and} \;\; \langle z \rangle = 0, \tag{2.4.7}$$

where ρ is the matter density, and the principal axis aligned with the coordinate axis:

$$\langle xy \rangle = 0, \;\; \langle yz \rangle = 0, \;\; \text{and} \;\; \langle zx \rangle = 0, \tag{2.4.8}$$

which means that the moment of inertia $I_{ij} = \langle x_i x_j \rangle$, $(i, j = 1, 2, 3)$ is diagonalized.

2.4.5 Quadrupole deformation

We impose constraints on the quadrupole deformations as well. Consider a quadrupole tensor

$$Q_{ij} \equiv \langle \hat{Q}_{ij} \rangle = \langle 3x_i x_j - \delta_{ij} r^2 \rangle, \tag{2.4.9}$$

whose off-diagonal components have already been removed [Eq. (2.4.8)] so that the principal axes are aligned on the coordinate axes. The remaining diagonal components

$$Q_x \equiv \langle 2x^2 - y^2 - z^2 \rangle, \;\; Q_y \equiv \langle 2y^2 - z^2 - x^2 \rangle, \;\; \text{and} \;\; Q_z \equiv \langle 2z^2 - x^2 - y^2 \rangle \tag{2.4.10}$$

describes the intrinsic quadrupole deformation of the nucleus. Notice that only two of the three components of Q_i $(i = x, y, z)$ are independent and the remaining one is dependent of the other two.

Suppose we need a solution with quadrupole deformations $Q_i = Q_i^0$ $(i = x, y, z)$. We consider

$$E' = E + \sum_i \left[\lambda_{Q_i}(Q_i - Q_i^0) + \frac{C_{Q_i}}{2}(Q_i - Q_i^0)^2 \right], \tag{2.4.11}$$

Here we did not explicitly write the constraint terms for the center of mass and the principal axes. The single-particle potential is given by taking a variation as

$$\begin{aligned} h' &= h + \sum_i [C_{Q_i}(Q_i - Q_{i0}) + \lambda_{Q_i}] \cdot \hat{Q}_i & (2.4.12) \\ &= h + \sum_i C'_{Q_i} \cdot \hat{Q}_i, & (2.4.13) \end{aligned}$$

where h and we have defined $C'_{Q_i} = C_{Q_i}(Q_i - Q_i^0) + \lambda_{Q_i}$. This expression can be further simplified as

$$h' = h + C_{x^2} x^2 + C_{y^2} y^2 + C_{z^2} z^2, \tag{2.4.14}$$

with

$$\begin{aligned} C_{x^2} &= 2C'_{Q_x} - C'_{Q_y} - C'_{Q_z} && (2.4.15)\\ C_{y^2} &= 2C'_{Q_y} - C'_{Q_z} - C'_{Q_x} && (2.4.16)\\ C_{z^2} &= 2C'_{Q_z} - C'_{Q_x} - C'_{Q_y}. && (2.4.17) \end{aligned}$$

Let us define a set of two parameters, (β, γ), which uniquely determines the intrinsic quadrupole deformation. The diagonal components of the quadrupole tensor given in Eq. (2.4.9) are related to (β, γ) as

$$\beta = \frac{\sqrt{5\pi}}{3}\frac{1}{AR^2}Q_0,\ \gamma = \mathrm{Tan}^{-1}\left(\frac{Q_x - Q_y}{\sqrt{3}Q_z}\right), \tag{2.4.18}$$

with $R = 1.2 \times A^{1/3}$ (fm) and $Q_0 = \sqrt{\frac{3}{2}(Q_x^2 + Q_y^2 + Q_z^2)}$. Conversely, for given (β, γ), Q_i are computed as

$$Q_x = -Q_0\cos(\gamma + 60^\circ),\ Q_y = -Q_0\cos(\gamma - 60^\circ),\ Q_z = Q_0\cos\gamma. \tag{2.4.19}$$

Constraints on the deformation parameters (β, γ) is replaced by constraints on the quadrupole moments Q_i using the above relations. The correspondence between (β, γ) and the nuclear shape is shown in Fig. 2.4. The parameters β and γ correspond to the radial and angular coordinates on this plane, respectively. The origin, $\beta = 0$, corresponds to a spherical shape. When $\beta \neq 0$ and $\gamma = 0^\circ$, 120°, and 300°, the nucleus has prolate shape with z, x, and y axes as symmetry axes. When $\gamma = 60^\circ$, 180°, and 240°, the nucleus has corresponding oblate shape. If $\beta \neq 0$ and γ is not a multiple of 60°, the nuclear shape is triaxially deformed, i.e., the lengths of nuclei along the three principal axes are all different.

It is sufficient to consider the region $\beta > 0$ and $0^\circ \leq \gamma \leq 60^\circ$ in order to cover all kinds of quadrupole deformation since any other region of $n \times 60^\circ \leq \gamma \leq (n+1) \times 60^\circ$ describes the identical shapes as covered in $0^\circ \leq \gamma \leq 60^\circ$ with the different choices of the orientation of the principal axes (See Fig. 2.4). Thus (β, γ) within the range of $0^\circ \leq \gamma \leq 60^\circ$ is sufficient to describe intrinsic quadrupole deformation without a double counting.

With all those constraints introduced in the previous and this section, i.e., the center of mass is fixed at the origin and the moment of inertia is diagonalized, we can draw a PES as a function of the quadrupole deformation on the (β, γ) plane with $0^\circ \leq \gamma \leq 60^\circ$.

2.4.6 Damping factor for constraint potentials

As we saw in the previous section, the constraint potential for quadrupole deformation behaves like r^2 and increase rapidly towards the edge of the numerical box, where the density of nucleus may be nearly vanishing. Furthermore, there is always one direction where the potential decreases as $-r^2$, which makes a nucleus asymptotically unstable [77]. These may cause unpleasant numerical instabilities. If we want constraints on

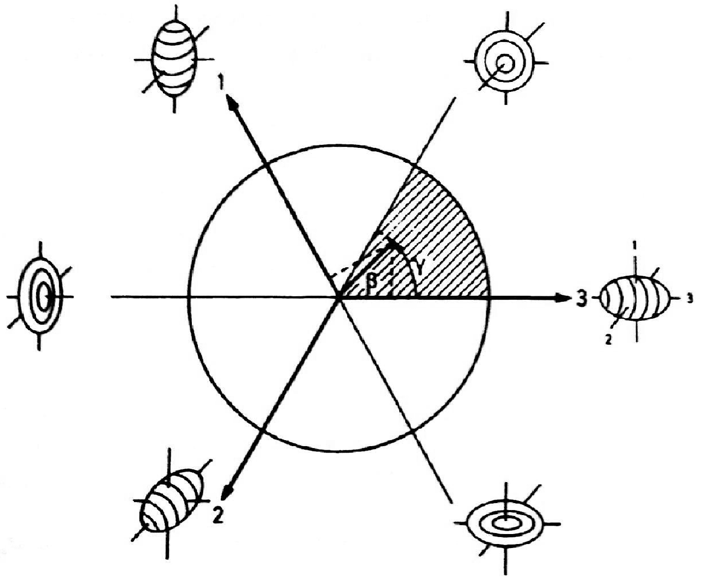

Figure 2.4: Nuclear shapes on (β, γ) plane. The hatched area corresponds to $0° \leq \gamma \leq 60°$. Figure is taken from Fig. 1.4 in Ref. [66]

higher multipole deformations, the problem must become even worse. In order to avoid instabilities, in Ref. [77], Rutz *et al.* have introduced a damping factor of Fermi function type into the constraint potentials. In our constrained calculations, we use a damping factor of the type

$$D(\boldsymbol{r}) = \tanh\left(\frac{\rho(\boldsymbol{r})}{f \cdot \rho_{\max}}\right), \tag{2.4.20}$$

with which the constraint potential $V_{\text{cnst}}(\boldsymbol{r})$ is modified as

$$V_{\text{cnst}}(\boldsymbol{r}) \to V_{\text{cnst}}(\boldsymbol{r}) \cdot D(\boldsymbol{r}). \tag{2.4.21}$$

In Eq. (2.4.20), $\rho(\boldsymbol{r})$ is the density of the nucleus and $\rho_{\max}$ is its maximum value. By this factor V_{cnst} is damped only in the low-density region, where V_{cnst} is quite large but has nearly no effect as constraining potential. f is a free parameter which determines how severely D suppresses V_{cnst}.

2.4.7 General deformation parameters

Although we have only considered the quadrupole (Y_2) deformations, and introduced a convenient parameter set (β, γ) for the quadrupole deformations, we will also discuss higher multipole (octupole, hexadecapole,...) deformations. Here we define deformation parameters which describes general multipole deformations.

In this work we follow the definition used by Takami *et al.* [33] for the deformation parameters. They are defined as

$$\alpha_{\ell m} = \frac{4\pi}{3AR^{\ell}} \int d^3r\ r^{\ell} X_{\ell m}(\hat{\boldsymbol{r}})\rho(\boldsymbol{r}),\ -\ell \leq m \leq \ell, \tag{2.4.22}$$

where $R = 1.2 \times A^{1/3}$ fm, and $X_{\ell m}$ is a real basis of the spherical harmonics,

$$X_{\ell m} = \begin{cases} Y_{\ell 0} & (m = 0) \\ \frac{1}{\sqrt{2}}(Y_{\ell,-m} + Y^*_{\ell,-m}) & (m > 0) \\ \frac{1}{\sqrt{2}i}(Y_{\ell,-m} - Y^*_{\ell,-m}) & (m < 0) \end{cases} . \tag{2.4.23}$$

The ordinary quadrupole parameters are related to α_{2m} as $\alpha_{20} = \beta\cos\gamma$ and $\sqrt{2}\alpha_{22} = \beta\sin\gamma$.

Chapter 3

Covariant Density Functional Theory

In this chapter we introduce the relativistic variant of the density functional theory, the covariant density functional theory (CDFT), and how it is realized in nuclear physics based on the relativistic mean-field theory.

3.1 Relativistic Kohn-Sham equations

In the previous chapter we have introduced the Hohenberg-Kohn and Kohn-Sham theorems in the non-relativistic DFT. The relativistic version of the two theorems can be proved after an appropriate renormalization procedure [13].

Let us consider a relativistic system of N interacting particles with an external four-potential $v^{\mu}_{\text{ext}}(\boldsymbol{r})$. In a relativistic density functional, the ground-state four current j^{μ} instead of the density ρ is the important variable. A relativistic EDF is given by a functional

$$E[j] = T_s[j] + E_{\text{H}}[j] + E_{\text{ext}}[j] + E_{\text{xc}}[j], \tag{3.1.1}$$

where T_s and E_{xc} are defined in a similar way as in the non-relativistic DFT. T_s and j^{μ} are the ground-state kinetic energy and current of the auxiliary non-interacting system,

$$T_s = \sum_i \psi_i^{\dagger}(\boldsymbol{\alpha}\cdot\boldsymbol{p} + \beta m)\psi_i, \text{and} \tag{3.1.2}$$

$$j^{\mu} = \sum_i \bar{\psi}_i \gamma^{\mu}\psi_i, \tag{3.1.3}$$

where ψ_i are the solutions of the relativistic Kohn-Sham equations with a local four-potential $v^{\mu}_s[j](\boldsymbol{r})$,

$$[\boldsymbol{\alpha}\cdot(-i\boldsymbol{\nabla} - \boldsymbol{v}_s(\boldsymbol{r})) + v^0_s(\boldsymbol{r}) + m\beta]\psi_i(\boldsymbol{r}) = \epsilon_i\psi_i(\boldsymbol{r}). \tag{3.1.4}$$

Note that the index i in Eqs. (3.1.2) and (3.1.3) runs over the lowest N occupied single-particle states in the Fermi sea and those in the Dirac sea which are fully occupied in the ground state.

$$\boldsymbol{\alpha} = \gamma^0\boldsymbol{\gamma} = \begin{pmatrix} 0 & \boldsymbol{\sigma}\cdot\boldsymbol{p} \\ \boldsymbol{\sigma}\cdot\boldsymbol{p} & 0 \end{pmatrix},\ \beta = \begin{pmatrix} 1 & 0 \\ 0 & -1 \end{pmatrix} \tag{3.1.5}$$

are the usual Dirac matrices. The Kohn-Sham local potential v_s^μ in Eq. (3.1.4) are given by the sum of the external field and the Hartree and exchange-correlation potentials,

$$v_s^\mu[j](\boldsymbol{r}) = v_{\mathrm{ext}}^\mu(\boldsymbol{r}) + v_{\mathrm{H}}^\mu[j](\boldsymbol{r}) + v_{\mathrm{xc}}^\mu[j](\boldsymbol{r}) = v_{\mathrm{ext}}^\mu(\boldsymbol{r}) + \frac{\delta E_{\mathrm{H}}}{\delta j_\mu(\boldsymbol{r})} + \frac{\delta E_{\mathrm{xc}}}{\delta j_\mu(\boldsymbol{r})}. \tag{3.1.6}$$

In the summation over i in Eqs. (3.1.2) and (3.1.3), one needs a cumbersome renormalization procedure for the Dirac sea states at every step of self-consistent iterations, which is intractable in general calculations. The so-called no-sea approximation is introduced, in which one neglects the effect of vacuum polarization [13]. With this approximation, contribution of the Dirac sea states to the current and the kinetic energy in Eqs. (3.1.2) and (3.1.3) is neglected, and the index i only runs over the Fermi sea states.

3.2 Relativistic mean field theory

Relativistic mean-field (RMF) theory has been employed as widely as non-relativistic mean-field theory [15, 17, 64, 78–80]. In this section we focus on the relativistic mean field approach in nuclear physics. The starting point is a Lorentz invariant Lagrangian density describing the effective nucleon-nucleon interaction mediated by exchange of mesons. An EDF is derived from such Lagrangian by mean-field (Hartree) approximation, in which the meson fields are replaced by their ground state expectation value. The adjustable parameters of the model are fitted to the known properties of nuclear matter and finite nuclei.

The relativistic effective interactions are classified into four types according to the range of the interaction (finite range or zero range) and its density dependence (with non-linear self-interaction terms of mesons or with explicit density dependence of the meson-nucleon coupling constants).

Finite-range interactions are mediated by mesons having specific spin-isospin and parity quantum numbers (J^π, T). The Lagrangian usually contains three mesons: σ with $(J^\pi, T) = (0^+, 0)$, ω with $(J^\pi, T) = (1^-, 0)$, ρ with $(J^\pi, T) = (1^-, 1)$. They are responsible for attraction at medium range and repulsion at short range between nucleons. Although the most important meson which gives attractive force is pion, it does not contribute at the mean-field level because it is a pseudo scalar and thus the expectation value vanishes with the ground state which has a good parity. Thus a phenomenological σ meson is introduced in order to effectively take into account the attraction due to one- or two-pion exchanges, and any more complicated effects, and its mass and coupling constant are considered as adjustable parameters of the model. The repulsion at shorter range is brought about by a heavier vector meson ω, which is considered as the measured vector meson with the mass of $m_\omega \simeq 783$ MeV. Its coupling constant is a free parameter. In addition, the model has a vector isovector meson ρ ($m_\rho \simeq 770$ MeV) to account for the isospin dependence of the inter-nucleon interaction.

The model with zero-range interaction [81–83] is referred to as relativistic point-coupling (RPC) model, which has also been widely employed [81, 82, 84–86]. This model is based on the zero-range approximation to meson exchanges, and is similar to the Skyrme interaction for non-relativistic model. In this model the mesonic degrees of freedom are all implicit, and it consists with four-fermion and derivative couplings, which correspond to the leading and the next-to-leading order terms of the expansion of meson propagators, respectively. The RPC model has several advantages compared to the meson exchange (finite-range) models. First, there is no need to solve the Klein-Gordon equations for mesons since the mesonic degrees of freedom are all implicit in the RPC model. Second, the Fock terms can easily be introduced by using the Fierz transformation [87] because of its zero-range nature [88–92]. Last, it is much easier to apply the model to beyond-mean-field methods such as the generator coordinate method (GCM), and angular momentum and particle number projections [66, 80]. In addition, due to its numerical simplicity, the zero-range model is suitable also for the 3D coordinate space calculations. We will show later the explicit expressions for the model Lagrangians and derive the relativistic mean-field (Kohn-Sham) equations for the RPC model.

The RMF model for nuclear system was first introduced by Walecka [16, 17] with a simple model with only σ and ω mesons without non-linear terms nor density-dependent couplings. Walecka applied the model to nuclear matter within the mean-field (Hartree) approximation, that is, replacing the meson fields by their ground-state expectation values. The model successfully reproduced the quantitative saturation property of the symmetric nuclear matter due to the interplay between scalar and vector potentials. The balance of large attractive scalar field and large repulsive vector field at lower density and dominance of the vector repulsion at high density limit lead to saturation [16, 17]. This is purely a relativistic effect which is absent in the non-relativistic theory. In the non-relativistic models one needs a three-body force or density dependent force in order to reproduce the saturation of nuclear matter.

The $\sigma - \omega$ model of Walecka is modified to be applied also to finite nuclei [17, 18] by including ρ meson as well to describe $N \neq Z$ nuclei. The relativistic Kohn-Sham equation is given by the following form of a Dirac equation

$$\begin{pmatrix} W_+ & \boldsymbol{\sigma} \cdot \boldsymbol{p} \\ \boldsymbol{\sigma} \cdot \boldsymbol{p} & W_- - 2m \end{pmatrix} \begin{pmatrix} f \\ g \end{pmatrix} = \epsilon \begin{pmatrix} f \\ g \end{pmatrix}, \tag{3.2.1}$$

where the mean fields W_+ and W_- are respectively defined as the sum and difference of scalar and vector mean fields,

$$W_+ = V + S \simeq 60 \text{ MeV}, \ W_- = V - S \simeq 700 \text{ MeV}. \tag{3.2.2}$$

The values given above are the rough depths of the potentials at the center of nuclei, and they are similar to their values for symmetric nuclear matter of the $\sigma - \omega$ model. The model reproduces the large spin-orbit splittings and the shell structure of nuclei quantitatively [17, 18]. The point is that the model naturally accounts for the large spin-orbit splittings without fitting any parameter to the empirical spin-orbit splittings. By eliminating the lower component of the Dirac spinor in Eq. (3.2.1) one obtains

$$\left[\boldsymbol{p} \cdot \frac{1}{\epsilon + m - W_-} \boldsymbol{p} + W_+ + \frac{1}{(\epsilon + m - W_-)^2} \frac{1}{r} \frac{dW_-}{dr} \boldsymbol{\ell} \cdot \boldsymbol{s}\right] f = \epsilon f,$$

from which where one can identify W_+ as the central potential and W_- as the spin-orbit potential in the non-relativistic reduction of the Dirac equation. The large attractive scalar and repulsive vector fields are understood as the origin of the spin-orbit splittings.

Non-linear self-coupling terms of σ meson were introduced by Bodmer et al,. [93] to improve agreement of the mean-field results with those of the non-relativistic models and the empirical data of nuclear deformation parameters, neutron-skin thickness, and the nuclear matter incompressibility [72, 93]. At present, the models with non-linear terms, which introduces an effective density dependence into the nucleon-meson coupling constant, are one of the standard choice for RMF model calculations [85, 94, 95].

An explicit density dependence of the coupling constants is another option introduced in modern effective interactions [86, 96–99]. Assuming some functional form with parameters for the density-dependent coupling constants, one determines the parameters from an relativistic Brückner Hartree-Fock (RBHF) calculations for nuclear matter based on bare nucleon-nucleon interactions. The first such attempt has been done by Brockmann and Toki [100]. They used an RBHF calculation to reduce density dependences of the coupling constants in the $\sigma-\omega$ model, and obtained reasonable agreements in observables of finite nuclei. The models with the density dependences deduced from such an *ab initio* type calculations (based on a bare nucleon-nucleon interaction without any reference to the data of finite nuclei) have become popular as well as the non-linear models. Recently, there were attempts to reduce the number of phenomenological parameters as much as possible by using the information from the *ab initio* method [86, 99]. The non-relativistic interaction constructed in Ref. [101] is also based on the same spirit.

3.3 Model Lagrangian

As mentioned in the previous section, there are four types of relativistic models according to the range of interaction and the density dependence. In this section we introduce the model Lagrangians for them and derive the mean-field equations for the RPC model.

The Lagrangian density for the finite-range (meson exchange) model is given by

$$\mathcal{L}^{\mathrm{ME}} = \mathcal{L}_{\mathrm{N}} + \mathcal{L}_{\mathrm{M}} + \mathcal{L}_{\mathrm{em}} + \mathcal{L}_{\mathrm{int}} \tag{3.3.1}$$

$\mathcal{L}_{\mathrm{N}}$ is the free part of nucleon given by

$$\mathcal{L}_{\mathrm{N}} = \bar{\psi}(i\gamma^\mu\partial_\mu - m)\psi, \tag{3.3.2}$$

where ψ and m are the nucleon field and nucleon mass, respectively, and $\mathcal{L}_{\mathrm{em}}$ is the electromagnetic part

$$\mathcal{L}_{\mathrm{em}} = -\frac{1}{4}F^{\mu\nu}F_{\mu\nu} - \bar{\psi}\frac{1-\tau_3}{2}\gamma^\mu\psi A_\mu, \tag{3.3.3}$$

where A^μ is the electromagnetic field and $F^{\mu\nu} = \partial^\mu A^\nu - \partial^\nu A^\mu$ is the electromagnetic field strength tensor. The free meson part is $\mathcal{L}_{\mathrm{M}}$ given by

$$\begin{aligned}\mathcal{L}_{\mathrm{M}} &= \frac{1}{2}(\partial^{\mu}\sigma)(\partial_{\mu}\sigma) + U(\sigma) - \frac{1}{4}\Omega^{\mu\nu}\Omega_{\mu\nu} + \frac{1}{2}m_{\omega}\omega^{\mu}\omega_{\mu} \\ &\quad -\frac{1}{4}\vec{R}^{\mu\nu}\cdot\vec{R}_{\mu\nu} + \frac{1}{2}m_{\rho}\vec{\rho}^{\mu}\cdot\vec{\rho}_{\mu},\end{aligned} \tag{3.3.4}$$

where m_i $(i = \sigma,\ \omega,\ \rho)$ are meson masses and $\Omega^{\mu\nu}$ and $\vec{R}^{\mu\nu}$ are the field tensors of ω and ρ mesons. The arrow indicates a vector in the isospin space. $U(\sigma) = -\frac{1}{2}m_{\sigma}^2\sigma^2 - \frac{1}{3}g_2\sigma^3 - \frac{1}{4}g_3\sigma^4$ is the mass term and non-linear self coupling terms of the σ meson. The nucleon-meson interaction part $\mathcal{L}_{\mathrm{int}}$ is given by

$$\mathcal{L}_{\mathrm{int}} = \bar{\psi}(-g_{\sigma}\sigma - g_{\omega}\omega^{\mu}\gamma_{\mu} - g_{\rho}\vec{\rho}^{\mu}\cdot\vec{\tau}\gamma_{\mu})\psi, \tag{3.3.5}$$

where g_i $(i = \sigma,\ \omega,\ \rho)$ are coupling constants of each mesons to nucleon. For a density-dependent version of the meson exchange interaction, the non-linear coupling constants are set $g_2 = g_3 = 0$ in $U(\sigma)$ and explicit density dependences of the coupling constants g_i are introduced.

The Lagrangian density for the relativistic point coupling model is given by

$$\mathcal{L}^{\mathrm{PC}} = \mathcal{L}_{\mathrm{N}} + \mathcal{L}_{\mathrm{em}} + \mathcal{L}_{\mathrm{int}}, \tag{3.3.6}$$

where $\mathcal{L}_{\mathrm{int}}$ describes the nucleon-nucleon zero-range interaction, which consists of four-fermion ($\mathcal{L}_{\mathrm{4f}}$), derivative ($\mathcal{L}_{\mathrm{der}}$), and higher-order ($\mathcal{L}_{\mathrm{hot}}$) terms. These are given as follows

$$\mathcal{L}_{\mathrm{int}} = \mathcal{L}_{\mathrm{4f}} + \mathcal{L}_{\mathrm{der}} + \mathcal{L}_{\mathrm{hot}}, \tag{3.3.7}$$

with

$$\begin{aligned}\mathcal{L}_{\mathrm{4f}} &= -\frac{1}{2}\alpha_S(\bar{\psi}\psi)(\bar{\psi}\psi) - \frac{1}{2}\alpha_V(\bar{\psi}\gamma_{\mu}\psi)(\bar{\psi}\gamma^{\mu}\psi) \\ &\quad -\frac{1}{2}\alpha_{TS}(\bar{\psi}\vec{\tau}\psi)\cdot(\bar{\psi}\vec{\tau}\psi) - \frac{1}{2}\alpha_{TV}(\bar{\psi}_N\gamma_{\mu}\vec{\tau}\psi_N)\cdot(\bar{\psi}_N\gamma^{\mu}\vec{\tau}\psi_N),\end{aligned} \tag{3.3.8}$$

$$\begin{aligned}\mathcal{L}_{\mathrm{der}} &= -\frac{1}{2}\delta_S(\partial_{\mu}\bar{\psi}\psi)(\partial^{\mu}\bar{\psi}\psi) - \frac{1}{2}\delta_V(\partial_{\mu}\bar{\psi}\gamma_{\nu}\psi)(\partial^{\mu}\bar{\psi}\gamma^{\nu}\psi) \\ &\quad -\frac{1}{2}\delta_{TS}(\partial_{\mu}\bar{\psi}\vec{\tau}\psi)\cdot(\partial^{\mu}\bar{\psi}\vec{\tau}\psi) - \frac{1}{2}\delta_{TV}(\partial_{\mu}\bar{\psi}\gamma_{\nu}\vec{\tau}\psi)\cdot(\partial^{\mu}\bar{\psi}\gamma^{\nu}\vec{\tau}\psi),\end{aligned} \tag{3.3.9}$$

and

$$\mathcal{L}_{\mathrm{hot}} = -\frac{1}{3}\beta_S(\bar{\psi}\psi)^3 - \frac{1}{4}\gamma_S(\bar{\psi}\psi)^4 - \frac{1}{4}\gamma_V\left[(\bar{\psi}\gamma_{\mu}\psi)(\bar{\psi}\gamma^{\mu}\psi)\right]^2. \tag{3.3.10}$$

Notice that the four different spin-isospin vertex structures labeled by the subscripts S, V, TS, and TV in the coupling constants correspond to σ, ω, δ, and ρ meson exchanges, respectively. Thus we can find one-to-one correspondence of each term to the meson exchange model. Although we included the scalar-isovector (TS) channel in the above equations, normally this channel is not taken into account, that is, only S, V, and TV channels are considered as in the meson exchange model. The density-dependent version of the RPC model is given by introduction of explicit density dependences into the coupling constants α_K ($K = S, TS, V, TV$), and setting $\beta_S = \gamma_S = \gamma_V = 0$.

Since we use in this thesis the RPC model with the non-linear couplings, which is given in Eqs. (3.3.7), (3.3.8), (3.3.9), and (3.3.10), we give here the expressions for the EDF and the relativistic Kohn-Sham equations derived from this model. The total energy, i.e., the EDF corresponding to the RPC model is obtained within the mean-field (Hartree) and the no-sea approximations. In the no-sea approximation, the densities are constructed with occupied Fermi sea states only, without the states in the Dirac sea, which means that the vacuum polarization effect is neglected [64]. For a nucleus with mass number A, the EDF for the RPC model is given by

$$\begin{aligned} E &= \int d^3r \left(\sum_{i=1}^{A} \psi_i^\dagger (-i\boldsymbol{\alpha} \cdot \boldsymbol{\nabla} + m\beta)\psi_i + \frac{1}{2} e A^0 \rho_V^{(\mathrm{p})} \right. \\ &\quad \left. + \frac{1}{2}\sum_K \alpha_K \rho_K^2 + \frac{1}{2}\sum_K \delta_K \rho_K \Delta\rho_K + \frac{1}{3}\beta_S\rho_S^3 + \frac{1}{4}\gamma_S\rho_S^4 + \frac{1}{4}\gamma_V\rho_V^4 \right), \end{aligned} \tag{3.3.11}$$

where we have assumed the time reversal invariance of the nuclear ground state. The densities appearing in Eq. (3.3.11) are defined as

$$\rho_S(\boldsymbol{r}) = \sum_{i=1}^{A} \bar{\psi}_i(\boldsymbol{r})\psi_i(\boldsymbol{r}), \tag{3.3.12}$$

$$\rho_V(\boldsymbol{r}) = \sum_{i=1}^{A} \psi_i^\dagger(\boldsymbol{r})\psi_i(\boldsymbol{r}), \tag{3.3.13}$$

$$\rho_{TS}(\boldsymbol{r}) = \sum_{i=1}^{A} \bar{\psi}_i(\boldsymbol{r})\tau_3\psi_i(\boldsymbol{r}), \tag{3.3.14}$$

$$\rho_{TV}(\boldsymbol{r}) = \sum_{i=1}^{A} \psi_i^\dagger(\boldsymbol{r})\tau_3\psi_i(\boldsymbol{r}), \tag{3.3.15}$$

Here $\psi_i(\boldsymbol{r})$ is the wave function for the i-th nucleon.

The relativistic Hartree equation, or the relativistic Kohn-Sham equation, for nucleons is given by

$$\left[-i\boldsymbol{\alpha} \cdot \boldsymbol{\nabla} + V_V + V_{TV}\tau_3 + V_C + (m + V_S + V_{TS}\tau_3)\,\beta\right]\psi_i = \epsilon_i\psi_i, \tag{3.3.16}$$

with

$$\begin{aligned} V_S &= \alpha_S \rho_S + \beta_S \rho_S^2 + \gamma_S \rho_S^3 + \delta_S \Delta \rho_S && (3.3.17) \\ V_V &= \alpha_V \rho_V + \gamma_V \rho_V^3 + \delta_V \Delta \rho_V && (3.3.18) \\ V_{TS} &= \alpha_{TS} \rho_{TS} + \delta_{TS} \Delta \rho_{TS}, && (3.3.19) \\ V_{TV} &= \alpha_{TV} \rho_{TV} + \delta_{TV} \Delta \rho_{TV}, && (3.3.20) \\ V_C &= e A^0 \frac{1-\tau_3}{2}, \ (\Delta A^0 = -e \rho_V^{(p)}), && (3.3.21) \end{aligned}$$

These are solved self-consistently to obtain the ground states of atomic nuclei.

After having solved these Hartree equations self-consistently, we obtain the total binding energy as

$$\begin{aligned} E_B &= \sum_{i=1}^{A} \epsilon_i - E_{\mathrm{CM}} - Am \\ &\quad - \int d^3 r \left(\frac{1}{2} \sum_K \alpha_K \rho_K^2 + \frac{1}{2} \sum_K \delta_K \rho_K \Delta \rho_K \right. && (3.3.22) \\ &\qquad \left. + \frac{2}{3} \beta_S \rho_S^3 + \frac{3}{4} \gamma_S \rho_S^4 + \frac{3}{4} \gamma_V \rho_V^4 + \frac{1}{2} e A^0 \rho_V^{(p)} \right), \end{aligned}$$

where the center of mass energy E_{CM} is calculated by taking the expectation value of the kinetic energy for the center of mass motion with respect to the many-body ground state wave function as [187]

$$E_{\mathrm{CM}} = \frac{\langle P_{\mathrm{CM}}^2 \rangle}{2Am}. \tag{3.3.23}$$

See Appendix F.1 for the explicit expressions for E_{CM}.

3.4 Features of the relativistic model

In this section we introduce some characteristic features of the relativistic models. As mentioned in Ch. 1, they are different to the non-relativistic models in several aspects mainly because of the stringent restriction by the Lorentz symmetry.

Despite the difficulties in the relativistic models, CDFT has been attracting much attention since it has remarkable features compared to the non-relativistic DFT. Here we illustrate the some advantages in relativistic density functionals in nuclear physics.

- Saturation property of nuclear matter
  The Walecka model [16,17] which consists of only σ and ω mesons gives a qualitative explanation for the saturation property of nuclear matter. In this model, ratios of the coupling constant and mass of the two mesons were fitted to reproduce the empirical saturation density and the binding energy at saturation.

Balance of large attractive scalar field and large repulsive vector field at lower density and dominance of the vector repulsion at high density limit lead to saturation [16,17]. This is purely a relativistic effect which is absent in the non-relativistic theory. In the non-relativistic models one needs three-body force or density dependent force in order to reproduce the saturation of nuclear matter.

- Large spin-orbit splittings in single-particle energies
  The strong spin-orbit interaction plays an essential role in nuclear structure. Its importance has been recognized since the early nuclear shell model. In the non-relativistic mean field theory, the spin-orbit interaction is introduced phenomenologically as an effective two-body interaction. On the other hand, in the relativistic theory, there is no explicit two-body spin-orbit interaction in the Lagrangian. By the non-relativistic reduction of a single-particle Dirac equation, the one-body spin-orbit field naturally arises as a consequence of an interplay between large scalar and vector fields.

  The Walecka model with a slight modification without any reference to empirical spin-orbit splittings are successful to roughly reproduce the shell structure of the nucleus [17, 18].

  It has also been pointed out for Λ hypernuclei [102] that an additional contribution of the Λ particle to the mean field substantially change the spin-orbit splittings of nucleon single-particle levels in very neutron-rich Ne isotopes, and stabilizes the nuclei against the neutron drip to extend the neutron drip line of Ne isotopes. Such an impurity effect of Λ on the nucleon spin-orbit splittings, which is brought about through the contribution of Λ to the spin-orbit field $V - S$, is unique in the relativistic models.

- Isospin-dependence of the spin-orbit potential
  It has been known that there is a kink in the isotope shift of charge radii of Pb isotopes at the neutron magic number $N = 126$, which could not be reproduced by Skyrme and Gogny forces [103, 104]. The relativistic models, from the traditional to modern ones, are able to well reproduce the kink [85, 96, 98, 105] (See Fig. 3.1).

  It was pointed out [103, 108] that isospin dependence of the spin-orbit potential in the Skyrme (and Gogny) forces are different from that of the relativistic models. Although the spin-orbit interaction in the non-relativistic models is an isoscalar at the operator level, the spin-orbit field at the mean-field level acquires an isovector nature through the exchange term. This is different from the relativistic mean-field models in which the isospin dependence of the spin-orbit potential entirely comes from the isovector ρ meson. This difference is considered to be the reason why the non-relativistic models fail to reproduce the kink.

  In order to cure the discrepancy, the non-relativistic Skyrme functionals need an additional parameter to tune the isospin dependence in the spin-orbit interaction

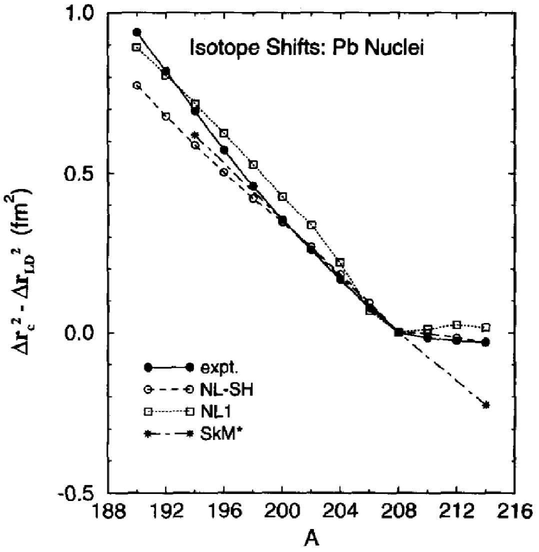

Figure 3.1: The isotope shifts of charge radii of Pb nuclei obtained with relativistic models (NL1 [106] and NL-SH [107]) and a non-relativistic Skyrme interaction (SkM*). The both relativistic models well reproduce the empirical kink at $N = 126$, while the SkM* values show a large deviation from the empirical data for $N > 126$. The figure is taken from Fig. 1 of Ref. [105].

[103, 108]. [1]

The difference in isospin dependence of the spin-orbit field also affect the spin-orbit splittings in neutron-rich nuclei. In Refs. [110, 111] it is pointed out that , with the relativistic models, the spin-orbit splittings in Ne, Mg, Ni, and Sn isotopes decrease as the neutron number is increased. This result is different from that obtained with the non-relativistic models, and is understood as the consequence of the difference in the isospin dependence of the spin-orbit field [110, 111]. This reduction of the spin-orbit splittings in the neuron-rich region may affect the location of the theoretical neutron drip line.

- Time-odd mean fields
  The parameters in the energy density functional are usually adjusted to the ground state properties of even-even nuclei, to which only the time-even components of the functional contribute. In non-relativistic theory it has been pointed out that there is an ambiguity in the time-odd components [23]. On the other hand, in covariant density functionals, the time-odd components have been entirely fixed by the Lorentz symmetry.

- Pseudo-spin symmetry
  It has been recognized for a long time that quasidegeneracy is seen between single-particle orbitals with quantum numbers $(n, \ell, j = \ell + 1/2)$ and $(n-1, \ell+2, j = \ell + 3/2)$, where n, ℓ, and j are the radial quantum number, the orbital angular momentum, and the total angular momentum of single nucleon, respectively. This is understood as a consequence of a (approximate) relativistic symmetry [19, 20].

Although we have illustrated the advantages of the relativistic mean-field, it also has unpleasant features. As was mentioned in Ch. 1, there are two major difficulties in the relativistic mean-field model. They are the *variational collapse* and *fermion doubling problems*, which prevents an application of the imaginary time method to the relativistic calculations. (These will be discussed in the following two chapters.) More minor disadvantages are the computational cost due to the four-component structure of the Dirac spinor. Another disadvantages is faced in random phase approximation (RPA) calculations. It has been known [65] that one has to take into account not only usual particle-hole excitations formed by a hole in the occupied Fermi sea and a particle above the Fermi sea but also configurations with a hole in the Fermi sea and a particle in the empty Dirac sea.

In addition to those drawbacks mentioned above and in Ch. 1, it has also been pointed out that, for many of relativistic functionals including modern ones [94, 95, 97, 98] there are spurious shell gap at $Z, N = 58$ and 92 [115, 116]. These spurious magicities give over binding compared to the measured masses in the region around them [115, 116], and a

---

[1] Recently, it has been suggested in Ref. [109] that the kink originates from the occupation of the high-j orbital above $N = 126$ shell, and the isospin dependence of the spin-orbit potential may not be an essential origin of the kink.

sudden change in two-neutron separation energy from $N = 58$ to $N = 60$ [117] which is not observed in the measured two-neutron separation energy.

Furthermore, in general, the nuclear properties under an extreme condition, e.g., properties of neutron-rich and unstable nuclei, asymmetric nuclear matter are quite different among the many existing parameter sets of relativistic and non-relativistic interactions, although the properties of symmetric nuclear matter (saturation density and binding energy) and the ground properties of stable nuclei are similar among different interactions. This is natural because the parameters are determined so as to reproduce those observables which are precisely measured in experiments, such as the binding energies and charge radii in stable nuclei. Other properties such as incompressibility and symmetry energy of nuclear matter, which should be closely related to the properties of unstable nuclei and neutron star, are less well determined from experiments and are therefore only used as rough guides in the determination of parameter sets. In Refs. [112–114], Yoshida et al. pointed out a characteristic difference in the isovector properties of the relativistic models from the non-relativistic ones. That is, the relativistic models tend to yield larger pressure of neutron matter, neutron-skin thickness, compared to the non-relativistic models. This difference may affect the nuclear properties at the extreme isospin or density.

As is seen in this chapter, the relativistic models have many characteristic features which are different from the non-relativistic models. It is not that the relativistic models are superior to the non-relativistic ones in every aspects, but it is important to compare the results obtained with different models and investigate whether a result is universal or model-dependent.

Chapter 4

Inverse Hamiltonian Method

The variational principle is a guiding principle to derive equations and to find approximate solutions in quantum mechanical problems. In this chapter we introduce the variational principle and its failure in relativistic systems, and a prescription to avoid this collapse of variational calculation.

4.1 Variational principle

4.1.1 General theory

The variational principle is a simple but very important principle in non-relativistic quantum mechanics. The principle tells us that if a Hamiltonian H has a spectrum bounded from below, its expectation value

$$\mathcal{H}[\Psi] \equiv \frac{\langle\Psi|H|\Psi\rangle}{\langle\Psi|\Psi\rangle}, \tag{4.1.1}$$

where Ψ is an element of the Hilbert space on which the Hamiltonian acts, gives a strict upper limit of the true ground state energy. This can be proved easily. Let E_k be a true eigenvalue of H and $|k\rangle$ be the normalized eigenstate associated with E_k. Then we have

$$\begin{aligned}
\frac{\langle\Psi|H|\Psi\rangle}{\langle\Psi|\Psi\rangle} &= \frac{\sum_n |\langle k|\Psi\rangle|^2 E_k}{\sum_k |\langle k|\Psi\rangle|^2} \\
&= \frac{E_0 \sum_k |\langle k|\Psi\rangle|^2 + \sum_k |\langle k|\Psi\rangle|^2 (E_k - E_0)}{\sum_k |\langle k|\Psi\rangle|^2} \\
&= E_0 + \frac{\sum_k |\langle k|\Psi\rangle|^2 (E_k - E_0)}{\sum_k |\langle k\,|\Psi\rangle|^2}.
\end{aligned}$$

If we choose the lowest eigenvalue, i. e., the true ground state energy, as E_0, then $E_k - E_0 \geq 0$ for all k. Thus the second term in the last line is greater than or equal to 0 for any Ψ, and we get a familiar inequality of the variational principle:

$$\frac{\langle\Psi|H|\Psi\rangle}{\langle\Psi|\Psi\rangle} \geq E_0. \tag{4.1.2}$$

This inequality tells us that we can obtain a better solution by minimizing the the energy as much as possible. The smaller the energy is, the more accurate the approximate solution is.

Let us derive an equation to obtain solutions based on this variational principle. Suppose that $|\bar{\psi}\rangle$ is the function corresponding to the absolute minimum of $\mathcal{H}$. Let the minimal value of energy be $\mathcal{H}[\bar{\psi}] = \bar{E}$. This means that $\mathcal{H}$ is stationary with respect to arbitrary variation $|\Psi\rangle \to |\Psi\rangle + |\delta\Psi\rangle$ at $\Psi = \bar{\psi}$. Thus, to the first order of the variation $|\delta\Psi\rangle$,

$$\begin{aligned}
\delta\mathcal{H} &= \frac{\langle\bar{\psi}+\delta\Psi|H|\bar{\psi}\rangle}{\langle\bar{\psi}+\delta\Psi|\bar{\psi}\rangle} - \frac{\langle\bar{\psi}|H|\bar{\psi}\rangle}{\langle\bar{\psi}|\bar{\psi}\rangle} \\
&\simeq \frac{1}{\langle\bar{\psi}|\bar{\psi}\rangle}\left(\langle\bar{\psi}|H|\bar{\psi}\rangle + \langle\delta\Psi|H|\bar{\psi}\rangle\right)\left(1 - \frac{\langle\delta\Psi|\bar{\psi}\rangle}{\langle\bar{\psi}|\bar{\psi}\rangle}\right) - \frac{\langle\bar{\psi}|H|\bar{\psi}\rangle}{\langle\bar{\psi}|\bar{\psi}\rangle} \\
&\simeq \frac{1}{\langle\bar{\psi}|\bar{\psi}\rangle}\langle\delta\Psi|\left(H|\bar{\psi}\rangle - \bar{E}|\bar{\psi}\rangle\right) = 0.
\end{aligned}$$

For this to hold for arbitrary $\langle\delta\Psi|$, one obtains

$$H|\bar{\psi}\rangle = \bar{E}|\bar{\psi}\rangle. \tag{4.1.3}$$

This is nothing but a Schrödinger equation with the eigenvalue $\bar{E}$. If the variation is restricted within some subspace, we shall get an approximate solution by the minimization.

The idea of the principle can be widely applied to a solution of general problems. In general, the original Schrödinger equation for a physical system is a complicated second-order differential equation. It can not analytically be solvable in most cases. Moreover, other approximation methods such as perturbation theory or semi-classical approximation are not always applicable. The variational method is powerful and efficient, and allows one to solve a problem which is difficult to handle with other methods. The method reduces a complicated differential equation to a minimization problem with respect to finite number of variational parameters. An excited state is obtained by minimizing the energy with constraints that the state is orthogonal to the lower states.

The quality of a variational solution depends on the choice of the trial functions although there is no universal way to construct a function which well approximates solutions of a problem. Generally speaking, if one takes a function which contains more variational parameters, the results becomes better since the subspace covered by the trial function becomes larger. In order to get a good approximate solution yet keeping the computational cost reasonable, one should choose a function and free parameters that are suitable for the system in consideration. In constructing a trial function one should take into account the boundary condition and the symmetry of the system, or one can guess an appropriate function by analogy with a similar system whose solution is already known.

It can be shown that if the error of the wave function is $\mathcal{O}(\epsilon)$, the error in the energy is $\mathcal{O}(\epsilon^2)$. Suppose that we have obtained an approximate solution $|\bar{\psi}\rangle$ which is expressed as

$$|\bar{\psi}\rangle = \big(|\psi_0\rangle + \epsilon|\psi_\perp\rangle\big)/\sqrt{1+\epsilon^2}, \tag{4.1.4}$$

where $|\psi_0\rangle$ is the true normalized ground state and $|\psi_\perp\rangle$ is a normalized linear combination of the other eigenstates $|\psi_n\rangle$ $(n \neq 0)$. Note that $\langle\psi_\perp|\psi_0\rangle = 0$. The energy expectation value of this state is

$$\langle\bar{\psi}|H|\bar{\psi}\rangle = \frac{1}{1+\epsilon^2}\big(\langle\psi_0|H|\psi_0\rangle + \epsilon^2\langle\psi_\perp|H|\psi_\perp\rangle\big) = E_0 + \mathcal{O}(\epsilon^2). \tag{4.1.5}$$

From this result it can be said that the energy can be obtained to a high accuracy if the trial function well approximates the true ground state. In other words, to obtain an accurate wave function is more difficult than to obtain an accurate energy.

As we have seen, the variational principle gives an upper limit for an energy eigenvalue. It is also possible to estimate a lower limit in the following way. Let us consider a dispersion of the Hamiltonian in a variational solution

$$\sigma = \langle\psi|H^2|\psi\rangle - \langle\psi|H|\psi\rangle^2 \equiv D - E_\psi^2 \tag{4.1.6}$$

Let the exact eigenvalue be E_n and the associated eigenvector $|n\rangle$: $H|n\rangle = E_n|n\rangle$. $|\psi\rangle$ can be expanded in terms of $|n\rangle$ as

$$|\psi\rangle = \sum_k a_k|k\rangle, \quad a_k = \langle k|\psi\rangle, \tag{4.1.7}$$

then

$$\sigma = \langle\psi|(H - E_\psi)^2|\psi\rangle = \sum_k |a_k|^2(E_k - E_\psi)^2 \tag{4.1.8}$$

Among the eigenvalues E_k let E_j be the one closest to E_ψ, so that

$$(E_j - E_\psi)^2 \leq (E_k - E_\psi)^2 \ \forall k. \tag{4.1.9}$$

We find that

$$\sigma = \sum_k |a_k|^2\big[(E_k - E_\psi)^2 - (E_j - E_\psi)^2\big] + (E_j - E_\psi)^2\sum_k |a_k|^2 \geq (E_j - E_\psi)^2. \tag{4.1.10}$$

Then we immediately obtain the Weinstein's formula [118]

$$E_\psi - \sqrt{\sigma} \leq E_j \leq E_\psi + \sqrt{\sigma}. \tag{4.1.11}$$

Thus one can conclude that there is at least one eigenvalue within the interval in Eq. (4.1.11). Although practically there may be a problem in estimating D in general variational calculations, Eq. (4.1.11) allow us to consider E_ψ as the estimate for E_j and σ as measure of its precision once D is available. Notice that we have not used the variational principle in the derivatio, thus the statement applies to general eigenvalue problems.

4.1.2 Rayleigh-Ritz method

In this section we explain a realization of the variational principle in the basis expansion method, which has already been introduced in Ch. 2. Thus the discussion here applies to a solution obtained with the basis expansion method in the non-relativistic theory.

In order to obtain the exact eigenstates, one has to introduce infinite number of variational parameters since the Hilbert space on which a general Hamiltonian acts has infinitely large dimensions. In practical calculations finite number of parameters are chosen so that the desired accuracy is achieved. Here let us consider solving a problem by basis expansion based on the variational principle. The solutions are expanded by a finite basis set $\{|\phi_i\rangle\}$ $(1 \leq i \leq N)$ as $|\Phi\rangle = \sum_{i=1}^{N} c_i^{(N)}|\phi_i\rangle$. We assume that $\{|\phi_i\rangle\}$ is orthonormal, i.e., $\langle\phi_i|\phi_j\rangle = \delta_{ij}$. In this case we restrict the variation within the subspace spanned by $\{|\phi_i\rangle\}$ $(1 \leq i \leq N)$. The variational parameter in this case are the expansion coefficient $c_i^{(N)}$, and the approximate solutions are obtained by minimizing

$$\mathcal{H}(\{c\}) = \frac{\langle\Phi|H|\Phi\rangle}{\langle\Phi|\Phi\rangle}. \tag{4.1.12}$$

As we have seen in the previous section, minimizing $\mathcal{H}(\{c\})$ is solving an eigenvalue problem

$$H|\Phi\rangle = E|\Phi\rangle. \tag{4.1.13}$$

This reduces to a matrix eigenvalue problem by multiplying by $\langle\phi_i|$ from the left,

$$\sum_{j=1}^{N} H_{ij}c_j^{(N)} = E^{(N)}c_i^{(N)}, \tag{4.1.14}$$

where $H_{ij} = \langle\phi_i|H|\phi_j\rangle$. This is a Schrödinger equation projected onto the subspace. Let the eigenvalues of Eq. (4.1.14) be $E_1^{(N)} \leq E_2^{(N)} \leq \cdots \leq E_N^{(N)}$, and associated eigenvectors $|\psi_i^{(N)}\rangle = \sum_{j=1}^{N} c_{ij}^{(N)}|\phi_j\rangle$, $1 \leq i \leq N$. The solutions $|\psi_i^{(N)}\rangle$ are orthonormal. The true eigenvalues and associated eigenstates are similarly defined as $E_1 \leq E_2 \leq \cdots$, and $|\psi_1\rangle,\ |\psi_2\rangle, \ldots$, respectively. It is clear that $E_1^{(N)}$ is strict upper limit for the ground state energy. Furthermore, it can be proved that all the other approximate energies as well as the ground state are upper limits for the exact energies as long as the exact spectrum is discrete:

$$E_1 \leq E_1^{(N)},\ E_2 \leq E_2^{(N)},\ \ldots,\ E_N \leq E_N^{(N)}, \tag{4.1.15}$$

which is known as Poincaré's theorem. It can also be shown that increasing the basis lowers the approximate energies

$$E_k^{(N+1)} \leq E_k^{(N)},\quad i = k,\ 2,\ \ldots, N, \tag{4.1.16}$$

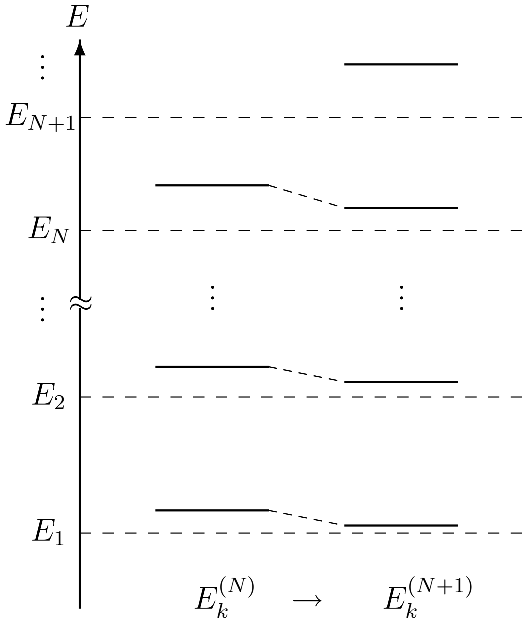

Figure 4.1: Change of the spectrum against the number of bases N. $E_1, E_2, ...$ are the exact eigenvalues, which are denoted by the horizontal dashed lines. Approximate eigenvalues of $E_k^{(N)}$ in Eq. (4.1.14) are represented by the solid lines. The approximate spectrum get closer down to the exact spectrum when number of bases is increased.

which is a consequence of the interlacing theorem [119]. From Eqs. (4.1.15) and (4.1.16), it follows that, by adding one more basis to the basis set, a new approximate eigenvalue is added on the top of the spectrum and push down all the rest of the eigenvalues (see Fig. 4.1). As the basis set becomes larger, all the eigenvalues of Eq. (4.1.14) approach to the true eigenvalues monotonically from above.

4.2 Variational collapse in relativistic quantum mechanics

In this section we introduce the variational collapse problem in relativistic quantum mechanics and how to avoid it in our 3D CDFT calculations.

4.2.1 Variational collapse

Let us consider a single-particle Dirac equation which is to be solved in a CDFT calculation.

$$[-i\boldsymbol{\alpha}\cdot\boldsymbol{\nabla}+V(\boldsymbol{r})+\beta(m+S(\boldsymbol{r}))]\psi(\boldsymbol{r})=\epsilon\psi(\boldsymbol{r}) \tag{4.2.1}$$

Its spectrum looks like Fig. 4.2(a). As seen in Fig. 4.2, for this Hamiltonian there is neither the lower bound and the upper bound, thus there is no variational principle for

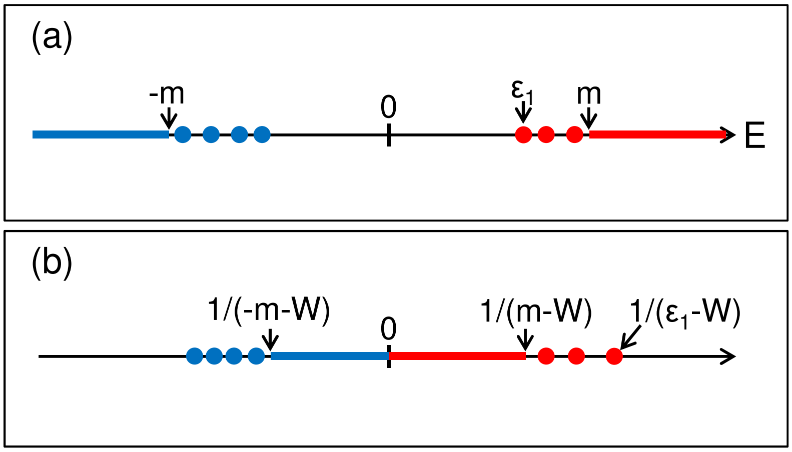

Figure 4.2: Schematic picture for spectrum of (a) a relativistic Hamiltonian H for a single-particle with mass m and (b) its inverse $1/(H-W)$. Positive and negative energy eigenvalues are denoted by red and blue color, respectively. The bound states are given by solid circles and the continuum states are represented by solid lines.

this eigenvalue problem. In the positive energy region there are discrete bound states and continuum states above up to the positive infinity, and in addition, there are discrete bound states in the negative energy region and continuum states below down to the negative infinity. Although one can solve a Dirac equation either with a basis expansion or with a coordinate space technique such as the Runge-Kutta method [120], there is no guarantee as described in Sec. 4.1 that the obtained eigenvalues are higher than the exact ones.

Of course, as the number of basis states is increased, i.e., as the model space approaches complete, the approximate solutions converges to the exact one, but the convergence behavior is not monotonic, in contrast to the non-relativistic case. Many prescriptions for basis expansion method to avoid the problem and to give a safe upper bound of the energy eigenvalue have been proposed in quantum chemistry [121–126].

The coordinate space solution is more difficult to obtain, especially in 3D calculations. The powerful imaginary time technique fails in relativistic systems since the method seeks for the lowest energy solutions. If we naively apply the method, the iterative solution dives into the continuum in the Dirac sea. This is numerically confirmed in Ref. [127] (see Fig. 4.3), This is not what we want since we need the lowest states in the Fermi sea and do not need the Dirac sea states at all in usual mean-field calculation with the no-sea approximation. Zhang *et al.* [127] have applied in Ref. [127] the imaginary time method to a Schrdinger-like equation obtained by eliminating the lower component from the Dirac equation. They have also applied in Ref. [128] their method to a Dirac equation with a non-local potential which may arise in relativistic Hartree-Fock calculations.

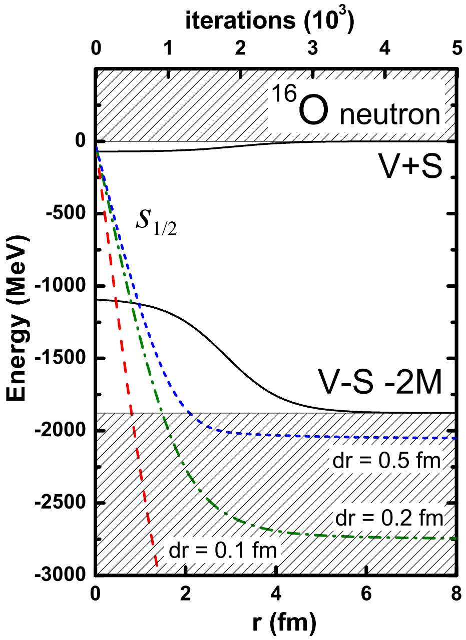

Figure 4.3: Imaginary time evolutions of the energy expectation value of a Dirac equation with a Woods-Saxon potential. The horizontal axis is energy, and the hatched area shows the energy region of the continuum states. The black solid curves denotes the potential as a function of the radial coordinate r shown in the lower horizontal axis, and the colored lines shows the imaginary time evolution of the energy expectation value as a function of the imaginary time iterations shown in the upper horizontal axis. The dotted, dot-dashed, and dashed line represents the result obtained with the radial mesh size dr = 0.5, 0.2, and 0.1 fm, respectively. The figure is taken from Ref. [127].

4.2.2 Maximization of the inverse of Hamiltonian

Here we introduce an idea to avoid the variational collapse proposed by Hill and Krauthauser [129], which is based on a variational principle for an operator $1/(H-W)$ where W is a real number not equal to any of the eigenvalue of H. As we mentioned, the ordinary variational principle is not applicable to a relativistic Hamiltonian itself because it has negative energy spectrum down to negative infinity as well as positive energy spectrum up to positive infinity (See Fig. 4.2(a)). The bound states just below and above the two continua are discrete.

Let the exact eigenvalues be

$$\cdots \leq E_{-2} \leq E_{-1} < E_1 \leq E_2 \leq \cdots \tag{4.2.2}$$

where E_i with positive (negative) i is an energy eigenvalue in the Fermi (Dirac) sea. Note that, in general, the number of bound states in the Dirac sea and the Fermi sea are different. We take a real constant $E_{-1} < W < E_1$ between the two seas and consider an operator $1/(H-W)$. This operator is hermitian and its spectrum looks like Fig. 4.2(b). The two continua of H comes to the middle of the spectrum of $1/(H-W)$, and the positive and negative energy bound states comes to the top and the bottom of the spectrum, respectively. The state on the top of the spectrum of $1/(H-W)$ corresponds to the lowest energy state in the Fermi sea and the one at the bottom to the highest state in the Dirac sea. Since $1/(H-W)$ is bound both from the above and below, there is a variational principle for this hermitian operator expressed by a inequality

$$\frac{1}{E_{-1}-W} \leq \frac{\langle\Psi|(H-W)^{-1}|\Psi\rangle}{\langle\Psi|\Psi\rangle} \leq \frac{1}{E_1-W}. \tag{4.2.3}$$

The approximate solutions in the Fermi sea are obtained by maximization of $\mathcal{H}[\Psi] = \langle\Psi|(H-W)^{-1}|\Psi\rangle/\langle\Psi|\Psi\rangle$. On the other hand, minimization of $\mathcal{H}$ leads to approximate solutions for the Dirac sea states. Let the true discrete eigenvalues for bound states of $1/(H-W)$ be

$$\lambda_{-1} \leq \lambda_{-2} \leq \cdots < 0 < \cdots \leq \lambda_2 \leq \lambda_1. \tag{4.2.4}$$

with

$$\lambda_k = \frac{1}{E_k - W}, \quad k = \pm 1, \pm 2, \ldots \tag{4.2.5}$$

The same discussion as that in Sec. 4.1.2 applies to $1/(H-W)$. If one expands the eigenstates of $1/(H-W)$ with a sufficiently large basis set consisting of N independent bases, the eigenvalues $\lambda_k^{(N)}$ in this subspace are

$$\lambda_{-1}^{(N)} \leq \lambda_{-2}^{(N)} \leq \cdots < 0, \tag{4.2.6}$$

$$0 < \cdots \leq \lambda_2^{(N)} \leq \lambda_1^{(N)}. \tag{4.2.7}$$

The Poincaré's theorem implies

$$\lambda_{-1} \leq \lambda_{-1}^{(N)},\ \lambda_{-2} \leq \lambda_{-2}^{(N)},\ \ldots \tag{4.2.8}$$

$$\ldots,\ \lambda_2^{(N)} \leq \lambda_2,\ \lambda_1^{(N)} \leq \lambda_1. \tag{4.2.9}$$

Thus we have

$$E_{-1} \geq \frac{1}{\lambda_{-1}^{(N)}} + W,\ E_{-2} \geq \frac{1}{\lambda_{-2}^{(N)}} + W,\ \dots \tag{4.2.10}$$

$$\dots,\ E_{2} \leq \frac{1}{\lambda_{2}^{(N)}} + W,\ E_{1} \leq \frac{1}{\lambda_{1}^{(N)}} + W. \tag{4.2.11}$$

With W taken in an open interval (E_{-1}, E_1), we will obtain the upper limits for the positive energy bound states and the lower limits for the negative energy bound states. Furthermore, let us take another value for W, $W' \in (E_1, E_2)$. In this case the state of E_1 comes to the bottom in the spectrum of $1/(H - W')$. Denoting the eigenvalues of $1/(H - W')$ by λ'_i, we obtain in a similar way as above,

$$E_{1} \geq \frac{1}{\lambda_{1}^{\prime(N)}} + W',\ E_{-1} \geq \frac{1}{\lambda_{-1}^{\prime(N)}} + W',\ E_{-2} \geq \frac{1}{\lambda_{-2}^{\prime(N)}} + W',\ \dots \tag{4.2.12}$$

$$\dots,\ E_{3} \leq \frac{1}{\lambda_{3}^{\prime(N)}} + W',\ E_{2} \leq \frac{1}{\lambda_{2}^{\prime(N)}} + W', \tag{4.2.13}$$

which yields the lower limit for the lowest state in the Fermi sea. This method gives both the upper and lower limits for the bound state energies, which are guaranteed by a rigorous variational principle. It is also guaranteed that both the upper and lower limits monotonically approach to the true eigenvalues by increasing the number of bases or variational parameters. This is indeed confirmed numerically in Ref. [130].

4.3 Inverse Hamiltonian method

In this section, we propose a new method [131], which we call **“inverse Hamiltonian method”**, for solving Dirac equations without variational collapse, based on the idea of Hill and Krauthauser [129] that applies the variational principle for the inverse of the Hamiltonian. It is to be applied in the mean-field calculations for nuclei in the 3-dimensional coordinate space representation. In Sec. 4.3.1, we introduce the method and explain how it works for a Dirac equation for a given potential. In Sec. and 4.3.2, we explain how to implement our method in self-consistent calculations in the 3-dimensional coordinate space.

4.3.1 Basic idea of the inverse Hamiltonian method

Now we proceed to our own method, for the relativistic calculations. In this section we consider a single-particle Dirac equation with a given potential. Our idea is analogous to the imaginary time method, but is based on the variational principle for an inverse of the single-particle Hamiltonian rather than the Hamiltonian itself. Here we consider a single-particle Dirac equation,

$$h\psi(\boldsymbol{r}) = \epsilon\psi(\boldsymbol{r}), \tag{4.3.1}$$

where ϵ is energy eigenvalue. The Hamiltonian h is given by

$$-i\boldsymbol{\alpha}\cdot\boldsymbol{\nabla}+V(\boldsymbol{r})+\beta[m+S(\boldsymbol{r})]-m. \tag{4.3.2}$$

The potential $V(\boldsymbol{r})$ corresponds to a mean field generated by the time-like component of a vector meson and the photon fields, and $S(\boldsymbol{r})$ corresponds to a field by a scalar meson. As stated in the preceding sections, the spectrum is bounded neither from the above nor below. The eigenvalues are labeled by an integer k according to energy so that

$$\ldots\leq\epsilon_{-2}\leq\epsilon_{-1}<\epsilon_1\leq\epsilon_2\leq\ldots, \tag{4.3.3}$$

where $k>0$ ($k<0$) corresponds to the Fermi (Dirac) sea solutions. Let $|\phi_k\rangle$ be the eigenstate associated to ϵ_k.

In our method, we prepare an initial state (a set of initial states) $|\psi^{(0)}\rangle$, which is not an eigenstate of the Hamiltonian, and evolve it by an operator $e^{T/(h-W)}$:

$$\exp\left(\frac{T}{h-W}\right)|\psi^{(0)}\rangle=\sum_k e^{T/(\epsilon_k-W)}|\phi_k\rangle\langle\phi_k|\psi^{(0)}\rangle\underset{T\to\infty}{\propto}|\phi_1\rangle, \tag{4.3.4}$$

where W is a real number set between the Fermi sea and the Dirac sea[1]. As we have done in Eq. (2.2.5), the initial state is expanded by the true eigenstates on the right hand side of Eq. (4.3.4). In the limit $T\to\infty$, the wave function converges to the lowest state in the Fermi sea, $|\phi_1\rangle$. With the evolution by $e^{T/(h-W)}$ all the negative energy eigenstates contained in the initial state will damp away because the exponent is all negative. On the other hand, all the positive energy states will grow up since the exponent is all positive, but among them, the state closest to W in the Fermi sea, $|\phi_1\rangle$, grows up most rapidly. Eventually the wave function will be dominated by $|\phi_1\rangle$. If we take $T\to-\infty$, the wave function converges to the state on the top of the Dirac sea. Hereafter we only consider a positive T. As discussed in Sec. 2.2.2, we can obtain the lowest energy states in the Fermi sea solutions if we orthonormalize them by the Gram-Schmidt method starting from the lowest state. With our method we can obtain only the positive energy solutions that are usually of interest in mean-field calculations.

Notice that the iterative solution converges to $|\phi_2\rangle$ if the shift parameter W is set between ϵ_1 and ϵ_2. Although this is a way to obtain the excited single-particle states, it has in principle a risk that $h-W$ becomes singular when W happens to be equal to an eigenvalue of h.

In a practical calculation, T is cut into steps by ΔT, and the evolution is performed iteratively by this step size in T. In every step, the exponential function $e^{\Delta T/(h-W)}$ is expanded to the first order of ΔT. The iterative wave function at $T=(n+1)\Delta T$ is given by the wave function at the previous step as

$$|\psi^{(n+1)}\rangle\propto\left(1+\frac{\Delta T}{h-W}\right)|\psi^{(n)}\rangle. \tag{4.3.5}$$

---

[1] Note that T has dimension of energy and has nothing to do with time.

Since the evolution operator is not unitary, we normalize the wave function at each step. In contrast to the imaginary time method, the step size ΔT in our method does not always have to be small in order to get the desired state. We will discuss this point in the next section.

Let us suppose that the step size ΔT is sufficiently small so that the second order of ΔT is negligible. It can be shown that the expectation value of the inverse of the Hamiltonian monotonically increases. To the first order of ΔT,

$$\begin{aligned}\frac{\langle\psi^{(n+1)}|h^{-1}|\psi^{(n+1)}\rangle}{\langle\psi^{(n+1)}|\psi^{(n+1)}\rangle} &= \frac{\langle\psi^{(n)}|\left(1+\frac{\Delta T}{h}\right)\frac{1}{h}\left(1+\frac{\Delta T}{h}\right)|\psi^{(n)}\rangle}{\langle\psi^{(n)}|\left(1+\frac{\Delta T}{h}\right)\left(1+\frac{\Delta T}{h}\right)|\psi^{(n)}\rangle} \\ &\simeq \frac{\langle\psi^{(n)}|h^{-1}|\psi^{(n)}\rangle+2\Delta T\langle\psi^{(n)}|h^{-2}|\psi^{(n)}\rangle}{1+2\Delta T\langle\psi^{(n)}|h^{-1}|\psi^{(n)}\rangle} \\ &\simeq \langle\psi^{(n)}|h^{-1}|\psi^{(n)}\rangle+2\Delta T\left[\langle\psi^{(n)}|h^{-2}|\psi^{(n)}\rangle-\left(\langle\psi^{(n)}|h^{-1}|\psi^{(n)}\rangle\right)^2\right].\end{aligned} \tag{4.3.6}$$

Since the second term of the last line is the dispersion of h^{-1},

$$\frac{\langle\psi^{(n+1)}|h^{-1}|\psi^{(n+1)}\rangle}{\langle\psi^{(n+1)}|\psi^{(n+1)}\rangle} \geq \langle\psi^{(n)}|h^{-1}|\psi^{(n)}\rangle. \tag{4.3.7}$$

On the other hand, the behavior of the energy expectation value, $\langle h\rangle$, is not necessarily monotonic:

$$\frac{\langle\psi^{(n+1)}|h|\psi^{(n+1)}\rangle}{\langle\psi^{(n+1)}|\psi^{(n+1)}\rangle} \simeq \langle\psi^{(n)}|h|\psi^{(n)}\rangle+2\Delta T\left(1-\langle\psi^{(n)}|h|\psi^{(n)}\rangle\langle\psi^{(n)}|h^{-1}|\psi^{(n)}\rangle\right), \tag{4.3.8}$$

where the sign of the second term in the right-hand-side depends on $\psi^{(n)}$. Notice that both in Eqs. (4.3.7) and (4.3.8), the second term in the last line converges to zero as the iterative wave function converges to an eigenstate of the Hamiltonian. The consequences given above are natural and reasonable since the method is based on the variational principle for the inverse of the Hamiltonian.

Advantages of our method is that, in contrast to some other methods [125–128,130], it is relatively straightforward to apply our method not only to the Dirac equation but also to other eigenvalue problems with unbound operators, such as non-relativistic Hartree-Fock-Bogoliubov equations (See Appendix A.).

4.3.2 Self-consistent calculations

In this section, we show how our method works in self-consistent mean-field calculations. We simply replace the imaginary time evolution introduced in Sect. 2.2.2. That is,

1. Prepare an initial set of single-particle wave functions $\{\psi_k^{(0)}\}$ $(k=1,2,...,A)$.
2. Construct the single-particle Hamiltonian $h^{(0)}$, which is a functional of the density $\rho^{(0)}$.

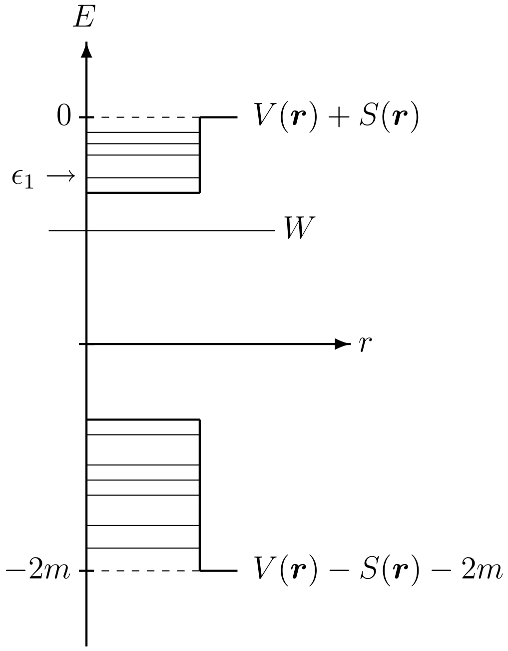

Figure 4.4: Schematic figure for the spectrum a Dirac equation. If W is taken between the Fermi sea and the Dirac sea, $1/(\epsilon_k - W) > 0$ for the Fermi sea states and $1/(\epsilon_k - W) < 0$ for the Dirac sea states. $\epsilon \geq 0$ and $\epsilon \leq -2m$ correspond to the continuum states.

3. Generate a new set of the single-particle wave functions, $\{\tilde{\psi}_k\}$, by applying the evolutions on each wave functions:

$$|\tilde{\psi}_k\rangle = \exp(\Delta T/(h^{(n)} - W^{(n)})|\psi_k^{(n)}\rangle, \ k = 1, \ \dots, \ A, \tag{4.3.9}$$

4. Orthonormalize the set $\{\tilde{\psi}_k\}$ to obtain $\{\psi_k^{(n+1)}\}$. Go back to the step 2.

Again, the steps from 2 to 4 are iterated until a convergence is achieved. The shift of energy $W^{(n)}$ may change. For a sufficiently small value of ΔT, we can show in the same way as in the imaginary time method that

$$\rho^{(n+1)} - \rho^{(n)} = \Delta T \left[\rho^{(n)} \frac{1}{h^{(n)} - W^{(n)}} (1 - \rho^{(n)}) + (1 - \rho^{(n)}) \frac{1}{h^{(n)} - W^{(n)}} \rho^{(n)} \right], \tag{4.3.10}$$

which leads to

$$\mathrm{Tr} \left[\frac{1}{h^{(n)} - W^{(n)}} (\rho^{(n+1)} - \rho^{(n)}) \right] = 2\Delta T \cdot \mathrm{Tr} \left[\rho^{(n)} \frac{1}{h^{(n)} - W^{(n)}} (1 - \rho^{(n)}) \frac{1}{h^{(n)} - W} \right] \tag{4.3.11}$$

Defining $B^\dagger = \rho^{(n)} (h^{(n)} - W)^{-1} (1 - \rho^{(n)})$, we obtain

$$\mathrm{Tr} \left[\frac{1}{h^{(n)} - W} (\rho^{(n+1)} - \rho^{(n)}) \right] = 2\Delta T \cdot \mathrm{Tr} \left[B^\dagger B \right] > 0 \tag{4.3.12}$$

The quantity

$$\mathrm{Tr}\left[\frac{1}{h^{(n)}-W^{(n)}}\rho^{(n)}\right]=\sum_{k=1}^{A}\left\langle \psi^{(n)}\left|\frac{1}{h^{(n)}-W^{(n)}}\right|\psi^{(n)}\right\rangle \tag{4.3.13}$$

always increases from iteration to iteration, which means that $\{|\psi_k^{(n+1)}\rangle\}$ are better solutions of $h^{(n)}$ than $\{|\psi_k^{(n)}\rangle\}$. This will eventually converge at its maximum (for a fixed W), and it implies $B^\dagger = 0$, or

$$\left[\frac{1}{h-W},\rho\right]=0. \tag{4.3.14}$$

Multiplying by $h-W$ from right and left on the both sides of the above equation, we get

$$[h,\rho]=0 \tag{4.3.15}$$

at the convergence.

Chapter 5

Fermion Doubling and Wilson Fermion

In the previous chapter we have introduced one of the major problems, variational collapse, in relativistic mean field calculations on 3D lattice and how to avoid it. In this chapter we will introduce another big problem, fermion doubling, and how to overcome it.

5.1 Fermion doubling

5.1.1 The mechanism

The fermion doubling problem has been known in the field of lattice QCD, in which the space-time is discretized and the first derivative in the action

$$S = \int d^3r \; \bar{\psi}(i\gamma^\mu \partial_\mu - m)\psi \tag{5.1.1}$$

is replaced by a finite difference. An essential origin of the problem is the first derivative in the action or the Dirac equation. Here we will show how the problem arises out of a static one-particle Dirac equation. For simplicity we consider a Dirac equation for a free particle in 1-dimensional space. That is,

$$(-i\alpha\partial_x + \beta m)\psi(x) = \epsilon\psi(x), \tag{5.1.2}$$

where $\psi(x)$ is a two-component spinor and

$$\alpha = \begin{pmatrix} 0 & 1 \\ 1 & 0 \end{pmatrix}, \; \beta = \begin{pmatrix} 1 & 0 \\ 0 & -1 \end{pmatrix}. \tag{5.1.3}$$

The coordinate x is discretized with a mesh size a within a box of size L, and the derivative in the kinetic term is approximated by 3-point difference formula

$$\partial_x \psi(x_i) = \frac{\psi(x_{i+1}) - \psi(x_{i-1})}{2a}, \tag{5.1.4}$$

where $x_i = ai$ is the i-th mesh point. If we impose either periodic $[\psi(x+L) = \psi(x)]$ or anti-periodic $[\psi(x+L) = -\psi(x)]$ boundary condition, the Fourier transform $\tilde{\psi}(k)$ of the wave function satisfies

$$\psi(x_j) = \int \frac{dk}{2\pi}\, e^{ikaj}\tilde{\psi}(k) \tag{5.1.5}$$

Substituting Eq. (5.1.5) into the discretized Dirac equation, we obtain

$$\int \frac{dk}{2\pi}\, \left[\frac{1}{2ai}\alpha e^{ikaj} \cdot 2i\sin(ka)\tilde{\psi}(k) + m\beta e^{ikaj}\tilde{\psi}(k)\right] = \epsilon \int \frac{dk}{2\pi}\, e^{ikaj}\tilde{\psi}(k). \tag{5.1.6}$$

Thus the Dirac equation in the momentum space reads

$$\left[\frac{1}{a}\alpha\sin(ka) + \beta m\right]\tilde{\psi}(k) = \epsilon\tilde{\psi}(k). \tag{5.1.7}$$

From Eq. (5.1.7) one obtains a dispersion relation

$$\epsilon^2 = \frac{1}{a^2}\sin^2(ka) + m^2, \tag{5.1.8}$$

which becomes the ordinary dispersion relation of a relativistic particle

$$\epsilon^2 = k^2 + m^2 \tag{5.1.9}$$

in the continuum limit ($a \to 0$). In Fig. 5.1, we show several dispersion relations of a fermion on lattice together with the one in the continuum limit. The solid curve is the exact dispersion relation given in Eq. (5.1.9), while the dashed curve shows the dispersion relation of a discretized Dirac equation given in Eq. (5.1.8). The dotted and dot-dashed curves are also discretized results obtained with 5- and 11-point finite difference formulas, respectively. With 5-point formula, the dispersion relation is given by

$$\epsilon^2 = \frac{1}{a^2}\left[\frac{4}{3}\sin(ka) - \frac{1}{6}\sin(2ka)\right]^2 + m^2, \tag{5.1.10}$$

and with 11-point formula, the dispersion relation is given by

$$\begin{aligned}\epsilon^2 = \frac{1}{a^2}\Big[&\frac{5}{3}\sin(ka) - \frac{10}{21}\sin(2ka) + \frac{5}{42}\sin(3ka) \\ &-\frac{5}{252}\sin(4ka) + \frac{1}{630}\sin(5ka)\Big]^2 + m^2.\end{aligned} \tag{5.1.11}$$

The expressions for the finite difference itself are given in Appendix D. In the continuum limit energy increases monotonically as a function of momentum as the solid curve in Fig. 5.1. In contrast, for the discretized fermions, one sees a spurious minimum at the edge of the Brillouin zone, i.e. the cut-off momentum $k = \pi/a$ in the model space. As seen in Fig. 5.1, this minimum does not disappear even if we take more accurate difference formula, although the lower momentum behavior is improved. If one solves the discretized Dirac equation, one obtains not only physical solutions with low energy and low momentum, but also solutions on the unphysical side with *low energy and high momentum.* In 1D case, one spurious state appears for each physical state, while in 3D case there are seven spurious states for each physical solution.

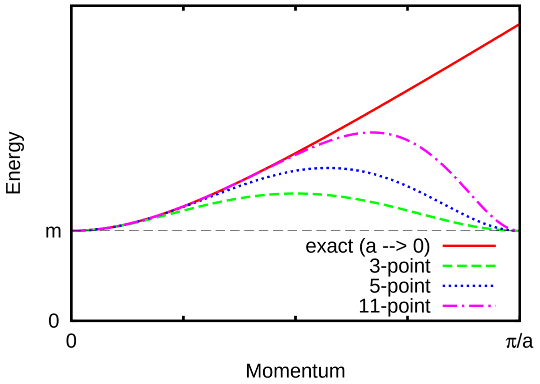

Figure 5.1: Dispersion relations for fermions with several different finite difference formulas for the kinetic term. Solid curve shows the exact dispersion relation given in Eq. (5.1.9). Dashed, dotted, and dot-dashed curves are the dispersion relations obtained with 3-, 5-, and 11-point difference formulas, respectively.

5.1.2 An example of fermion doubling

In this section we show a real example of fermion doubling. We solve a 1-dimensional Dirac equation with a Woods-Saxon (WS) potential by using the inverse Hamiltonian method, and investigate the properties of energy spectrum and wave functions.

Here we consider a single-particle Dirac equation in 1-dimension with two potentials:

$$[-i\alpha\partial_x + V(x) + \beta(m + S(x)) - m]\psi(x) = \epsilon\psi(x), \tag{5.1.12}$$

$V(x)$ corresponds to a mean field generated by the time-like component of a vector meson, and $S(x)$ corresponds to a field by a scalar meson. If we define the two-component spinor as

$$\psi(x) = \begin{pmatrix} \psi_1(x) \\ i\psi_2(x) \end{pmatrix}, \tag{5.1.13}$$

we get the coupled equations

$$\begin{pmatrix} V+S & \partial_x \\ -\partial_x & V-S-2m \end{pmatrix} \begin{pmatrix} \psi_1(x) \\ \psi_2(x) \end{pmatrix} = \epsilon \begin{pmatrix} \psi_1(x) \\ \psi_2(x) \end{pmatrix}. \tag{5.1.14}$$

For the potentials $V(x)$ and $S(x)$ we take a Woods-Saxon type

$$\begin{aligned} V(x) + S(x) \equiv U(x) &= \frac{U_0}{1 + e^{(|x|-R_U)/a_U}}, \text{ and} \\ V(x) - S(x) \equiv W(x) &= \frac{W_0}{1 + e^{(|x|-R_W)/a_W}}. \end{aligned} \tag{5.1.15}$$

The parameters in the potentials, which are taken from Ref. [132], are shown in Table 5.1. In the following, we take $N = Z = 20$, $A = N + Z = 40$. The mass of the particle m is set to be the nucleon mass, 939 MeV.

Table 5.1: Parameters in the Woods-Saxon potentials in Eq. (5.1.15) [132].

U_0 (MeV)	W_0 (MeV)	R_U (fm)	R_W (fm)	a_U (fm)	a_W (fm)
$-71.28(1-0.462\frac{N-Z}{A})$	$-11.12U_0$	$1.233A^{1/3}$	$1.144A^{1/3}$	0.614	0.648

We solve the Dirac equation in the coordinate space. We discretize the coordinate x with mesh size $a = 0.1$ fm with 400 mesh points. The box boundary condition is imposed. Note that for bound-state solutions the box and the periodic boundary conditions gives the same result if box size is sufficiently large. The parameters of the inverse Hamiltonian method are are taken as $W = U_0$ and $\Delta T = 100$ MeV. For inversion of the Hamiltonian, we employ the Conjugate Residual (CR) method [133] (See also Appendix C). We will compare the results with the exact result which is obtained by directly diagonalizing the coordinate space Hamiltonian.

First, we show in Fig. 5.2 the convergence of the iterative solutions. The first derivative in the kinetic term in the Hamiltonian is approximated by the 3-point formula. We can see in Fig. 5.2(a) that iterative solutions converge to degenerate pairs of states. Since the mean squared deviations of energy converges to small values (Fig. 5.2), they are the eigenstates of the Hamiltonian. None of the states has fallen down to the Dirac sea. By this result we have confirmed that our inverse Hamiltonian method gives the correct solutions in the positive energy spectrum without a variational collapse. The energy eigenvalues and expectation values of p^2, $\langle p^2\rangle/2m$, after all bound state solutions well converge, are summarized in Table 5.2. There are 10 bound state solutions (including the spurious states). Expectation value of p^2 is extremely large for one state in each pair, which implies that these states are the spurious solutions.

In Fig. 5.3 we show the wave functions of the three lowest pairs after 1000 iterations. The left panels ((a), (c), and (e)) and the right panels ((b), (d), and (f)) correspond to the physical and the spurious states, respectively. The spurious states has the same amplitude as the corresponding physical states but they change their signs at every mesh point. This can be understood by the nature of the 3-point formula $f_i' = \frac{f_{i+1}-f_{i-1}}{\Delta x}$. The 3-point formula can not distinguish them because even and odd mesh points decouple in this difference formula.

We have seen that each pair of physical and spurious states is degenerate in energy if we use 3-point formula for the kinetic term. What happens to the spurious states if we approximate the derivative in the kinetic term with more accurate difference formula? In Fig. 5.4 the spectra of the Dirac equation obtained with 3-, 5-, 7-, 9-, and 11-point formulas for the kinetic term are plotted. See Appendix D for the coefficients of various finite difference formulas. The physical and the spurious solutions are shown by blue circles and red crosses, respectively. They can be easily distinguished by looking at the wave function or the value of $\langle p^2\rangle/2m$. Wave functions of an unphysical state oscillates very rapidly, and the value of $\langle p^2\rangle/2m$ is accordingly quite large compared to typical value of kinetic energy of a nucleon ($\lesssim$ 30 MeV). With the formulas better than 3-point

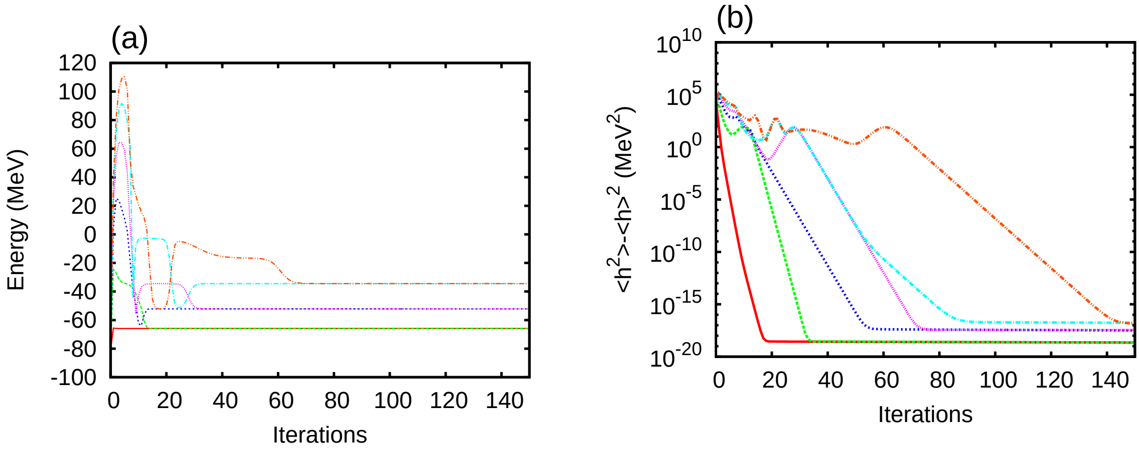

Figure 5.2: Convergences of (a) energy and (b) mean squared deviation of h, for the 1-dimensional Dirac equation. The first derivative in the kinetic term is approximated by 3-point formula.

Table 5.2: Energy eigenvalues and expectation values of p^2 (divided by $2m$) of the eigenstates of Dirac equation. The first derivative in the kinetic term is approximated by 3-point formula.

k	ϵ_k (MeV)	$\langle p^2\rangle/2m$ (MeV)
1	-65.8951	2.06
2	-65.8951	8291.43
3	-52.1765	7.40
4	-52.1765	8286.09
5	-34.4873	14.00
6	-34.4873	8279.48
7	-16.6596	18.78
8	-16.6596	8274.71
9	-2.9595	15.00
10	-2.9595	8278.49

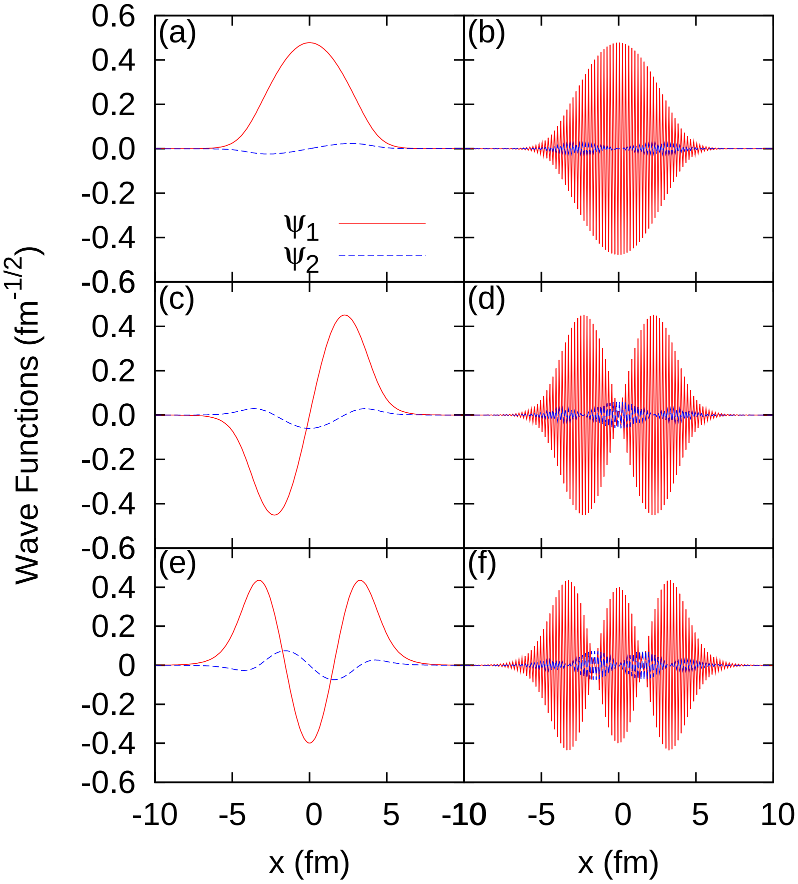

Figure 5.3: Six lowest energy eigenstates of the Dirac equation. The kinetic term in the Hamiltonian is approximated by 3-point formula. (a) to (e) corresponds to $k = 1$ to 6 in Table 5.2, respectively. Note that any linear combination of wave functions in the same pair is an eigenstate of the Hamiltonian.

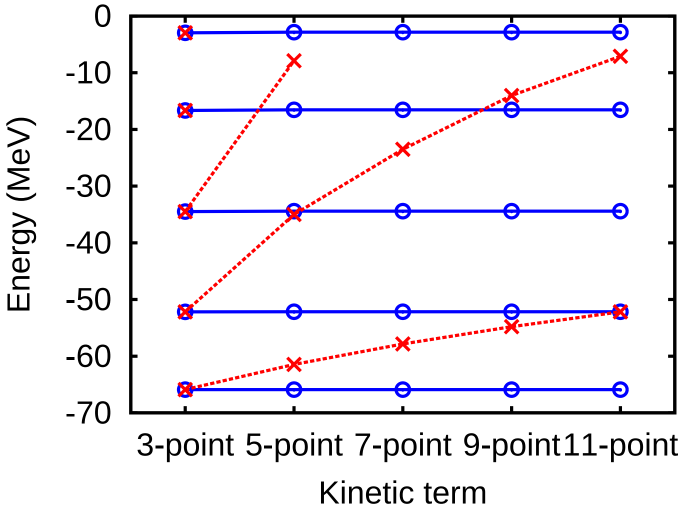

Figure 5.4: Energy spectra of a 1-dimensional Dirac equation obtained by using several different difference formulae for the kinetic term in the Hamiltonian. The open circles and the crosses correspond to physical and spurious states, respectively. Some of the spurious states are pushed up to the continuum region for 5-, 7-, 9-, and 11-point formulas.

formula, spurious states are no longer degenerate to the corresponding physical states. With 5-point formula, the spurious states in the 4th and 5th pairs are already pushed away to the continuum region, while the lower spurious states are still in the bound region. With 7-point formula, the 3rd unphysical state also go up to the continuum region. The energy shifts of higher spurious states are larger than that of the lower ones. Therefore, the better difference formulas for the kinetic term violate the degeneracies and lift up the spurious states although the shifts of energies may not be sufficient to remove all of them from the energy region considered in ordinary mean-field calculations.

5.2 Wilson fermion and its improvement

In this section, we introduce the method of “Wilson fermion” and its extension which is employed to eliminate the spurious solutions of discretized Dirac equation.

5.2.1 Wilson fermion

The Wilson fermion [134,135] is widely adopted method to eliminate the spurious fermions in lattice QCD calculations. Wilson introduced a term proportional to p^2 into the action, which gives an additional contribution to the dispersion relation to separate the energy of the spurious states on the high-momentum sides from that of the physical states on the low-momentum side.

Let us introduce the Wilson term in the language of the static 1D Dirac equation. Action of Hamiltonian on a wave function for a Wilson fermion in the 1D case is given by

$$\begin{aligned}(h_W\psi)(x_i) &= -i\alpha\frac{1}{2a}[\psi(x_{i+1})-\psi(x_{i-1})]+\beta m\psi(x_i)\\ &- \beta\frac{R}{a}[\psi(x_{i+1})-2\psi(x_i)+\psi(x_{i-1})]. \end{aligned}\tag{5.2.1}$$

The last term which is added in the Hamiltonian is called "Wilson term." Here R is a dimensionless free parameter called "Wilson parameter." The corresponding Hamiltonian in the continuum limit may be formally written as

$$h_W = -i\alpha\partial_x + \beta(m - aR\partial_x^2), \tag{5.2.2}$$

which could be straightforwardly extended to the 3D space as

$$h_W = -i\boldsymbol{\alpha}\cdot\boldsymbol{\nabla} + \beta(m - aR\Delta). \tag{5.2.3}$$

Notice that, in the continuum limit (that is, in the limit of $a \to 0$), the Wilson term vanishes and the original form of a Hamiltonian is recovered. Since the Wilson term, $-aR\beta\Delta$, is proportional to p^2, this term lifts up the spurious minimum of the dispersion relation at the edge of the Brillouin zone. Due to the addition of the Wilson term, energies of the spurious states are all pushed upwards. Of course, the physical states are also affected by the Wilson term, but the effect is much less since their $\langle p^2\rangle$ is smaller than that of the spurious states. Thus, in order to avoid the trouble with the doubling, one should take the value of R so that all the spurious states are pushed away from the single-particle energy region relevant to the calculation, i.e., all the spurious states are above the fermi energy for mean-field level calculations.

For simplicity let us again consider a 1D case, in which a Dirac equation is given by

$$[-i\alpha\partial_x + \beta(m - aR\partial_x^2)]\psi(x) = \epsilon\psi(x). \tag{5.2.4}$$

The dispersion relation for this particle with 3-point formula for the kinetic term is given by

$$\epsilon^2 = \frac{1}{a^2}\sin^2(ka) + \left[m + \frac{2R}{a}(1-\cos(ka))\right]^2. \tag{5.2.5}$$

This also becomes the exact dispersion relation given in Eq. (5.1.9) in the continuum limit. Fig. 5.5 shows a comparison of dispersion relations with and without the Wilson term. The dispersion relations corresponding to the dot-dashed curve (11-point + $R = 0.2$) in Fig. 5.5 is given by

$$\begin{aligned}\epsilon^2 &= \frac{1}{a^2}\left[\frac{5}{3}\sin(ka) - \frac{10}{21}\sin(2ka) + \frac{5}{42}\sin(3ka)\right.\\ &\left. -\frac{5}{252}\sin(4ka) + \frac{1}{630}\sin(5ka)\right]^2 + \left[m + \frac{2R}{a}(1-\cos(ka))\right]^2. \end{aligned}\tag{5.2.6}$$

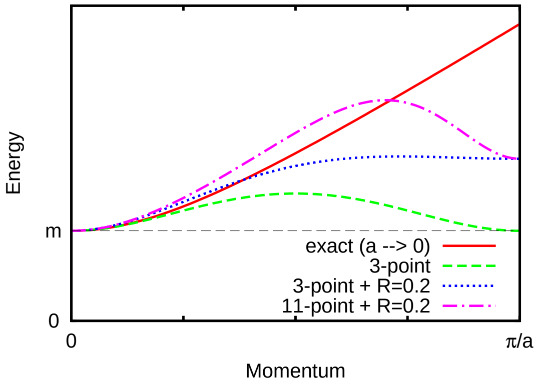

Figure 5.5: Comparison of the dispersion relations with and without the Wilson term, which is given in Eq. (5.2.4). Solid and dashed curves are the same as Fig. 5.1. The dotted and dot-dashed curves are dispersion relations with the Wilson term with $R = 0.2$. The dotted curve is obtained with 3-point formula for the kinetic term and the dot-dashed one with 11-point formula.

As one can see in the Figure, the spurious minimum at $k = \pi/a$ has now disappeared due to the effect of the Wilson term, and the effect is vanishing at $k = 0$. However, the lower momentum side also deviates from the exact dispersion relation. The Wilson term influences not only the spurious states but also the physical states as expected.

We note here that, for $a = 0.8$ fm which may be a typical mesh size for 3D calculations, the fermi momentum of nucleons $k_F \simeq 230$ MeV corresponds to $0.3 \times \pi/a$. Thus it is required in this case that the dispersion relation agree well with the exact one up to $k \simeq 0.3 \times \pi/a$. We must also notice that the fermi energy of nucleons is $\epsilon_F = k_F^2/2m \simeq 30\text{MeV} \simeq 0.03m$, thus, the upward shift of the unphysical minimum due to the Wilson term is required to be larger than $\sim 0.03m$ in mean-field level calculations. In Fig. 5.5, we have chosen the value $R = 0.2$ rather arbitrarily so that the effect of the Wilson term is clearly visible in the dispersion relation. Therefore, the value taken in Fig. 5.5, in which the shift of minimum is comparable to m, was much larger than its realistic value. In any case, it is true that the physical solutions are affected by the Wilson term and we should keep the effect as small as possible.

Not only the Wilson fermion for lattice field theory, but also other prescriptions have been proposed in the field of chemistry and solid state physics [136–138]. Although they were shown to give solutions without doubling [136–138], they are not very suitable to apply to our 3D calculations employing an accurate difference formula, e.g., 11-point difference, for the kinetic term. Therefore we persist on the Wilson fermion with an extension introduced in the next section, which is straightforwardly applicable to our calculations.

5.2.2 Extension to high-order derivative

In the previous section, we have introduced the Wilson term, which lifts up the spurious minimum of the dispersion relation. Since it affects the physical solutions as well, here we consider a way to reduce the effect on the physical solutions so that we could obtain more accurate physical solutions. Since the dispersion relation The typical value in non-relativistic mean-field calculations is $a = 0.8$ for the mesh size In order to obtain better physical solutions, we consider an improvement on the Wilson term by increasing the power of p,

$$-aR\beta\sum_{i=1}^{3}\partial_i^2 \;\rightarrow\; (-)^m a^{2m-1}R\beta\sum_{i=1}^{3}\partial_i^{2m}, \tag{5.2.7}$$

for which we can expect much more effect on the spurious states and much less effect on the physical states. We show in Fig. 5.6 the dispersion relations for 1D case obtained with the prescription given in Eq. (5.2.7). The dashed curve shows the result of normal Wilson fermion corresponding to $(m, R) = (1, 0.2)$ with 3-point difference for the kinetic term, which has already been shown in Fig. 5.5. Dotted and dot-dashed curves show the improved $[(m, R) = (4, 0.003)]$ dispersion relations with 3-point and 11-point difference for the kinetic term, respectively. The one with 3-point + $m = 4$ (dotted curve in Fig. 5.6) is given by

$$\begin{aligned}\epsilon^2 &= \frac{1}{a^2}\sin^2(ka) \\ &+\left\{m+\frac{2R}{a}[35-56\cos(ka)+28\cos(2ka)-8\cos(3ka)+\cos(4ka)]\right\}^2,\end{aligned} \tag{5.2.8}$$

and the other with 11-point + $m = 4$ (dot-dashed curve in Fig. 5.6) is given by

$$\begin{aligned}\epsilon^2 &= \frac{1}{a^2}\left[\frac{5}{3}\sin(ka)-\frac{10}{21}\sin(2ka)\right. \\ &\left.+\frac{5}{42}\sin(3ka)-\frac{5}{252}\sin(4ka)+\frac{1}{630}\sin(5ka)\right]^2 \\ &+\left\{m+\frac{2R}{a}[35-56\cos(ka)+28\cos(2ka)-8\cos(3ka)+\cos(4ka)]\right\}^2.\end{aligned} \tag{5.2.9}$$

The difference formula for the eighth derivative with $m = 4$ is given in Appendix D. It is clear that with the improved ($m > 1$) Wilson term we can realize both good agreement to the dispersion relation in the continuum limit and elimination of the spurious minimum on the unphysical (high-momentum) side.

5.2.3 Dirac equation with a Wilson term

Here we solve the same 1-dimensional Dirac equation as in Sec. 5.1.2 with the inverse Hamiltonian method and the Wilson fermion, and investigate the properties of energy

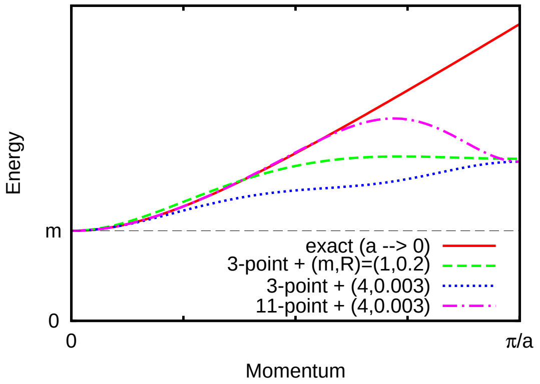

Figure 5.6: Dispersion relations of the improved Wilson fermion compared to the exact relation and the normal Wilson fermion. The parameters (m, R) are defined in Eq. (5.2.7).

spectrum and wave functions. In contrast to Sec. 5.1.2 we switch on the Wilson term. Notice that the Wilson term is proportional to ∂^{2m} (or p^{2m}), where $m = 1$ corresponds to the normal Wilson term, and $m \geq 2$ to the improved ones (See Eq. (5.2.7)). We will investigate how a change in the spectrum is influenced by choice of difference formula for the Wilson term and of the value of m in Eq. (5.2.7). In Fig. 5.7 we compare energy spectra of the Dirac equation with several different versions of the Wilson term. The Wilson parameter is kept constant at $R = 0.0005$ in all the calculations. With the Wilson term present, all the spurious states are shifted up by a similar amount. There is a small improvement from 3-point ($m = 1$) to 11-point ($m = 1$). By setting $m \geq 2$, the shifts become significantly larger and, for $m = 4$ (Wilson term $\propto p^8$), all spurious states are removed away to the continuum region for the present value of the Wilson parameter $R = 0.0005$. In these cases with the Wilson term, wave functions and energy eigenvalues of the physical states are also slightly modified. We show in Table 5.3 the physical spectrum obtained with different versions of the Wilson term. As we can see from Table 5.3 and Fig. 5.7, a high-order Wilson term with $m \geq 2$ has much more effect on the spurious states and much less effect on the physical states, as expected. With a Wilson term of 3-point ($m = 1$), energy differences to the exact value (energies obtained by $R = 0$) are order of 10^{-3} MeV. On the other hand, with a Wilson term of 9-point ($m = 4$) energy differences are as small as order 10^{-5} MeV. We will later discuss the modification on the wave functions by the Wilson term.

Next we investigate change of the spectrum as a function of the Wilson parameter R. In Fig. 5.8, we show the energy spectrum of the Dirac equation as functions of R. Fig. 5.8(a) is obtained by an ordinary Wilson term ($m = 1$) computed with 3-point formula. The kinetic term is also approximated by 3-point formula in this case. Fig. 5.8(b) shows the result obtained with an high-order Wilson term ($m = 4$) computed by 9-point formula. The kinetic term is computed by 11-point formula. We can see that the energy shifts of the unphysical states is proportional to the Wilson parameter R both in Fig. 5.8(a) and 5.8(b). In the case of $m = 1$, all the unphysical state are pushed up to the continuum

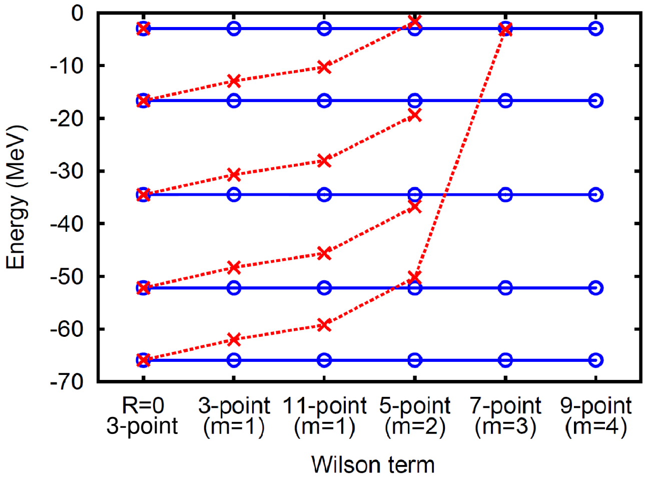

Figure 5.7: Energy spectra of the same Dirac equation with Fig. 5.4 with the Wilson term obtained by several different difference formula for the Wilson term and different values of m. The Wilson parameter is taken to be $R = 0.0005$ for all calculations with the Wilson term. The kinetic term in the Hamiltonian is approximated by the 3-point formula. The open circles and the crosses correspond to physical and spurious states, respectively.

Table 5.3: Spectra of the physical states obtained by several different versions of the Wilson term. Single-particle energies are shown in MeV. The Wilson parameter is taken to be $R = 0.0005$ for all calculations. The kinetic term is computed by 3-point formula.

$R = 0$	3-point ($m = 1$)	11-point ($m = 1$)	5-point ($m = 2$)	7-point ($m = 3$)	9-point ($m = 4$)
-65.89515	-65.89418	-65.89419	-65.89514	-65.89515	-65.89515
-52.17647	-52.17306	-52.17306	-52.17645	-52.17647	-52.17647
-34.48731	-34.48101	-34.48101	-34.48725	-34.48731	-34.48731
-16.65951	-16.65122	-16.65123	-16.65940	-16.65950	-16.65951
-2.95954	-2.95297	-2.95299	-2.95940	-2.95949	-2.95947

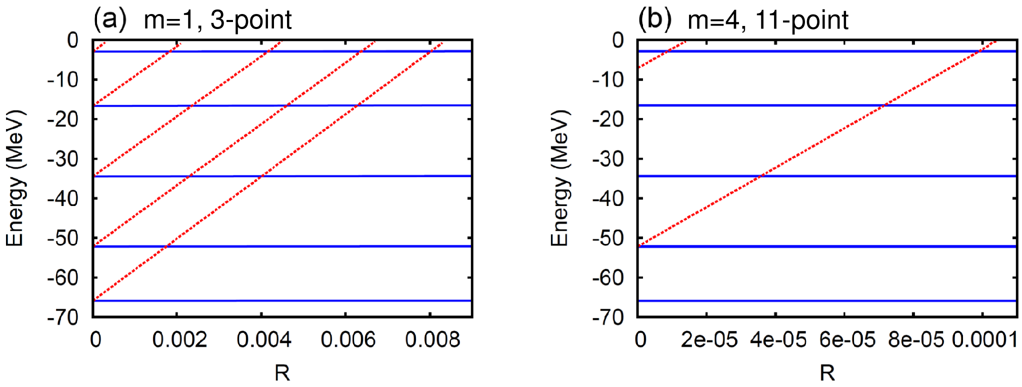

Figure 5.8: Energy spectra of the Dirac equation as functions of the Wilson parameter R. The blue solid lines and the red dashed lines correspond to physical and spurious states, respectively. The left panel (a) shows the case of a normal Wilson term ($m = 1$) with 3-point formula both for the kinetic and the Wilson terms. The right panel (b) shows the result obtained with 11-point formula for the kinetic term and an high-order Wilson term ($m = 4$) computed by 9-point formula.

region around $R = 0.008$, while they are all pushed up to continuum already around $R = 0.0001$. The high-order Wilson term is much more powerful than the normal one.

Finally, we investigate the wave functions. In Fig. 5.9 we show comparisons of the wave functions of the lowest single-particle state obtained with the Wilson term to the exact ones. The left panel (a) shows the case of a normal Wilson term ($m = 1$ and $R = 0.01$) with 3-point formula. The right panel (b) shows the result obtained with an high-order Wilson term ($m = 4$ and $R = 0.00015$) computed by 9-point formula. In both cases the kinetic term is approximated by 11-point formula. The exact wave functions are obtained by solving the equation without the Wilson term. In both cases all bound spurious states have gone away to the continuum region for the values of R taken in these calculations. The energies of the state with a Wilson term is $\epsilon = -65.8918$ MeV and $\epsilon = -65.8726$ MeV for the case (a) and (b), respectively, which are to be compared to the exact energy $\epsilon = -65.8918$ MeV (with 11-point formula for the kinetic term). Although the energies coincide between (a) and (b) within only three digits, the difference in wave

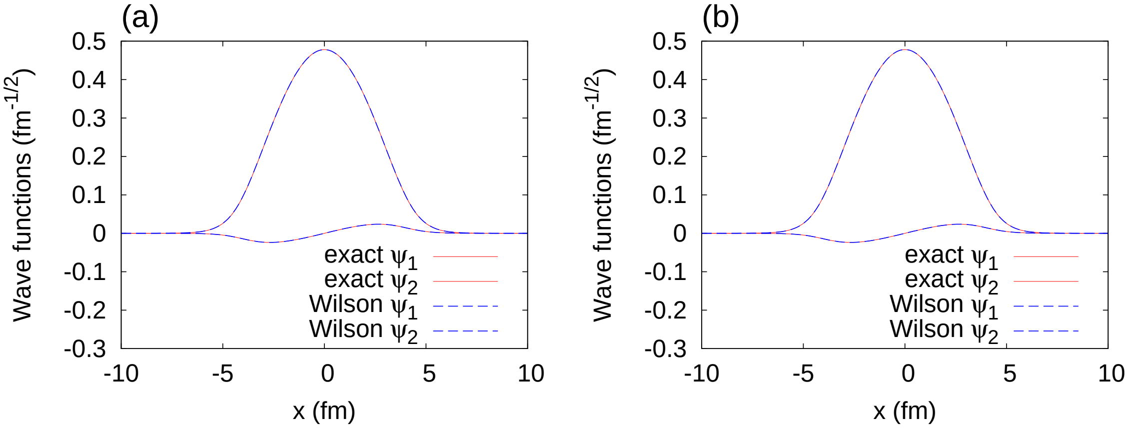

Figure 5.9: Comparisons of the wave functions obtained with the Wilson term to the exact ones. Wave functions of the lowest single-particle state are shown. The exact wave functions are shown by solid lines, whereas the ones obtained with the Wilson term are shown by dashed lines. The left panel (a) shows the case of a normal Wilson term ($m = 1$ and $R = 0.01$) computed by 3-point formula. The right panel (b) shows the result obtained with an high-order Wilson term ($m = 4$ and $R = 0.00015$) computed by 9-point formula. In both cases the kinetic term is approximated by 11-point formula. The exact wave functions are obtained by solving the equation without the Wilson term. The energies of the state with a Wilson term is $\epsilon = -65.8918$ MeV and $\epsilon = -65.8726$ MeV for the case (a) and (b), respectively, which are to be compared to the exact energy $\epsilon = -65.8918$ MeV.

functions are almost invisible in the scale shown in Figs. 5.9(a) and 5.9(b). In order to evaluate the discrepancy in wave functions, we can compute the overlap probability $|\langle\psi_{\mathrm{ex}}|\psi_{\mathrm{W}}\rangle|^2$, where ψ_{ex} is the exact wave function and ψ_{W} is the one obtained with the Wilson term. The values are almost exactly 1 to the double-precision for both cases (a) and (b).

The properties of the Wilson fermion and spectrum of the spurious states are summarized as follows.

- Without the Wilson term, there are pairs of degenerate physical and unphysical states if the first derivative in the kinetic term is approximated by 3-point formula. When more accurate difference formula is used to compute the kinetic term, the degeneracies are resolved: the spurious state are pushed upwards while the physical ones stay unchanged. However, energy shifts of the unphysical states are not enough to remove all of them up to the continuum.

- By switching the Wilson term on, the spurious states are moved upwards all by a similar amount of energy. The energy shifts are nearly proportional to the Wilson parameter R.

- An improvement on difference formula used in the Wilson term, for a given value of m (power of p^2), does not significantly make the shifts of unphysical states larger. On the other hand, an increase of m drastically makes the shifts of the spurious states larger and the shifts of the physical states smaller. Thus a Wilson term with $m \geq 2$ has more effect on the spurious states and less effect on the physical states.
- Solutions obtained with the high-order Wilson fermion are close to the exact solution to sufficient accuracy both in the energy eigenvalues and in the wave functions.

Chapter 6

Convergence Check

In this chapter, we apply our inverse Hamiltonian method and Wilson fermion to several problems, and investigate validity of our method. We will begin with Dirac equations with a given potential (Sec. 6.1). In Sec. 6.2, we perform self-consistent relativistic point-coupling model calculations for atomic nuclei. These are relativistic density functional calculations realized on 3-dimensional coordinate space for the first time.

6.1 Dirac equations with a given potential

In this section, we check the numerical performance of our method in 3-dimensional calculation and to see how accurate the solutions with the high-order Wilson fermion are. Here we solve a Dirac equation in 3-dimensional space

$$[-i\boldsymbol{\alpha}\cdot\boldsymbol{\nabla}+V(\boldsymbol{r})+\beta(m+S(\boldsymbol{r}))-m]\psi(\boldsymbol{r})=\epsilon\psi(\boldsymbol{r}), \tag{6.1.1}$$

where

$$\boldsymbol{\alpha}=\begin{pmatrix} 0 & \boldsymbol{\sigma} \\ \boldsymbol{\sigma} & 0 \end{pmatrix},\ \beta=\begin{pmatrix} I & 0 \\ 0 & -I \end{pmatrix}. \tag{6.1.2}$$

$\boldsymbol{\sigma}$ is the Pauli matrices and I is 2×2 identity matrix. The potentials $V(\boldsymbol{r})$ and $S(\boldsymbol{r})$ are taken to be spherical Woods-Saxon form,

$$\begin{aligned} V(r)+S(r)\equiv U(r)&=\frac{U_0}{1+e^{(r-R_U)/a_U}},\ \text{and} \\ V(r)-S(r)\equiv W(r)&=\frac{W_0}{1+e^{(r-R_W)/a_W}}, \end{aligned} \tag{6.1.3}$$

for which we take the same parameters as given in Table 5.1.

We solve this Dirac equation in the 3-dimensional coordinate space. We take mesh points on uniform cubic lattice. Let mesh size be a and the number of mesh points be N_x, N_y, and N_z, respectively in x, y, and z direction. The (i,j,k)-th mesh point in (x,y,z)

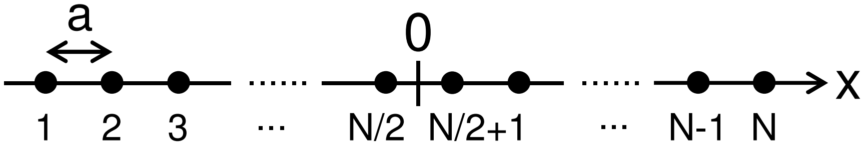

Figure 6.1: Distribution and numbering of mesh points in 3-dimensional calculations. Mesh points along y and z directions are taken in the same manner.

direction are taken at

$$
\begin{aligned}
x_i &= a\left(i - \frac{N_x - 1}{2}\right), \; i = 1,\ 2,\ \ldots, N_x && (6.1.4)\\
y_j &= a\left(j - \frac{N_y - 1}{2}\right), \; j = 1,\ 2,\ \ldots, N_y && (6.1.5)\\
z_k &= a\left(k - \frac{N_z - 1}{2}\right), \; k = 1,\ 2,\ \ldots, N_z. && (6.1.6)
\end{aligned}
$$

In Fig 6.1 we show the distribution and the numbering of mesh points in x direction. The mesh points along y and z directions are taken in the same manner. Thus we have $N_x N_y N_z$ mesh points in total. We discretize the Hamiltonian on the mesh points taken in this way and solve it with the inverse Hamiltonian method and the Wilson fermion. As in the 1-dimensional calculations we take the box boundary condition. Note that we can solve problems not only with the spherical potential but also with arbitrarily deformed potential.

On the other hand, when the potentials are spherically symmetric, the wave functions take the form [139, 140]

$$
\psi(\boldsymbol{r}) = \frac{1}{r}\begin{pmatrix} G(r)\mathscr{Y}_{\ell jm}(\theta,\phi) \\ iF(r)\mathscr{Y}_{\ell' jm}(\theta,\phi) \end{pmatrix}, \tag{6.1.7}
$$

where $\ell' = 2j - \ell$, and $\mathscr{Y}_{\ell jm} = \sum_{m'm''}\langle \ell m' \tfrac{1}{2} m'' | jm\rangle Y_{\ell m'}\chi_{m''}$ with $Y_{\ell m}$ and χ_m are the spherical harmonics and the spin wave function, respectively. The Dirac equation of Eq. (6.1.1) then reduces to the following coupled equations for radial wave functions

$$
\begin{pmatrix} U(r) & -\frac{d}{dr} + \frac{\kappa}{r} \\ \frac{d}{dr} + \frac{\kappa}{r} & W(r) - 2m \end{pmatrix}\begin{pmatrix} G(r) \\ F(r) \end{pmatrix} = \epsilon \begin{pmatrix} G(r) \\ F(r) \end{pmatrix}, \tag{6.1.8}
$$

where $\kappa = \mp(j + 1/2)$ for $j = \ell \pm 1/2$. This can be easily solved by the Runge-Kutta method. We compare our solutions on 3-dimensional mesh with the exact solutions obtained by solving Eq. (6.1.8).

As in the case of 1-dimensional case, we can get excited single-particle states by orthonormalization. Note that the Hamiltonian in Eq. (6.1.1) has time-reversal invariance since the potentials only depend on the coordinate and there is no time-odd component in the Hamiltonian. Thus, if a state $\psi_i(\boldsymbol{r})$ is an eigenstate of the Hamiltonian, its time reversed state $\psi_{\bar{i}}(\boldsymbol{r})$ is also an eigenstate which has the same eigenvalue as $\psi_i(\boldsymbol{r})$. The time reversed wave function of a state i is given by [140]

$$\psi_{\bar{i}}(\boldsymbol{r}) = i\gamma^1\gamma^3 K\psi_i(\boldsymbol{r}), \tag{6.1.9}$$

where K is the complex conjugation. When we orhogonalize a wave function to that of a state i in the orthonormalization, we also normalize it simultaneously to state $\bar{i}$. In this way the number of states to be explicitly calculated is halved.

Now we solve Eq. (6.1.1) with our method and compare the results with the exact ones. We set $N = Z = 8$ in the Woods-Saxon potentials in Eq. (6.1.3). The parameters in the inverse Hamiltonian method are taken to be $W = U_0$ and $\Delta T = 100$ MeV. Inversion of the Hamiltonian is performed by the Conjugate Residual (CR) method (See Appendix C). 28 mesh points along each axis (28^3 mesh points in total) are taken with a mesh size of $a = 0.6$ fm. The initial wave functions are given as the form

$$\psi^{(0)}(\boldsymbol{r}) = r^\ell e^{-r^2/b^2} \begin{pmatrix} \mathscr{Y}_{\ell jm}(\theta,\phi) \\ \begin{pmatrix} 0 \\ 0 \end{pmatrix} \end{pmatrix}, \tag{6.1.10}$$

where $b = 2.5$ fm and $0 < m \leq j$.

Results with the normal Wilson fermion

First we show the results obtained with a normal Wilson term, i.e., $m = 1$, $R = 0.01$. In Fig. 6.2 we show the convergence of mean squared deviations of energy a as functions of the number of iterations. In this calculation, 10 states are simultaneously evolved, and each state corresponds to each line in Fig. 6.2. The speed of convergence depends on the single-particle energy because of the factor $1 + \Delta T/(\epsilon - W)$. The one which converges most quickly is the lowest $1s_{1/2}$ state while the slowest ones are $1d_{3/2}$ states, which have the highest energy. The mean squared deviations of energy all converge to small values, which indicates that the iterative solutions converge to the eigenstates of the Hamiltonian. In Table 6.1 the energy eigenvalues and $\langle p^2\rangle/2m$ obtained by our method in comparison to the exact values, are summarized in the third and the fourth columns. The energies obtained are well close to the exact ones. Their differences are ~ 0.1 MeV. The expectation values of p^2 are also similar, which indicates that the fermion doubling is suppressed almost perfectly. Small splittings of the three states whose energies are nearly equal to $\epsilon_{d_{5/2}}$ are due to violation of rotational symmetry by lattice discretization [1]. If we take finer mesh, the splittings become smaller. The splitting is so small for the mesh size taken in this calculation that it is not a problem and we can identify the states as the $j = 5/2$ multiplet in the continuum limit. However, the overall discrepancies of 0.1

---

[1] By discretizing the space by cubic mesh, the rotational symmetry, $SO(3)$, of the Hamiltonian given in Eq. (6.1.1) is broken down to a discrete symmetry, O_h, of a cube (octahedron). Thus degenerate eigenstates of the discretized Hamiltonian belongs to an irreducible representation of the group O_h. It can be shown that $O(3)$ half-integer spin multiplets with $j \geq 5/2$ are reducible with respect to O_h and those with $j \leq 3/2$ are already irreducible. See Appendix E for detail.

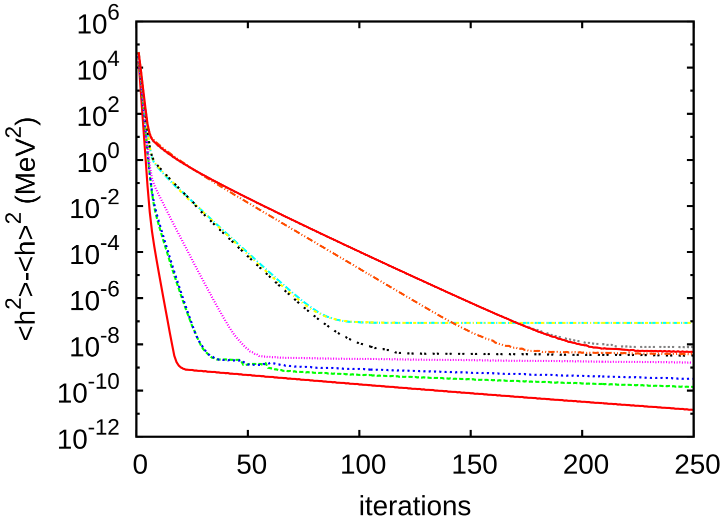

Figure 6.2: Convergences of the mean-squared deviations of energy in 3-dimensional calculations. Parameters in the inverse Hamiltonian method are taken as $\Delta T = 100$ MeV and $W = U_0$.

MeV in single-particle energies may not be acceptable in practical calculations for atomic nuclei. Thus we need a way to correct them. As we experienced in 1-dimensional case in the previous section, energies may be corrected just by subtracting the expectation value of the Wilson term from the energy eigenvalues of the Hamiltonian with the Wilson term, i. e., we treat the Wilson term as the first order perturbation:

$$\epsilon' = \epsilon - \epsilon_W = \epsilon - R \left\langle \beta(-)^m a^{2m-1} \sum_{i=1}^{3} \partial_i^{2m} \right\rangle \tag{6.1.11}$$

On wave functions, we do not make a correction. In the fifth and the sixth columns in Table 6.1 are shown the energies so corrected. The agreement with the energies is drastically improved with the correction, although they still have error of ~ 0.01 MeV. Notice that $\langle p^2 \rangle$ is unchanged by the correction since the wave function is unchanged. Therefore we do not list it in Tables 6.1 (and 6.2).

Results with high-order Wilson fermion

Next we employ the high-order Wilson term. The energy eigenvalues obtained with the high-order Wilson term, $m = 4$ and $R = 0.0006$, are shown in Table 6.2. In this case the energy eigenvalues of the Hamiltonian with the Wilson term is much closer than in the previous case with $m = 1$ to the exact energy eigenvalues due to the improvement on the Wilson term. The agreement of $\langle p^2 \rangle / 2m$ is also fairly well, which indicates that the wave functions are also more accurate than the solutions with the normal Wilson term. After the correction on the single-particle energy, their error is ~ 0.0001 MeV, which may be small enough for practical calculations.

Table 6.1: Comparison of energy eigenvalues obtained by our 3-dimensional calculation to the exact energies obtained by Runge-Kutta method. Expectation values of $p^2/2m$ are also shown. In 3-dimensional calculation, parameters of the Wilson term are $m = 1$ and $R = 0.01$. In the fifth and sixth columns, energies corrected by the first order perturbation and mean-squared deviations of the original Hamiltonian without the Wilson term are shown, respectively. All energies are given in unit of MeV, whereas values in the last columns given in MeV^2.

	Exact		inv. H with Wilson			
			without correction		with correction	
	ϵ	$p^2/2m$	ϵ	$p^2/2m$	ϵ'	$\langle h^2 \rangle - \langle h \rangle^2$
$1s_{1/2}$:	$-$ 43.18927	10.40	-42.62272	10.23	-43.18483	2.5×10^{-1}
$1p_{3/2}$:	$-$ 24.66482	17.63	-23.71563	17.25	-24.65562	4.9×10^{-1}
			-23.71563	17.25	-24.65562	4.9×10^{-1}
$1p_{1/2}$:	$-$ 19.01942	16.39	-18.15340	16.00	-19.01033	4.6×10^{-1}
$1d_{5/2}$:	$-$ 7.52898	22.74	-6.31674	22.92	-7.50793	7.5×10^{-1}
			-6.31674	22.94	-7.50857	7.5×10^{-1}
			-6.31673	22.94	-7.50874	7.5×10^{-1}
$2s_{1/2}$:	$-$ 3.65962	13.97	-2.90315	13.61	-3.62394	1.0×10^{0}
$1d_{3/2}$:	$-$ 1.27841	17.16	-0.34638	16.85	-1.24835	7.5×10^{-1}
			-0.34638	16.85	-1.24835	7.5×10^{-1}

A pattern of degeneracies is the same as the one obtained with the normal Wilson term: the states with $j \leq 3/2$ are degenerate but the state with $j = 5/2$ split. Here let us mention the relation between the symmetry of the high-order Wilson term and this pattern of the spectrum. A high-order Wilson term,

$$(-)^m a^{2m-1} R\beta \sum_{i=1}^{3} \partial_i^{2m} \tag{6.1.12}$$

with $m \geq 2$ explicitly violates the rotational symmetry. It leads to violation of the degeneracies due to the $SO(3)$ symmetry, which is possessed by the Hamiltonian in the continuum limit. (Of course the Wilson term vanishes in the continuum limit and so it is only defined for finite mesh size a.) However, on lattice, the kinetic term and the potential term as well as the Wilson term are discretized. Then the Wilson term violates the rotational symmetry in the same way as the kinetic term for finite a, irrespective of the value of m. Therefore, a discretized Hamiltonian still has O_h symmetry even with a Wilson term with $m \geq 2$. From this fact we can conclude that no further splitting is induced by a Wilson term and the pattern of level splitting is the same for all values of m. Of course the size of splitting and level ordering may be changed. Even if potentials are deformed, this conclusion holds since in this case the potential term do not have higher symmetry than O_h. In any case the splitting is completely an artifact of discretization of space and introduction of the high-order Wilson term. Thus one should take sufficiently small a and R such that the effect is negligible. The results shown in this section demonstrate that we can do it indeed. We will also discuss in Sec. 6.2 how much the hexadecapole deformation of nucleus is affected by the symmetry breaking of discretization and the high-order Wilson term.

To summarize this section, we have confirmed that our method can achieve a sufficient accuracy for calculations for atomic nuclei not only in 1-dimensional but also in 3-dimensional calculations.

6.2 Self-consistent calculations

In this section we apply our methods to self-consistent mean-field calculations with a relativistic point coupling model on 3D lattice. We employ the relativistic point-coupling model which has already been introduced in Ch. 3.

6.2.1 Initial set of wave functions

In the calculations performed in this thesis, the initial set of single-particle wave functions are given by bound state solutions of a deformed Woods-Saxon potential,

$$\begin{aligned} V(\boldsymbol{r}) + S(\boldsymbol{r}) \equiv U(\boldsymbol{r}) &= \frac{U_0}{1 + e^{(r - R_U(\theta,\phi))/a_U}}, \\ V(\boldsymbol{r}) - S(\boldsymbol{r}) \equiv W(\boldsymbol{r}) &= \frac{W_0}{1 + e^{(r - R_W(\theta,\phi))/a_W}}, \end{aligned} \tag{6.2.1}$$

Table 6.2: The same as Table. 6.1 but obtained with an inproved Wilson term. Parameters of the Wilson term are $m = 4$ and $R = 0.0006$. All energies are given in unit of MeV, whereas values in the last columns are MeV^2.

	Exact		inv. H with Wilson			
			without correction		with correction	
	ϵ	$p^2/2m$	ϵ	$p^2/2m$	ϵ	$\langle h^2\rangle - \langle h\rangle^2$
$1s_{1/2}$:	$-$ 43.18927	10.40	-43.18860	10.40	-43.18925	3.4×10^{-4}
$1p_{3/2}$:	$-$ 24.66482	17.63	-24.66282	17.63	-24.66533	1.1×10^{-3}
			-24.66282	17.63	-24.66533	1.1×10^{-3}
$1p_{1/2}$:	$-$ 19.01942	16.39	-19.01820	16.39	-19.02008	6.2×10^{-4}
$1d_{5/2}$:	$-$ 7.52898	22.74	-7.52558	22.74	-7.52982	1.2×10^{-3}
			-7.52438	22.73	-7.53039	2.2×10^{-3}
			-7.52409	22.73	-7.53053	2.4×10^{-3}
$2s_{1/2}$:	$-$ 3.65962	13.97	-3.65789	13.97	-3.66105	3.2×10^{-3}
$1d_{3/2}$:	$-$ 1.27841	17.16	-1.27784	17.16	-1.28034	4.6×10^{-3}
			-1.27784	17.16	-1.28034	4.6×10^{-3}

with

$$R_U(\theta,\phi) = R_U\left\{1 + \beta_0(\cos\gamma_0 Y_{20}(\theta) + \frac{1}{\sqrt{2}}\sin\gamma_0[Y_{22}(\theta,\phi) + Y_{2,-2}(\theta,\phi))]\right\}, \tag{6.2.2}$$

and

$$R_W(\theta,\phi) = R_W\left\{1 + \beta_0(\cos\gamma_0 Y_{20}(\theta) + \frac{1}{\sqrt{2}}\sin\gamma_0[Y_{22}(\theta,\phi) + Y_{2,-2}(\theta,\phi))]\right\} \tag{6.2.3}$$

The parameters other than β_0 and γ_0 are again taken from Ref. [132]. They are different between proton and neutron. In Table 6.3 we summarize the parameters for proton as well as the ones for neutron. β_0 and γ_0 are the deformation parameters. $\beta_0 = 0$ corresponds to a spherical Woods-Saxon potential given in Eq. (6.1.3). When $\beta_0 \neq 0$ and γ_0 is a multiple of 60°, the potential is axially deformed. If $\beta_0 \neq 0$ and γ_0 is not a multiple of 60°, the potential shape is triaxially deformed. In order to prepare the initial wave functions, the Dirac equation with the above deformed potential is solved on 3-dimensional mesh by our numerical code used in the previous section.

In principle the initial potential can be anything, but it is better to have an initial configuration which is likely to be the desired solution in order that the iterative solution quickly converge to a self-consistent solution. For instance, if one wants a solution which has some desired deformation, one may start with a potential (or density) which has a similar deformation as the desired one.

If the initial configuration has certain symmetry, it is preserved during the self-consistent iterations. Thus one has to be careful especially in 3D calculations like ours

Table 6.3: Parameters in the Woods-Saxon potentials in Eq. (6.2.1) [132]. The values for neutron have already been given in Table 5.1

	U_0 (MeV)	W_0 (MeV)	R_U (fm)	R_W (fm)	a_U (fm)	a_W (fm)
neutron	$-71.28(1-0.462\frac{N-Z}{A})$	$-11.12U_0$	$1.233A^{1/3}$	$1.144A^{1/3}$	0.614	0.648
proton	$-71.28(1+0.462\frac{N-Z}{A})$	$-11.12U_0$	$1.250A^{1/3}$	$1.144A^{1/3}$	0.612	0.647

whether there is any further symmetry breaking which leads to lower energy, or whether a converged solution really corresponds to the ground state. It is also the case in investigation of fission properties, in which various deformation degrees of freedom have impacts on heights of fission barriers and fission paths. In order not to miss solutions with broken symmetry, one may introduce some random fluctuation in initial potential or density as is done in [141]. Another possible way is to prepare Gaussian wave packets for each single-particle wave function whose center is distributed randomly in space.

6.2.2 Convergence of result

In this section we examine the convergence of the result with respect to the box size L and mesh size a, and check the validity of our strategy for self-consistent calculations. To this end we consider, for a while, ^{16}O nucleus without the Coulomb interaction. Later on we switch on the Coulomb interaction and also examine ^{40}Ca nucleus. We perform calculations in a cubic box whose dimension is $L = a(N-1)$ fm long, where N is the number of mesh points taken along each direction. The kinetic term is at first approximated by 11-point formula. The Wilson parameter is fixed as $(m, R) = (5, 0.00015)$ for all calculations shown in this section. We examine two different boundary conditions, i.e., the box boundary condition (BBC) and the periodic boundary condition (PBC). We employ PC-F1 functional given in Ref. [84]. In order to ensure that the iterative solution convergences to the self consistent one, we impose a severe condition, that is, we stop the iteration when the dispersions of energy of all the occupied single-particle states becomes less than 10^{-8} (MeV^2).

Box size

First let us see the result as a function of the box size L. Fig. 6.3 shows convergence of the total energy with respect to L. The open squares and crosses are results of BBC and PBC, respectively. The red dashed lines connect energies, E, before correction for the Wilson term, while the blue solid ones connect results after the correction, $E - E_W$, where E_W is the total expectation value of the Wilson term. Thus difference between lines of the two types means the total expectation value of the Wilson term. One sees that with the both boundary conditions the result converges to a certain value as L increases.

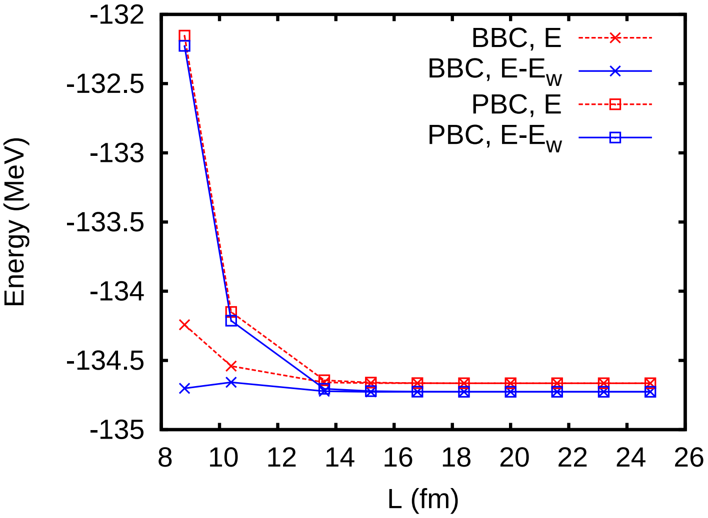

Figure 6.3: Convergence of the total binding energy of ^{16}O nucleus with respect to the box size L. The mesh size is fixed as $a = 0.8$ fm. Coulomb interaction and center-of-mass correction is not included. Open squares and crosses indicate results obtained with periodic and box boundary conditions, respectively. Red dashed lines connect energies, E, before correction for the Wilson term, while blue solid lines connect results after the correction, $E - E_W$, where E_W is the total expectation value of the Wilson term.

Moreover, the two boundary conditions gives the same result for large L, as is expected. From Fig. 6.3 $L \simeq 15$ fm provides a well converged results for ^{16}O nucleus. However, the two boundary conditions show quite different behavior at small L; a change of the result wit respect to L obtained with PBC is much larger than that with BBC. This can be understood as follows. With a small box size, there can be a spurious contribution in the kinetic energy from the neighboring box, where an identical nucleus is considered to exist, since the difference formula for the kinetic energy makes reference to the region outside the box around the boundary.

Fig. 6.4 shows the single-particle energies as functions of L. The symbols and line types have the same meaning as in Fig. 6.3. We see that $L \simeq 15$ fm is sufficiently large for the occupied states ($1s_{1/2}$, $1p_{3/2}$, and $1p_{1/2}$) to well converge, while a larger box size is required for convergence of the less bound single-particle states ($1d_{5/2}$ and $2s_{1/2}$) whose wave functions have a long tail.

Mesh size

Next we see the convergence with respect to the mesh size a. Here we fix the box size at $L = (N - 1) \times a \simeq 25$ fm, which turned out to be large enough so that all the bound single-particle energies seem to well converge. (N is the number of mesh points along each direction. See Eq. 6.1.6.) We keep L as constant as possible by tuning the value

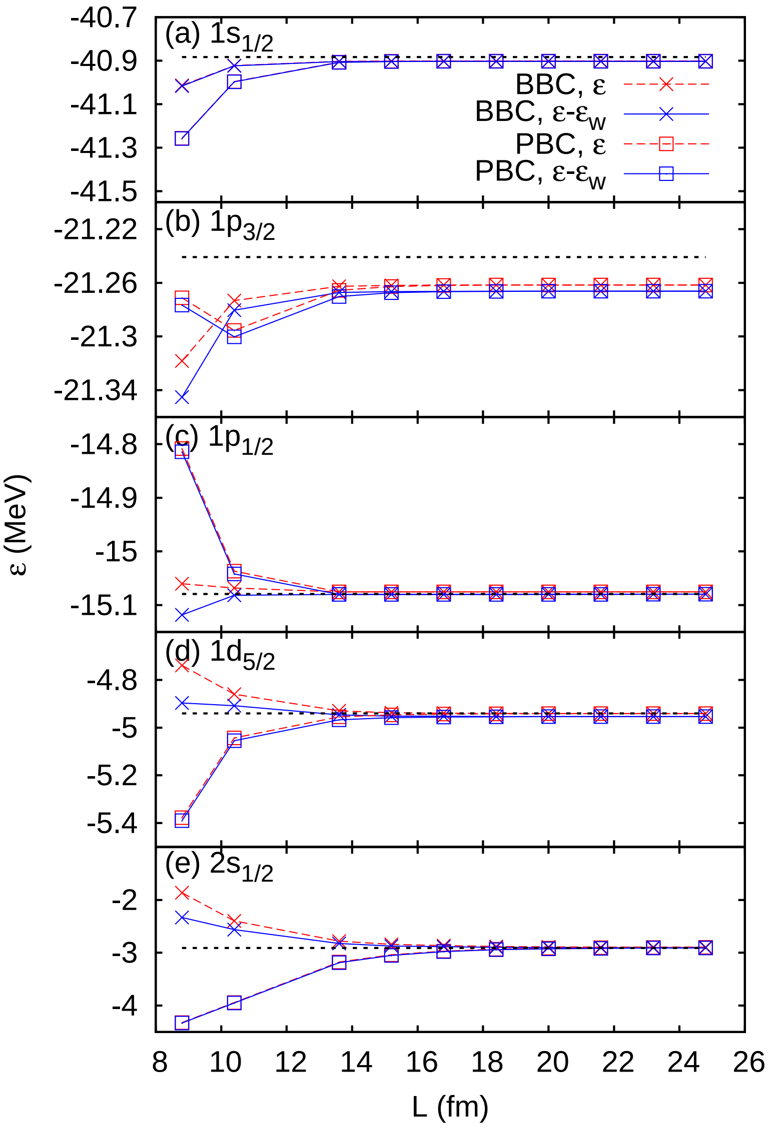

Figure 6.4: Convergence of the single-particle energies in ^{16}O nucleus with respect to the box size L. The mesh size is fixed as $a = 0.8$ fm. Coulomb interaction is not included. The symbol and line types has the same meaning as Fig. 6.3. In each panel, the exact single-particle energy obtained with the spherical code is represented by a black dotted line.

of N. Note that $L \simeq 15$ fm is sufficient for a mean-field calculation for ^{16}O in which the states up to $1p_{1/2}$ are occupied and the all above are completely empty. In Fig. 6.5, we show the total binding energy of ^{16}O obtained as a function of a. Again the symbols and the line types indicate the same as in Figs. 6.3 and 6.4. In addition, the black dotted line represents the exact value obtained with the spherical code, in which the Dirac equation is solved by the Runge-Kutta method with the radial box of 20 fm radius. The total energy converges to the exact value to quite a high accuracy as the mesh becomes finer. Furthermore, the correction energy for the Wilson term becomes practically negligible for $a = 0.6$ fm or less. This is because the Wilson term is proportional to a^{10} in this case and vanishes in the continuum limit. Since the box size is large in this case there is nearly no difference between the two boundary conditions.

It is found that the total energy increases as a becomes smaller, which is opposite to what one would expect from the variational principle in non-relativistic calculations. This is not surprising nor mysterious since there is no variational principle for energy in the relativistic calculations. A similar phenomenon has been observed in a relativistic calculation with basis expansion [28]. In Ref. [28] it was found that the total binding energy of a nucleus increases as the number of basis for the upper component of the Dirac spinor is increased. This is due to a variational collapse discussed in Ref. [123]. If basis for the lower component is increased by one, one state will be added to the negative energy single-particle spectrum and it will "push upwards" all the states in the fermi sea. On the other hand, if a basis for the upper component is added, a new state appears on the top of the positive energy spectrum and it "push downwards" all the rest.

Fig. 6.6 shows the single-particle energies as functions of a. We observe that not only the total energy but also single-particle energies also agree well with the exact results as a decreases. For $L \simeq 25$ fm, the two boundary conditions gives almost identical results except for the least bound $2s_{1/2}$ state. For this weakly bound state there is still a finite volume effect which leads to a difference between the two boundary conditions.

Finite difference formula for the kinetic term

Here we see the convergence and accuracy of the 3D code with several different difference formulas for the kinetic term. We take ^{40}Ca as well as ^{16}O as examples. The box size and the mesh size for ^{16}O is taken to be $L = 15$ fm, and $a = 0.6$ fm, respectively. For ^{40}Ca, $a = 0.6$ fm and $L = 18.6$ fm. The Coulomb interaction is now switched on. The Poisson equation for the discretized Coulomb potential is solved within a larger numerical box. The Poisson equation with 3-point difference is detailed in Appendix F.2

In Table. 6.4 we show the results for ^{16}O and ^{40}Ca obtained with 7-, 9-, ..., 15-point formulas for the kinetic term. The kinetic energy K, the nuclear part of potential energy V_{N}, the Coulomb energy V_{C}, the center of mass energy E_{CM}, and the root-mean-squared radius r_{rms} are compared to the exact values obtained with the spherical code. The total binding energy is given by $E_{\mathrm{tot}} = K + V_{\mathrm{N}} + V_{\mathrm{C}} - E_{\mathrm{CM}}$. We see that, for the both nuclei, each component of energy and the radius obtained with our 3D results converge to the exact values with a few keV errors except for the Coulomb energy, V_{C}. The Coulomb

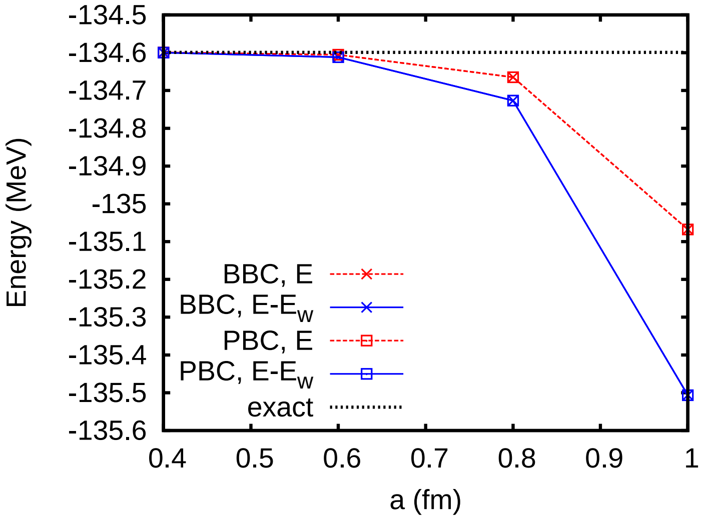

Figure 6.5: Convergence of the total binding energy of ^{16}O nucleus with respect to the mesh size a. The box size is kept $L \simeq 25$ fm for all mesh sizes. Coulomb interaction and center-of-mass correction is not included. The symbol and line types has the same meaning as Fig. 6.3. The black dotted line indicates the exact energy obtained with a spherical code.

energy differs from the exact values by ~ 100 keV. It can be seen from Table 6.4 that the errors in the total binding energy predominantly come from the errors in V_{C}. This error is due to the poor approximation of the 3-point formula for the Laplacian in the Poisson equation. The relatively large discrepancy in the Coulomb energy may be cured by taking more accurate formula for approximating the Laplacian in the Poisson equation.

Accuracy of wave function

Finally we confirm that the wave functions calculated with the 3D code is as accurate as the total and the single-particle energies. To this end we compare the total density of ^{16}O nucleus obtained with the 3D code to that with the spherical code. The 3D result is given with the box size of $L = 25$ fm, the mesh size $a = 0.6$ fm, and the 11-point formula for the kinetic term, without the Coulomb interaction. This set up is the same as for the results shown in Figs. 6.5 and 6.6.

We show in Fig. 6.7 a comparison of the density of ^{16}O obtained with the two numerical codes. The 3D code gives almost identical result to the spherical code. The data points of 3D result is denser at larger r because there are many mesh points with similar distance from the origin for a large r. In Fig. 6.8 we make a similar comparison but the density is shown in logarithmic scale. Notice also that the range of r is wider than in Fig. 6.7. We can see that the 3D code yields quite an accurate result up to large r. This indicates the advantage of real-space representation over HO basis representation in description of the

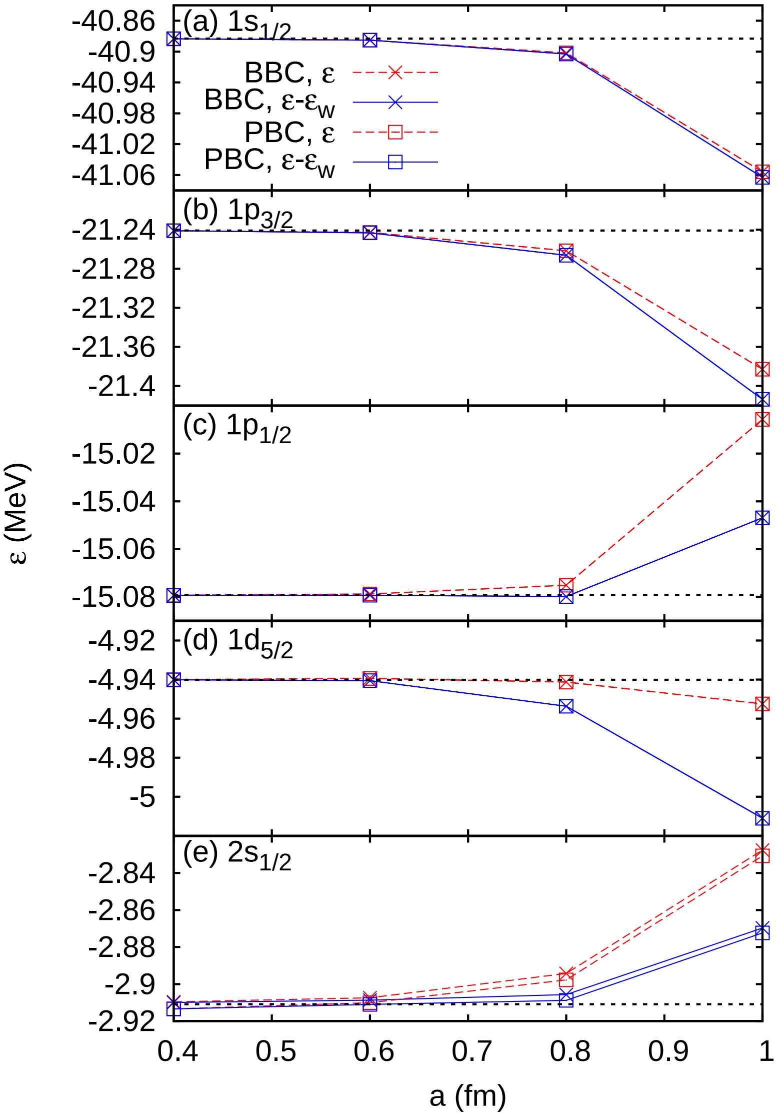

Figure 6.6: Convergence of the single-particle energies in ^{16}O nucleus with respect to the mesh size a. Coulomb interaction is not included. The symbol and line types has the same meaning as Fig. 6.3. In each panel, the exact single-particle energy obtained with the spherical code is represented by a black dotted line.

Table 6.4: Results for ^{16}O and ^{40}Ca with several difference formulas for the kinetic term. The kinetic energy K, nuclear part of the potential energy V_{N}, Coulomb energy V_{C}, center of mass energy E_{CM}, and root-mean-squared radius r_{rms} are compared to their exact values obtained by a spherical code. All energies are given in units of MeV, and the radius in fm. For both nuclei the mesh size was taken to be $a = 0.6$ fm. The box size was set to be $L = 15$ fm for ^{16}O and $L = 18.6$ fm for ^{40}Ca.

			^{16}O			
	K	V_{N}	V_{C}	E_{CM}	E_{tot}	r_{rms}
7-point	209.122	−343.832	16.753	9.912	−127.873	2.630
9-point	209.148	−343.670	16.740	9.897	−127.678	2.631
11-point	209.151	−343.645	16.738	9.893	−127.649	2.632
13-point	209.150	−343.639	16.738	9.892	−127.642	2.632
15-point	209.149	−343.636	16.738	9.892	−127.641	2.632
Exact	**209.148**	**−343.633**	**16.680**	**9.891**	**−127.696**	**2.632**

			^{40}Ca			
	K	V_{N}	V_{C}	E_{CM}	E_{tot}	r_{rms}
7-point	524.225	−942.074	80.679	8.267	−345.438	3.359
9-point	524.532	−941.877	80.628	8.251	−344.969	3.361
11-point	524.568	−941.851	80.620	8.248	−344.910	3.362
13-point	524.572	−941.843	80.619	8.247	−344.900	3.362
15-point	524.572	−941.840	80.618	8.247	−344.897	3.362
Exact	**524.567**	**−941.839**	**80.460**	**8.248**	**−345.060**	**3.361**

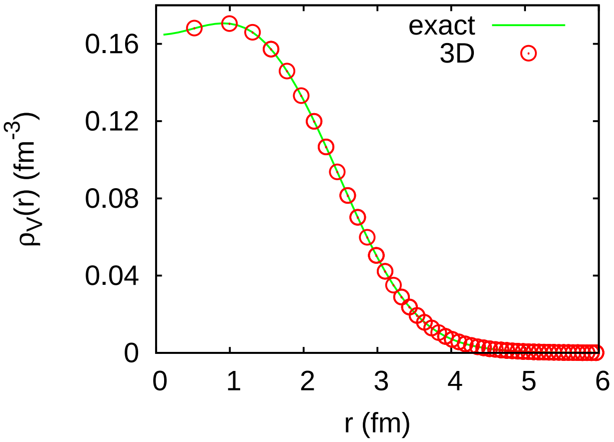

Figure 6.7: Comparison between the results obtained with the 3D code and the spherical code for the total density of ^{16}O nucleus. The 3D result is obtained with the box size of $L = 25$ fm, the mesh size $a = 0.6$ fm, and the 11-point formula for the kinetic term. The Coulomb interaction is switched off. The solid line and the open circles show the densities obtained with the spherical and the 3D codes, respectively.

asymptotic tail of a wave function.

6.2.3 Artificial violation of the rotational symmetry

We also check the violation of spherical symmetry which may be caused by the lattice discretization, the finite volume effect, or the explicit violation of rotational symmetry of the k^{2m} term with $m \geq 2$. We take ^{16}O nucleus in a cubic box again as an example. The Coulomb interaction is switched off.

Since the ground state of the doubly closed ^{16}O nucleus is spherical, all the deformation parameters are expected to vanish. However, in our 3D calculations, there are several artificial defects which may distort the spherical shape. The lattice discretization and finite difference approximation for the derivatives violate the rotational symmetry as discussed in Sec. 6.1. The anisotropic boundary of a cubic box may also affect the nuclear shape if the box size is not large enough. Furthermore, the k^{2m} term with $m \geq 2$ explicitly violates the rotational symmetry. All of them violate the rotational symmetry $SO(3)$ down to O_h (for a cubic box), and it is expected that they induce spurious hexadecapole deformation. Therefore, we investigate in particular the hexadecapole deformations.

Indeed, we have found that α_{40} and α_{44} in Eq. (2.4.22) have small but finite values whereas all the others are almost zero (less than 5×10^{-5}, more precisely) in the self-consistent solutions. In Table 6.5 is shown the hexadecapole deformation parameters α_{40} and α_{44} for ^{16}O nucleus obtained with several different box sizes. The mesh size is kept to be $a = 0.8$ fm. The deformations decrease as L increases and converges to a small value which is practically negligible. The decrease is due to a reduction of the finite volume

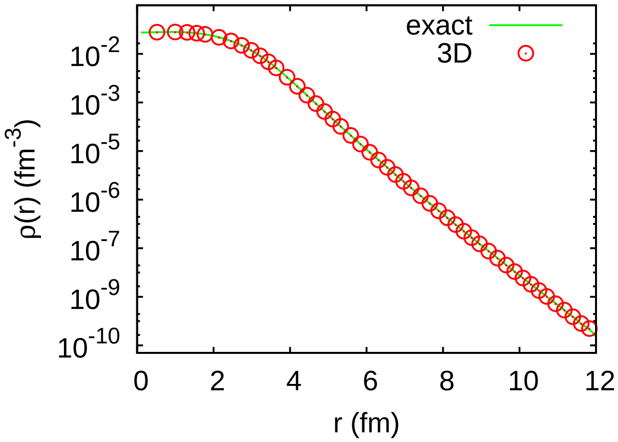

Figure 6.8: A similar comparison as Fig. 6.7, but shown with the logarithmic scale for the density. Data for the 3D result have been thinned out.

effect which distorts the nucleus by the anisotropic boundary condition. The finite values which still remain at large L are attributed to the discretization error and the effect of the k^{2m} term.

In Table 6.6, we show the hexadecapole deformation parameters as a function of the mesh size a. The box size is kept to be a large value $L \simeq 25$ fm. We see that the deformation becomes smaller as a decreases, i.e., as it approaches the continuum limit where the discretization error and the effect of the k^{2m} term vanish.

Table 6.5: Hexadecapole deformation parameters α_{40} and α_{44} for ^{16}O nucleus obtained with several different box sizes. The mesh size is kept at $a = 0.8$ fm. For all calculations quadrupole, octupole, and the other components of hexadecapole deformations (α_{4m} with $m = \pm 1,\ \pm 2,\ \pm 3, -4$) are zero.

L (fm)	α_{40}	α_{44}
8.8	-0.0226	-0.0191
10.4	-0.0098	-0.0083
13.6	-0.0018	-0.0015
15.2	-0.0007	-0.0006
16.8	-0.0005	-0.0004
18.4	-0.0004	-0.0003
20.0	-0.0003	-0.0003
21.6	-0.0003	-0.0003
23.2	-0.0003	-0.0003
24.8	-0.0003	-0.0003

Table 6.6: Hexadecapole deformation parameters α_{40} and α_{44} for ^{16}O nucleus obtained with several different mesh sizes. The box size is kept at $L \simeq 25$ fm.

a (fm)	α_{40}	α_{44}
1.0	-0.0025	-0.0021
0.8	-0.0003	-0.0003
0.6	-0.0001	-0.0001
0.4	0.0000	0.0000

Chapter 7

Applications to Deformed Nuclei

In this chapter we apply our method to deformed nuclei. First, in Sec. 7.1, we show that our method indeed works for deformed nuclei and deformation constrained calculations. Next we present in Sec. 7.2 the results of an application of our 3D code to the discussion of a possibility of octupole deformations in $N = Z \simeq 40$ nuclei, for which static octupole deformation was predicted in the previous calculations based on Skyrme Hartree-Fock.

7.1 Deformation constrained calculations

In the previous chapter we have seen that our method are able to give accurate solutions for relativistic self-consistent calculations in the 3D coordinate space representation without the problems of variational collapse and fermion doubling. Now we apply the method to deformation constrained calculations. Such calculations are important for discussions of deformation properties and fission properties of nuclei. They will also be used as inputs for investigation of spectroscopic properties of nuclei with the quantum number projections and the generator coordinate method (GCM) or Bohr's five-dimensional collective Hamiltonian (5DCH) taking into account the quantum fluctuation of shape degrees of freedom [66, 80].

We first calculate the potential energy surfaces (PES) of ^{24}Mg and ^{28}Si on the (β, γ) deformation plane and the potential energy curve (PEC) of ^{8}Be as a function of β. ^{24}Mg and ^{28}Si have prolate and oblate shapes, respectively in their ground state. In particular, ^{28}Si is a typical oblate nucleus which has the oblate magic number $N = Z = 14$ appearing in the Nilsson diagram [66]. ^{8}Be is considered to have a well pronounced two α cluster structure. We expect that the cluster structure will more and more developed as the deformation of ^{8}Be is constrained at larger value. Thus ^{8}Be is the lightest nucleus which is expect to fission into two fragments and to show a cluster structure.

7.1.1 Potential energy surfaces on (β, γ) plane in ^{24}Mg and ^{28}Si

First we calculate the ground state of ^{24}Mg and ^{28}Si nuclei. The calculations with the 3D code indicate that they are axially deformed in their ground state. In Tables 7.1 and 7.2

we summarize the bulk properties and the neutron single-particle energies, respectively, in the ground states of the two nuclei in comparison to the results obtained by basis expansion method. In these calculations we set the mesh size as $a = 0.8$ fm and the number of mesh points as $N_x = N_y = N_z = 20$. The results obtained with the mesh size $a = 0.6$ fm and the number of mesh points $N_x = N_y = N_z = 26$ are also shown. The results of HO basis are calculated by expanding the single-particle wave functions with the eigenstates of a spherical harmonic oscillator up to 14 major shells. We see that the 3D results agree reasonably well with the HO results within a error of ~ 0.1 MeV in the total energy. Both in the bulk properties and the single-particle energies, the result $a = 0.6$ fm agree better than $a = 0.8$ fm. We have also tried calculation with $a = 0.5$ fm and $N_x = N_y = N_z = 30$, but the slight changes in the total energy (~ 0.01 MeV) and the single-particle energies (~ 0.001 MeV) from those obtained with $a = 0.6$ fm do not further improve the agreement to the HO results. The small deviation from the HO results which still remains with $a = 0.6$ fm is probably due to the error in the Coulomb energy observed in the previous chapter or the truncation error in the HO basis.

The measured binding energies of ^{24}Mg and ^{28}Si are -198.26 MeV and -236.54 MeV, respectively, which are significantly underestimated by an order of MeV in the present mean-field results with the PC-F1 interaction both for 3D and HO calculations. This underestimation might be partially attributed to the dynamical correlation energy [142]. This is the beyond-mean-field effect associated with the rotational and vibrational degrees of freedom which could be taken into account with GCM and angular momentum projection (AMP). In Ref [142], it is shown with a CDFT interaction PC-PK1 [85] that the rotational correction energy associated with AMP dominates the dynamical correlation energy, and the rotational correction energy varies between 1.5 MeV and 3 MeV for well-deformed nuclei to improve the agreement between calculated and measured nuclear masses. Thus we could expect that the agreement to the experimental masses of the present calculations can also be improved by taking into account these corrections.

Next we constrain the quadrupole deformations (β, γ) and obtain the PES of the two nuclei. In the deformation constrained calculations we set the mesh size to be $a = 0.8$ fm and the number of mesh points $N_x = N_y = N_z = 20$ as in the ground state. They are shown in Fig. 7.1. We see a minimum on the axial prolate side and oblate side in the PES of ^{24}Mg and ^{28}Si, respectively, which corresponds to the ground state shown in Tables 7.1 and 7.2.

7.1.2 Large deformation and cluster structure in ^{8}Be

Next we show the results for the ^{8}Be nucleus. The nucleus in reality is not bound and is considered to be a resonance state of two α particles. However, in the mean-field calculations, the ground state of the nucleus is obtained as a bound state since the relative motion of two α particles are not explicitly considered.

Calculations with a constraint on β is performed up to a large deformation of $\beta = 5.4$, where the nucleus is well fragmented into two α clusters. The triaxiality parameter γ is kept to be 0°. For this nucleus we set $a = 0.8$ fm and take $(N_x, N_y, N_z) = (16, 16, 22)$ for

Table 7.1: Comparisons of neutron single-particle energies in the ground states of ^{24}Mg and ^{28}Si nuclei between the results obtained with our 3D code and the harmonic oscillator (HO) basis expansion. The 3D results are obtained with mesh size of $a = 0.8$ fm and 0.6 fm. The HO results are obtained with basis up to 14th HO major shells. Quantum number $|K|^\pi$ denotes the absolute value of the projection of the total angular momentum and the parity of the single-particle states. Energies are given in unit of MeV. The results with basis are provided by Prof. J. M. Yao.

	^{24}Mg			^{28}Si		
	3D		HO basis	3D		HO basis
	$a = 0.8$ fm	$a = 0.6$ fm	$N_{\mathrm{sh}} = 14$	$a = 0.8$ fm	$a = 0.6$ fm	$N_{\mathrm{sh}} = 14$
E_B (MeV)	-193.73	-193.52	-193.49	-231.78	-231.53	-231.48
(β, γ)	$(0.516, 0°)$	$(0.518, 0°)$	$(0.517, 0°)$	$(0.366, 60°)$	$(0.366, 60°)$	$(0.366, 60°)$
$\langle r^2 \rangle$ (fm)	2.975	2.978	2.979	3.058	3.061	3.062

Table 7.2: Comparisons of neutron single-particle energies in the ground states of ^{24}Mg and ^{28}Si nuclei between the results obtained with our 3D code and the harmonic oscillator (HO) basis expansion. The 3D results are obtained with mesh size of $a = 0.8$ fm and 0.6 fm. The HO results are obtained with basis up to 14th HO major shells. Quantum number $|K|^\pi$ denotes the absolute value of the projection of the total angular momentum and the parity of the single-particle states. Energies are given in unit of MeV. The results with basis are provided by Prof. J. M. Yao.

	^{24}Mg				^{28}Si		
	3D		HO basis		3D		HO basis
$\|K\|^\pi$	$a = 0.8$ fm	$a = 0.6$ fm	$N_{\mathrm{sh}} = 14$	$\|K\|^\pi$	$a = 0.8$ fm	$a = 0.6$ fm	$N_{\mathrm{sh}} = 14$
$\frac{1}{2}^+$	-48.45	-48.36	-48.35	$\frac{1}{2}^+$	-51.82	-51.73	-51.73
$\frac{1}{2}^-$	-34.68	-34.60	-34.58	$\frac{3}{2}^-$	-35.02	-34.96	-34.96
$\frac{3}{2}^-$	-26.10	-26.05	-26.04	$\frac{1}{2}^-$	-33.24	-33.19	-33.18
$\frac{1}{2}^-$	-20.62	-20.62	-20.63	$\frac{1}{2}^-$	-22.91	-22.91	-22.92
$\frac{1}{2}^+$	-18.00	-17.96	-17.93	$\frac{5}{2}^+$	-19.12	-19.08	-19.06
$\frac{3}{2}^+$	-14.05	-14.01	-14.00	$\frac{3}{2}^+$	-16.45	-16.42	-16.40
$-$	$-$	$-$	$-$	$\frac{1}{2}^+$	-16.00	-15.97	-15.93

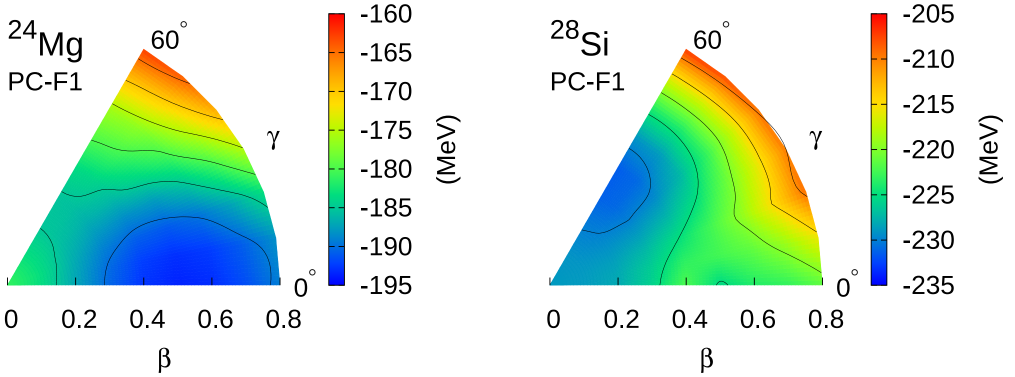

Figure 7.1: The potential energy surfaces of ^{24}Mg (left) and ^{28}Si (right) on the (β, γ) plane. An absolute minimum on the plane corresponds to the ground state of the nucleus.

$\beta \leq 1.0$, $(16, 16, 28)$ for $1.0 < \beta \leq 2.0$, and $(14, 14, 36)$ for $2.2 \leq \beta$. The number of mesh points are changed because the shape of nuclei is more and more elongated as β becomes larger, and accordingly, longer box is needed to cover the system. In Fig. 7.2 is shown the PEC of ^{8}Be as a function of β. The red open squares shows the results obtained with our 3D code. The results with HO basis with $N_{\rm sh} = 10$, 12 and 14 are also shown with the magenta, blue, and green solid squares are also shown for comparison. The sub panels shown on the top of Fig. 7.2 are the slice of the matter density distributions on the plane which includes the symmetry axis at various values of β.

The mean-field ground-state deformation, which corresponds to the minimum of the PEC, is $\beta = 1.28$. The ground-state density is drawn on the second panel from the left, which shows an obscure two α structure. As the deformation becomes larger, the two α cluster structure is more and more developed, and at $\beta = 4.2$, the nucleus is almost completely separated into two α clusters.

In Fig. 7.3, we show the difference of the total binding energy between our 3D results and the HO results, $E_{\rm HO} - E_{\rm 3D}$, as a function of $N_{\rm sh}$. The differences at $\beta = 1.2$, $\beta = 3.0$, and $\beta = 5.1$ are shown with the solid squares, the open squares, and the open circles, respectively. One can see that the HO results approach the 3D results as $N_{\rm sh}$ becomes larger at all the values of deformation shown in Fig. 7.3, but they are not completely convergent with $N_{\rm sh} = 14$ for the larger deformation.

The comparison of the results between 3D and HO basis evidently shows an advantage of the 3D calculations for deformed nuclei. At smaller deformation the 3D and HO results well agree with each other. However, the results with basis deviate from the 3D results at larger deformation. Moreover, for a fixed deformation, the results with basis shows a convergence towards our 3D results as the basis set is enlarged, as seen in Fig. 7.3. This implies that, in the present setup, the 3D code gives better solutions at large deformation, and that the truncation of the basis at $N_{\rm sh} = 10$ is not enough to get a good solution. An optimization of the basis parameter or the relaxation of the basis truncation is needed. The optimization process is much more complicated when many shape degrees of freedom are involved such as a fission process in a heavy element [27, 28]. In such a case, the accuracy of the solution depends on the several deformation parameters of the solution, as is observed in Fig. 7.2, and the optimization should be done in a multi-dimensional parameter space. On the other hand, in the 3D calculation, the optimization of the lattice parameters, the mesh size and the box size, is much simpler since there is only two free parameters and the accuracy does not depend on the deformation as long as the box size is large enough to cover the size of the system.

7.2 Applications: octupole deformations of $N = Z = 30 - 40$ nuclei

In the previous chapter and the preceding sections in this chapter, we have shown the benchmark tests of our 3D code, and we have found that our code gives an accurate solutions both for spherical and deformed nuclei. Here we show an application of our 3D code giving a new results, which are not easy to obtain with existing methods. To this end we investigate a possibility of octupole deformations in $N = Z = 30-40$ nuclei, for which octupole deformation is expected due to the octupole correlations [30, 33–35]. However, in experiments no sign of octupole deformation, i.e., the negative parity bands [30], is observed for these two nuclei [67, 68]. Thus it is important to study the possibility of octupole deformations in those nuclei with another interaction and clarify whether the conclusions in Refs. [33–35] holds independently to the nucleon-nucleon interaction. Note that with our code we are able to describe any kind of octupole deformations including the non-axial ones as well as the axial one without any additional computational cost.

Especially, the tetrahedral (Y_{32}) deformation is of particular interest since a strong shell effect is expected due to the high degeneracies in single-particle states with the tetrahedral deformation [36, 37]. With the spherical symmetry, the "magnetic" $(2j + 1)$-fold degeneracies together with the strong spin-orbit interaction produce shell gaps at the well-known magic numbers. Once a nucleus is deformed, in general, an $SO(3)$ multiplet splits into several levels whose degeneracies are determined from the symmetry of nuclear shape. In most of possible deformations including the axially symmetric ones, degeneracies surviving are only two-fold, the Kramers degeneracy [143] due to the time reversal symmetry. The size of level splittings becomes larger as the nucleus becomes deformed, that is, the shell structure becomes more and more vague. In this respect, the tetrahedral deformation is special since it yields degeneracies more than the Kramers degeneracy. A tetrahedral shape is invariant under the transformations of the point group T_d, which has two two-dimensional and one four-dimensional irreducible representations [26] (see also Appendix E). The four-dimensional representation yields four-fold degeneracies in the single-particle spectrum. This leads to bunching of single-particle states and rather large shell gaps, which result to stability of the tetrahedral deformation[1]. Figs. 7.4(a) and

---

[1] From the same group theoretical consideration, another type of exotic symmetry, octahedral deformation, is also expected to have enhanced shell effect [38]. In fact, apart from the spherical symmetry, only tetrahedral, octahedral, and icosahedral symmetries produce the single-particle degeneracies higher

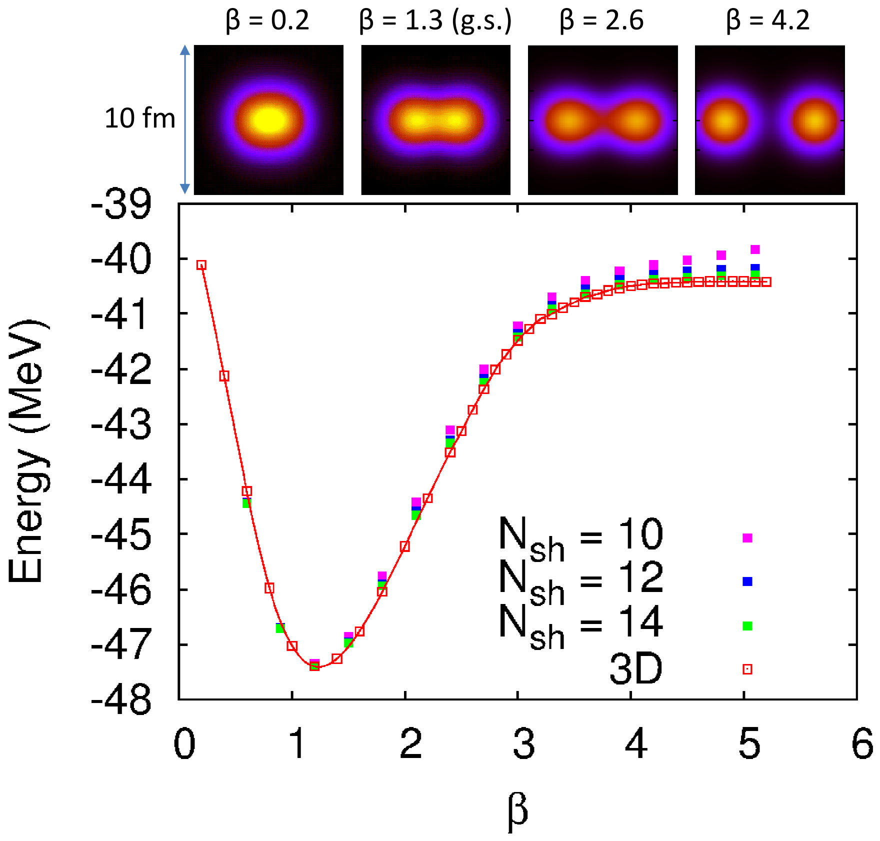

Figure 7.2: The potential energy surface of ^{8}Be as a function of the quadrupole deformation β. All the solutions are axially symmetric, that is, $\gamma = 0°$. The red open squares connected by a line show the results obtained with our 3D code. The solid squares are the results obtained with the HO basis expansion. The magenta, blue, and green correspond to the results with 10, 12, and 14 major HO shells, respectively. The four sub panels on the top are the slices of the matter density distributions on a plane including the symmetry axis at $\beta = 0.2$, 1.3 (the ground state), 2.6, and 4.2, from the left to right. Each side of the panels is 10 fm long. The results with basis are provided by Ms. H. Mei.

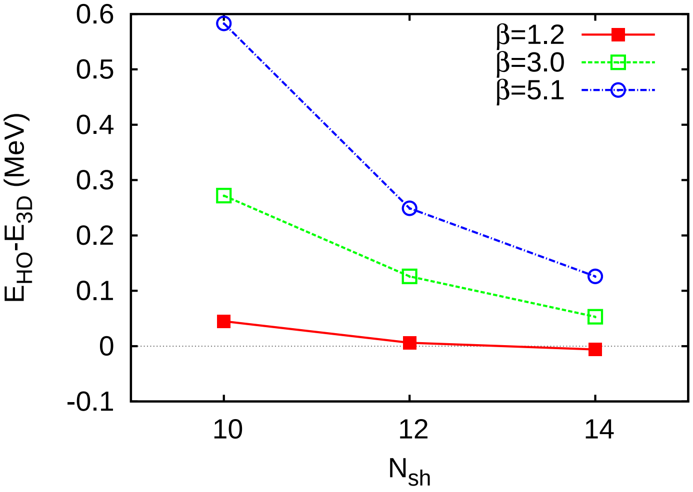

Figure 7.3: The difference $E_{\mathrm{HO}} - E_{\mathrm{3D}}$ of the total binding energy between our 3D results and the HO results as a function of N_{sh}. The differences at $\beta = 1.2$, $\beta = 3.0$, and $\beta = 5.1$ are shown with the solid squares, the open squares, and the open circles, respectively. The results with basis are provided by Ms. H. Mei.

7.4(b) show the single-particle spectra of deformed Woods-Saxon potentials as functions of Y_{32} (tetrahedral) and Y_{31} deformations, respectively. $\alpha_{32} = 0$ ($\alpha_{31} = 0$) corresponds to the spherical shape. One can see the well pronounced shell gaps with the tetrahedral deformation. On the other hand, no such large gap is developed with the Y_{31} deformation. Note that the symmetry of Y_{31} deformation, C_{2v}, has only one two-dimensional irreducible representation [26], which implies that all the single-particle levels are two-fold degenerate and repel one another due to the no-crossing rule. This explains why the levels tend toward equidistant distribution as α_{31} increases in Fig. 7.4(b). Among “tetrahedral magic” numbers the predicted in Ref. [37] are $Z = 40$ and $N = 40$. The ^{80}Zr nucleus is thus predicted to be doubly magic with respected to the tetrahedral deformation.

Here we briefly mention to experimental observation to detect tetrahedral symmetries. With a group theoretical consideration (See Refs. [145,146] and Appendix E), a rotational band built on such doubly-closed-shell configuration of the tetrahedral symmetry is expected to have a sequence of spin-parity as

$$0^{\pm}, 3^{-}, 4^{+}, 6^{\pm}, 7^{-}, 8^{+}, 9^{\pm}, 10^{\pm}, \ldots \tag{7.2.1}$$

The characteristic feature of the spectrum is that states of spin $I = 1, 2,$ and 5 are missing in the doubly magic tetrahedral band [146]. Possible spin-parities and electric transitions of general tetrahedral rotor is discussed in Ref. [145]. Although experimental data for

---

than two [26, 144]. These high degeneracies reflect rather high symmetries of those isotropic shapes of tetrahedron, octahedron, and icosahedron. Although the icosahedral group, which has the highest symmetry, has a six-dimensional irreducible representation, it generates regular shapes too close to the spherical one to be of interest in the nuclear physics applications [144]. See Appendix E for details.

the doubly magic ^{80}Zr are rather poor and no sign of tetrahedral deformation is found, the observed ground state rotational band suggests the presence of a large quadrupole deformation in this nucleus [147, 148]. Heavier $A \simeq 160$ systems which are predicted theoretically to have tetrahedral deformations [38] have also been measured, but it was concluded that they are unlikely to have the tetrahedral shape [149, 150]. More recently, Sumikama et al. [151] have discussed the possibility of tetrahedral deformation in an isomer they have observed in ^{108}Zr, although more data are required to confirm whether the isomer has a tetrahedral shape or not. So far, no experimental evidence of tetrahedral deformation has been found.

We here study two nuclei, ^{68}Se and ^{80}Zr, allowing the full octupole deformation. These nuclei have been studied with non-relativistic Skyrme Hartree-Fock + BCS [33] and Skyrme Hartree-Fock-Bogoliubov [35] calculations. The predictions given by the two models are similar to each other; the oblate ground state of ^{68}Se is extremely soft against Y_{33} (triangular) deformation and slightly deformed into the triangular shape in the ground state, on the other side, the local minimum at $\beta = 0$ of ^{80}Zr is extremely soft against Y_{32} (tetrahedral) deformation and it has the tetrahedral shape.

In the present calculations, we set $a = 0.8$ fm and $N_x = N_y = N_z = 24$, and we use PC-F1 interaction as in the preceding sections. In Table 7.3 we show the quadrupole deformation parameters of at the local minima of ^{68}Se and ^{80}Zr without any octupole deformations obtained with the present 3D calculations. To obtain this result, we start the self-consistent iterations without octupole deformation, that is, the octupole deformed solutions have been excluded. We do not find another minimum than those shown in the table either on the prolate nor the oblate sides. Although we have also tried to perform quadrupole constraint calculations, some numerical instability prevented the stable convergence of the solution for both of the nuclei[2].

Next we explore the possibility of the octupole deformations of the two nuclei by performing the self-consistent iterations starting from the three solutions shown in Table 7.3, giving an additional octupole distortion on the initial mean-field potential. Notice that the might not be the minimum with respect to the octupole deformation. In Refs. [33, 35], an triangular deformation was observed in the oblate ground state of ^{68}Se and a tetrahedral deformation superposed on the spherical shape is observed in a local minimum of ^{80}Zr.

As the result, we did not find an octupole minimum around the oblate minimum of ^{68}Se, which is different from the non-relativistic calculations in Refs. [33, 35]. We have confirmed that the solution converges to the reflection-symmetric solution (no octupole

---

[2] We suspect that the origin of the numerical instability is single-particle level crossings around the fermi level occurring more frequently in heavier nuclei as compared to the lighter nuclei examined in the preceding sections. In the mean-field level calculations, the occupation probabilities of single-particle states are given by a step function $\Theta(\epsilon - \epsilon_F)$, where ϵ_F is the fermi energy, of the single-particle energy. When two single-particle levels cross around the desired deformation parameter, the single-particle configuration jumps between the two during the self-consistent iterations to prevent the iteration from a convergence. In order to get rid of the instability we probably need to take into account the pairing correlation so that the occupation probability of the single-particle levels around the fermi energy is somewhat smeared because of scatterings of the Cooper pairs over the fermi level.

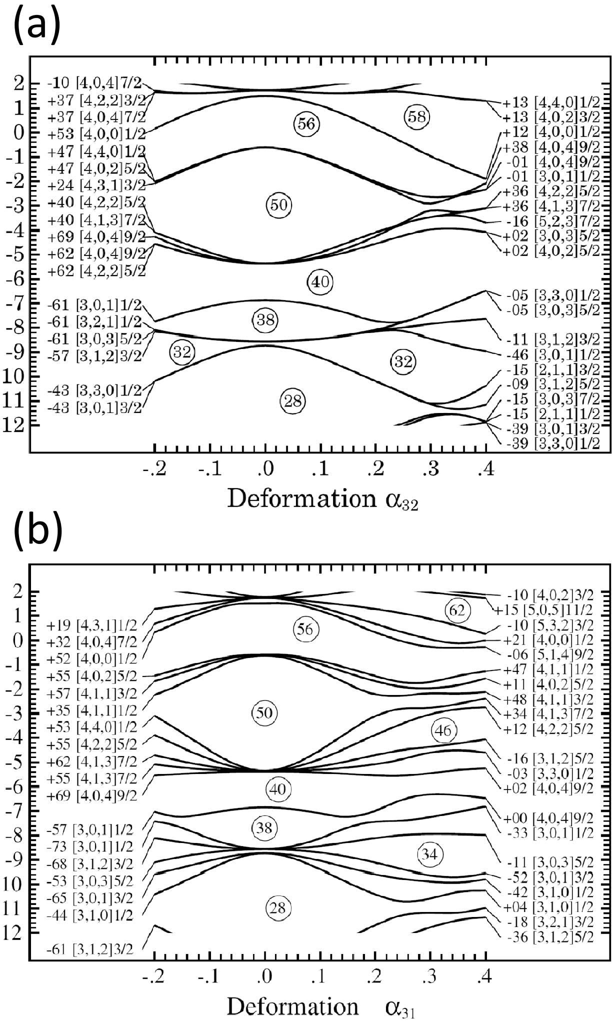

Figure 7.4: Single-particle spectra of deformed Woods-Saxon potentials with (a) Y_{32} (tetrahedral) and (b) Y_{31} deformations. The Nilsson quantum numbers indicate the strongest Nilsson basis at the extremes of the deformation axis. The numbers in front of the Nilsson quantum numbers give the expectation values of parity ($\times 100$). The figure is taken from Ref. [37].

Table 7.3: Local minima of ^{68}Se and ^{80}Zr without any octupole deformations obtained with the present 3D calculations. For ^{68}Se, the relative energy of the minima with respect to the oblate minimum is shown. The quadrupole deformation parameters are also shown. The solutions are classified into three groups, spherical, prolate, and oblate, according to their deformation parameters.

	Spherical	Prolate	Oblate
^{68}Se	—	1.07 MeV $(\beta, \gamma) = (0.25, 0°)$	0.0 MeV $(\beta, \gamma) = (0.27, 60°)$
^{80}Zr	0.0 MeV $\beta = 0.0$	—	—

deformation) even if we tried starting with all kind of the octupole distortions α_{3m}. The prolate solution of ^{68}Se does not either have an octupole deformation. This is consistent with the non-relativistic results in Refs [33, 35].

On the other hand, for ^{80}Zr, we found two octupole minima with Y_{32} (tetrahedral) and Y_{30} deformation, respectively. In Table 7.4 the octupole deformations, the energy gains with respect to the pure spherical shape of the two minima are shown. The one with the tetrahedral shape has a lower energy than the other with the axial octupole deformation, which is consistent with the results obtained in Refs. [33, 35].

In Fig. 7.5 , we show the change of the neutron single-particle energies around the fermi level ($2p_{1/2}$) at $\alpha_{32} = 0$ and $\alpha_{32} = 0.18$. One observes that the gap at $N = 40$ between $1g_{9/2}$ and $2p_{1/2}$ levels of the spherical configuration becomes larger as the α_{32} deformation develops. The instability of the spherical shape of ^{80}Zr against the tetrahedral deformation is attributed to the shell effect. As α_{32} increases, because of the octupole correlation between $g_{9/2}$ and $p_{3/2}$, the orbitals coming from $2p_{3/2}$ (and $2p_{1/2}$) are lowered in energy while those from $1g_{9/2}$ rise up to enhance the shell gap. Similar shell effects were observed also in Refs. [33, 35] for the spherical configuration of ^{80}Zr.

Finally, in Figs. 7.6 and 7.7 are shown the matter density distributions of the 1st solution with tetrahedral deformation, and in Fig. 7.8 are shown the matter density distributions of the 2nd solution with Y_{30} deformation. In the density distribution of the tetrahedral state on the xy-plane ($z = 0$ fm) shown in Fig. 7.6 (a) looks isotropic since $Y_{32}(\theta, \phi)$ is vanishing at $\theta = 90°$. If one takes a parallel slice at negative z [Fig. 7.7 (a)] the distribution is compressed along x direction, on the other hand, if one takes another slice at positive z [Fig. 7.7 (c)], the distribution is compressed along the other direction (y direction). These together with Fig. 7.6 indicate that this state indeed has the tetrahedral shape. On the other hand, from Fig. 7.8 showing the density of the 2nd state, we can see that it has a shape like a cone with the z-axis the axis of symmetry.

In summary, we have found with the relativistic model that the spherical shape of ^{80}Zr nucleus is unstable against the α_{32} deformation, which is consistent with the result obtained with the non-relativistic calculations by Takami et al. [33] and by Yamagami et

Table 7.4: The octupole minima found in ^{80}Zr. The quadrupole deformation parameters are $\beta = 0$ in the both solutions. The minimum denoted by "1st" has a tetrahedral shape, and the other denoted by "2nd" has an axially symmetric octupole deformation. Only the non-vanishing octupole deformation parameter in each minimum is shown in the second column. The energy with respect to the spherical solution is shown in the last column.

	Octpole deformation	Energy
1st	$\alpha_{32} = 0.18$	-0.66 MeV
2nd	$\alpha_{30} = 0.14$	-0.40 MeV

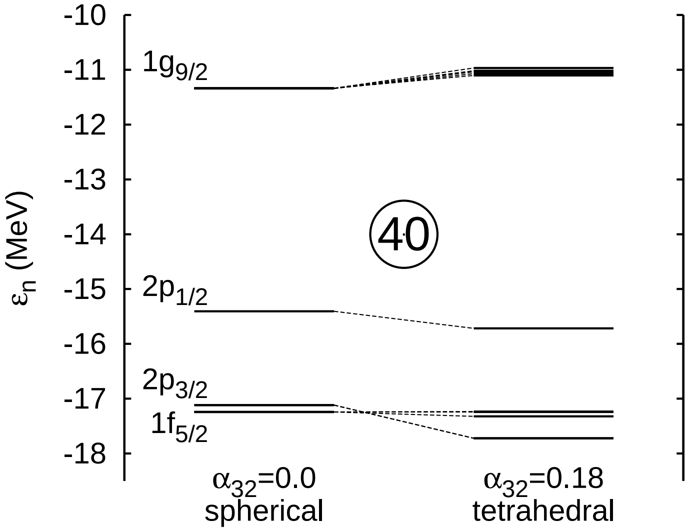

Figure 7.5: The neutron single-particle energies at $\alpha_{32} = 0$ (spherical) and $\alpha_{32} = 0.18$ (tetrahedral minimum), which are obtained in the present calculations. The levels up to $1p_{1/2}$ at the spherical configuration are occupied, and those above are all empty. Pairs of states which have large overlaps are connected by the dotted lines.

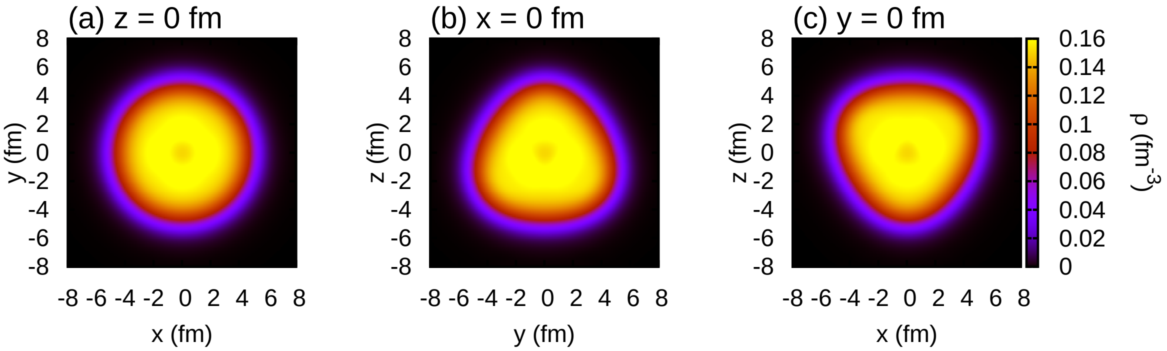

Figure 7.6: The density distributions on (a) xy-, (b) yz-, and (c) zx-planes of the 1st solution shown in Table 7.4 which has a tetrahedral shape. The quadrupole deformation parameters are $\beta = 0$ and the octupole deformation parameters are $\alpha_{32} = 0.18$ and $\alpha_{3m} = 0$ for $m \neq 2$.

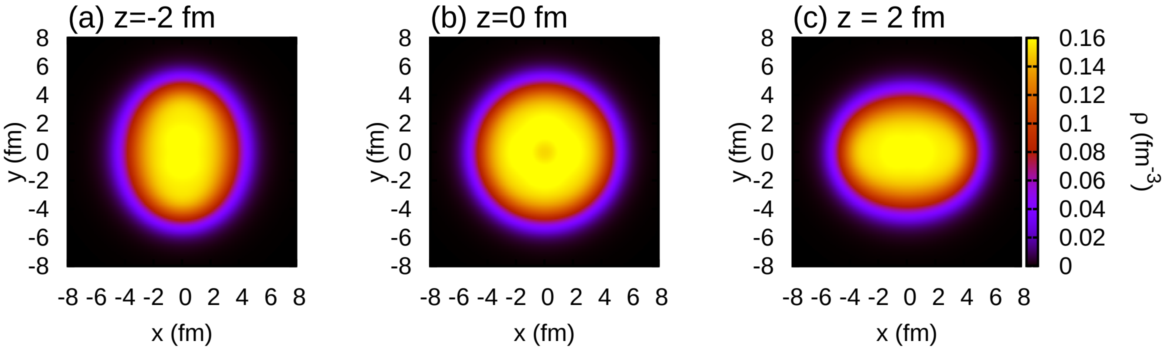

Figure 7.7: The density distributions as a function of x and y at (a) $z = -2$ fm, (b) $z = 0$ fm, and (c) $z = 2$ fm of the 1st solution shown in Table 7.4. (b) is the same as Fig. 7.6 (a). The quadrupole deformation parameter is $\beta = 0$ and the octupole deformation parameters are $\alpha_{32} = 0.18$ and $\alpha_{3m} = 0$ for $m \neq 2$.

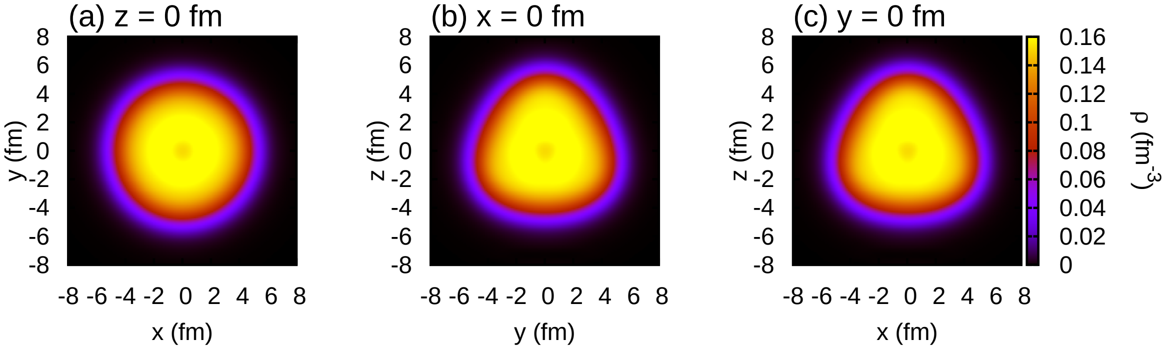

Figure 7.8: The density distributions on (a) xy-, (b) yz-, and (c) zx-planes of the 2nd solution shown in Table 7.4 which has an axially symmetric octupole shape. The quadrupole deformation parameters are $\beta = 0$ and the octupole deformation parameters are $\alpha_{30} = 0.14$ and $\alpha_{3m} = 0$ for $m \neq 0$.

al. [35]. Since the pairing correlation favors the spherical shape and it is not taken into account in the present relativistic calculations, the same investigation with the pairing correlation, where the pairing competes with the tetrahedral shell effect is also interesting. The pairing correlation may also be necessary for numerical stability in deformation constrained calculations. In contrast, the triangular deformation in the oblate ground state of ^{68}Se, which was observed in Refs. [33, 35] is not observed in the present calculation. In any case, further study with deformation constrained calculation and with the pairing correlation is still required in order to make more detailed comparison to the non-relativistic results.

Chapter 8

Summary and Perspectives

In this thesis, we have developed a new code for relativistic mean-field calculations. With this code, for the first time, we have realized density functional calculations based on the relativistic mean-field theory in the 3-dimensional coordinate space representation. We have introduced the two different prescriptions and combined them to overcome the two difficulties, i.e., variational collapse and fermion doubling, which had prevented one from carrying out a 3D coordinate space calculation with the covariant density functionals for a long time. For the variational collapse, we have employed a method based on the variational principle for the inverse of the single-particle Hamiltonian [129], and for the fermion doubling, we have extended the method of Wilson fermion, which is widely employed in lattice QCD calculations.

We have confirmed in Ch. 6 that our strategy gives accurate solutions for self-consistent mean-field calculations for light spherical nuclei with neither being suffered from the negative energy spectrum nor the spurious solutions of a discretized Dirac equation.

We have also performed in Sec. 7.1 the deformation constrained calculations and showed that the 3D code gives correct result for light deformed nuclei as well as for spherical ones. The results obtained here evidently showed the advantage of the calculations on 3D lattice that the accuracy of the result is not much affected by the shape of the solutions.

We have proceeded to the first application of our code in Sec. 7.2 to studies of the possible octupole deformations in $N = Z$ nuclei, ^{68}Se and ^{80}Zr, and compared the results with the ones obtained with the non-relativistic models in Refs. [33, 35]. The authors of Refs. [33, 35] have predicted for these two nuclei that the oblate ground state of ^{68}Se is extremely soft against Y_{33} (triangular) deformation and slightly deformed into the triangular shape in its ground state, and that the local minimum at $\beta = 0$ of ^{80}Zr is extremely soft against Y_{32} (tetrahedral) deformation and its deformation is the tetrahedral shape.

For ^{68}Se, we have obtained a result different from the non-relativistic calculations showing that the position of the local minimum on the oblate side of this nucleus is located at zero octupole deformations, whereas for ^{80}Zr, we have found a similar result to the non-relativistic one, i.e., the local minimum at $\beta = 0$ of ^{80}Zr is very soft against the tetrahedral deformation and possesses a finite tetrahedral deformation. These results indicate that the octupole deformation in these nuclei may be model dependent.

In order to discuss in more details the deformation properties of these nuclei, e.g., the evolution of the single-particle shell structure or the softness (or stiffness) of the nuclei against the octupole deformations, we definitely need to perform constrained calculations. Although we faced some numerical instability, we expect that it could be improved by taking into account the pairing correlation. Thus one of our most important next task is to implement the BCS approximation in our code so that we can obtain more detailed result.

There are several ways to improve our code to make it more widely applicable to various nuclear phenomena. These include:

- We should implement the pairing correlation in our code for discussion of open shell nuclei. The BCS approximation is the first to be tried. It may also be practically important for a stability of convergence in the deformation constrained calculations. The Hartree-Fock-Bogoliubov (HFB) theory, which treats the pairing correlation in a unified way within the self-consistent mean-field framework [66], is more robust and appropriate for drip-line nuclei. Especially, the halo structure with deformation in drip-line nuclei can be discussed if the HFB is introduced in our code.

  We show in Appendix A an application of the inverse Hamiltonian method to an HFB equation in the coordinate space representation.

- Constraints on the octupole and higher multipole deformations are important in particular to investigate the exotic deformation and fission properties.

- A relaxation of the time reversal symmetry assumed in the present version of the code makes it possible to study, for instance, the ground states of odd-mass and odd-odd nuclei [21], the collective vibrational excitations with RPA, and the high-spin states with the cranked CDFT [21], all without an assumption of geometrical symmetry, thus including exotic shapes or exotic excitation modes.

- The deformation properties of Λ hypernuclei can be calculated by adding the nucleon-Λ interaction part into the code. We have developed a new relativistic ΛN interaction for this purpose as shown in Appendix B.

In more technical and practical aspects, the following improvements are also possible.

- Accelerating the inversion of the single-particle Hamiltonian is crucial. Since inversion of Hamiltonian is the most time-consuming part of the code, the speed of the code is dominated by the efficiency of the inversion. Unfortunately, there is no firmly promising way for the acceleration. The preconditioning techniques [133,152] may be of help.

- In order to save the computational cost, a reduction of the number of mesh points is effective. The adaptive mesh points [153] is to be introduced. It is non-uniform mesh points which is denser in the region inside and around the nuclear surface, but sparser outside the nucleus, where wave functions are either almost vanishing or quite flat. This is a useful technique especially for weakly-bound systems, for which a larger box size is required.

  Another way to reduce the mesh points is to use a spherical numerical box instead of a cubic box. Suppose we need a box of the size L. With a uniform cubic lattice, the number of mesh points are proportional to the volume of the numerical box. For a cubic box the volume is $V = L^3$, whereas for a spherical box with diameter L, $V = \frac{4\pi}{3}(\frac{L}{2})^3$. Thus, by taking only those points which are located inside a sphere of the diameter L, the number of mesh points are reduced by factor of $\simeq 0.52$ compared to that of a cubic box.

- A parallelization of the numerical code is a straightforward way to make it faster.

To summarize, we have realized for the first time relativistic density functional calculations on 3D lattice. Despite the numerical instabilities we met for the medium heavy nuclei, we emphasize that our new relativistic 3D code allows us to study arbitrary shape of nuclei such as exotic deformations, halo structure, complicated shape of a fissioning nucleus, or even a cluster structure without any restriction on the spatial symmetry and without increase of the numerical cost. Therefore this work is an important step to drastically extend the flexibility of the CDFT calculations. Our method can also be exported to the field of relativistic quantum chemistry, where one meets completely the same problems as in the nuclear CDFT discussed in this thesis.

Acknowledgment

I am deeply grateful to my supervisor, Prof. Kouichi Hagino, for his continuous guidance throughout the period of my master and doctor courses, for more than five years since I joined the Nuclear Theory Group, Tohoku University. His advice and suggestions through discussions were indispensable for proceeding and completing this work.

I am also grateful to Dr. Haozhao Liang, who suggested us a future collaboration for applying our 3D RMF code to charge-exchange nuclear excitations. Discussions with him and his suggestions were helpful to improve the numerical performance of our code.

I would like to express my sincere gratitude to Prof. Jiangmimg Yao for his kind encouragement, fruitful discussions, and many useful advices on practical aspects in mean-field calculations. I also thank him and Ms. Hua Mei for providing us with their numerical results.

I would like to thank Prof. Shoichi Sasaki and Prof. Akira Ono for their valuable advice and comments in our group seminars and discussions. Especially, discussions with Prof. Sasaki were very helpful for understanding the nature of fermion doubling problem of lattice fermion.

I would like to thank Prof. Hiroyuki Sagawa for helpful discussions and his kind support for finding a job. I have also learned a lot through collaborations with him on proton-neutron pairing. I would also like to thank Prof. Peter Ring, Prof. Masayuki Matsuo, Dr. Ying Zhang, and Mr. Kazuya Hirokawa, for meaningful discussions and suggestions.

Finally, I would like to thank my family for letting me learn at Tohoku University and for their continuous support, understanding, and encouragement.

This work was supported by the Japan Society for the Promotion of Science (JSPS) Research Fellowships for Young Scientists and the Grant-in-Aid for JSPS fellows.

Yusuke Tanimura, August 2014

Appendix A

Application of the Inverse Hamiltonian Method to an HFB Equation

In this appendix we show results of an application of our inverse Hamiltonian method to an Hartree-Fock-Bogoliubov (HFB) equation in the coordinate space representation. Since the spectrum of an HFB equation is neither bounded from the above nor below like a Dirac equation, one is suffered from the problem of variational collapse in solving it. What is presented in this appendix is based on our published paper [154].

Pairing correlations between nucleons play an important role in open shell nuclei [66,155]. Hartree-Fock-Bogoliubov (HFB) theory is a powerful method which treats these correlations in a self-consistent way in the framework of a single generalized Slater determinant of independent quasi-particles [66,156,157]. The method has been widely used in recent years for the study of the structure of neutron rich nuclei far from stability up to the neutron drip line, where the coupling to the continuum has an influence.

The HFB equations are a set of coupled differential equations [66],

$$\begin{pmatrix} h-\lambda & \Delta \\ -\Delta^* & -h^*+\lambda \end{pmatrix} \begin{pmatrix} U \\ V \end{pmatrix} = E \begin{pmatrix} U \\ V \end{pmatrix}, \tag{A.0.1}$$

where h is the mean-field Hamiltonian, λ is the chemical potential, and Δ is the pairing field. U and V are quasi-particle wave functions. Notice that, if $(U_k, V_k)^T$ is a solution of Eq. (A.0.1) with an eigenvalue E_k, $(V_k^*, U_k^*)^T$ is also an eigenstate with eigenvalue $-E_k$. Because of this property, quasi-particle spectrum is symmetric with respect to $E = 0$, that is, it has neither lower bound nor upper bound like Dirac equations (See Fig. A.1). This inhibits a direct application of the imaginary time method to HFB, which has been successfully employed in self-consistent mean field calculations in the coordinate space representation [49, 73]. That is, if the imaginary time evolution is naively applied, the iterative solution inevitably dives into the quasi-particle negative continuum.

To avoid a variational collapse in HFB, the two-basis method has been introduced in Ref. [57] where, in each step of the iteration, the HFB equations are solved by expansion

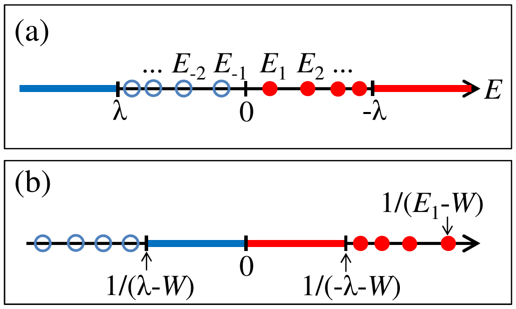

Figure A.1: Spectra of (a) a quasi-particle Hamiltonian H itself and (b) the inverse of the Hamiltonian $1/(H-W)$. λ is the chemical potential. The bound states of positive and negative energies are indicated by solid and open circles, respectively. The continuum states are represented by the thick solid lines. The energy shift W is taken between the positive and negative spectra. The eigenvalues are labeled by an integer k such that $E_{-k}=-E_k$ and $E_k>0$ for $k>0$.

of the quasi-particle wave functions in a Hartree-Fock basis calculated by the imaginary time method on a 3D mesh in the coordinate space. In Ref. [158] the HFB equation on a 3D mesh has been solved in the canonical basis.

We propose our inverse Hamiltonian method as another way to solve the HFB equation. As a first step we will show that an HFB equation with spherical mean-field and pairing potentials can be solved successfully without variational collapse.

When the mean-field and pairing potentials are local and spherical, a quasi-particle wave function is given by the form

$$\psi(\boldsymbol{r})=\begin{pmatrix} U(r)\mathscr{Y}_{\ell jm}(\theta,\phi) \\ V(r)\mathscr{Y}_{\ell jm}(\theta,\phi) \end{pmatrix} \tag{A.0.2}$$

The HFB equation in the coordinate space then reduces to the radial equation

$$\begin{pmatrix} h-\lambda & \Delta(r) \\ \Delta(r) & -h+\lambda \end{pmatrix}\begin{pmatrix} U(r) \\ V(r) \end{pmatrix}=E\begin{pmatrix} U(r) \\ V(r) \end{pmatrix}, \tag{A.0.3}$$

where the mean-field Hamiltonian h is given as

$$h=-\frac{\hbar^2}{2m}\boldsymbol{\nabla}^2+v(r). \tag{A.0.4}$$

Following the authors of Refs. [159, 160], we use a phenomenological Woods-Saxon-type potentials, which simulates medium-heavy neutron-rich nuclei around ^{84}Ni, for the mean field and the pairing potentials. The potential $v(r)$ in the mean field Hamiltonian h and the paring potential $\Delta(r)$ are thus taken as

$$\begin{aligned} v(r) &= v_0 f(r) + v_{\ell s}\frac{1}{r}\frac{df}{dr}\boldsymbol{\ell}\cdot\boldsymbol{s}, && \text{(A.0.5)}\\ \Delta(r) &= \Delta_0 f(r), && \text{(A.0.6)}\\ f(r) &= \frac{1}{1+e^{(r-R_0)/a}}, && \text{(A.0.7)} \end{aligned}$$

with $v_0 = -38.5$ MeV, $v_{\ell s} = 14$ MeV·fm^2, $R_0 = 5.63$ fm, and $a = 0.66$ fm [159,160]. The strength of pairing potential Δ_0 is determined so that the average pairing gap $\bar{\Delta}$ defined by [159]

$$\bar{\Delta} = \frac{\int_0^\infty r^2 dr\ \Delta(r) f(r)}{\int_0^\infty r^2 dr\ f(r)} \tag{A.0.8}$$

is equal to 1.0 MeV. The chemical potential λ is fixed to $\lambda = -0.5$ MeV in the present calculation. We solve Eq. (A.0.3) by discretizing the radial coordinate r with mesh size Δr, and imposing the box boundary condition. The second derivative of ψ at the ith mesh point is approximated by 3-point difference formula.

Let us now apply the inverse Hamiltonian method and numerically solve the HFB equation, Eq. (A.0.3). We also solve the equation exactly by directly diagonalizing the coordinate space Hamiltonian. The parameters of the inverse Hamiltonian method are set $W = 0.1$ MeV and $\Delta T = 10$ MeV. The excited states are also calculated simultaneously by orthogonalizing a set of wave functions at every step of iteration. In order to invert the Hamiltonian, We here employ an iterative method for linear systems, that is, the conjugate gradient normal residual (CGNR) method [133]. This is one of the Krylov subspace methods. CGNR solves a linear system $A\boldsymbol{x} = b$ by applying the conjugate gradient method to an equivalent system $A^\dagger A\boldsymbol{x} = A^\dagger b$. The radial coordinate is discretized up to $r_{\max} = 30$ fm with $\Delta r = 0.1$ fm. Initial quasi-particle wave functions are taken to be a Gaussian form

$$\begin{pmatrix} U_k^{(0)}(r) \\ V_k^{(0)}(r) \end{pmatrix} = N_k \begin{pmatrix} r^{\ell+1} e^{-r^2/b_k^2} \\ r^{\ell+1} e^{-r^2/b_k^2} \end{pmatrix}, \tag{A.0.9}$$

where ℓ is the orbital angular momentum and N_k is an appropriate normalizing constant. The width parameter of the Gaussian b_k is taken as $b_k = 2.0 \times 1.05^{k-1}$ fm, $(k = 1, 2, ...)$.

Let us first discuss the convergence properties of the energy $\langle H \rangle$ and the expectation value of the inverse of Hamiltonian $\langle (H-W)^{-1} \rangle$ for the lowest $s_{1/2}$ quasi-particle state. In Fig. A.2, we show the evolution of the two quantities as functions of the number of iteration steps. As is observed in Ref. [131] for a Dirac equation, $\langle (H-W)^{-1} \rangle$ converges monotonically up to a certain value as the iteration step increases. At the same time, $\langle H \rangle$ converges to the lowest $s_{1/2}$ eigenvalue, $E = 0.424$ MeV.

In Table A.1, we show quasi-particle energies and occupation probabilities v_k^2 for the three lowest $s_{1/2}$ states in comparison with the exact values which are obtained by diagonalizing the Hamiltonian. The occupation probabilities are defined in terms of quasi-particle wave function by

$$v_k^2 = \int_0^\infty dr\ |V_k(r)|^2. \tag{A.0.10}$$

Table A.1: A comparison between the exact calculations and the inverse Hamiltonian method for the three lowest $s_{1/2}$ quasi-particle energies E and occupation probabilities v_k^2. The exact values are calculated by diagonalizing the real space Hamiltonian.

E (MeV)		v_k^2	
exact	inv. H method	exact	inv. H method
0.42414	0.42414	0.5574	0.5574
1.0383	1.0383	3.972×10^{-2}	3.972×10^{-2}
2.3063	2.3063	9.689×10^{-3}	9.689×10^{-3}

The agreement is perfect both in the energies and the occupation probabilities for the digits shown in the table. Fig. A.3 shows comparisons of wave functions of the three $s_{1/2}$ states. The dashed lines show the exact wave functions, whereas the solid lines show the wave functions obtained with the inverse Hamiltonian method. The left and right panels show the upper component $U_k(r)$ and the lower component $V_k(r)$ of a quasi-particle wave function, respectively. As is seen in Fig A.3, the inverse Hamiltonian method reproduces the wave functions almost identically to the exact ones for both the bound state and the excited continuum states. We have also obtained the other s-wave states with an accuracy as high as the lower states shown in Table A.1 and Fig. A.3.

We have checked the performance of the inverse Hamiltonian method for other angular momentum quantum numbers and confirmed that the method solves the HFB equation as accurately as for the $s_{1/2}$ states. It is apparent that the inverse Hamiltonian method gives practically the exact solutions of the HFB equation in the coordinate space representation and is safe against the variational collapse.

While the method has been developed for solving Dirac equations, we have shown that it can almost exactly solve a coordinate space HFB equation as well with spherical mean field and pairing potentials without variational collapse. This indicates that the inverse Hamiltonian method provides an alternative coordinate space method for 3-dimensional HFB calculations, in addition to the existing methods such as the two-basis method and the canonical basis method. The inverse Hamiltonian method has an advantage in that it can also be applied in a straightforward manner to relativistic Bogoliubov calculations on 3-dimensional mesh, for which the Dirac sea spectrum in a mean-field Hamiltonian prevents a direct application of the two-basis method in combination with the imaginary time method. An obvious future work is the application of the method to self-consistent HFB calculations on 3D mesh.

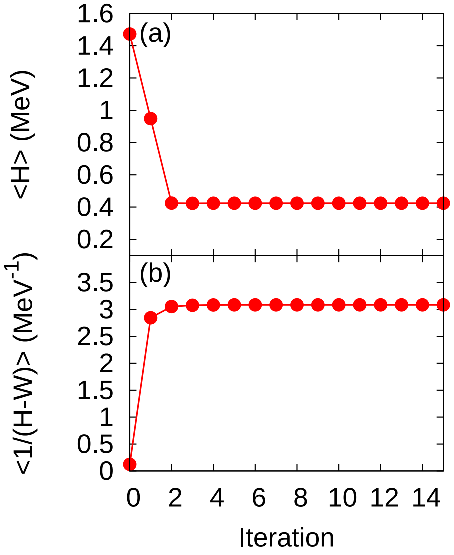

Figure A.2: Covergence properties of (a) the energy expectation value $\langle H \rangle$ and (b) the expectation value of the inverse of Hamiltonian $\langle (H - W)^{-1} \rangle$ for the lowest $s_{1/2}$ quasi-particle state. The energy shift and the step size of T are taken to be $W = 0.1$ MeV and $\Delta T = 10$ MeV, respectively. The Figure is taken from Ref. [154].

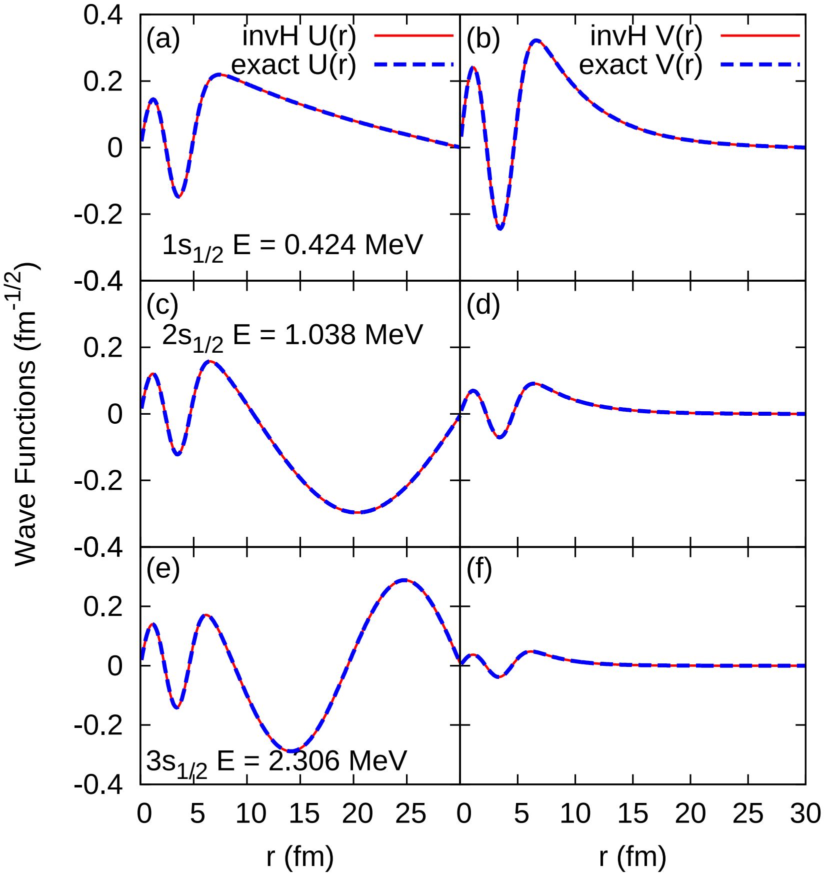

Figure A.3: Comparisons of wave functions for the three lowest $s_{1/2}$ states. Figures 3(a), 3(c), and 3(e) show the upper components $[U_k(r)]$ while Figs. 3(b), 3(d), and 3(f) show the lower components $[V_k(r)]$ of the quasi-particle wave function, respectively. The exact wave functions are shown with the dashed lines and the ones obtained by the inverse Hamiltonian method are drawn with the solid lines. The Figure is taken from Ref. [154].

Appendix B

Relativistic Point-Coupling Model for Λ Hypernuclei

In this appendix we give a new relativistic nucleon-Λ interaction we have developed in Ref. [161]. The Λ hypernuclei have been extensively studied both theoretically and experimentally [164]. In Ref. [161], we have extended the relativistic point-coupling model to single-Λ hypernuclei. For this purpose, we added N-Λ effective contact couplings to the model Lagrangian and determined the parameters by fitting to the experimental data for Λ binding energies. Our model well reproduces the data over a wide range of mass region although some of our interactions yield the reverse ordering of the spin-orbit partners from that of nucleons for heavy hypernuclei.

B.1 Model Lagrangian

Our model Lagrangian for single-Λ hypernuclei is given by

$$\mathcal{L} = \mathcal{L}_{\mathrm{N}} + \mathcal{L}_{\mathrm{em}} + \mathcal{L}_{\mathrm{int}} + \mathcal{L}_{\Lambda} + \mathcal{L}_{\mathrm{int}}^{N\Lambda}. \tag{B.1.1}$$

In this Lagrangian, $\mathcal{L}_{\mathrm{N}}$, $\mathcal{L}_{\mathrm{em}}$, and $\mathcal{L}_{\mathrm{int}}$ are the free nucleon part, the electromagnetic part, and the nucleon-nucleon interaction part, respectively, whose explicit expressions are already given in Eqs. (3.3.2), (3.3.3), (3.3.7), (3.3.8), (3.3.9), and (3.3.10). $\mathcal{L}_{\Lambda}$ in Eq. (B.1.1) is the free part of the Λ particle given by

$$\mathcal{L}_{\Lambda} = \bar{\psi}_{\Lambda}(i\partial\!\!\!/ - m_{\Lambda})\psi_{\Lambda}, \tag{B.1.2}$$

where ψ_{Λ} is the field of the Λ particle and $m_{\Lambda} = 1115.6$ MeV is the mass of the Λ particle. Noticing that Λ only couples to the scalar and vector mesons, we construct nucleon-Λ (N-Λ) interaction, $\mathcal{L}_{\mathrm{int}}^{N\Lambda}$, as

$$\mathcal{L}_{\mathrm{int}}^{N\Lambda} = \mathcal{L}_{\mathrm{4f}}^{N\Lambda} + \mathcal{L}_{\mathrm{der}}^{N\Lambda} + \mathcal{L}_{\mathrm{ten}}^{N\Lambda}, \tag{B.1.3}$$

where

$$\begin{aligned}\mathcal{L}_{\mathrm{4f}}^{N\Lambda} = & -\alpha_S^{(N\Lambda)}(\bar{\psi}_N\psi_N)(\bar{\psi}_\Lambda\psi_\Lambda) \\ & -\alpha_V^{(N\Lambda)}(\bar{\psi}_N\gamma_\mu\psi_N)(\bar{\psi}_\Lambda\gamma^\mu\psi_\Lambda),\end{aligned} \tag{B.1.4}$$

$$\begin{aligned}\mathcal{L}^{N\Lambda}_{\text{der}} =& -\delta^{(N\Lambda)}_S(\partial_\mu\bar{\psi}_N\psi_N)(\partial^\mu\bar{\psi}_\Lambda\psi_\Lambda)\\ &-\delta^{(N\Lambda)}_V(\partial_\mu\bar{\psi}_N\gamma_\nu\psi_N)(\partial^\mu\bar{\psi}_\Lambda\gamma^\nu\psi_\Lambda),\end{aligned} \tag{B.1.5}$$

and

$$\mathcal{L}^{N\Lambda}_{\text{ten}} = -\alpha^{(N\Lambda)}_T(\bar{\psi}_\Lambda\sigma^{\mu\nu}\psi_\Lambda)(\partial_\mu\bar{\psi}_N\gamma_\nu\psi_N). \tag{B.1.6}$$

ψ_N in these equations is the nucleon field. For simplicity, we do not consider the higher order term for the $N\Lambda$ coupling, $\mathcal{L}^{N\Lambda}_{\text{hot}}$, in this paper. $\mathcal{L}^{N\Lambda}_{\text{ten}}$ in Eq. (B.1.6) simulates the Λ-ω tensor coupling $\mathcal{L}^{\Lambda\omega}_{\text{ten}} = \frac{f_{\Lambda\omega}}{2m_\Lambda}(\bar{\psi}_\Lambda\sigma^{\mu\nu}\psi_\Lambda)(\partial_\nu\omega_\mu)$. The quark model suggests that the tensor coupling of Λ to ω meson is much stronger than that of nucleon. That is, the quark model yields the ratio of Λ-ω tensor-to-vector coupling constants, $f_{\Lambda\omega}/g_{\Lambda\omega}$, to be -1, while it yields the corresponding ratio for nucleon to be $f_{N\omega}/g_{N\omega} = -0.09$ [162]. Thus this type of coupling plays an important role in hypernuclei. Since this term is proportional to the derivative of the mean field, it mainly affects the spin-orbit splittings of Λ single-particle energies [163]. It is expected that the small spin-orbit splittings of lambda can be reproduced by tuning the tensor coupling $\alpha^{(N\Lambda)}_T$. We will discuss this point in the next Section.

The EDF corresponding to the Lagrangian in Eq. (B.1.1) for a single-Λ hypernucleus with mass number A (*i.e.*, a single Λ particle with $A-1$ nucleons) in the mean-field (Hartree) and the no-sea approximations is given by

$$\begin{aligned} E \;=\; \int d^3r\, \Bigg(& \sum_{i=1}^{A-1}\psi_i^\dagger(\boldsymbol{\alpha}\cdot\boldsymbol{p}+m_N\beta)\psi_i + \psi_\Lambda^\dagger(\boldsymbol{\alpha}\cdot\boldsymbol{p}+m_\Lambda\beta)\psi_\Lambda + \frac{1}{2}eA^0\rho_V^{(\mathrm{p})}\\ &+\frac{1}{2}\sum_K\alpha_K\rho_K^2 + \frac{1}{2}\sum_K\delta_K\rho_K\Delta\rho_K + \frac{1}{3}\beta_S\rho_S^3 + \frac{1}{4}\gamma_S\rho_S^4 + \frac{1}{4}\gamma_V\rho_V^4\\ &+\sum_{K=S,V}\alpha_K^{(N\Lambda)}\rho_K\rho_K^{(\Lambda)} + \sum_{K=S,V}\delta_K^{(N\Lambda)}\rho_K\Delta\rho_K^{(\Lambda)} + \alpha_T^{(N\Lambda)}\rho_T^{(\Lambda)}\rho_V\Bigg), \end{aligned} \tag{B.1.7}$$

Here, we have assumed the time reversal invariance of the nuclear ground state. The densities appearing in Eq. (B.1.8) are defined as

$$\rho_S = \sum_{i=1}^{A-1}\bar{\psi}_i\psi_i, \qquad \rho_V = \sum_{i=1}^{A-1}\psi_i^\dagger\psi_i, \tag{B.1.8}$$

$$\rho_{TS} = \sum_{i=1}^{A-1}\bar{\psi}_i\tau_3\psi_i, \quad \rho_{TV} = \sum_{i=1}^{A-1}\psi_i^\dagger\tau_3\psi_i, \tag{B.1.9}$$

$$\rho_S^{(\Lambda)} = \bar{\psi}_\Lambda\psi_\Lambda, \qquad \rho_V^{(\Lambda)} = \psi_\Lambda^\dagger\psi_\Lambda, \tag{B.1.10}$$

$$\rho_T^{(\Lambda)} = \boldsymbol{\nabla}\cdot(\bar{\psi}_\Lambda i\boldsymbol{\alpha}\psi_\Lambda). \tag{B.1.11}$$

Here ψ_i is the wave function for the i-th nucleon, and ψ_Λ is the wave function for the Λ particle.

Variation with respect to the nucleon wave function leads to the Hartree equation for nucleons,

$$[\boldsymbol{\alpha}\cdot\boldsymbol{p} + V_V + V_{TV}\tau_3 + V_C + (m_N + V_S + V_{TS}\tau_3)\,\beta]\,\psi_i = \epsilon_i\psi_i, \tag{B.1.12}$$

with

$$\begin{aligned}
V_S &= (\alpha_S + \delta_S\Delta)\rho_S + \beta_S\rho_S^2 + \gamma_S\rho_S^3 \\
&\quad +(\alpha_S^{(N\Lambda)} + \delta_S^{(N\Lambda)}\Delta)\rho_S^{(\Lambda)}, && \text{(B.1.13)}\\
V_V &= (\alpha_V + \delta_V\Delta)\rho_V + \gamma_V\rho_V^3 \\
&\quad +(\alpha_V^{(N\Lambda)} + \delta_V^{(N\Lambda)}\Delta)\rho_V^{(\Lambda)} + \alpha_T^{(N\Lambda)}\rho_T^{(\Lambda)}, && \text{(B.1.14)}\\
V_{TS} &= (\alpha_{TS} + \delta_{TS}\Delta)\rho_{TS}, && \text{(B.1.15)}\\
V_{TV} &= (\alpha_{TV} + \delta_{TV}\Delta)\rho_{TV}, && \text{(B.1.16)}\\
V_C &= eA^0\frac{1-\tau_3}{2},\ (\Delta A^0 = -e\rho_V^{(p)}), && \text{(B.1.17)}
\end{aligned}$$

while variation with respect to the lambda wave function leads to the Hartree equation for the lambda particle:

$$[\boldsymbol{\alpha}\cdot\boldsymbol{p} + U_V + U_T + (m_\Lambda + U_S)\,\beta]\,\psi_\Lambda = \epsilon_\Lambda\psi_\Lambda, \tag{B.1.18}$$

with

$$\begin{aligned}
U_S &= (\alpha_S^{(N\Lambda)} + \delta_S^{(N\Lambda)}\Delta)\rho_S, && \text{(B.1.19)}\\
U_V &= (\alpha_V^{(N\Lambda)} + \delta_V^{(N\Lambda)}\Delta)\rho_V, && \text{(B.1.20)}\\
U_T &= -i\alpha_T^{(N\Lambda)}\beta\boldsymbol{\alpha}\cdot(\boldsymbol{\nabla}\rho_V). && \text{(B.1.21)}
\end{aligned}$$

After having solved these Hartree equations self-consistently, we obtain the total binding energy as

$$\begin{aligned}
E_B &= \sum_{i=1}^{A-1}\epsilon_i + \epsilon_\Lambda - E_{\mathrm{CM}} - (A-1)m_N - m_\Lambda \\
&\quad -\int d^3r\,\Bigg(\frac{1}{2}\sum_K \alpha_K\rho_K^2 + \frac{1}{2}\sum_K \delta_K\rho_K\Delta\rho_K + \frac{2}{3}\beta_S\rho_S^3 + \frac{3}{4}\gamma_S\rho_S^4 + \frac{3}{4}\gamma_V\rho_V^4 \\
&\quad + \sum_{K=S,V}\alpha_K^{(N\Lambda)}\rho_K\rho_K^{(\Lambda)} + \sum_{K=S,V}\delta_K^{(N\Lambda)}\rho_K\Delta\rho_K^{(\Lambda)} + \alpha_T^{(N\Lambda)}\rho_T^{(\Lambda)}\rho_V + \frac{1}{2}eA^0\rho_V^{(p)}\Bigg),
\end{aligned} \tag{B.1.22}$$

where the center of mass energy E_{CM} is calculated by taking the expectation value of the kinetic energy for the center of mass motion with respect to the many-body ground state wave function as

$$E_{\mathrm{CM}} = \frac{\langle P_{\mathrm{CM}}^2\rangle}{2[(A-1)m_N + m_\Lambda]}. \tag{B.1.23}$$

See Appendix F.1 for the explicit expression for this term.

The relation of the point coupling model to the meson exchange model can be made as follows (See also Eqs. (6)-(10) in Ref. [84]). By eliminating the meson fields and expanding the meson propagators to the leading order, the following approximate relations between the two models can be obtained [84]:

$$\alpha_S \approx -\frac{g_{N\sigma}^2}{m_\sigma^2},\ \alpha_V \approx \frac{g_{N\omega}^2}{m_\omega^2}, \tag{B.1.24}$$

$$\alpha_S^{(N\Lambda)} \approx -\frac{g_{N\sigma}g_{\Lambda\sigma}}{m_\sigma^2},\ \alpha_V^{(N\Lambda)} \approx \frac{g_{N\omega}g_{\Lambda\omega}}{m_\omega^2},\ \alpha_T^{(N\Lambda)} \approx -\frac{g_{N\omega}f_{\Lambda\omega}}{2m_\Lambda m_\omega^2}, \tag{B.1.25}$$

where g's and m's are the baryon-meson coupling constants and the meson masses, respectively. $f_{\Lambda\omega}$ is the Λ-ω tensor coupling constant. Notice that it has been demonstrated that α_S and α_V obtained phenomenologically approximately follow these relations [84] (on the other hand, it has been shown that the derivative terms, δ_S and δ_V, do not follow the corresponding expected relations [84]). If we assume the naive quark counting ratios $g_{\Lambda\sigma} = \frac{2}{3}g_{N\sigma}$ and $g_{\Lambda\omega} = \frac{2}{3}g_{N\omega}$, together with the quark model prediction for the tensor coupling, $f_{\Lambda\omega}/g_{\Lambda\omega} = -1$ [162], we obtain

$$\alpha_S^{(N\Lambda)} \approx \frac{2}{3}\alpha_S,\ \alpha_V^{(N\Lambda)} \approx \frac{2}{3}\alpha_V,\ \alpha_T^{(N\Lambda)} \approx -\frac{\alpha_V}{3m_\Lambda}. \tag{B.1.26}$$

We will show in the next section that these expected relations indeed hold if we include the N-Λ tensor coupling given by Eq. (B.1.6) in the Lagrangian.

B.2 Parameter sets obtained by fitting

With the model described in the previous section, we calculate Λ binding energies defined by the mass difference

$$m(^{A-1}Z) + m_\Lambda - m(^{A}_{\Lambda}Z) = E_B(^{A-1}Z) - E_B(^{A}_{\Lambda}Z). \tag{B.2.1}$$

To this end, we assume spherical symmetry, and neglect the pairing correlations for simplicity. For the valence orbital, we use the filling approximation to determine the occupation probability. We use the parameter set PC-F1 [84] for the N-N part of interaction and fit the five parameters in the N-Λ part (see Eqs. (B.1.4), (B.1.5) and (B.1.6)) to the experimental data. The data to be fitted to are Λ binding energies for s and p orbitals in $^{16}_{\Lambda}$O, s, p and d in $^{40}_{\Lambda}$Ca, s and d in $^{51}_{\Lambda}$V, s, p, d, and f in $^{89}_{\Lambda}$Y, s, p, d, f, and g in $^{139}_{\Lambda}$La, and s, p, d, f, and g in $^{208}_{\Lambda}$Pb. These are taken from Refs. [164,165]. In addition, the spin-orbit splitting for the p orbital of Λ in $^{16}_{\Lambda}$O [166] is included in the fitting procedure. The value deduced in Ref. [166] is 300 keV $\leq \epsilon_{\Lambda p_{1/2}} - \epsilon_{\Lambda p_{3/2}} \leq$ 600 keV, where the variation comes from a choice of the interactions. Notice that this value is model dependent, and we merely regard it as a criterion. The coupling constants in the strange

Table B.1: The best fit parameter set PCY-S1 for the relativistic point coupling model for hypernuclei. PC-F1 [84] is used for the N-N part. The uncorrelated errors and the ratios R defined in Eq. (B.2.3) with the expected values given in Eq. (B.1.26) are also shown in the table. The chi-square value per degree of freedom is $\chi^2_{\text{dof}} = 0.55$.

coupling const.	value	uncorr. error (%)	R
$\alpha_S^{(N\Lambda)}$	-2.0305×10^{-4} MeV^{-2}	8.2×10^{-2}	0.79
$\alpha_V^{(N\Lambda)}$	1.6548×10^{-4} MeV^{-2}	9.7×10^{-2}	0.96
$\delta_S^{(N\Lambda)}$	2.2929×10^{-9} MeV^{-4}	5.4×10^{-1}	–
$\delta_V^{(N\Lambda)}$	-2.3872×10^{-9} MeV^{-4}	5.0×10^{-1}	–
$\alpha_T^{(N\Lambda)}$	-1.0603×10^{-7} MeV^{-3}	6.8×10^{0}	1.37

sector are determined by performing a least-squares fit to the data, that is, by minimizing the quantity

$$\chi^2 = \sum_{i=1}^{N} \left(\frac{O_i^{\text{theor}} - O_i^{\text{expt}}}{\Delta O_i^{\text{expt}}} \right)^2 . \tag{B.2.2}$$

Here, N is the number of data points, and O_i^{theor} and O_i^{expt} are theoretical and experimental values of the observables, respectively, with the experimental uncertainties of ΔO_i^{expt}. To find the minimum of χ^2 in the five dimensional parameter space, we employ an automatic search algorithm *Oak-ridge and Oxford method* [167].

The parameter set PCY-S1 so obtained is summarized in Table B.1. We also show the uncorrelated errors for the parameters, that are defined as the range of a parameter which changes the χ^2 value by unity around the minimum value when the other parameters are kept to be the same. Together with the coupling constants and their uncorrelated errors, the ratios R of the resultant N-Λ coupling constants to the expected values given in Eq. (B.1.26),

$$R = (\text{resulted value})/(\text{expected value}), \tag{B.2.3}$$

are also shown. These ratios are $R = 0.79$, 0.96, and 1.37 for $\alpha_S^{(N\Lambda)}$, $\alpha_V^{(N\Lambda)}$, and $\alpha_T^{(N\Lambda)}$, respectively, and the expected values are approximately realized.

The calculated binding energies of Λ with this interaction are shown in Fig. B.1(a). One observes that the calculated Λ binding energies agree with the experimental values fairly well, although the binding energies for $^{28}_{\Lambda}$Si and $^{32}_{\Lambda}$S are somewhat overestimated. The less satisfactory result for these latter nuclei, which has been observed also in the previous RMF calculations for hypernuclei [163,168–170], is within expectation, as we do not take into account a strong deformation of the core nucleus nor the pairing correlation. We have confirmed that the situation does not change even if we include these two nuclei in the fitting.

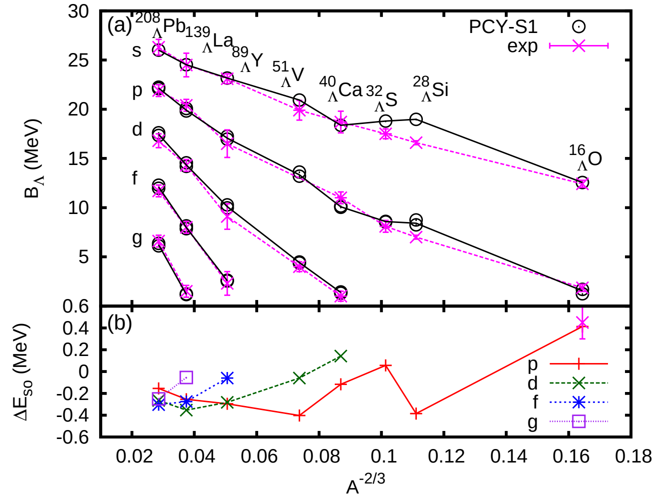

Figure B.1: Comparison between (a) the experimental data and the calculated Λ binding energies B_Λ and (b) spin-orbit splittings of Λ single-particle energies $\Delta E_{\rm so}$ obtained with the parameter set PCY-S1. The experimental data are taken from Refs. [164–166].

In order to investigate the role of the tensor coupling, we show in Table B.2 the parameter set PCY-S2 obtained *without* including the tensor coupling term. The Lambda binding energies calculated with this interaction is shown in Fig. B.2 (a). As one sees, the ratios R for $\alpha_S^{(N\Lambda)}$ and $\alpha_V^{(N\Lambda)}$ are strongly suppressed compared to unity. On the other hand, the sum $\alpha_S^{(N\Lambda)} + \alpha_V^{(N\Lambda)}$ has similar values around -3×10^{-5} MeV^{-2} both for PCY-S1 and PCY-S2. The suppression of the ratios can be understood as follows. In the non-relativistic reduction of a Dirac equation without the tensor coupling contribution, the central potential and the spin-orbit potential read

$$V_{\rm central} = V + S, \;\; V_{\rm ls} = \frac{1}{2m^2}\frac{1}{r}\frac{d}{dr}(V - S), \tag{B.2.4}$$

where V and S are the vector and the scalar potentials, respectively. Therefore, to reproduce a small spin-orbit splitting of Λ without the tensor interaction, the difference of the vector and the scalar potential have to be small, keeping their sum constant. This can be achieved only by lowering the values of the four fermion N-Λ couplings, $\alpha_S^{(N\Lambda)}$ and $\alpha_V^{(N\Lambda)}$, which roughly determine the strengths of mean potential felt by Λ. Notice that $V - S$ does not have to be small in the presence of the tensor coupling, as there is another contribution to the spin-orbit potential from the tensor coupling. The importance of the N-Λ tensor coupling (originated from the Λ-ω tensor coupling) is thus evident. It yields small spin-orbit splittings, keeping $\alpha_S^{(N\Lambda)}$ and $\alpha_V^{(N\Lambda)}$ at the natural values. In PCY-S1, the two quark model predictions, that is, the quark counting ratios and the importance of the tensor coupling ($f_{\Lambda\omega}/g_{\Lambda\omega} = -1$), are simultaneously satisfied.

Let us now discuss the calculated spin-orbit splittings, $\Delta E_{\rm so}$. These are estimated as a difference of Λ single-particle energies between spin-orbit partners, $\Delta E_{\rm so} = \epsilon_{\Lambda,j=l-1/2} -$

Table B.2: The parameter set PCY-S2 obtained by the omitting the tensor coupling. χ^2_{dof} is 0.86.

coupling const.	value	uncorr. error (%)	R
$\alpha_S^{(N\Lambda)}$	-4.2377×10^{-5} MeV^{-2}	3.6×10^{-1}	0.17
$\alpha_V^{(N\Lambda)}$	1.4268×10^{-5} MeV^{-2}	1.0×10^{0}	0.08
$\delta_S^{(N\Lambda)}$	1.2986×10^{-9} MeV^{-4}	8.3×10^{-1}	–
$\delta_V^{(N\Lambda)}$	-1.3850×10^{-9} MeV^{-4}	7.4×10^{-1}	–
$\alpha_T^{(N\Lambda)}$	0	–	–

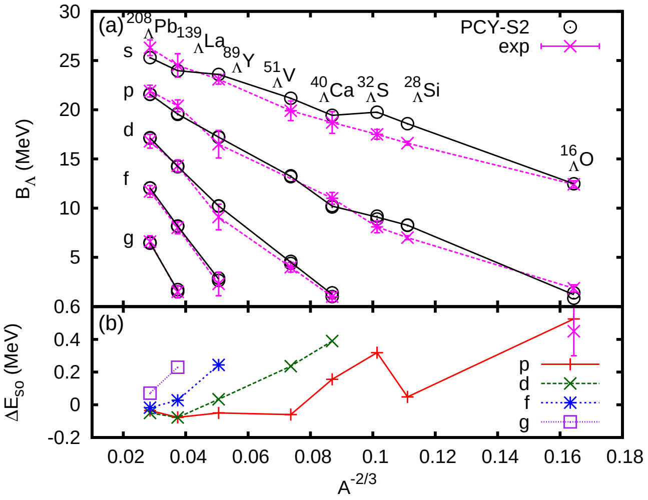

Figure B.2: Same as Fig. B.1, but with the parameter set PCY-S2.

Table B.3: The parameter set PCY-S3 obtained without fitting to the spin-orbit splitting in ${}^{16}_{\Lambda}$O. $\chi^2_{\rm dof}$ is 0.58.

coupling const.	value	uncorr. error (%)	R
$\alpha_S^{(N\Lambda)}$	-2.0197×10^{-4} MeV^{-2}	7.4×10^{-2}	0.79
$\alpha_V^{(N\Lambda)}$	1.6449×10^{-4} MeV^{-2}	9.1×10^{-2}	0.95
$\delta_S^{(N\Lambda)}$	2.3514×10^{-9} MeV^{-4}	4.5×10^{-1}	–
$\delta_V^{(N\Lambda)}$	-2.4993×10^{-9} MeV^{-4}	4.5×10^{-1}	–
$\alpha_T^{(N\Lambda)}$	-4.0820×10^{-9} MeV^{-3}	5.5×10^{2}	0.05

$\epsilon_{\Lambda,j=l+1/2}$, when the Λ particle is put in the lowest s-orbital. Those obtained with PCY-S1 and PCY-S2 are shown in Figs. B.1(b) and B.2(b), respectively. For both the parameter sets, although the absolute values of $\Delta E_{\rm so}$ are smaller by roughly a factor of 10 than those for nucleon, $\Delta E_{\rm so}$ alters its sign depending on the mass number. Notice that the spin-orbit splittings may be inverted depending on the strength of the tensor coupling term, as one can see in Fig. 2 of Ref. [163]. One may consider this inversion somewhat ill-favored. We mention, however, that at present there have been no experimental data which exclude the possible inversion of the spin-orbit splitting in the medium and heavier mass region.

If we exclude the spin-orbit splitting of the $1p$ state of Λ in ${}^{16}_{\Lambda}$O from the fitting, that is, if we fit only the energy centroid of each spin-orbit partner, we obtain Fig. B.3 for the lambda binding energies and the spin-orbit splittings. The parameters for this set, PCY-S3, are summarized in Table B.3. For this parameter set, the vector and scalar couplings of Λ to nucleon remain natural, but the tensor coupling is far smaller than the expected value in Eq. (B.1.26). Since there is no constraint on the value of spin-orbit splitting, this parameter set yields unacceptably large spin-orbit splitting, some of them stretching even beyond the experimental uncertainties (*i.e.,* the upper bounds for the spin-orbit splittings).

Lastly, we examine the role played by the derivative terms in the Lagrangian. In Ref. [171], it was pointed out that only one derivative term is well constrained by the bulk nuclear observables, *i.e.*, inclusion of a single derivative term is sufficient to obtain a good fit. Normally, the scalar derivative coupling constant δ_S is included rather than the vector one δ_V. Since the σ meson, which is simulated by the scalar couplings, is lighter ($m_\sigma \approx 500$ MeV) than the vector meson ω ($m_\omega \approx 780$ MeV), the finite-range effect of σ is expected to be more important than that of ω. Moreover, the σ meson is completely phenomenological, whereas the ω meson is less phenomenological in that it is considered to be the existing ω meson, thus it is more natural to choose δ_S than to choose δ_V as a free parameter. Finelli *et al.* have shown that their model with only a scalar derivative coupling indeed reproduces well the data for normal nuclei [172] and hypernuclei [173].

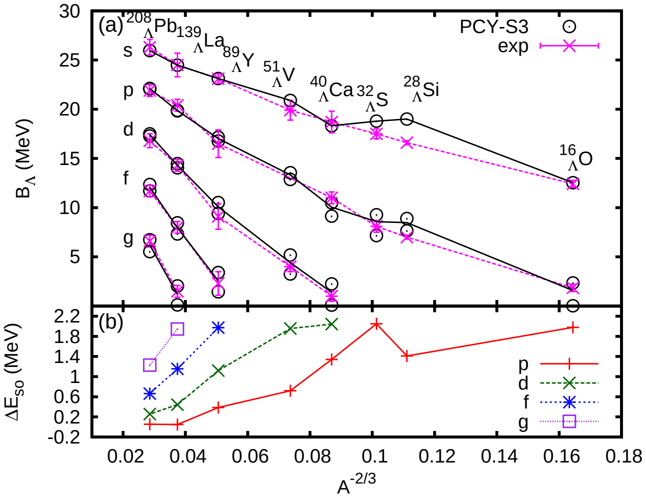

Figure B.3: Same as Fig. B.1, but with the parameter set PCY-S3.

Table B.4: The parameter set PCY-S4 obtained by setting the vector derivative coupling, $\delta_V^{(N\Lambda)}$, to be zero. $\chi^2_{\rm dof}$ is 0.93.

coupling const.	value	uncorr. error (%)	R
$\alpha_S^{(N\Lambda)}$	-1.8594×10^{-4} MeV^{-2}	8.7×10^{-2}	0.72
$\alpha_V^{(N\Lambda)}$	1.4981×10^{-4} MeV^{-2}	1.0×10^{-1}	0.87
$\delta_S^{(N\Lambda)}$	-1.9958×10^{-10} MeV^{-4}	6.1×10^{0}	–
$\delta_V^{(N\Lambda)}$	0	–	–
$\alpha_T^{(N\Lambda)}$	-5.5322×10^{-8} MeV^{-3}	1.7×10^{1}	0.71

For the same reason, Nikšić *et al.* [86] constructed their point coupling interaction with only the scalar derivative coupling. Following Refs. [86, 172, 173], we construct another parameter set PCY-S4 by omitting the vector derivative coupling, $\delta_V^{(N\Lambda)}$. The results are shown in Table B.4 and Fig. B.4. One observes that the quality of the fit is as good as the other parameter sets. The agreement with the quark model prediction is also well, and the inversion of the spin-orbit partner is not seen for this force. Furthermore, we find that the spin-orbit splittings in the medium-mass region are relatively larger than those in the light- and the heavy- mass regions. This is in a similar trend as in the results of the meson exchange interaction PK1-Y1 [169]. Therefore, PCY-S4 provides an alternative parameter set to PCY-S1, where the main difference between the two interactions is whether the spin-orbit splitting is normal (PCY-S4) or inverted (PCY-S1).

To summarize this appendix, we have constructed a new relativistic point coupling model to describe single-Λ hypernuclei in the mean-field approximation. This is a straight-

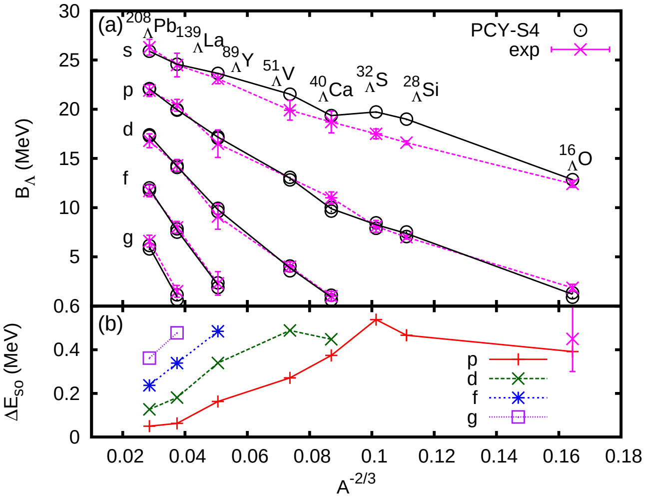

Figure B.4: Same as Fig. B.1, but with the parameter set PCY-S4.

forward extension of the relativistic point-coupling model for nucleons, To this end, we added effective contact N-Λ interactions, corresponding to the Λ-σ and Λ-ω couplings, to the model Lagrangian. In addition, we introduced the zero-range N-Λ tensor coupling as well to mimic the tensor coupling between Λ and ω meson, following the quark model suggestion.

We fitted the coupling constants in the strange sector to the experimental data of lambda binding energies. The four parameter sets, PCY-S1, PCY-S2, PCY-S3, and PCY-S4 were proposed, which well reproduce the experimental data through the whole mass region. The resulting spin-orbit splittings in PCY-S1, PCY-S2, and PCY-S4 are smaller than that of nucleon by roughly a factor of 10 in their absolute values, although PCY-S3 yields too large spin-orbit splittings. For PCY-S1 and PCY-S2 their signs are opposite to that of nucleon in some nuclei in the heavier region. On the other hand, for PCY-S4 obtained without taking into account the vector derivative term, the sign of the spin-orbit splitting is the same as that for nucleons.

We have confirmed that the tensor coupling, which is usually ignored in the N-N interaction, is quite important to reproduce the small spin-orbit splittings of Λ particle. Without the tensor coupling, the scalar and the vector couplings of Λ to nucleon are forced to be unnaturally weak (PCY-S2). The tensor coupling suppresses the spin-orbit splittings, keeping the scalar and the vector couplings consistent with the naive quark counting. Those good consistency with the quark model found in our interaction can be a useful guide in further extending the point coupling model to multi-Λ or Ξ hypernuclei.

The model can be an appropriate tool for investigation of Λ hypernuclei with relativistic calculations on 3D mesh. Further extensions of the point coupling model to multi-Λ and Ξ hypernuclei, and an introduction of explicit density dependences into the coupling constants are also interesting future works.

The N-Λ interaction based on the model introduced here has already been employed in a very recent work on ${}^{9}_{\Lambda}$Be nucleus [174] with the microscopic particle-rotor model.

Appendix C

Krylov Subspace Methods

In this appendix we illustrate, without proofs, the numerical algorithms of various iterative methods for inversion of sparse matrices, i.e. for solving sparse linear systems, which are employed in our inverse Hamiltonian method calculations. Those iterative methods are called *Krylov subspace methods*. A method of this kind is also used for solving the Poisson equation for the Coulomb part of a single-particle Hamiltonian (See Appendix F.2). For the mathematical details and rigorous proofs, see textbooks, e.g., by van der Vorst [152], Saad [133]. We will also compare the convergence properties of these iterative methods in inversions of Dirac and Hartree-Fock-Bogoliubov (HFB) Hamiltonians.

C.1 Iterative methods for sparse linear systems

To invert a matrix A is to solve a linear system

$$A\boldsymbol{x} = \boldsymbol{b}, \tag{C.1.1}$$

where $\boldsymbol{b}$ is a known vector while $\boldsymbol{x}$ is an unknown. In contrast to the so-called direct method, such as the Gauss elimination method, the inversion is performed by an iteration. Starting from an initial guess for the solution $\boldsymbol{x}_0$, it is iteratively improved so that the residual norm $|\boldsymbol{r}| = |\boldsymbol{b} - A\boldsymbol{x}|$ decreases. Iterative methods have the following features:

- One does not need to explicitly store the elements of a matrix A nor its inverse A^{-1}.
- Only matrix-to-vector operation and binary operations of two vectors (addition, and scalar product) are necessary.
- It can achieve quick convergence if the initial guess $\boldsymbol{x}_0$ well approximates the exact solution.
- Computer time can be saved by controlling the required accuracy.
- Compared to direct solver, numerical cost of iterative solver moderately increases as the size of the linear system becomes larger.

Thanks to the above features, the iterative method is suitable to, e.g, partial differential equations discretized on 3D spatial grid, which are given by large sparse linear system.

C.2 Numerical algorithms

Here we show the numerical algorithms of various iterative Krylov methods without proofs.

- **Conjugate gradient (CG) method**

```
$\boldsymbol{x}_0$ is an initial guess
$\boldsymbol{r}_0 = \boldsymbol{b} - A\boldsymbol{x}_0$
$\beta_{-1} = 0$
for $n = 0, 1, ...$ do
    $\boldsymbol{p}_n = \boldsymbol{r}_n + \beta_{n-1}\boldsymbol{p}_{n-1}$
    $\alpha_n = \frac{(\boldsymbol{r}_n, \boldsymbol{r}_n)}{(\boldsymbol{p}_n, A\boldsymbol{p}_n)}$
    $\boldsymbol{x}_{n+1} = \boldsymbol{x}_n + \alpha_n\boldsymbol{p}_n$
    $\boldsymbol{r}_{n+1} = \boldsymbol{r}_n - \alpha_n A\boldsymbol{p}_n$
    if $\|\boldsymbol{r}_{n+1}\| < \epsilon$ then
        quit
    end if
    $\beta_n = \frac{(\boldsymbol{r}_{n+1}, \boldsymbol{r}_{n+1})}{(\boldsymbol{r}_n, \boldsymbol{r}_n)}$
end for
```

- **Conjugate gradient normal residual (CGNR) method**

```
CG for an equivalent system $A^\dagger A\boldsymbol{x} = A^\dagger\boldsymbol{b}$
$\boldsymbol{x}_0$ is an initial guess
$\boldsymbol{r}^t_0 = \boldsymbol{b} - A\boldsymbol{x}_0$ is residual of the original equation
$\boldsymbol{r}_0 = A^\dagger(\boldsymbol{b} - A\boldsymbol{x}_0)$ is residual of the normal equation
$\beta_{-1} = 0$
for $n = 0, 1, ...$ do
    $\boldsymbol{p}_n = \boldsymbol{r}_n + \beta_{n-1}\boldsymbol{p}_{n-1}$
    $\alpha_n = \frac{(\boldsymbol{r}_n, \boldsymbol{r}_n)}{(A\boldsymbol{p}_n, A\boldsymbol{p}_n)}$
    $\boldsymbol{x}_{n+1} = \boldsymbol{x}_n + \alpha_n\boldsymbol{p}_n$
    $\boldsymbol{r}^t_{n+1} = \boldsymbol{r}^t_n - \alpha_n A\boldsymbol{p}_n$
    $\boldsymbol{r}_{n+1} = A^\dagger\boldsymbol{r}^t_{n+1}$
    if $\|\boldsymbol{r}^t_{n+1}\| < \epsilon$ then
        quit
    end if
    $\beta_n = \frac{(\boldsymbol{r}_{n+1}, \boldsymbol{r}_{n+1})}{(\boldsymbol{r}_n, \boldsymbol{r}_n)}$
end for
```

- **Biconjugate gradient (BiCG) method**

```
$\boldsymbol{x}_0$ is an initial guess
$\boldsymbol{r}_0 = \boldsymbol{b} - A\boldsymbol{x}_0$
$\boldsymbol{r}_0^*$ is an arbitrary vector such that $(\boldsymbol{r}_0^*, \boldsymbol{r}_0) \neq 0$
$\beta_{-1} = 0$
for $n = 0, 1, ...$ do
    $\boldsymbol{p}_n = \boldsymbol{r}_n + \beta_{n-1}\boldsymbol{p}_{n-1}$
    $\boldsymbol{p}_n^* = \boldsymbol{r}_n^* + \bar{\beta}_{n-1}\boldsymbol{p}_{n-1}^*$
    $\alpha_n = \dfrac{(\boldsymbol{r}_n^*, \boldsymbol{r}_n)}{(\boldsymbol{p}_n^*, A\boldsymbol{p}_n)}$
    $\boldsymbol{x}_{n+1} = \boldsymbol{x}_n + \alpha_n \boldsymbol{p}_n$
    $\boldsymbol{r}_{n+1} = \boldsymbol{r}_n - \alpha_n A\boldsymbol{p}_n$
    if $\|\boldsymbol{r}_{n+1}\| < \epsilon$ then
        quit
    end if
    $\boldsymbol{r}_{n+1}^* = \boldsymbol{r}_n^* - \bar{\alpha}_n A^\dagger \boldsymbol{p}_n^*$
    $\beta_n = \dfrac{(\boldsymbol{r}_{n+1}^*, \boldsymbol{r}_{n+1})}{(\boldsymbol{r}_n^*, \boldsymbol{r}_n)}$
end for
```

- **Conjugate gradient squared (CGS) method**

```
$\boldsymbol{x}_0$ is an initial guess
$\boldsymbol{r}_0 = \boldsymbol{b} - A\boldsymbol{x}_0$
$\boldsymbol{r}_0^*$ is an arbitrary vector such that $(\boldsymbol{r}_0^*, \boldsymbol{r}_0) \neq 0$
set $\beta_{-1} = 0$
for $n = 0, 1, ...$ do
    $\boldsymbol{p}_n = \boldsymbol{r}_n + \beta_{n-1}\boldsymbol{z}_{n-1}$
    $\boldsymbol{u}_n = \boldsymbol{p}_n + \beta_{n-1}(\boldsymbol{z}_{n-1} + \beta_{n-1}\boldsymbol{u}_{n-1})$
    $\alpha_n = \dfrac{(\boldsymbol{r}_0^*, \boldsymbol{r}_n)}{(\boldsymbol{r}_0^*, A\boldsymbol{u}_n)}$
    $\boldsymbol{z}_n = \boldsymbol{p}_n - \alpha_n A\boldsymbol{u}_n$
    $\boldsymbol{x}_{n+1} = \boldsymbol{x}_n + \alpha_n(\boldsymbol{p}_n + \boldsymbol{z}_n)$
    $\boldsymbol{r}_{n+1} = \boldsymbol{r}_n - \alpha_n A(\boldsymbol{p}_n + \boldsymbol{z}_n)$
    if $\|\boldsymbol{r}_{n+1}\| < \epsilon$ then
        quit
    end if
    $\beta_n = \dfrac{(\boldsymbol{r}_0^*, \boldsymbol{r}_{n+1})}{(\boldsymbol{r}_0^*, \boldsymbol{r}_n)}$
end for
```

- **BiCG stabilized (BiCGSTAB) method**

```
$\boldsymbol{x}_0$ is an initial guess
```

```
$\boldsymbol{r}_0 = \boldsymbol{b} - A\boldsymbol{x}_0$
$\boldsymbol{r}_0^*$ is an arbitrary vector such that $(\boldsymbol{r}_0^*, \boldsymbol{r}_0) \neq 0$
set $\beta_{-1} = 0$
for $n = 0, 1, ...$ do
    $\boldsymbol{p}_n = \boldsymbol{r}_n + \beta_{n-1}(\boldsymbol{p}_{n-1} - \zeta_{n-1} A\boldsymbol{p}_{n-1})$
    $\alpha_n = \dfrac{(\boldsymbol{r}_0^*, \boldsymbol{r}_n)}{(\boldsymbol{r}_0^*, A\boldsymbol{p}_n)}$
    $\boldsymbol{t}_n = \boldsymbol{r}_n - \alpha_n A\boldsymbol{p}_n$
    $\zeta_n = \dfrac{(A\boldsymbol{t}_n, \boldsymbol{t}_n)}{(A\boldsymbol{t}_n, A\boldsymbol{t}_n)}$
    $\boldsymbol{x}_{n+1} = \boldsymbol{x}_n + \alpha_n \boldsymbol{p}_n + \zeta_n \boldsymbol{t}_n$
    $\boldsymbol{r}_{n+1} = \boldsymbol{t}_n - \zeta_n A\boldsymbol{t}_n$
    if $\|\boldsymbol{r}_{n+1}\| < \epsilon$ then
        quit
    end if
    $\beta_n = \dfrac{\alpha_n}{\zeta_n} \dfrac{(\boldsymbol{r}_0^*, \boldsymbol{r}_{n+1})}{(\boldsymbol{r}_0^*, \boldsymbol{r}_n)}$
end for
```

- **Generalized product type conjugate gradient (GPBiCG) method**

```
$\boldsymbol{x}_0$ is an initial guess
$\boldsymbol{r}_0 = \boldsymbol{b} - A\boldsymbol{x}_0$
$\boldsymbol{r}_0^*$ is an arbitrary vector such that $(\boldsymbol{r}_0^*, \boldsymbol{r}_0) \neq 0$
$\beta_{-1} = 0$
$\boldsymbol{t}_{-1} = \boldsymbol{0}$
$\boldsymbol{w}_{-1} = \boldsymbol{0}$
for $n = 0, 1, ...$ do
    $\boldsymbol{p}_n = \boldsymbol{r}_n + \beta_{n-1}(\boldsymbol{p}_{n-1} - \boldsymbol{u}_{n-1})$
    $\alpha_n = \dfrac{(\boldsymbol{r}_0^*, \boldsymbol{r}_n)}{(\boldsymbol{r}_0^*, A\boldsymbol{p}_n)}$
    $\boldsymbol{y}_n = \boldsymbol{t}_{n-1} - \boldsymbol{r}_n - \alpha_n \boldsymbol{w}_{n-1} + \alpha_n A\boldsymbol{p}_n$
    $\boldsymbol{t}_n = \boldsymbol{r}_n - \alpha_n A\boldsymbol{p}_n$
    $\zeta_n = \dfrac{(\boldsymbol{y}_n, \boldsymbol{y}_n)(A\boldsymbol{t}_n, \boldsymbol{t}_n) - (\boldsymbol{y}_n, \boldsymbol{t}_n)(A\boldsymbol{t}_n, \boldsymbol{y}_n)}{(\boldsymbol{y}_n, \boldsymbol{y}_n)(A\boldsymbol{t}_n, A\boldsymbol{t}_n) - (\boldsymbol{y}_n, A\boldsymbol{t}_n)(A\boldsymbol{t}_n, \boldsymbol{y}_n)}$
    $\eta_n = \dfrac{(\boldsymbol{y}_n, \boldsymbol{t}_n)(A\boldsymbol{t}_n, A\boldsymbol{t}_n) - (\boldsymbol{y}_n, A\boldsymbol{t}_n)(A\boldsymbol{t}_n, \boldsymbol{t}_n)}{(\boldsymbol{y}_n, \boldsymbol{y}_n)(A\boldsymbol{t}_n, A\boldsymbol{t}_n) - (\boldsymbol{y}_n, A\boldsymbol{t}_n)(A\boldsymbol{t}_n, \boldsymbol{y}_n)}$
    $\boldsymbol{u}_n = \zeta_n A\boldsymbol{p}_n + \eta_n(\boldsymbol{t}_{n-1} - \boldsymbol{r}_n + \beta_{n-1}\boldsymbol{u}_{n-1})$
    $\boldsymbol{z}_n = \zeta_n \boldsymbol{r}_n + \eta_n \boldsymbol{z}_{n-1} - \alpha_n \boldsymbol{u}_n$
    $\boldsymbol{x}_{n+1} = \boldsymbol{x}_n + \alpha_n \boldsymbol{p}_n + \boldsymbol{z}_n$
    $\boldsymbol{r}_{n+1} = \boldsymbol{t}_n - \eta_n \boldsymbol{y}_n - \zeta_n A\boldsymbol{t}_n$
    if $\|\boldsymbol{r}_{n+1}\| < \epsilon$ then
        quit
    end if
```

```
    $\beta_n = \frac{\alpha_n}{\zeta_n} \frac{(\boldsymbol{r}_0^*, \boldsymbol{r}_{n+1})}{(\boldsymbol{r}_0^*, \boldsymbol{r}_n)}$
    $\boldsymbol{w}_n = A\boldsymbol{t}_n + \beta_n A\boldsymbol{p}_n$
end for
```

- **Conjugate residual (CR) method**

```
$\boldsymbol{x}_0$ is an initial guess
$\boldsymbol{r}_0 = \boldsymbol{b} - A\boldsymbol{x}_0$
Compute $A\boldsymbol{r}_0$
set $\beta_{-1} = 0$
for $n = 0, 1, ...$ do
    $\boldsymbol{p}_n = \boldsymbol{r}_n + \beta_{n-1}\boldsymbol{p}_{n-1}$
    $(A\boldsymbol{p}_n = A\boldsymbol{r}_n + \beta_{n-1}A\boldsymbol{p}_{n-1})$
    $\alpha_n = \frac{(\boldsymbol{r}_n, A\boldsymbol{r}_n)}{(A^\dagger \boldsymbol{p}_n, A\boldsymbol{p}_n)}$
    $\boldsymbol{x}_{n+1} = \boldsymbol{x}_n + \alpha_n \boldsymbol{p}_n$
    $\boldsymbol{r}_{n+1} = \boldsymbol{r}_n - \alpha_n A\boldsymbol{p}_n$
    if $\|\boldsymbol{r}_{n+1}\| < \epsilon$ then
        quit
    end if
    $\beta_n = \frac{(\boldsymbol{r}_{n+1}, A\boldsymbol{r}_{n+1})}{(\boldsymbol{r}_n, A\boldsymbol{r}_n)}$
end for
```

- **Biconjugate residual (BiCR) method**

```
$\boldsymbol{x}_0$ is an initial guess
$\boldsymbol{r}_0 = \boldsymbol{b} - A\boldsymbol{x}_0$
$\boldsymbol{r}_0^*$ is an arbitrary vector such that $(\boldsymbol{r}_0^*, \boldsymbol{r}_0) \neq 0$
Compute $A\boldsymbol{r}_0$
set $\beta_{-1} = 0$
for $n = 0, 1, ...$ do
    $\boldsymbol{p}_n = \boldsymbol{r}_n + \beta_{n-1}\boldsymbol{p}_{n-1}$
    $\boldsymbol{p}_n^* = \boldsymbol{r}_n^* + \bar{\beta}_{n-1}\boldsymbol{p}_{n-1}^*$
    $(A\boldsymbol{p}_n = A\boldsymbol{r}_n + \beta_{n-1}A\boldsymbol{p}_{n-1})$
    $\alpha_n = \frac{(\boldsymbol{r}_n^*, A\boldsymbol{r}_n)}{(A^\dagger \boldsymbol{p}_n^*, A\boldsymbol{p}_n)}$
    $\boldsymbol{x}_{n+1} = \boldsymbol{x}_n + \alpha_n \boldsymbol{p}_n$
    $\boldsymbol{r}_{n+1} = \boldsymbol{r}_n - \alpha_n A\boldsymbol{p}_n$
    if $\|\boldsymbol{r}_{n+1}\| < \epsilon$ then
        quit
    end if
    $\boldsymbol{r}_{n+1}^* = \boldsymbol{r}_n^* - \bar{\alpha}_n A^\dagger \boldsymbol{p}_n^*$
```

```
    $\beta_n = \dfrac{(\boldsymbol{r}^*_{n+1}, A\boldsymbol{r}_{n+1})}{(\boldsymbol{r}^*_n, A\boldsymbol{r}_n)}$
end for
```

- **Conjugate residual squared (CRS) method**

```
$\boldsymbol{x}_0$ is an initial guess
$\boldsymbol{r}_0 = \boldsymbol{b} - A\boldsymbol{x}_0$
$\boldsymbol{r}^*_0$ is an arbitrary vector such that $(\boldsymbol{r}^*_0, \boldsymbol{r}_0) \neq 0$
set $\beta_{-1} = 0$
for $n = 0, 1, ...$ do
    $\boldsymbol{e}_n = \boldsymbol{r}_n + \beta_{n-1}\boldsymbol{h}_{n-1}$
    $\boldsymbol{p}_n = \boldsymbol{e}_n + \beta_{n-1}(\boldsymbol{h}_{n-1} + \beta_{n-1}\boldsymbol{p}_{n-1})$
    $\alpha_n = \dfrac{(A^\dagger \boldsymbol{r}^*_0, \boldsymbol{r}_n)}{(A^\dagger \boldsymbol{r}^*_0, A\boldsymbol{p}_n)}$
    $\boldsymbol{h}_n = \boldsymbol{e}_n - \alpha_n A\boldsymbol{p}_n$
    $\boldsymbol{x}_{n+1} = \boldsymbol{x}_n + \alpha_n(\boldsymbol{e}_n + \boldsymbol{h}_n)$
    $\boldsymbol{r}_{n+1} = \boldsymbol{r}_n - \alpha_n A(\boldsymbol{e}_n + \boldsymbol{h}_n)$
    if $\|\boldsymbol{r}_{n+1}\| < \epsilon$ then
        quit
    end if
    $\beta_n = \dfrac{(A^\dagger \boldsymbol{r}^*_0, \boldsymbol{r}_{n+1})}{(A^\dagger \boldsymbol{r}^*_0, \boldsymbol{r}_n)}$
end for
```

- **BiCR stabilized (BiCRSTAB) method**

```
$\boldsymbol{x}_0$ is an initial guess
$\boldsymbol{r}_0 = \boldsymbol{b} - A\boldsymbol{x}_0$
set $\beta_{-1} = 0$
for $n = 0, 1, ...$ do
    $\boldsymbol{p}_n = \boldsymbol{r}_n + \beta_{n-1}(\boldsymbol{p}_{n-1} - \zeta_{n-1}A\boldsymbol{p}_{n-1})$
    $\alpha_n = \dfrac{(A^\dagger \boldsymbol{r}_0, \boldsymbol{r}_n)}{(A^\dagger \boldsymbol{r}_0, A\boldsymbol{p}_n)}$
    $\boldsymbol{t}_n = \boldsymbol{r}_n - \alpha_n A\boldsymbol{p}_n$
    $\zeta_n = \dfrac{(A\boldsymbol{t}_n, \boldsymbol{t}_n)}{(A\boldsymbol{t}_n, A\boldsymbol{t}_n)}$
    $\boldsymbol{x}_{n+1} = \boldsymbol{x}_n + \alpha_n\boldsymbol{p}_n + \zeta_n\boldsymbol{t}_n$
    $\boldsymbol{r}_{n+1} = \boldsymbol{t}_n - \zeta_n A\boldsymbol{t}_n$
    if $\|\boldsymbol{r}_{n+1}\| < \epsilon$ then
        quit
    end if
    $\beta_n = \dfrac{\alpha_n}{\zeta_n}\dfrac{(A^\dagger \boldsymbol{r}_0, \boldsymbol{r}_{n+1})}{(A^\dagger \boldsymbol{r}_0, \boldsymbol{r}_n)}$
```

```
**end for**
```

- **Generalized product type BiCR (GPBiCR) method**

```
$\boldsymbol{x}_0$ is an initial guess
$\boldsymbol{r}_0 = \boldsymbol{b} - A\boldsymbol{x}$
compute and store $A^\dagger \boldsymbol{r}_0$
set
$\beta_{-1} = 0$
$\boldsymbol{t}_{-1} = \mathbf{0}$
$\boldsymbol{w}_{-1} = \mathbf{0}$
**for** $n = 0, 1, ...$ **do**
    $\boldsymbol{p}_n = \boldsymbol{r}_n + \beta_{n-1}(\boldsymbol{p}_{n-1} - \boldsymbol{u}_{n-1})$
    $\alpha_n = \dfrac{(A^\dagger \boldsymbol{r}_0, \boldsymbol{r}_n)}{(A^\dagger \boldsymbol{r}_0, A\boldsymbol{p}_n)}$
    $\boldsymbol{y}_n = \boldsymbol{t}_{n-1} - \boldsymbol{r}_n - \alpha_n \boldsymbol{w}_{n-1} + \alpha_n A\boldsymbol{p}_n$
    $\boldsymbol{t}_n = \boldsymbol{r}_n - \alpha_n A\boldsymbol{p}_n$
    $\zeta_n = \dfrac{(\boldsymbol{y}_n, \boldsymbol{y}_n)(A\boldsymbol{t}_n, \boldsymbol{t}_n) - (\boldsymbol{y}_n, \boldsymbol{t}_n)(A\boldsymbol{t}_n, \boldsymbol{y}_n)}{(\boldsymbol{y}_n, \boldsymbol{y}_n)(A\boldsymbol{t}_n, A\boldsymbol{t}_n) - (\boldsymbol{y}_n, A\boldsymbol{t}_n)(A\boldsymbol{t}_n, \boldsymbol{y}_n)}$
    $\eta_n = \dfrac{(\boldsymbol{y}_n, \boldsymbol{t}_n)(A\boldsymbol{t}_n, A\boldsymbol{t}_n) - (\boldsymbol{y}_n, A\boldsymbol{t}_n)(A\boldsymbol{t}_n, \boldsymbol{t}_n)}{(\boldsymbol{y}_n, \boldsymbol{y}_n)(A\boldsymbol{t}_n, A\boldsymbol{t}_n) - (\boldsymbol{y}_n, A\boldsymbol{t}_n)(A\boldsymbol{t}_n, \boldsymbol{y}_n)}$
    $\boldsymbol{u}_n = \zeta_n A\boldsymbol{p}_n + \eta_n(\boldsymbol{t}_{n-1} - \boldsymbol{r}_n + \beta_{n-1}\boldsymbol{u}_{n-1})$
    $\boldsymbol{z}_n = \zeta_n \boldsymbol{r}_n + \eta_n \boldsymbol{z}_{n-1} - \alpha_n \boldsymbol{u}_n$
    $\boldsymbol{x}_{n+1} = \boldsymbol{x}_n + \alpha_n \boldsymbol{p}_n + \boldsymbol{z}_n$
    $\boldsymbol{r}_{n+1} = \boldsymbol{t}_n - \eta_n \boldsymbol{y}_n - \zeta_n A\boldsymbol{t}_n$
    **if** $\|\boldsymbol{r}_{n+1}\| < \epsilon$ **then**
        quit
    **end if**
    $\beta_n = \dfrac{\alpha_n}{\zeta_n} \dfrac{(A^\dagger \boldsymbol{r}_0, \boldsymbol{r}_{n+1})}{(A^\dagger \boldsymbol{r}_0, \boldsymbol{r}_n)}$
    $\boldsymbol{w}_n = A\boldsymbol{t}_n + \beta_n A\boldsymbol{p}_n$
**end for**
```

C.3 Convergence properties in inversions of Dirac and HFB Hamiltonians

In this section we compare the numerical performance of various iterative Krylov methods in inversions of a Dirac and a HFB Hamiltonians in the 3D coordinate space representation.

In the inverse Hamiltonian method, the wave function is evolved as

$$|\psi^{(n+1)}\rangle \propto \left(1 + \frac{\Delta T}{\hat{H} - W}\right) |\psi^{(n)}\rangle, \tag{C.3.1}$$

where $\hat{H}$ is Hamiltonian of the system. In this evolution one needs to know

$$|\phi\rangle = (\hat{H} - W)^{-1}|\psi^{(n)}\rangle, \tag{C.3.2}$$

where $\psi^{(n)}$ is a known wave function while a ϕ is an unknown function. That is, one needs to solve the linear equation

$$(\hat{H} - W)\phi = \psi^{(n)}. \tag{C.3.3}$$

This linear equation is solved with the Krylov subspace methods. Since a Hamiltonian in the coordinate space representation is sparse as long as the potential is local, the iterative methods are suitable to solve this problem.

Here we solve Eq. (C.3.3) with a Dirac and a HFB Hamiltonian. The potentials are fixed to be the spherical Woods-Saxon types which have been already given in Ch. 6 and Appendix A. The Dirac Hamiltonian is given as

$$\hat{H}_{\mathrm{Dirac}} = \begin{pmatrix} U(r) & \boldsymbol{\sigma}\cdot\boldsymbol{p} \\ \boldsymbol{\sigma}\cdot\boldsymbol{p} & W(r) - 2m \end{pmatrix}, \tag{C.3.4}$$

where

$$\begin{aligned} U(r) &= \frac{U_0}{1 + e^{(r-R_U)/a_U}}, \text{ and} \\ W(r) &= \frac{W_0}{1 + e^{(r-R_W)/a_W}}. \end{aligned} \tag{C.3.5}$$

The right-hand-side vector ψ in Eq. (C.3.3) is given with an appropriate normalizing constant N as

$$\psi = N \begin{pmatrix} e^{-r^2/b^2} \\ 0 \\ 0 \\ 0 \end{pmatrix}. \tag{C.3.6}$$

The shift parameter W in the case of Dirac is set to be $W = U_0$.

The HFB Hamiltonian is given by

$$\hat{H}_{\mathrm{HFB}} = \begin{pmatrix} -\hbar^2\boldsymbol{\nabla}^2/2m + v(r) - \lambda & \Delta(r) \\ \Delta(r) & \hbar^2\boldsymbol{\nabla}^2/2m - v(r) + \lambda \end{pmatrix}, \tag{C.3.7}$$

where

$$v(r) = v_0 f(r) + v_{\ell s}\frac{1}{r}\frac{df}{dr}\boldsymbol{\ell}\cdot\boldsymbol{s}, \tag{C.3.8}$$

$$\Delta(r) = \Delta_0 f(r), \tag{C.3.9}$$

$$f(r) = \frac{1}{1 + e^{(r-R_0)/a}}. \tag{C.3.10}$$

The right-hand-side vector ψ in Eq. (C.3.3) is given with an appropriate normalizing constant N as

$$\psi = N \begin{pmatrix} e^{-r^2/b^2} \\ 0 \\ e^{-r^2/b^2} \\ 0 \end{pmatrix}. \tag{C.3.11}$$

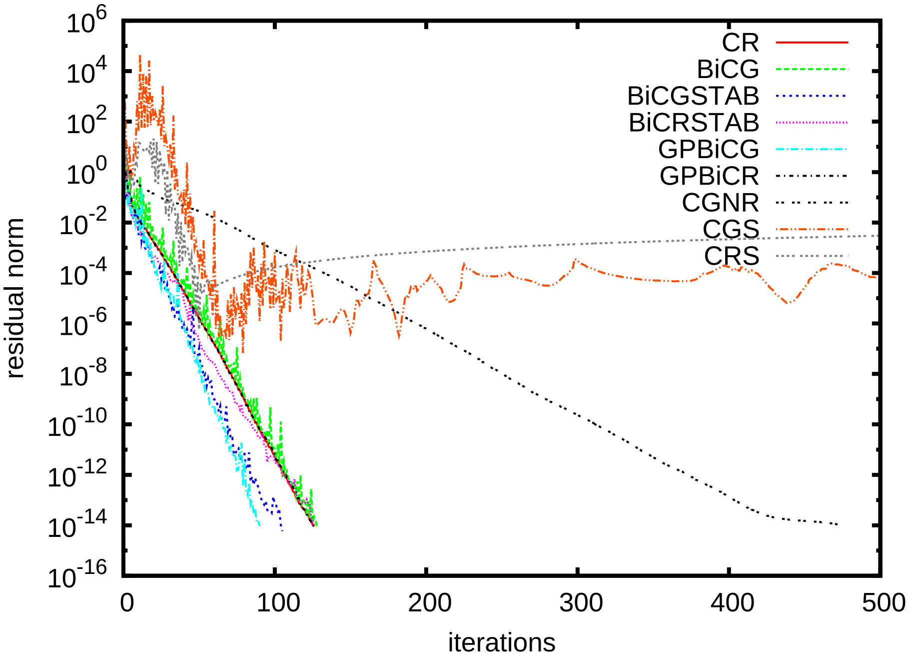

Figure C.1: Convergence of the residual norm in inversion of a Dirac Hamiltonian. Initial guess for the solution is set to be a zero vector.

The shift parameter W in the case of HFB is set to be $W = 0.1$ MeV.

Both of the Hamiltonians are discretized on 24^3 mesh points with the mesh size $a = 0.8$ fm. The initial guess ϕ_0 for a solution of Eq. (C.3.3) is set to be a zero vector for all the calculations performed here.

In Fig. C.1 convergence of the residual norm with the Dirac Hamiltonian as a function of the number of Krylov iterations for the various iterative solvers are shown. The residual norm at n-th step is defined as

$$\text{(residual norm)} = \left\{ \int d^3r [(\hat{H} - W)\phi_n(\boldsymbol{r}) - \psi(\boldsymbol{r})]^2 \right\}^{1/2}, \qquad \text{(C.3.12)}$$

where ϕ_n is the iterative solution for Eq. (C.3.3) at the n-th step. If the residual norm is exactly zero, ϕ_n is the exact solution. One can see in Fig. C.1 that the speed of convergence is largely different among the different iterative methods. CR, BiCG, BiCGSTAB, BiCRSTAB, GPBiCG, and GPBiCR give a relatively quick convergence. Among these CR, GPBiCR, and GPBiCR smoothly converge. (Note that “quick” means a quick convergence as a function of the number of iteration, and does not always mean that the computer time is shorter.) With CGNR, the convergence is much slower although the residual smoothly converges. The CGS and CRS lead to a divergence.

Next, in Fig. C.2 we show convergence of the residual norm with the HFB Hamiltonian. Notice the logarithmic scale in the horizontal axis, the number of iteration. As compared

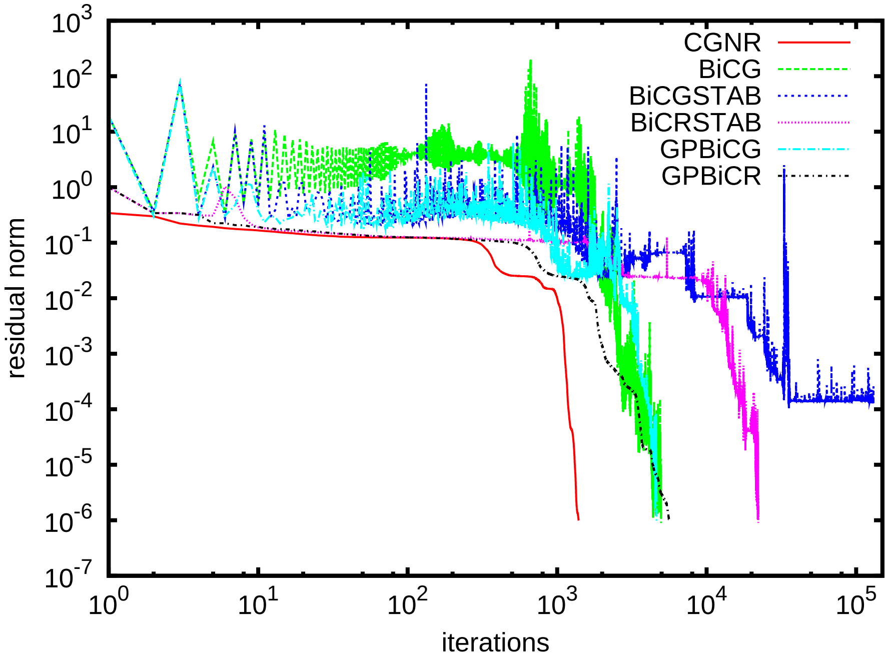

Figure C.2: Convergence of the residual norm in inversion of an HFB Hamiltonian. Initial guess for the solution is set to be a zero vector.

to the previous case of a Dirac Hamiltonian, the convergence is much slower in an inversion of an HFB Hamiltonian. The reason is attributed to the property of the eigenvalue spectrum of the inverted matrix [133,152]. Since a spectrum of HFB Hamiltonian is denser than that of a Dirac Hamiltonian, which has a large gap between positive and negative spectrum, convergence of iterative solver are expected to be slower [133,152]. Among the methods examined here, CGNR gives the best performance for the HFB Hamiltonian, but it is still much more time consuming than the inversion of a Dirac Hamiltonian. Although we had shown in Appendix A that our inverse Hamiltonian method is also applicable to HFB equation, this slow convergence in inversion of HFB Hamiltonian makes it practically difficult to apply the inverse Hamiltonian method to 3D HFB calculations.

As seen in the two cases examined in this appendix, an iterative method which provides an efficient convergence for a certain problem does not always perform well for another problem. This lack of robustness is a widely recognized drawback of the iterative solver compared to the direct solver [133, 152]. Unfortunately, there is no general way to determine an appropriate solver for a given problem. One needs to find an efficient iterative method by trial and error.

Appendix D

Finite Difference Formulas

In numerical calculations in the coordinate space representation, one knows the values of the wave functions and the fields only at given mesh points. Thus one needs to evaluate the derivatives of the functions by some numerical method. A simple way is the finite difference, which evaluates a derivative at a certain mesh point by taking a linear combinations of the values of the function on several mesh points nearby. In this appendix we tabulate the coefficients of finite difference formulas for the derivatives of several different order and for several different levels of accuracy. Here we assume a uniform lattice.

Suppose we need a derivative of a function $f(x)$, whose values are known only at discrete points $x_i = ih$. i is an integer and h is the mesh size. We denote the value of a function at i-th mesh point, $f(x_i)$, by f_i. $(2N+1)$-point central finite difference formula for nth derivative of $f(x)$ at $x = ih$ is given by

$$h^n \left(\frac{d^n f}{dx^n} \right)_i = \sum_{j=-N}^{N} c_j^n f_{i+j}, \tag{D.0.1}$$

where N is a positive integer. The coefficients c_j^n can be computed by using the following sequence of equations.

$$\begin{aligned}
f_{i\pm1} &= f_i \pm h f_i' + \tfrac{1}{2} h^2 f_i'' \pm \tfrac{1}{3!} h^3 f_i''' + \tfrac{1}{4!} h^4 f_i^{(4)} \pm \tfrac{1}{5!} h^5 f_i^{(5)} + \cdots \\
f_{i\pm2} &= f_i \pm 2h f_i' + \tfrac{2^2}{2} h^2 f_i'' \pm \tfrac{2^3}{3!} h^3 f_i''' + \tfrac{2^4}{4!} h^4 f_i^{(4)} \pm \tfrac{2^5}{5!} h^5 f_i^{(5)} + \cdots \\
f_{i\pm3} &= f_i \pm 3h f_i' + \tfrac{3^2}{2} h^2 f_i'' \pm \tfrac{3^3}{3!} h^3 f_i''' + \tfrac{3^4}{4!} h^4 f_i^{(4)} \pm \tfrac{3^5}{5!} h^5 f_i^{(5)} + \cdots \\
f_{i\pm4} &= f_i \pm 4h f_i' + \tfrac{4^2}{2} h^2 f_i'' \pm \tfrac{4^3}{3!} h^3 f_i''' + \tfrac{4^4}{4!} h^4 f_i^{(4)} \pm \tfrac{4^5}{5!} h^5 f_i^{(5)} + \cdots \\
&\vdots
\end{aligned} \tag{D.0.2}$$

Let us see a simple example. The three-point formula for the second derivative is given by

$$f_i'' = \frac{f_{i-1} - 2f_i + f_{i+1}}{h^2}. \tag{D.0.3}$$

This is derived by picking up the leading three terms in the equations in the first line in

Eq. (D.0.2),

$$\begin{aligned} f_{i+1} &= f_i + hf'_i + \tfrac{1}{2}h^2 f''_i + \mathcal{O}(h^3) \\ f_{i-1} &= f_i - hf'_i + \tfrac{1}{2}h^2 f''_i + \mathcal{O}(h^3), \end{aligned} \tag{D.0.4}$$

and taking the sum of these two to eliminate f'. This formula has an error of order h^3. Any other formula can be derived by choosing a proper set of equations from Eq. (D.0.2) up to the desired accuracy and eliminating the unwanted terms. In Table D.1 we summarize the coefficients of various derivatives. One can also obtain the coefficients for the *off-central* $(2N+1)$-point difference formulae, which makes reference to the mesh points asymmetrically with respect to the point where a derivative is evaluated:

$$h^n \left(\frac{d^n f}{dx^n} \right)_i = \sum_{j=-N_1}^{N_2} c_j^n f_{i+j}, \tag{D.0.5}$$

where $0 \leq N_{1,2} \leq N$ and $N_1 + N_2 = N$. Those are summarized in Table D.2.

Here we did not mention to even-points formulae, e. g. forward/backward, four-point or six-point etc., which may be of less use due to their non-hermiticity. They can be easily obtained in the same way as odd-points formulae. Many variations of difference formulae which is more efficient and accurate are proposed in the literature. See Refs. [175–179] and the references therein.

Table D.1: Coefficients c_j^n for $j \geq 0$ in Eq. (D.0.1) of central $(2N+1)$-point formulas for nth derivatives. The coefficients for $j < 0$ are given by $c_{-|j|}^n = (-)^n c_{|j|}^n$.

n	$2N+1$	Error	j								
			0	+1	+2	+3	+4	+5	+6	+7	+8
1	3	$\mathcal{O}(h^3)$	0	$\frac{1}{2}$	0	0	0	0	0	0	0
	5	$\mathcal{O}(h^5)$	0	$\frac{2}{3}$	$-\frac{1}{12}$	0	0	0	0	0	0
	7	$\mathcal{O}(h^7)$	0	$\frac{3}{4}$	$-\frac{3}{20}$	$\frac{1}{60}$	0	0	0	0	0
	9	$\mathcal{O}(h^9)$	0	$\frac{4}{5}$	$-\frac{1}{5}$	$\frac{4}{105}$	$-\frac{1}{280}$	0	0	0	0
	11	$\mathcal{O}(h^{11})$	0	$\frac{5}{6}$	$-\frac{5}{21}$	$\frac{5}{84}$	$-\frac{5}{504}$	$\frac{1}{1260}$	0	0	0
	13	$\mathcal{O}(h^{13})$	0	$\frac{6}{7}$	$-\frac{15}{56}$	$\frac{5}{63}$	$-\frac{1}{56}$	$\frac{1}{385}$	$-\frac{1}{5544}$	0	0
	15	$\mathcal{O}(h^{15})$	0	$\frac{7}{8}$	$-\frac{7}{24}$	$\frac{7}{72}$	$-\frac{7}{264}$	$\frac{7}{1320}$	$-\frac{7}{10296}$	$\frac{1}{24024}$	0
	17	$\mathcal{O}(h^{17})$	0	$\frac{8}{9}$	$-\frac{14}{45}$	$\frac{56}{495}$	$-\frac{7}{198}$	$\frac{56}{6435}$	$-\frac{2}{1287}$	$\frac{8}{45045}$	$-\frac{1}{102960}$
2	3	$\mathcal{O}(h^3)$	-2	1	0	0	0	0	0	0	0
	5	$\mathcal{O}(h^5)$	$-\frac{5}{2}$	$\frac{4}{3}$	$-\frac{1}{12}$	0	0	0	0	0	0
	11	$\mathcal{O}(h^{11})$	$-\frac{5269}{1800}$	$\frac{5}{3}$	$-\frac{5}{21}$	$\frac{5}{126}$	$-\frac{5}{1008}$	$\frac{1}{3150}$	0	0	0
4	5	$\mathcal{O}(h^5)$	6	-4	1	0	0	0	0	0	0
6	7	$\mathcal{O}(h^7)$	-20	15	-6	1	0	0	0	0	0
8	9	$\mathcal{O}(h^9)$	70	-56	28	-8	1	0	0	0	0
10	11	$\mathcal{O}(h^{11})$	-252	210	-120	45	-10	1	0	0	0

Table D.2: Off-central $(2N+1)$-point formulae for nth derivative.

n	$2N+1$	Error	j										
			0	+1	+2	+3	+4	+5	+6	+7	+8	+9	+10
1	3	$\mathcal{O}(h^3)$	$-\frac{3}{2}$	2	$-\frac{1}{2}$	0	0	0	0	0	0	0	0
	4	$\mathcal{O}(h^4)$	$-\frac{11}{6}$	3	$-\frac{3}{2}$	$\frac{1}{3}$	0	0	0	0	0	0	0
	5	$\mathcal{O}(h^5)$	$-\frac{25}{12}$	4	-3	$\frac{4}{3}$	$-\frac{1}{4}$	0	0	0	0	0	0
	6	$\mathcal{O}(h^6)$	$-\frac{137}{60}$	5	-5	$\frac{10}{3}$	$-\frac{5}{4}$	$\frac{1}{5}$	0	0	0	0	0
	7	$\mathcal{O}(h^7)$	$-\frac{49}{20}$	6	$-\frac{15}{2}$	$\frac{20}{3}$	$-\frac{15}{4}$	$\frac{6}{5}$	$-\frac{1}{6}$	0	0	0	0
	9	$\mathcal{O}(h^9)$	$-\frac{761}{280}$	8	-14	$\frac{56}{3}$	$-\frac{35}{2}$	$\frac{56}{5}$	$-\frac{14}{3}$	$\frac{8}{7}$	$-\frac{1}{8}$	0	0
	11	$\mathcal{O}(h^{11})$	$-\frac{7381}{2520}$	10	$-\frac{45}{2}$	40	$-\frac{105}{2}$	$\frac{252}{5}$	-35	$\frac{120}{7}$	$-\frac{45}{8}$	$\frac{10}{9}$	$-\frac{1}{10}$

n	$2N+1$	Error	j										
			-1	0	+1	+2	+3	+4	+5	+6	+7	+8	+9
1	4	$\mathcal{O}(h^4)$	$-\frac{1}{3}$	$-\frac{1}{2}$	1	$-\frac{1}{6}$	0	0	0	0	0	0	0
	5	$\mathcal{O}(h^5)$	$-\frac{1}{4}$	$-\frac{5}{6}$	$\frac{3}{2}$	$-\frac{1}{2}$	$\frac{1}{12}$	0	0	0	0	0	0
	7	$\mathcal{O}(h^7)$	$-\frac{1}{6}$	$-\frac{77}{60}$	$\frac{5}{2}$	$-\frac{5}{3}$	$\frac{5}{6}$	$-\frac{1}{4}$	$\frac{1}{30}$	0	0	0	0
	9	$\mathcal{O}(h^9)$	$-\frac{1}{8}$	$-\frac{223}{140}$	$\frac{7}{2}$	$-\frac{7}{2}$	$\frac{35}{12}$	$-\frac{7}{4}$	$\frac{7}{10}$	$-\frac{1}{6}$	$\frac{1}{56}$	0	0
	11	$\mathcal{O}(h^{11})$	$-\frac{1}{10}$	$-\frac{4609}{2520}$	$\frac{9}{2}$	-6	7	$-\frac{63}{10}$	$\frac{21}{5}$	-2	$\frac{9}{14}$	$-\frac{1}{8}$	$\frac{1}{90}$

n	$2N+1$	Error	j										
			-2	-1	0	+1	+2	+3	+4	+5	+6	+7	+8
1	7	$\mathcal{O}(h^7)$	$\frac{1}{30}$	$-\frac{2}{5}$	$-\frac{7}{12}$	$\frac{4}{3}$	$-\frac{1}{2}$	$\frac{2}{15}$	$-\frac{1}{60}$	0	0	0	0
	9	$\mathcal{O}(h^9)$	$\frac{1}{56}$	$-\frac{2}{7}$	$-\frac{19}{20}$	2	$-\frac{5}{4}$	$\frac{2}{3}$	$-\frac{1}{4}$	$\frac{2}{35}$	$-\frac{1}{168}$	0	0
	11	$\mathcal{O}(h^{11})$	$\frac{1}{90}$	$-\frac{2}{9}$	$-\frac{341}{280}$	$\frac{8}{3}$	$-\frac{7}{3}$	$\frac{28}{15}$	$-\frac{7}{6}$	$\frac{8}{15}$	$-\frac{1}{6}$	$\frac{2}{63}$	$-\frac{1}{360}$

n	$2N+1$	Error	j										
			-3	-2	-1	0	+1	+2	+3	+4	+5	+6	+7
1	9	$\mathcal{O}(h^9)$	$-\frac{1}{168}$	$\frac{1}{14}$	$-\frac{1}{2}$	$-\frac{9}{20}$	$\frac{5}{4}$	$-\frac{1}{2}$	$\frac{1}{6}$	$-\frac{1}{28}$	$\frac{1}{280}$	0	0
	11	$\mathcal{O}(h^{11})$	$-\frac{1}{360}$	$\frac{1}{24}$	$-\frac{3}{8}$	$-\frac{319}{420}$	$\frac{7}{4}$	$-\frac{21}{20}$	$\frac{7}{12}$	$-\frac{1}{4}$	$\frac{3}{40}$	$-\frac{1}{72}$	$\frac{1}{840}$

n	$2N+1$	Error	j										
			-4	-3	-2	-1	0	+1	+2	+3	+4	+5	+6
1	11	$\mathcal{O}(h^{11})$	$\frac{1}{840}$	$-\frac{1}{63}$	$\frac{3}{28}$	$-\frac{4}{7}$	$-\frac{11}{30}$	$\frac{6}{5}$	$-\frac{1}{2}$	$\frac{4}{21}$	$-\frac{3}{56}$	$\frac{1}{105}$	$-\frac{1}{1260}$

Appendix E

Point Group Symmetries

In this appendix we discuss the point group symmetry associated with the tetrahedral and octahedral deformation of nuclear shape and with the artificial violation of the rotational symmetry caused by taking a cubic lattice in the coordinate space, and how the single-particle spectrum, or the shell structure, is affected by the symmetry violations.

We first introduce the basic theorems and formulas of group theory [26, 180, 181] for preparation.

E.1 Basics of group theory

The theory of group and its representations is a very powerful tool, especially in quantum mechanics, to deal with symmetries. It gives a plenty of quite non-trivial consequences on the properties of energy spectrum and eigenfunctions of a system which has certain symmetries. This information, which are extracted from pure group theory, do not depend on the physical details of the system that one is concerned. It helps us with simplifying problems for complicated systems and solving them more efficiently.

The group (representation) theory is widely applied in physics and chemistry. In particle physics, Lie groups have always been playing essential roles in understanding the mathematical structure of the theory and the nature of interactions among fundamental particles [87, 181, 182]. In nuclear physics, various types of low-lying collective excitations in nuclei have been studied based on dynamical symmetries, which are also described by chains of Lie groups, possessed by model Hamiltonians in the interacting boson models and Bohr's collective model [183, 184]. Finite groups (point groups and space groups) are important as well in solid state physics and chemistry to compute, e.g., molecular orbitals, excitation spectrum of molecules, and electronic band structure of crystal [26, 180].

E.1.1 Theory of group and its representation

In this section we introduce some useful theorems for finite groups.

Group and representation

Definition E.1.1 (Group) *A group G is a set on which a binary operation, product, is defined, satisfying:*

1. If $f, g \in G$ then $h = fg \in G$.
2. For $f, g, h \in G$, $(fg)h = f(gh)$.
3. There is an identity element, e, such that $ef = fe = f$ for all $f \in G$
4. Every element $f \in G$ has an inverse, f^{-1}, such that $f^{-1}f = ff^{-1} = e$.

A group is characterized with multiplication law for every (orderd) pair of elements in the group. For finite groups, the number of elements N is called **order** of the group. We introduce a useful concept, **conjugacy class**:

Definition E.1.2 (Conjugacy class) *A subset H of a group G satisfying*

$$g^{-1}hg \in H \ \forall \ h \in H, \ g \in G \tag{E.1.1}$$

is called conjugacy class.

Note that a conjugacy class is not necessarily a subgroup of G. If H is a subgroup, it is called an **invariant** or **normal subgroup**.

A group is a set of abstract operations such as rotations, translations, or interchange, and so on. A **representation** defined below makes those abstract things more concrete and easy to mathematically handle.

Definition E.1.3 (Representation) *A representation of a group G is mapping, D of $g \in G$ onto a set of linear operators with the following properties:*

1. $D(e) = 1$, where 1 is the identity operator in the space on which the linear operators act.
2. $D(g_1)D(g_2) = D(g_1 g_2)$, in other words the group multiplication law is mapped onto the multiplication of the linear operators.

A good feature of representations is that, in linear space, we are free to choose the basis vectors. Change of basis to represent states and matrices in more convenient way can be done by making similarity transformations,

$$D \to D' = SDS^{-1}. \tag{E.1.2}$$

Clearly the new set of operators has the same multiplication law as the old one. Thus D' is also a representation if D is. D and D' are said to be **equivalent** because they just differ by the basis to represent them.

A representation is **reducible** if it is equivalent to a block diagonal form, that is, if there exists a transformation such that

$$D(g) \to D'(g) = SD(g)S^{-1} = \begin{pmatrix} D_1(g) & 0 & \cdots \\ 0 & D_2(g) & \cdots \\ \vdots & \vdots & \ddots \end{pmatrix} \text{ for all } g \in G. \tag{E.1.3}$$

A representation is **irreducible** if it is not reducible.

It can be proved that a representation of finite group is always equivalent to a unitary representation.

Theorem E.1.1 (Unitarity) *Every representation of a finite group is equivalent to a unitary representation.*

Proof: Suppose $D(g)$ is a representation of a group G. Consider an operator defined by

$$S = \sum_{g \in G} D(g)^\dagger D(g). \tag{E.1.4}$$

S is hermitian and positive-semidefinite. Assume that S has a zero eigenvalue, i.e., there exists a vector v such that $Sv = 0$. Then

$$v^\dagger S v = 0 = \sum_{g \in G} |D(g)v|^2. \tag{E.1.5}$$

Thus $D(g)v$ must be zero vector for all $g \in G$, which is impossible because $D(e) = 1$. Therefore, S is positive-definite and invertible, and we can construct the square-root of S, $X \equiv S^{1/2}$. Of course X is also hermitian and invertible. Now we define

$$D' = XDX^{-1}. \tag{E.1.6}$$

This representation is unitary because

$$D'(g)^\dagger D'(g) = X^{-1} D(g)^\dagger S D(g) X^{-1} \tag{E.1.7}$$

and

$$\begin{aligned} D(g)^\dagger S D(g) &= D(g)^\dagger \sum_h D(h)^\dagger D(h) D(g) && \text{(E.1.8)} \\ &= \sum_{hg} D(hg)^\dagger D(hg) && \text{(E.1.9)} \\ &= \sum_g D(g)^\dagger D(g) = S = X^2, && \text{(E.1.10)} \end{aligned}$$

where the last line follows from the fact that hg runs over all elements of G. ■ Because of this theorem we only have to consider unitary representations.

Orthogonality relations

The following **Schur's lemma** is important in representation theory of finite groups.

Theorem E.1.2 (Schur's lemma 1) *If* $D_1(g)A = AD_2(g)$ *for all* $g \in G$ *where* D_1 *and* D_2 *are inequivalent irreducible representations, then* $A = 0$*.*

Theorem E.1.3 (Schur's lemma 2) *If* $D(g)A = AD(g)$ *for all* $g \in G$ *where* D *is a finite dimensional irreducible representations, then* $A \propto I$*.*

For proofs see Refs. [26,181]. Using Schur's lemma we can prove the orthogonality relation for elements of representation matrices.

Theorem E.1.4 (Great orthogonality relation) *Matrix elements of unitary irreducible representations satisfies the following orthogonality relation*

$$\sum_{g\in G}[D^{(\alpha)}(g)]^*_{ij}[D^{(\beta)}(g)]_{kl} = \frac{N}{n_\alpha}\delta_{\alpha\beta}\delta_{ik}\delta_{jl}, \tag{E.1.11}$$

where α *and* β *label irreducible representations and* n_α *is dimension of the irreducible representation* α*.*

Proof: Let $D^{(\alpha)}$ and $D^{(\beta)}$ finite dimensional irreducible representations of a group G. Consider an operator

$$A^{\alpha\beta} = \sum_{g\in G} D^{(\alpha)}(g^{-1})BD^{(\beta)}(g), \tag{E.1.12}$$

where B is an arbitrary linear operator. We multiply $A^{\alpha\beta}$ by $D^{(\alpha)}(h^{-1})$ from the left and $1 = D^{(\beta)}(h)D^{(\beta)}(h^{-1})$ from the right:

$$\begin{aligned}
D^{(\alpha)}(h^{-1})A^{\alpha\beta} &= \sum_{g\in G} D^{(\alpha)}(h^{-1})D^{(\alpha)}(g^{-1})BD^{(\beta)}(g)D^{(\beta)}(h)D^{(\beta)}(h^{-1}) \\
&= \sum_{g\in G} D^{(\alpha)}((gh)^{-1})BD^{(\beta)}(gh)D^{(\beta)}(h^{-1}) \\
&= \sum_{g'\in G} D^{(\alpha)}(g')BD^{(\beta)}(g')D^{(\beta)}(h^{-1}) \\
&= A^{\alpha\beta}D^{(\beta)}(h^{-1}).
\end{aligned}$$

Thus we have

$$D^{(\alpha)}(h)A^{\alpha\beta} = A^{\alpha\beta}D^{(\beta)}(h) \ \ \forall\ h \in G. \tag{E.1.13}$$

Now Theorems E.1.2 and E.1.3 imply that if α and β are inequivalent, $A^{\alpha\beta} = 0$ and that if α and β are equivalent, $A^{\alpha\beta} \propto I$. Thus we can write

$$\sum_{g\in G} D^{(\alpha)}(g^{-1})BD^{(\beta)}(g) = \delta_{\alpha\beta}\lambda I, \tag{E.1.14}$$

where I is the $n_\alpha \times n_\alpha$ identity matrix.

Let us take $B = |\alpha, i\rangle\langle\beta, k|$, where $|\alpha, i\rangle$ is the i-th normalized basis state of the irreducible representation α. (j, l)-element of B is given by $\delta_{ij}\delta_{kl}$. Note that the ket (bra) vector can be viewed as $n_\alpha \times 1$ ($1 \times n_\beta$) matrix. Now we take trace of both sides in Eq. (E.1.14),

$$\begin{aligned}\lambda n_\alpha \delta_{\alpha\beta} &= \delta_{\alpha\beta} \sum_{g\in G} \mathrm{Tr}\left[D^{(\alpha)}(g^{-1})|\alpha, i\rangle\langle\alpha, k|D^{(\alpha)}(g)\right] \\ &= \delta_{\alpha\beta} \sum_{g\in G} \mathrm{Tr}\left[\langle\alpha, k|D^{(\alpha)}(g)D^{(\alpha)}(g^{-1})|\alpha, i\rangle\right] \\ &= N\delta_{\alpha\beta}\delta_{ik},\end{aligned}$$

where we make use of the cyclic property of traces. Thus we have obtained $\lambda = \delta_{ik}N/n_\alpha$. Taking matrix element of Eq. (E.1.14) with $B = |\alpha, i\rangle\langle\beta, k|$, we finally get

$$\sum_{g\in G}[D^{(\alpha)}(g^{-1})]_{ji}[D^{(\beta)}(g)]_{kl} = \frac{N}{n_\alpha}\delta_{\alpha\beta}\delta_{ik}\delta_{jl}. \tag{E.1.15}$$

For unitary representations we can write

$$\sum_{g\in G}[D^{(\alpha)}(g)]^*_{ij}[D^{(\beta)}(g)]_{kl} = \frac{N}{n_\alpha}\delta_{\alpha\beta}\delta_{ik}\delta_{jl}. \blacksquare \tag{E.1.16}$$

Definition E.1.4 (Character) *The characters $\chi_D(g)$ of a representation D is defined by the traces of the representation matrix,*

$$\chi_D(g) = \mathrm{Tr}[D(g)] = \sum_i [D(g)]_{ii}. \tag{E.1.17}$$

Because of the cyclic property of traces, the characters have the following two properties.

- $\chi_D(g) = \chi_{D'}(g)\ \forall g \ \Rightarrow D$ and D' are equivalent.
- $g_1, g_2 \in G$ belong to the same conjugacy class $\Rightarrow \chi_D(g_1) = \chi_D(g_2)$.

The characters are constant on a conjugacy class. In other words, characters may be considered as a function of conjugacy classes $\chi_D(\mathscr{C}_i)$, where $\mathscr{C}_i$ represents the i-th conjugacy class in the group.

By setting $i = j$ and $k = l$, and taking summations over i and k in Eq. (E.1.11), we obtain an orthogonality relation for characters:

Theorem E.1.5 (Orthogonality relation of characters) *For unitary irreducible representations α and β of a group G, their characters satisfies the following orthogonality relation*

$$\sum_{g\in G} \chi^{(\alpha)}(g)\chi^{(\beta)}(g) = N\delta_{\alpha\beta}, \tag{E.1.18}$$

where N is order of G. In terms of the conjugacy classes it can be written as

$$\sum_{i=1}^{n_c} h_i \chi^{(\alpha)}(\mathscr{C}_i)\chi^{(\beta)}(\mathscr{C}_i) = N\delta_{\alpha\beta}, \tag{E.1.19}$$

where n_c is the number of conjugacy classes and h_i is the number of elements of $\mathscr{C}_i$.

Using Eq. (E.1.18), the orthogonality of irreducible characters, one can carry out reduction of a representation to a direct sum of irreducible representations. Suppose a reducible representation D can be reduced to a direct sum of irreducible representations

$$D(g) \to \bigoplus_{\alpha=1}^{n_r} m_\alpha^D D^{(\alpha)}(g) \tag{E.1.20}$$

Then its character satisfies

$$\chi_D(g) = \sum_{\alpha=1}^{n_r} m_\alpha^D \chi^{(\alpha)}(g) \tag{E.1.21}$$

It follows from the orthogonality relation that

$$m_\alpha^D = \frac{1}{N}\sum_{g\in G} \chi^{(\alpha)}(g)^* \chi_D(g) \tag{E.1.22}$$

As is clear from the above discussions, character is a powerful tool to decompose a reducible representation into a direct sum of irreducible representations. Once we have the character of a reducible representation, we should expand it with the irreducible characters of the group, then, the expansion coefficients m_α^D are the number of times each irreducible representation appears in the decomposition. We shall use this remarkable property of character in order to find residual degeneracies when a representation becomes reducible by a reduction of the size of the symmetry group.

E.2 Point groups

In this section we first introduce the two important point groups that are the symmetries associated with exotic nuclear deformations or the cubic-lattice discretization. A point group is a group of spatial operations, which leaves at least one point in space unchanged, such as rotations and reflections. Point group is used to specify the symmetries in molecules [26, 180]. Note that it does not include a translation, which could be a symmetry of a crystal. In the latter half of this section we discuss how the degeneracy of an $SO(3)$ multiplet is violated when the $SO(3)$ symmetry is broken down to the point group symmetries.

E.2.1 Tetrahedral and octahedral groups

The important point groups in this thesis are the tetrahedral group T_d and the octahedral group O_h, which are the sets of operations leaving a regular tetrahedron and a regular octahedron invariant, respectively.

First we consider only *rotations* leaving a regular tetrahedron and a regular octahedron unchanged. The point groups associated with those symmetries are named T and O, respectively. Figs. E.1(a) and E.1(b) shows the symmetry operations of T and O, respectively. The group, T, of rotations leaving a tetrahedron unchanged is composed of the following elements,

$$T = \{e, 4C_3, 4C_3^2, 3C_2\}, \tag{E.2.1}$$

where e is the identity, C_n is a rotation by angle $2\pi/n$ about a certain rotation axis. An axis of C_n rotational symmetry is called an n-fold axis. The numbers in front of the symbols denote the number of the elements which belong to the same conjugacy class, e.g., $4C_3$ represents the four C_3 rotations with the four different choices of the rotation axis, all of which belong to the same conjugacy class[1]. A regular tetrahedron has four three-fold axes and three two-fold axes. The two classes, $4C_3$ and $4C_3^2$, in T are considered to be the clockwise and counterclockwise rotations by $2\pi/3$ about the four three-fold axes, each of which normally passing through the center of a face of the tetrahedron. The group T consists of 12 symmetry transformations.

The group, O, of rotations corresponding to the symmetry of an octahedron is given by

$$O = \{e, 8C_3, 6C_2', 3C_2(= C_4^2), 6C_4\}. \tag{E.2.2}$$

It has six four-fold axes, eight three-fold axes, and two distinct classes of three and six two-fold axes. Fig. E.1(b) shows these rotations.

Next we consider the full symmetry operations including reflections as well as rotations. The full symmetry group of a tetrahedron is the point group T_d, which consists of the following elements,

$$T_d = \{e, 8C_3, 3C_2, 6\sigma_d, 6S_4\}. \tag{E.2.3}$$

In addition to all the elements of T[2], it contains the operations σ_d and S_4 involving reflections. σ_d denotes a reflection in a plane which bisects the tetrahedron and passes through one of the edges of the tetrahedron. There are six similar operations corresponding to each edge of the tetrahedron, and they form a conjugacy class denoted by $6\sigma_d$. S_4 is called an "improper rotation" or "rotary reflection", a C_4 rotation around a two-fold axis (See Fig. E.1(a)) followed by a reflection in the plane perpendicular to the rotation axis. The six such distinct operations (two opposite directions of the rotation each for the three choices of the axis) comprise another conjugacy class $6S_4$. Thus, in total, there are 24 symmetry operations for a regular tetrahedron.

---

[1] Intuitively, a conjugacy class is a subset of a group consisting of similar operations.

[2] Now, in the full symmetry group T_d, the conjugacy class denoted by "$8C_3$" corresponds to the union of the two conjugacy classes $4C_3$ and $4C_3^2 = 4C_3^{-1}$ of the subgroup T. In general, C_n and C_n^{-1} belong to the same conjugacy class if the reflection, σ, in the plane containing the rotation axis is also an element of the same group, since $\sigma C_n \sigma^{-1} = C_n^{-1}$.

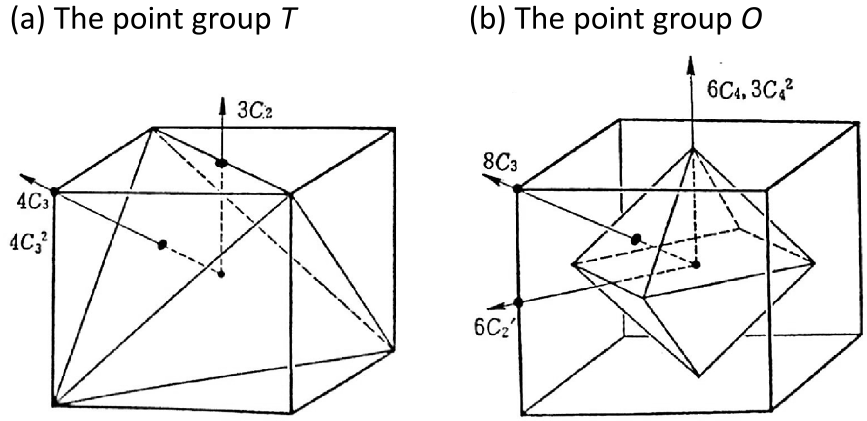
(a) The point group T

(b) The point group O

Figure E.1: The symmetry operations of the point group O and T, which leaves an octahedron and a tetrahedron invariant, respectively. The symbol C_n is a rotation by angle $2\pi/n$. The arrows indicate rotation axes. The numbers before the symbols denote the number of similar rotations, i.e., the number of choices of the axis for similar rotations. The figure is taken from Ref. [26].

The group associated with the full symmetry of an octahedron is named O_h. Since a regular octahedron is symmetric under the space inversion (the parity transformation), the group is given by a direct-product group $O_h = O \times C_i$ [3] , where C_i is the group of the space inversion:

$$C_i = \{e, i\}. \tag{E.2.4}$$

The element i denotes the parity operation. Notice that any rotations and the parity operation commutes, and the label of irreducible representation, or the quantum number of a state associated with O and C_i can be determined separately.

E.2.2 Decomposition of $SO(3)$ multiplets into irreps of a point group

In this section we discuss how the "magnetic" $(2j+1)$-fold degeneracy of an eigenstate of angular momentum is violated with the spherical symmetry broken down to tetrahedral or octahedral, using the formulas derived in Sec. E.1. We here consider symmetry breaking occurring when 1) nuclear shape is deformed from the spherical one, or 2) coordinate space is discretized into 3D lattice. For the case 1), we consider the tetrahedral and octahedral deformations, where strong shell effects are expected compared to the other kind of deformations. In the case 2), the rotational invariance of the mean-field Hamiltonian is broken down to O_h artificially by the discretization.

---

[3] If we have two groups $G = \{e, g_2, \dots, g_{N_a}\}$ and $H = \{e, h_2, \dots, h_{N_b}\}$ such that all of G commutes with all of H, then $G \times H = \{e, g_2, \dots, g_{N_a}, h_2, g_2h_2, g_3h_2, \dots, g_{N_a}h_{N_b}\}$ forms a group of N_aN_b elements. $G \times H$ is called direct-product group of the two groups.

Table E.1: The character table of the point group T_d. The symbols A_1, A_2, ..., T_2 denotes the single-valued representations, and $E_{1/2}$, $E_{5/2}$, and $G_{3/2}$ are the double-valued representations.

	e		$8C_3$		$3C_2$	$6\sigma_d$	$6S_4$	
A_1	1		1		1	1	1	
A_2	1		1		1	-1	-1	
E	2		-1		2	0	0	
T_1	3		0		-1	-1	1	
T_2	3		0		-1	1	-1	
$E_{1/2}$	2	-2	1	-1	0	0	$\sqrt{2}$	$-\sqrt{2}$
$E_{5/2}$	2	-2	1	-1	0	0	$-\sqrt{2}$	$\sqrt{2}$
$G_{3/2}$	4	-4	-1	1	0	0	0	0

We make use of Eq. (E.1.22) to decompose $SO(3)$ multiplets into the irreps of the point groups. What we need are

- The characters of all the irreps (irreducible representations) of the point group, and
- The characters of the $SO(3)$ irreps,

and we expand the latter with the former and read the expansion coefficients to get how many times each irrep of the point group appears in the decomposition. The composition of the representation so obtained together with the dimension of the irreps give information of the pattern of the level splittings which occurs when the spherical symmetry is broken to the point group symmetry.

In Tables E.1 and E.2, we tabulate the characters of all the irreducible representations of the point groups T_d and O, respectively. In the both tables, A_1, A_2, E, T_1, and T_2 are the single-valued representations, which gives how integer-spin states are transformed under the group elements, while $E_{1/2}$, $E_{5/2}$, and $G_{3/2}$ are the double-valued representations, which correspond to the transformation properties of half-integer-spin states. For half-integer-spin states, there are two different representations corresponding to one rotation, e.g., spin-1/2 state gains a sign under a 2π rotation, and a 4π rotation makes the state back to completely the same including the phase. Thus one can consider that a representation of the half-integer-spin states is double-valued[4]. The integer- and half-integer-spin multiplets are decomposed into the single-valued and the double-valued representations, respectively. We also note that A_1, whose characters are all 1, corresponds to the trivial, or "scalar" representation of each group.

The remaining task is to compute characters of the $SO(3)$ multiplets for the point group transformations. Let us consider a state with the spin parity j^π and denote its

---

[4] Another way to deal with the half-integer-spin states is to consider a *double group*, in which "2π" rotations and "4π" rotations are distinguished, and thus the order of the group is doubled [26].

Table E.2: The character table of the point group O. The symbols A_1, A_2, ..., T_2 denotes the single-valued representations, and $E_{1/2}$, $E_{5/2}$, and $G_{3/2}$ are the double-valued representations. In the double-valued representations there are two different representations whose signs are opposite to each other for each rotation. Accordingly there are two different characters for each rotation.

	e		$6C_4$		$3C_2$	$6C_2'$	$8C_3$	
A_1	1		1		1	1	1	
A_2	1		-1		1	-1	1	
E	2		0		2	0	-1	
T_1	3		1		-1	-1	0	
T_2	3		-1		-1	1	0	
$E_{1/2}$	2	-2	$\sqrt{2}$	$-\sqrt{2}$	0	0	1	-1
$E_{5/2}$	2	-2	$-\sqrt{2}$	$\sqrt{2}$	0	0	1	-1
$G_{3/2}$	4	-4	0	0	0	0	-1	1

character with $\chi^{(j^\pi)}(g)$. The character of the identity e is simply the dimension of the multiplet

$$\chi^{(j^\pi)}(e) = 2j + 1. \tag{E.2.5}$$

The character for a rotation by an angle α about z-axis for a multiplet with angular momentum j is given by

$$\mathrm{Tr}\begin{pmatrix} e^{ij\alpha} & & & \\ & e^{i(j-1)\alpha} & & \\ & & \ddots & \\ & & & e^{-ij\alpha} \end{pmatrix} = \frac{\sin(j+\frac{1}{2})\alpha}{\sin\frac{\alpha}{2}} \tag{E.2.6}$$

This formula applies to rotation about arbitrary axis because of the cyclic property of traces. The rotation matrix R_α for a rotation by angle α is transformed by an orthogonal matrix O under a rotation of the system (wave functions) as

$$R_\alpha \to R'_\alpha = O R_\alpha O^{-1}. \tag{E.2.7}$$

One can take O in such a way that the quantization axis of the wave functions aligns the rotation axis. Then R'_α looks just like the one in Eq. (E.2.6), but the trace of R'_α is the same as that of the rotation matrix R_α in the original frame. Thus characters of any rotation C_n (and C_n^{-1}) for an irreducible representation of $SO(3)$ is given by Eq. (E.2.6), or

$$\chi^{(j^\pi)}(C_n) = \chi^{(j^\pi)}(C_n^{-1}) = \frac{\sin[(2j+1)\pi/n]}{\sin(\pi/n)}. \tag{E.2.8}$$

For more detailed properties of characters for rotation, see Ref. [185]. Next we compute the character of σ_d of T_d, a reflection in a plane. Noticing that a reflection is a sequence of the parity transformation i and a rotation by angle π about the axis perpendicular to the reflection plane, one obtains

$$\chi^{(j^\pi)}(\sigma_d) = \chi^{(j^\pi)}(iC_2) = \chi^{(j^\pi)}(C_2 i) = \pi \times \chi^{(j^\pi)}(C_2). \tag{E.2.9}$$

Finally we consider the rotary reflection S_4, a product of a reflection and a $\pi/2$ rotation with its axis perpendicular to the reflection plane. The character of S_4 is given by

$$\chi^{(j^\pi)}(S_4) = \chi^{(j^\pi)}(C_4\sigma) = \chi^{(j^\pi)}(C_4C_2 i) = \chi^{(j^\pi)}(C_4 i) = \pi \times \chi^{(j^\pi)}(C_4). \tag{E.2.10}$$

Notice that we have rewritten the reflection as the product $C_2 i$ and that C_2 and C_4 have common rotation axis. Eqs. (E.2.5), (E.2.8), (E.2.9), and (E.2.10) gives the necessary formulas in the decomposition of the $SO(3)$ multiplets into the irreps of T_d and O_h.

Now we can carry out the reduction. In Table E.3, we show the number of times each irrep of T_d appears in the decomposition of states with half-integer spin j and parity π. One can see that $s_{1/2}$, $p_{3/2}$, $p_{1/2}$, $d_{3/2}$ states contain only a single irrep of T_d, while those with $j \geq 5/2$ contain more than one. Thus single-particle states with $j \leq 3/2$ do not split and the others do split for tetrahedral deformation. For instance, $f_{5/2}$ splits into two levels with two-fold ($E_{1/2}$) and four-fold ($G_{3/2}$) degeneracy, and $g_{9/2}$ into one two-fold level and two four-fold levels.

Table E.4 is similar to Table E.3 but corresponds to integer-spin states. According to Table E.4, spins larger than or equal to 2 contains more than one irreps of T_d.

Another thing we can learn from Table E.4 is the possible nuclear spins of tetrahedral magic nuclei [146]. Closed spherical shell (spherical magic) nuclei has the spin parity 0^+, which is the scalar representation of $SO(3)$. Analogously, a tetrahedral magic configuration should be A_1 representation of T_d which is the scalar under the tetrahedral symmetry. Thus, by reading the columns of A_1 in Table E.4, we notice that the tetrahedral closed configuration can only have spin parity

$$0^\pm, 3^-, 4^+, 6^\pm, 7^-, 8^+, 9^\pm, 10^\pm, 11^-, 12^\pm, 13^\pm, 14^\pm, 15^\pm, 16^\pm, \ldots \tag{E.2.11}$$

This is numerically confirmed in Ref. [146] by performing angular momentum projection on the tetrahedral magic nuclei. The characteristic feature of the spectrum is that states of spin $I = 1, 2$, and 5 are missing in the sequence of vibrational states or in the rotational band on top of the tetrahedral shape [146].

In Table E.5 we tabulate the decomposition of both integer and half-integer spins for the octahedral group O. Here we do not have to consider the parity. Since every element of O commutes with parity, a state can be a simultaneous eigenstate of the O symmetry and parity. The parity quantum number of the state is conventionally distinguished by an additional subscript g and u for even and odd parity, respectively, e.g., A_{1g} for an even-parity A_1 state[5]. From the table one can see that single-particle states with $j \geq 5/2$ splits when the spherical symmetry is broken down to the octahedral symmetry.

---

[5] g and u come from german words "gerade" and "ungerade", which mean "even" and "odd", respectively.

We can consider two different cases for this kind of symmetry breaking. One is the case that the nuclear mean-field is deformed into octahedral shape. The other is the case of an artifact of the discretization, that is, the coordinate space is discretized into the cubic lattice although the mean-field is spherical. The same discussion applies to both cases since all the above discussions are based on the pure group theory, which is independent from detailed nature of individual problems. Note that the group theory only tells us the number of splittings and degeneracy of each level. The size of splitting and level ordering may depend on the individual problem. The artificial symmetry breaking brought about by lattice discretization is also discussed recently in Ref. [186].

Let us discuss here the shell effects in the tetrahedral or octahedral deformed nuclei [36–38]. As is mentioned, particularly strong shell effects would be expected because of the highly degenerate single-particle levels for these deformations. The spherical symmetry, which is the highest symmetry, exhibits strong shell effect at the well known magic numbers due to the $(2j+1)$-fold high degeneracy. In general, once a nucleus is deformed, an $SO(3)$ multiplet splits into several levels whose degeneracies are determined from the shape symmetry. In most of possible deformations including the axially symmetric one, the surviving degeneracy is only two-fold one, the Kramers degeneracy [143]. The level splittings becomes larger and larger as the nucleus becomes deformed, and the shell structure becomes more and more vague. In this respect, the tetrahedral and octahedral symmetries are special since they yield degeneracies more than the Kramers degeneracy. Since we are concerned with a fermion, we should focus on the double-valued representations. We notice that in both T_d and O (or O_h), there is one representation, $G_{3/2}$, whose dimension is four, yielding a four-fold degeneracy. This high degeneracy reflects rather high symmetries in those isotropic shapes of regular tetrahedron and octahedron. The unique degeneracy with tetrahedral and octahedral symmetries lead to bunching of single-particle levels and well developed shell gaps (magic numbers) in the single-particle spectrum [36–38]. This is the reason why one may expect tetrahedral and octahedral ground state or isomers in nuclei with specific number of nucleons.

Table E.3: The number of times each irrep appears in the reduction of $SO(3)$ multiplets with half-integer spins into the irreps of T_d. Positive and negative parity cases are separately shown.

j^π	$E_{1/2}$	$E_{5/2}$	$G_{3/2}$	j^π	$E_{1/2}$	$E_{5/2}$	$G_{3/2}$
$\frac{1}{2}^+$	1	0	0	$\frac{1}{2}^-$	0	1	0
$\frac{3}{2}^+$	0	0	1	$\frac{3}{2}^-$	0	0	1
$\frac{5}{2}^+$	0	1	1	$\frac{5}{2}^-$	1	0	1
$\frac{7}{2}^+$	1	1	1	$\frac{7}{2}^-$	1	1	1
$\frac{9}{2}^+$	1	0	2	$\frac{9}{2}^-$	0	1	2
$\frac{11}{2}^+$	1	1	2	$\frac{11}{2}^-$	1	1	2
$\frac{13}{2}^+$	1	2	2	$\frac{13}{2}^-$	2	1	2
$\frac{15}{2}^+$	1	1	3	$\frac{15}{2}^-$	1	1	3
$\frac{17}{2}^+$	2	1	3	$\frac{17}{2}^-$	1	2	2
$\frac{19}{2}^+$	2	2	3	$\frac{19}{2}^-$	2	2	3
$\frac{21}{2}^+$	1	2	4	$\frac{21}{2}^-$	2	1	4
$\frac{23}{2}^+$	2	2	4	$\frac{23}{2}^-$	2	2	4
$\frac{25}{2}^+$	3	2	4	$\frac{25}{2}^-$	2	3	4
$\frac{27}{2}^+$	2	2	5	$\frac{27}{2}^-$	2	2	5
$\frac{29}{2}^+$	2	3	5	$\frac{29}{2}^-$	3	2	5
$\frac{31}{2}^+$	3	3	5	$\frac{31}{2}^-$	3	3	5
$\frac{33}{2}^+$	3	2	6	$\frac{33}{2}^-$	2	3	6

Table E.4: The number of times each irrep appears in the reduction of $SO(3)$ multiplets with integer spins into the irreps of T_d. Positive and negative parity cases are separately shown.

ℓ^π	A_1	A_2	E	T_1	T_2	ℓ^π	A_1	A_2	E	T_1	T_2
0^+	1	0	0	0	0	0^-	0	1	0	0	0
1^+	0	0	0	1	0	1^-	0	0	0	0	1
2^+	0	0	1	0	1	2^-	0	0	1	1	0
3^+	0	1	0	1	1	3^-	1	0	0	1	1
4^+	1	0	1	1	1	4^-	0	1	1	1	1
5^+	0	0	1	2	1	5^-	0	0	2	1	1
6^+	1	1	1	1	2	6^-	1	1	1	2	1
7^+	0	1	1	2	2	7^-	1	0	1	2	2
8^+	1	0	2	2	2	8^-	0	1	2	2	2
9^+	1	1	1	3	2	9^-	1	1	1	2	3
10^+	1	1	2	2	3	10^-	1	1	2	3	2
11^+	0	1	2	3	3	11^-	1	0	2	3	3
12^+	2	1	2	3	3	12^-	1	2	2	3	3
13^+	1	1	2	4	3	13^-	1	1	2	3	4
14^+	1	1	3	3	4	14^-	1	1	3	4	3
15^+	1	2	2	4	4	15^-	2	1	2	4	4
16^+	2	1	3	4	4	16^-	1	2	3	4	4

Table E.5: The number of times each irreducible representation appears of O in the reduction of $SO(3)$ multiplets for integer spins and half-integer spins.

ℓ	A_1	A_2	E	T_1	T_2	j	$E_{1/2}$	$E_{5/2}$	$G_{3/2}$
0	1	0	0	0	0	$\frac{1}{2}$	1	0	0
1	0	0	0	1	0	$\frac{3}{2}$	0	0	1
2	0	0	1	0	1	$\frac{5}{2}$	0	1	1
3	0	1	0	1	1	$\frac{7}{2}$	1	1	1
4	1	0	1	1	1	$\frac{9}{2}$	1	0	2
5	0	0	1	2	1	$\frac{11}{2}$	1	1	2
6	1	1	1	1	2	$\frac{13}{2}$	1	2	2
7	0	1	1	2	2	$\frac{15}{2}$	1	1	3
8	1	0	2	2	2	$\frac{17}{2}$	2	1	3
9	1	1	1	3	2	$\frac{19}{2}$	2	2	3
10	1	1	2	2	3	$\frac{21}{2}$	1	2	4
11	0	1	2	3	3	$\frac{23}{2}$	2	2	4
12	2	1	2	3	3	$\frac{25}{2}$	3	2	4
13	1	1	2	4	3	$\frac{27}{2}$	2	2	5
14	1	1	3	3	4	$\frac{29}{2}$	2	3	5
15	1	2	2	4	4	$\frac{31}{2}$	3	3	5
16	2	1	3	4	4	$\frac{33}{2}$	3	2	6

Appendix F

Miscellaneous

F.1 Center of mass correction

In the mean-field solutions for finite nuclei, mean field is localized and fixed in space, thus the solution breaks the translational symmetry. This spontaneous breaking of translational symmetry leads to a spurious center of mass motion. In the PC-F1 interaction used in our calculations, center of mass motion is corrected after variation. Since the relativistic kinematics plays no important role in nuclear ground states, the center of mass (c.m.) correction can be calculated in non-relativistic approximation in relativistic models [187].

The expectation value of the squared center of mass momentum P^2_{CM} in a general BCS state is given by [187]

$$\begin{aligned} \langle P^2_{\mathrm{CM}} \rangle \;=\; -\hbar^2 \Bigg[& \sum_{\alpha \gtrless 0} v^2_\alpha \langle \alpha | \Delta | \alpha \rangle + \sum_{\alpha,\beta \gtrless 0} \big(v^2_\alpha v^2_\beta \langle \alpha | \boldsymbol{\nabla} | \beta \rangle \cdot \langle \alpha | \boldsymbol{\nabla} | \beta \rangle^* \\ & - v_\alpha v_\alpha u_\beta u_\beta \langle \alpha | \boldsymbol{\nabla} | \beta \rangle \cdot \langle \bar{\alpha} | \boldsymbol{\nabla} | \bar{\beta} \rangle \big) \Bigg], \qquad \text{(F.1.1)} \end{aligned}$$

where α and β label the single-particle state and $\bar{\alpha} \equiv -\alpha$ denotes the time-reversal state of α. The coefficients v_α in Eq. (F.1.1) is the probability amplitude that a state α is occupied, while u_α satisfies $v^2_\alpha + u^2_\alpha = 1$. The expectation value $\langle P^2_{\mathrm{CM}} \rangle$ for a time-even mean-field state reduces to

$$\langle P^2_{\mathrm{CM}} \rangle = -2\hbar^2 \left[\sum_{\alpha > 0} \langle \alpha | \Delta | \alpha \rangle + \sum_{\alpha\beta > 0} \left(|\langle \alpha | \boldsymbol{\nabla} | \beta \rangle|^2 + |\langle \alpha | \boldsymbol{\nabla} | \bar{\beta} \rangle|^2 \right) \right], \qquad \text{(F.1.2)}$$

where the summations run over the occupied single-particle states only. For a time-even state, if α is occupied, its time-reversed partner $\bar{\alpha} = -\alpha$ is also occupied.

We also give here the expression of Eq. (F.1.2) for spherical case [161]. With the spherical symmetry, single-particle states are labeled by $\alpha = \{a, m_\alpha\}$, where a is a shorthanded notation for $\{n_a, \ell^{(+)}_a, j_a\}$, while $m_\alpha = j_z$ is projection of the total angular momentum.

Here, n_a is the principal quantum number, $\ell_a^{(+)}$ is the orbital angular momentum of the upper component of the single particle spinor, and j_a is the total angular momentum. A single-particle wave functions are given as

$$\psi_\alpha(\boldsymbol{r}) = \psi_{am_\alpha}(\boldsymbol{r}) = \begin{pmatrix} \psi_a^{(+)}(r)\mathscr{Y}_{\ell_a^{(+)} j_a m_\alpha}(\theta,\phi) \\ i\psi_a^{(-)}(r)\mathscr{Y}_{\ell_a^{(-)} j_a m_\alpha}(\theta,\phi) \end{pmatrix}, \tag{F.1.3}$$

where the spherical spinor $\mathscr{Y}_{\ell jm}$ is defined by $\mathscr{Y}_{\ell jm} = \sum_{m'm''}\langle \ell m' \tfrac{1}{2} m'' | jm\rangle Y_{\ell m}\chi_{\frac{1}{2}m''}$, where $\chi_{\frac{1}{2}m''}$ is the spin wave function. The orbital angular momentum of the lower component $\ell_a^{(-)}$ is given by $\ell_a^{(-)} = 2j_a - \ell_a^{(+)}$. The expectation value $\langle P_{\mathrm{CM}}^2\rangle$ with a mean-field many-body state reads

$$\begin{aligned} \langle P_{\mathrm{CM}}^2\rangle &= -\hbar^2 \sum_a w_a \sum_{m_\alpha} \langle \psi_{am_\alpha}|\Delta|\psi_{am_\alpha}\rangle \\ &\quad -\hbar^2 \sum_{a,b}\Big(w_a w_b + \sqrt{w_a w_b (1-w_a)(1-w_b)}\Big) \sum_{m_\alpha, m_\beta} |\langle \psi_{am_\alpha}|\boldsymbol{\nabla}|\psi_{bm_\beta}\rangle|^2, \end{aligned} \tag{F.1.4}$$

with

$$\sum_{m_\alpha}\langle \psi_{am_\alpha}|\Delta|\psi_{am_\alpha}\rangle = (2j_a+1)\sum_{\eta=\pm}\int dr\ r^2 \psi_a^{(\eta)}\left[\frac{\partial^2}{\partial r^2} + \frac{2}{r}\frac{\partial}{\partial r} - \frac{\ell_a^{(\eta)}(\ell_a^{(\eta)}+1)}{r^2}\right]\psi_a^{(\eta)}, \tag{F.1.5}$$

and

$$\begin{aligned} &\sum_{m_\alpha, m_\beta} |\langle \psi_{am_\alpha}|\boldsymbol{\nabla}|\psi_{bm_\beta}\rangle|^2 \\ &= (2j_a+1)(2j_b+1)\sum_{\eta,\eta'}(-)^{\ell_a^{(\eta)}+\ell_b^{(\eta')}+1} \begin{Bmatrix} j_b & j_a & 1 \\ \ell_a^{(\eta)} & \ell_b^{(\eta)} & \frac{1}{2} \end{Bmatrix} \begin{Bmatrix} j_b & j_a & 1 \\ \ell_a^{(\eta')} & \ell_b^{(\eta')} & \frac{1}{2} \end{Bmatrix} \\ &\times \Bigg[\delta_{\ell_a^{(\eta)},\ell_b^{(\eta)}+1}\sqrt{\ell_a^{(\eta)}}\int dr\ r^2\psi_a^{(\eta)}\left(\frac{\partial}{\partial r} - \frac{\ell_b^{(\eta)}}{r}\right)\psi_b^{(\eta)} \\ &\quad - \delta_{\ell_b^{(\eta)},\ell_a^{(\eta)}+1}\sqrt{\ell_b^{(\eta)}}\int dr\ r^2\psi_a^{(\eta)}\left(\frac{\partial}{\partial r} + \frac{\ell_b^{(\eta)}+1}{r}\right)\psi_b^{(\eta)}\Bigg] \\ &\times \Bigg[\delta_{\ell_b^{(\eta')},\ell_a^{(\eta')}+1}\sqrt{\ell_b^{(\eta')}}\int dr\ r^2\psi_b^{(\eta')}\left(\frac{\partial}{\partial r} - \frac{\ell_a^{(\eta')}}{r}\right)\psi_a^{(\eta')} \\ &\quad - \delta_{\ell_a^{(\eta')},\ell_b^{(\eta')}+1}\sqrt{\ell_a^{(\eta')}}\int dr\ r^2\psi_b^{(\eta')}\left(\frac{\partial}{\partial r} + \frac{\ell_a^{(\eta')}+1}{r}\right)\psi_a^{(\eta')}\Bigg], \end{aligned} \tag{F.1.6}$$

where w_a is the occupation probability of the level a determined by the filling approximation.

F.2 Solution of the Poisson equation for the Coulomb potential

We solve the Poisson equation in order to calculate the Hartree contribution of the electromagnetic interaction to the single-particle potential. The Poisson equation is given by

$$-\boldsymbol{\nabla}^2\phi(\boldsymbol{r}) = 4\pi\rho_c(\boldsymbol{r}), \tag{F.2.1}$$

where ϕ is the electrostatic potential and ρ_c is the charge density distribution. Because of the long range of the Coulomb interaction, the Poisson equation has to be dealt with in a special way. In this section we demonstrate how to numerically solve the Poisson equation in the 3D real space.

It is solved on 3D mesh in the following way:

1. The numerical box is temporarily extended and a boundary condition for ϕ is given at the surface of the extended box by using a multipole expansion of ρ_c.
2. The Poisson equation is discretized according to the boundary condition.
3. The discretized equation is solved numerically within the large box.
4. Only $\phi(\boldsymbol{r})$ inside the original box is taken and used for the calculations in the other parts of the numerical code, e.g., single-particle Hamiltonian h and the total energy E.

In the subsequent sections we explain in some detail how to deal with the first three steps given above.

F.2.1 Boundary condition

Since the Coulomb potential has a long tail ($\phi(\boldsymbol{r}) \to Ze/r$ for $r \to \infty$), a box boundary condition is clearly inappropriate. In order to fix the boundary condition for ϕ, we temporarily consider a box larger than the original numerical box as shown in Fig. F.1. In Fig. F.1, the blue ellipsoid denotes the charge distribution and R is its rough size. The black square represents the edge of the original box. Single-particle wave functions, densities and nuclear fields are computed on the mesh points within the black box. The red square represents the larger box newly considered, whose surface is located further away from the charge distribution. We denote a coordinate on the boundary of the large box by $\boldsymbol{r}_b$. The value of ϕ at a point $\boldsymbol{r}_b$ is given by the following multipole expansion

$$\begin{aligned}\phi(\boldsymbol{r}_b) &= \int d^3r'\,\frac{\rho_c(\boldsymbol{r}')}{|\boldsymbol{r}_b-\boldsymbol{r}'|}\\ &= \sum_\ell \frac{4\pi}{2\ell+1}\frac{1}{r_b^{\ell+1}}Y_\ell(\hat{\boldsymbol{r}}_b)\cdot\int r'^\ell Y_\ell(\hat{\boldsymbol{r}'})\rho_c(\boldsymbol{r}')\ d^3r', \qquad \text{(F.2.2)}\\ &= \frac{Ze}{r_b}+\frac{\boldsymbol{r}_b\cdot\boldsymbol{d}}{r_b^3}+\cdots\,,\end{aligned}$$

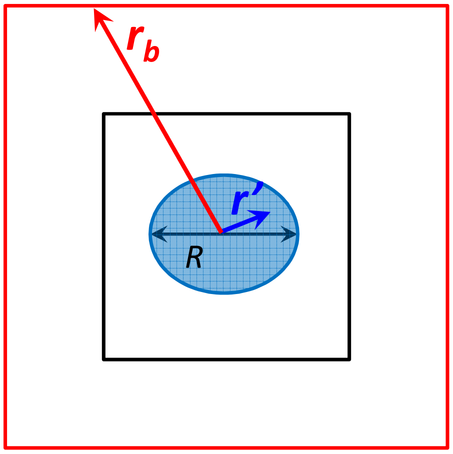

Figure F.1: A schematic picture of the boxes considered for numerical calculations. The blue ellipsoid represents the charge distribution, whose rough size is denoted by R. The black square indicates the original box, in which single-particle wave functions and nuclear fields have been confined. The red square is the new larger box for solution of the Poisson equation. The vector denoted by a red arrow ($\boldsymbol{r}_b$) is a coordinate on the boundary of the larger box, and the one denoted by a blue arrow ($\boldsymbol{r}'$) is a point inside the original box. Note their correspondence with the arguments in Eq. (F.2.3).

where the integral over $\boldsymbol{r}'$ has to be performed only inside the black box since we assume that ρ_c is vanishing outside, and the dot $(\cdot)$ in the second line is understood as the scalar product of two spherical harmonics. Notice that the integral in the second line of Eq. (F.2.3) is the electric multipole moment of the given charge distribution. In the third line of Eq. (F.2.3) the first two terms in the expansion ($\ell = 0$ and $\ell = 1$) are explicitly shown, where $\boldsymbol{d}$ is the electric dipole moment defined as

$$\boldsymbol{d} = \int \boldsymbol{r}' \rho_c(\boldsymbol{r}')\ d^3r'. \tag{F.2.3}$$

Since we take the large box so that $R/r_b < 1$, contribution from higher multipole moments is suppressed since their magnitudes are roughly estimated to be $\sim Ze \cdot R^\ell$. As long as ρ_c is confined within a finite-size region around the origin, $\ell \geq 1$ terms are vanishing as $r_b \to \infty$. The expansion up to $\ell = 4$ has been included in our calculations. In this case, leading error comes from $\ell = 5$ if proton density has corresponding deformation. One needs high-ℓ components if the nucleus takes a complicated shape, e.g., cluster structure.

F.2.2 Discretization

In this section we show how to construct a difference equation for the Poisson equation, which is expressed by a finite system of linear equation of the form $A\boldsymbol{x} = \boldsymbol{b}$. For simplicity

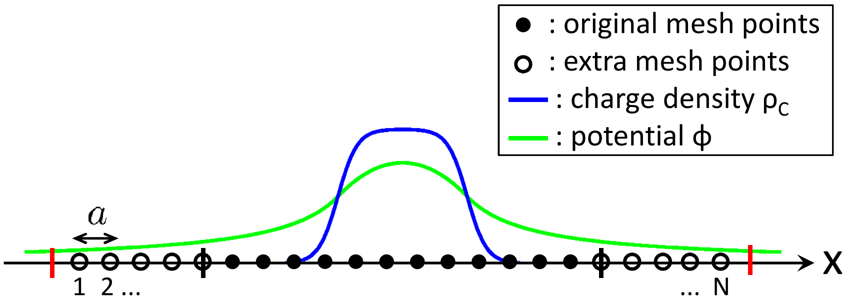

Figure F.2: A schematic picture of a charge distribution and the resulting Coulomb potential. Black tick marks and red tick marks indicate the edges of the original and extended boxes, respectively. The mesh points inside the original box are denoted by solid circles, while the extra mesh points introduced by the extension of the box are denoted by open circles. An integer below a mesh point (1, 2, ..., N) is the number assigned to each mesh point.

we consider a 1D case and show the explicit expression for the matrix A and the vector $\boldsymbol{b}$. Extension to 2D or 3D may be straightforward.

The coordinate x is discretized with mesh size a throughout the large box as shown in Fig. F.2. Mesh points are numbered according to x, i.e., $x_1 < x_2 < \cdots < x_N$, where x_i is the value of x at i-th mesh point. The functions of x at the mesh points are denoted as

$$\phi(x_i) = \phi_i \text{ and } \rho_c(x_i) = \rho_{ci} \ (i = 1, 2, \ldots, N). \tag{F.2.4}$$

The second derivative of the potential ϕ is approximated by the 3-point difference:

$$\frac{d^2\phi(x_i)}{dx^2} = \begin{cases} \dfrac{\phi_{i+1} - 2\phi_i + \phi_{i-1}}{a^2} & (1 < i < N) \\ \dfrac{\phi_2 - 2\phi_1 + \phi_b^<}{a^2} & (i = 1) \\ \dfrac{\phi_b^> - 2\phi_N + \phi_{N-1}}{a^2} & (i = N) \end{cases}, \tag{F.2.5}$$

where the values of ϕ at the two edges of the large box are denoted as $\phi_b^<$ and $\phi_b^>$, which may be computed by the multipole expansion for a 3D case. $\phi_b^<$ ($\phi_b^>$) is the value at the boundary at far left (right) in Fig. F.2.

Regarding ϕ and ρ_c as row vectors, we can write a discretized Poisson equation as the following matrix form

$$\frac{1}{a^2}\begin{pmatrix} 2 & -1 & & & & & \\ -1 & 2 & -1 & & & & \\ & -1 & 2 & -1 & & & \\ & & \ddots & \ddots & \ddots & & \\ & & & & & & \\ & & & \ddots & \ddots & \ddots & \\ & & & & -1 & 2 & -1 \\ & & & & & -1 & 2 \end{pmatrix}\begin{pmatrix} \phi_1 \\ \phi_2 \\ \vdots \\ \\ \\ \\ \vdots \\ \phi_N \end{pmatrix} + \frac{1}{a^2}\begin{pmatrix} -\phi_b^< \\ 0 \\ 0 \\ \vdots \\ \vdots \\ 0 \\ 0 \\ -\phi_b^> \end{pmatrix} = 4\pi\begin{pmatrix} \rho_{c1} \\ \rho_{c2} \\ \vdots \\ \\ \\ \\ \vdots \\ \rho_{cN} \end{pmatrix}$$

or

$$\begin{pmatrix} 2 & -1 & & & & & \\ -1 & 2 & -1 & & & & \\ & -1 & 2 & -1 & & & \\ & & \ddots & \ddots & \ddots & & \\ & & & & & & \\ & & & \ddots & \ddots & \ddots & \\ & & & & -1 & 2 & -1 \\ & & & & & -1 & 2 \end{pmatrix}\begin{pmatrix} \phi_1 \\ \phi_2 \\ \vdots \\ \\ \\ \\ \vdots \\ \phi_N \end{pmatrix} = 4\pi a^2\begin{pmatrix} \rho_{c1} \\ \rho_{c2} \\ \vdots \\ \\ \\ \\ \vdots \\ \rho_{cN} \end{pmatrix} + \begin{pmatrix} \phi_b^< \\ 0 \\ 0 \\ \vdots \\ \vdots \\ 0 \\ 0 \\ \phi_b^> \end{pmatrix}. \tag{F.2.6}$$

The matrix on the left hand side is tridiagonal. Eq. (F.2.6) has the form of

$$A\boldsymbol{x} = \boldsymbol{b}, \tag{F.2.7}$$

where $\boldsymbol{b}$ is a known vector and $\boldsymbol{x}$ is an unknown vector to be obtained by solving the equation.

F.2.3 Numerical method to solve the discretized Poisson equation

The discretized Poisson equation given in Eq. (F.2.6) is solved numerically. Similar to the equation encountered in inversion of single-particle Hamiltonian, it is a large and sparse linear system, which could be efficiently solved by the Krylov iterative methods [133,152]. We employ the conjugate gradient (CG) method [133,152], which is applicable to positive definite A. The numerical algorithm of CG method is already given in Appendix C.

It shares the advantages in common with the other Krylov subspace methods introduced in Appendix C.

- It is not necessary to explicitly store the matrix elements of A nor A^{-1}.
- Only needs matrix-vector operation and scalar product of two vectors.
- Quickly converges if the initial guess for the solution $\boldsymbol{x}_0$ is good.

In self-consistent calculations, we use the solution of the Poisson equation at the previous step as an initial guess for CG iteration. At the first self-consistent iteration, when we solve the Poisson equation for the first time, we input zero vector as an initial guess.

Bibliography

[1] Robert Roth, Angelo Calci, Joachim Langhammer, Sven Binder, Few-Body Systems **55**, 659 (2014).

[2] J. Carlson, Phys. Rev. C **36**, 2026 (1987).

[3] B. S. Pudliner, V. R. Pandharipande, J. Carlson, S. C. Pieper, and R. B. Wiringa, Phys. Rev. C **56**, 1720 (1997).

[4] R. B. Wiringa, Steven C. Pieper, J. Carlson, and V. R. Pandharipande Phys. Rev. C **62**, 014001 (2000).

[5] Bruce R. Barrett, Petr Navrátil, James P. Vary, Prog. Part. Nucl. Phys. **69**, 131 (2013).

[6] H. Kümmel, K. H. Lürhmann, J. G. Zabolitsky, Phys. Rep. C **36**, 1 (1978).

[7] K. Varga and Y. Suzuki, Phys. Rev. C **52**, 2885 (1995).

[8] E. Caurier, G. Martinez-Pinedo, F. Nowacki, A. Poves, and A. P. Zuker, Rev. Mod. Phys. **77**, 427 (2005).

[9] G.F. Bertsch, D.J. Dean, and W. Nazarewicz, SciDAC Review **6**, 42 (2007).

[10] T. H. R. Skyrme, Nucl. Phys. **9** (1959).

[11] J. Decharge and D. Gogny Phys. Rev. C **21**, 1568 (1980).

[12] P. Hohenberg and W. Kohn, Phys. Rev. **136**, B864 (1964).

[13] E. Engel and R. M. Dreizler, *Density Functional Theory* (Springer-Verlag Berlin Heidelberg, 2011).

[14] W. Kohn and L. J. Sham, Phys. Rev. **140**, A1133 (1965).

[15] G. A. Lalazissis, P. Ring, and D. Vretenar, *Extended Density Functionals in Nuclear Physics*, (Springer-Verlag Berlin Heidelberg, 2011).

[16] J. D. Walecka, Ann. Phys. **83**, 491 (1974).

[17] B. D. Serot and J. D. Walecka, Adv. Nucl. Phys. **16**, 1 (1986).

[18] C. J. Horowitz and B. D. Serot, Nucl. Phys. **A368**, 503 (1981).

[19] J. N. Ginocchio, Phys. Rev. Lett. **78**, 436 (1997).

[20] J. N. Ginocchio, Phys. Rep. **414**, 165 (2005)

[21] A. V. Afanasjev and H. Abusara, Phys. Rev. C **81**, 014309 (2010).

[22] A. V. Afanasjev and H. Abusara, Phys. Rev. C **82**, 034329 (2010).

[23] J. Dobaczewski and J. Dudek, Phys. Rev. C **52**, 1827 (1995).

[24] B. L. Berman and S. C. Fultz, Rev. Mod. Phys. **47**, 713 (1975).

[25] J. R. Leigh, N. Rowley, R. C. Lemmon, D. J. Hinde, J. O. Newton, J. X. Wei, J. C. Mein, C. R. Morton, S. Kuyucak, and A. T. Kruppa, Phys. Rev. C **47**, R437 (1993).

[26] T. Inui and Y. Tanabe, and Y. Onodera, 応用群論–群表現と物理学– (Shokabo, 1976).

[27] Bing-Nan Lu, En-Guang Zhao, and Shan-Gui Zhou, Phys. Rev. C **85** 011301(R) (2012).

[28] Bing-Nan Lu, Jie Zhao, En-Guang Zhao, and Shan-Gui Zhou, Phys. Rev. C **89**, 014323 (2014).

[29] I. Hamamoto, B. Mottelson, H. Xie, and X. Z. Zhang, Z. Phys. D **21** 163 (2001).

[30] P. A. Butler and W. Nazarewicz, Rev. Mod. Phys. **68**, 349 (1996).

[31] R. H. Spear and W. N. Catford, Phys. Rev. C **41** R1351 (1990).

[32] L. M. Robledo and G. F. Bertsch, Phys. Rev. C **84**, 054302 (2011).

[33] S. Takami, K. Yabana, M. Matsuo, Phys. Lett. B **431** 242 (1998).

[34] M. Matsuo, S. Takami, K. Yabana AIP Conf. Proc. **481**, 345 (1999); arXiv:nucl-th/9810067 (1998).

[35] M. Yamagami, K. Matsuyanagi, and M.Matsuo, Nucl. Phys. **A693**, 579 (2001).

[36] Xunjun Li and Jerzy Dudek, Phys. Rev. C **49**, R1250 (1994).

[37] J. Dudek, A. Goźdź, N. Schunck, and M. Miśkiewicz, Phys. Rev. Lett. **88**, 252502 (2002).

[38] J. Dudek, D. Curien, N. Dubray, J. Dobaczewski, V. Pangon, P. Olbratowski, and N. Schunck, Phys. Rev. Lett. **97**, 072501 (2006).

[39] Jerzy Dudek, Dominique Curien, David Rouvel, Katarzyna Mazurek, Yoshifumi Shimizu, and Shingo Tagami, arXiv:1404.5777 [nucl-th] (2014).

[40] Jie Zhao, Bing-Nan Lu, En-Guang Zhao, and Shan-Gui Zhou, Phys. Rev. C **86**, 057304 (2012).

[41] Z. P. Li, B. Y. Song, J. M. Yao, D. Vretenar, and J. Meng, Phys. Lett. B **726** 866 (2013).

[42] Christian Beck, *Clusters in Nuclei* Volume 1, (Springer-Verlag Berlin Heidelberg, 2010); *Clusters in Nuclei* Volume 2, (Springer-Verlag Berlin Heidelberg, 2012).

[43] Yoshiko Kanada-En'yo, Masaaki Kimura, and Akira Ono, Prog. Theor. Exp. Phys. 01A202 (2012).

[44] M. Girod and P. Schuck, Phys. Rev. Lett **111**, 132503 (2013).

[45] J.-P. Ebran, E. Khan, T. Nikšić, and D. Vretenar, Nature **487**, 341 (2012).

[46] J.-P. Ebran, E. Khan, T. Nikšić, and D. Vretenar, Phys. Rev. C **87**, 044307 (2013).

[47] J.-P. Ebran, E. Khan, T. Nikšić, and D. Vretenar, arXiv:1402.5080 [nucl-th] (2014).

[48] K. T. R. Davies, H. Flocard, S. Krieger, and M. S. Weiss, Nucl. Phys. A **342**, 111 (1980).

[49] P. Bonche, H. Flocard, and P. H. Heenen, Comput. Phys. Commun. **171**, 49 (2005).

[50] N. Tajima, S. Takahara, N. Onishi, Nucl. Phys. **A603**, 23 (1996).

[51] N. Tajima, Prog. Theor. Phys. Supplement **142**, 265 (2001).

[52] T. Inakura, T. Nakatsukasa, and K. Yabana, Phys. Rev. C **84**, 021302(R) (2011).

[53] M. Yamagami, K. Matsuyanagi, Nucl. Phys. **A672**, 123 (2000).

[54] T. Ichikawa, J. A. Maruhn, N. Itagaki, and S. Ohkubo, Phys. Rev. Lett. **107**, 112501 (2011).

[55] T. Ichikawa, J. A. Maruhn, N. Itagaki, K. Matsuyanagi, P.-G. Reinhard, and S. Ohkubo, Phys. Rev. Lett. **109**, 232503 (2012).

[56] Myaing Thi Win, K. Hagino, and T. Koike, Phys. Rev. C **83**, 014301 (2011).

[57] J. Terasaki, R.-H. Heenen, H. Flocard, R Bonche, Nucl. Phys. **A600**, 371 (1996).

[58] Bing-Nan Lu, En-Guang Zhao, and Shan-Gui Zhou, Phys. Rev. C **84**, 014328 (2011).

[59] Bing-Nan Lu, Emiko Hiyama, Hiroyuki Sagawa, Shan-Gui Zhou, arXiv:1403.5866 [nucl-th] (2014).

[60] Shan-Gui Zhou, Jie Meng, P. Ring, and En-Guang Zhao, Phys. Rev. C **82**, 011301(R) (2010).

[61] Lulu Li, Jie Meng, P. Ring, En-Guang Zhao, and Shan-Gui Zhou, Phys. Rev. C **85** 024312 (2012).

[62] Ying Chen, Lulu Li, Haozhao Liang, and Jie Meng Phys. Rev. C **85** 067301 (2012).

[63] Shan-Gui Zhou, Jie Meng, and P. Ring, Phys. Rev. C **68**, 034323 (2003).

[64] P. Ring, Prog. Part. Nucl. Phys. **37**, 193 (1996).

[65] P. Ring, Zhong-yu Ma, Nguyen Van Giai, D. Vretenar, A. Wandelt, and Li-gang Cao, Nucl. Phys. **A694**, 249 (2001).

[66] P. Ring and P. Schuck, *The Nuclear Many-Body Problem*, (Springer-Verlag Berlin Heidelberg, 1980).

[67] E. A. McCutchan, Nuclear Data Sheets **113**, 1735 (2012).

[68] B. Singh, Nuclear Data Sheets **105**, 223 (2005).

[69] W. Kohn, Rev. Mod. Phys. **71**, 1253 (1998)

[70] D. Vautherin and D. M. Brink, Phys. Rev. C **5**, 626 (1972).

[71] D. Vautherin, Phys. Rev. C **7**, 296 (1973).

[72] W. Pannert, P. Ring, and J. Boguta Phys. Rev. Lett. **59**, 2420 (1987).

[73] P. Bonche, H. Flocard, P. H. Heenen, S. J. Krieger, and M. S. Weiss, Nucl. Phys. A **443**, 39 (1985).

[74] H. Flocard, S. E. Koonin, and M. S. Weiss, Phys. Rev. C **17**, 1682 (1978).

[75] M. Stoitsov, P. Ring, D. Vretenar, and G. A. Lalazissis Phys. Rev. C **58** 2086 (1998).

[76] A. Staszczak, M. Stoitsov, A. Baran, and W. Nazarewicz, Eur. Phys. J. **A46**, 85 (2010).

[77] K. Rutz, J. A. Maruhn, P.-G. Reinhard, and W. Greiner, Nucl. Phys. **A590**, 680 (1995).

[78] D. Vretenar, A.V. Afanasjev, G. A. Lalazissis, and P. Ring, Phys. Rep. **409**, 101 (2005).

[79] J. Meng, H. Toki, S.G. Zhou, S.Q. Zhang, W.H. Long, L.S. Geng, Prog. Part. Nucl. Phys. **57**, 470 (2006).

[80] T. Nikšić, D. Vretenar, and P. Ring, Prog. Part. Nucl. Phys. **66**, 519 (2011).

[81] P. Manakos and T. Mannel, Z. Phys. A **330**, 223 (1988).

[82] B. A. Nikolaus, T. Hoch, and D. G. Madland, Phys. Rev. C **46**, 1757 (1992).

[83] T. Nikšić, D. Vretenar, G. A. Lalazissis, and P. Ring, Phys. Rev. C **77**, 034302 (2008).

[84] T. Bürvenich, D. G. Madland, J. A. Maruhn, and P.-G. Reinhard, Phys. Rev. C **65**, 044308 (2002).

[85] P. W. Zhao, Z. P. Li, J. M. Yao, and J. Meng, Phys. Rev. C **82**, 054319 (2010).

[86] T. Nikšić, D. Vretenar, and P. Ring, Phys. Rev. C **78**, 034318 (2008).

[87] M. E. Peskin and D. V. Schröder, *An Introduction to Quantum Field Theory*, (Westview Press, 1995).

[88] T. Hoch, D. Madland, P. Manakos, T. Mannel, B.A. Nikolaus, D. Strottman, Phys. Rep. **242**, 253 (1994).

[89] D. G. Madland, T. J. Bürvenich, J. A. Maruhn, and P.-G. Reinhard, Nucl. Phys. **A741**, 52 (2004).

[90] A. Sulaksono, T. Bürvenich, J. A. Maruhn, P.-G. Reinhard, W. Greiner, Ann. Phys. **306**, 36 (2003).

[91] J. A. Maruhn, T. Bürvenich, and D. G. Madland, J. Comput. Phys. **169**, 238 (2001).

[92] Haozhao Liang, Pengwei Zhao, Peter Ring, Xavier Roca-Maza, and Jie Meng, Phys. Rev. C **86**, 021302(R), (2012).

[93] J. Boguta and A. R. Bodmer, Nucl. Phys. **A292**, 413 (1977).

[94] G. A. Lalazissis, J. König, and P. Ring, Phys. Rev. C **55** 540 (1997).

[95] Y. Sugahara and H. Toki, Nucl. Phys. **A579**, 557 (1997).

[96] T. Nikšić, D. Vretenar, P. Finelli and P. Ring, Phys. Rev. C **66** 024306 (2002).

[97] G. A. Lalazissis, T. Nikšić, D. Vretenar, and P. Ring, Phys. Rev. C **71** 024312 (2005).

[98] W. H. Long, Nguyen van Giai, S. G. Zhou, S. Q. Zhang, Phys. Rev. C **69** 034319 (2004).

[99] X. Roca-Maza, X. Viñas, M. Centelles, P. Ring, and P. Schuck, Phys. Rev. C **84**, 054309 (2011).

[100] R. Brockmann and H. Toki, Phys. Rev. Lett. **68**, 3408 (1992).

[101] M. Baldo, P. Schuck, and X. Viñas, Phys. Lett. B **663**, 390 (2008).

[102] D. Vretenar, W. Pöschl, G. A. Lalazissis, and P. Ring, Phys. Rev. C **57**, R1060 (1998).

[103] M. M. Sharma, G. Lalazissis, J. König, and P. Ring, Phys. Rev. Lett. **74**, 3744 (1995).

[104] N. Tajima, P. Bonche, H. Flocard, P.-H. Heenen, and M. S. Weiss, Nucl. Phys. **A551** 434 (1993).

[105] M. M. Sharma, G. A. Lalazissis, and P. Ring, Phys. Lett. **B317**, 9 (1993).

[106] P.-G. Reinhard, M. Rufa, J. Maruhn, W. Greiner, and J. Friedrich, Z. Phys. A **323**, 13 (1986).

[107] M. M. Sharma, M. A. Nagarajan, and P. Ring, Phys. Lett. **B312** (1993) 377

[108] P.-G. Reinhard and H. Flocard Nucl. Phys. **A584** 467 (1995).

[109] P. M. Goddard, P. D. Stevenson, and A. Rios, Phys. Rev. Lett. **110**, 032503 (2013).

[110] G. A. Lalazissis, D. Vretenar, W. Pöschl, and P. Ring, Phys. Lett. **B418**, 7 (1998).

[111] G. A. Lalazissis, D. Vretenar, and P. Ring, Phys. Rev. C **57**, 2294 (1998).

[112] Satoshi Yoshida and Hiroyuki Sagawa, Phys. Rev. C **69**, 024318 (2004).

[113] Satoshi Yoshida and Hiroyuki Sagawa, Phys. Rev. C **73**, 044320 (2006).

[114] Satoshi Yoshida and Hiroyuki Sagawa, J. Phys.: Conf. Ser. **321** 012059 (2011).

[115] L. Geng, H. Toki, and J. Meng, Prog. Theor. Phys. **113**, 785 (2005).

[116] L. Geng, J. Meng, H. Toki, W. Long, and S. Gang, Chin. Phys. Lett. **23**, 1139 (2006).

[117] W. H. Long, H. Sagawa, Nguyen Van Giai, and J. Meng, Phys. Rev. C **76**, 034314 (2007).

[118] K. Konishi and G. Paffuti, *Quantum Mechanics A New Introduction* (Oxford University Press, 2009).

[119] G. W. Stewart, *Matrix Algorithms vol. I* (Society for Industrial and Applied Mathematics, 1998); *Matrix Algorithms vol. II* (Society for Industrial and Applied Mathematics, 2001).

[120] S. E. Koonin and D. C. Meredith, *Computational Physics*, (Addison-Wesley, 1990).

[121] Y. S. Lee and A. D. McLean, J. Chem. Phys. **76**, 735 (1982).

[122] Y. Ishikawa, R. C. Binning, Jr., K. M. Sando, Chem. Phys. Lett. **101**, 111 (1983).

[123] R. E. Stanton and S. Havriliak, J. Chem. Phys. **81**, 1910 (1984).

[124] F. A. Parpia and A. K. Mohanty, Phys. Rev. A **52**, 962 (1995).

[125] H. Wallmeier and W. Kutzelnigg, Chem. Phys. Lett. **78**, 341 (1981).

[126] H. Wallmeier and W. Kutzelnigg, Phys. Rev. A **28**, 3092 (1983).

[127] Y. Zhang, H. Liang, and J. Meng, Int. J. Mod. Phys. E **19**, 55 (2010).

[128] Y. Zhang, H. Liang, and J. Meng, Chin. Phys. Lett. **26**, 092401 (2009).

[129] R. N. Hill and C. Krauthauser, Phys. Rev. Lett. **72**, 2151 (1994).

[130] P. Falsaperla, G. Fonte, J. Z. Chen, Phys. Rev. A **56**, 1240 (1997).

[131] K. Hagino and Y. Tanimura, Phys. Rev. C **82**, 057301 (2010).

[132] W. Koepf and P. Ring, Z. Phys. A **339**, 81 (1991).

[133] Y. Saad, *Iterative Methods for Sparse Linear Systems* (Society for Industrial and Applied Mathematics, Philadelphia, PA, 2003).

[134] K. G. Wilson, *New Phenomena in Subnuclear Physics*, Part A, The Subnuclear Series Volume 13, 69 (1977).

[135] J. B. Kogut, Rev. Mod. Phys. **55**, 775 (1983).

[136] Oliver Busic, Norbert Grün, Werner Scheid, Phys. Lett. A **254**, 337 (1999).

[137] Francois Fillion-Gourdeau, Emmanuel Lorin, Andre D. Bandrauk, Comput. Phys. Commun. **183**, 1403 (2012).

[138] A. R. Hernández and C. H. Lewenkopf Phys. Rev. B **86**, 155439 (2012).

[139] J. J. Sakurai, *Advanced Quantum Mechanics* (Addison-Wesley, Redwood City, CA, 1967).

[140] W. Greiner, *Relativistic Quantum Mechanics* (Springer-Verlag, Berlin, 1997).

[141] L. M. Robledo and G. F. Bertsch, Phys. Rev. C **84**, 014312 (2011).

[142] Q. S. Zhang, Z. M. Niu, Z. P. Li, J. M. Yao, and J. Meng, arXiv:1305.1736v2 [nucl-th] (2014).

[143] J. J. Sakurai, *Modern Quantum Mechanics*, (Addison-Wesley, 1994).

[144] J Dudek, A Góźdź, K Mazurek, and H Molique, J. Phys. G**37**, 064032 (2010).

[145] N. Schunck, J. Dudek, A. Góźdź, and P. H. Regan, Phys. Rev. C **69**, 061305(R) (2004).

[146] Shingo Tagami, Yoshifumi R. Shimizu, and Jerzy Dudek, Phys. Rev. C **87**, 054306 (2013).

[147] C. J. Lister *et al.*, Phys. Rev. Lett. **59**, 1270 (1987).

[148] S. M. Fischer *et al.*, Phys. Rev. Lett. **87**, 132501 (2001).

[149] R. A. Bark, *et al.*, Phys. Rev. Lett. **104**, 022501 (2010).

[150] M. Jentschel, *et al.*, Phys. Rev. Lett. **104**, 222502 (2010).

[151] T. Sumikama, *et al.*, Phys. Rev. Lett. **106**, 202501 (2011).

[152] H. A. Van der Vorst, *Iterative Krylov Methods for Large Linear Systems* (Cambridge University Press, Cambridge, England, 2003).

[153] T. Nakatsukasa and K. Yabana, Phys. Rev. C **71**, 024301 (2005).

[154] Y. Tanimura, K. Hagino, and P. Ring, Phys. Rev. C **88**, 017301 (2013).

[155] D. M. Brink and R. A. Broglia, "*The Nuclear Superfluidity Pairing in Finite Systems*", (Cambridge University Press, 2005).

[156] M. Bender, P.-H. Heenen, and P.-G. Reinhard, Rev. Mod. Phys. **75**, 121 (2003).

[157] J. Dobaczewski, W. Nazarewicz, T. R. Werner, J. F. Berger, C. R. Chinn, and J. Dechargé, Phys. Rev. C **53**, 2809 (1996).

[158] N. Tajima, Phys. Rev. C **69**, 034305 (2004).

[159] M. Kohno, Y. Fujiwara, and Y. Akaishi, Phys. Rev. C **68**, 034302 (2003); I. Hamamoto and B. R. Mottelson, ibid. **69**, 064302 (2004).

[160] K. Hagino and H. Sagawa, Phys. Rev. C **71**, 044302 (2005).

[161] Y. Tanimura and K. Hagino, Phys. Rev. C **85**, 014306 (2012).

[162] J. Cohen and H. J. Weber, Phys. Rev. C **44**, 1181 (1991).

[163] Y. Sugahara and H. Toki, Prog. Theor. Phys. **92**, 803 (1994).

[164] O. Hashimoto and H. Tamura, Prog. Part. Nucl. Phys. **57**, 564 (2006).

[165] Q. N. Usmani and A. R. Bodmer, Phys. Rev. C **60**, 055215 (1999).

[166] T. Motoba, Nucl. Phys. **A639**, 135c (1998).

[167] B. Alder, S. Fernbach, and M. Rotenberg, *Methods in Computational Physics vol. 6 Nuclear Physics* (Academic Press, New York and London, 1966).

[168] J. Mareš and B. K. Jennings, Phys. Rev. C **49**, 2472 (1994).

[169] C. Y. Song, J. M. Yao, H. F. Lü, and J. Meng, Int. J. Mod. Phys. E **19**, 2538 (2010).

[170] K. Tsubakihara, H. Maekawa, H. Matsumiya, and A. Ohnishi, Phys. Rev. C **81**, 065206 (2010).

[171] R. J. Furnstahl and B. D. Serot, Nucl. Phys. **A671**, 447 (2000).

[172] P. Finelli, N. Kaiser, D. Vretenar, and W. Weise, Nucl. Phys. **A770**, 1 (2006).

[173] P. Finelli, N. Kaiser, D. Vretenar, and W. Weise, Nucl. Phys. A **831** 163 (2009); P. Finelli, ibid. **835**, 418 (2010).

[174] H. Mei, K. Hagino, J. M. Yao, T. Motoba, arXiv:1406.4604 [nucl-th] (2014).

[175] S. Dürr and G. Koutsou, Phys. Rev. D **83** 114512 (2011).

[176] W. F. Spotz and G.F. Carey, Num. Meth. Part. Diff. Eqs. **12**, 235 (1996).

[177] M. M. Gupta and J. Kouatchou, Num. Meth. Part. Diff. Eqs. **14**, 593 (1998).

[178] A. Kumar, J. Comput. Phys. **201**, 109 (2004).

[179] M. Patra and M. Karttunen, Num. Meth. Part. Diff. Eqs. **22**, 936 (2006).

[180] S. Fujinaga and S. Narita, 化学や物理のためのやさしい群論入門 (Iwanami Shoten, 2001).

[181] H. Georgi, *Lie Algebras in Particle Physics*, (Westview Press, 1999).

[182] H. Georgi, *Weak Interactions and Modern Particle Theory*, (Dover Publications, Mineola, New York,2009).

[183] I. Talmi, *Simple Models of Complex Nuclei*, (Harwood Academic Publishers, 1993).

[184] D. J. Rowe and J. L. Wood, *Fundamentals of Nuclear Models*, (World Scientific, Singapore, 2010).

[185] D. A. Varshalovich, A. N. Moskalev, and V. K. Khersonskii, *Quantum Theory of Angular Momentum*, (World Scientific, 1988).

[186] Bing-Nan Lu, Timo A. Lähde, Dean Lee, Ulf-G. Meissner, arXiv:1403.8056 [nucl-th] (2014).

[187] M. Bender, K. Rutz, P.-G. Reinhard, J. A. Maruhn, Eur. Phys. J. A **7**, 467 (2000).